



National Nanotechnology Infrastructure Network Research Experience for Undergraduates (NNIN REU) Programs

2014 NNIN REU RESEARCH ACCOMPLISHMENTS

— 20 μ m

National Nanotechnology Infrastructure Network

***Research Experience for Undergraduates
(NNIN REU) Program***

***International Research Experience
for Graduates (NNIN iREG) Program***

***International Research Experience
for Undergraduates (NNIN iREU) Program***

2014
Research
Accomplishments





The National Nanotechnology Infrastructure Network (NNIN) is an integrated partnership of fourteen user facilities, supported by the National Science Foundation. NNIN provides opportunities for nanoscience and nanotechnology research, including support in fabrication, synthesis, characterization, modeling, design, computation, and hands-on training in an open environment. While all fourteen sites did not participate in the 2014 NNIN REU Program, the members are:



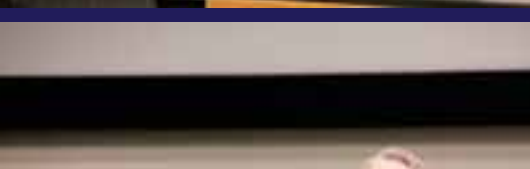
ASU NanoFab, Arizona State University



Cornell NanoScale Science & Technology Facility,
Cornell University



Institute for Electronics and Nanotechnology,
Georgia Institute of Technology



Center for Nanoscale Systems, Harvard University



Howard Nanoscale Science & Engineering Facility,
Howard University



Penn State Nanofabrication Facility,
The Pennsylvania State University



Stanford Nanofabrication Facility, Stanford University

UCSB Nanofabrication Facility,
University of California, Santa Barbara

Colorado Nanofabrication Laboratory,
University of Colorado, Boulder

Lurie Nanofabrication Facility,
University of Michigan, Ann Arbor

Minnesota Nano Center, University of Minnesota

Microelectronics Research Center,
The University of Texas at Austin

Washington Nanofabrication Facility &
Molecular Analysis Facility, University of Washington

Nano Research Facility, Washington University at St. Louis

<http://www.nnin.org/>

2014 NNIN REU

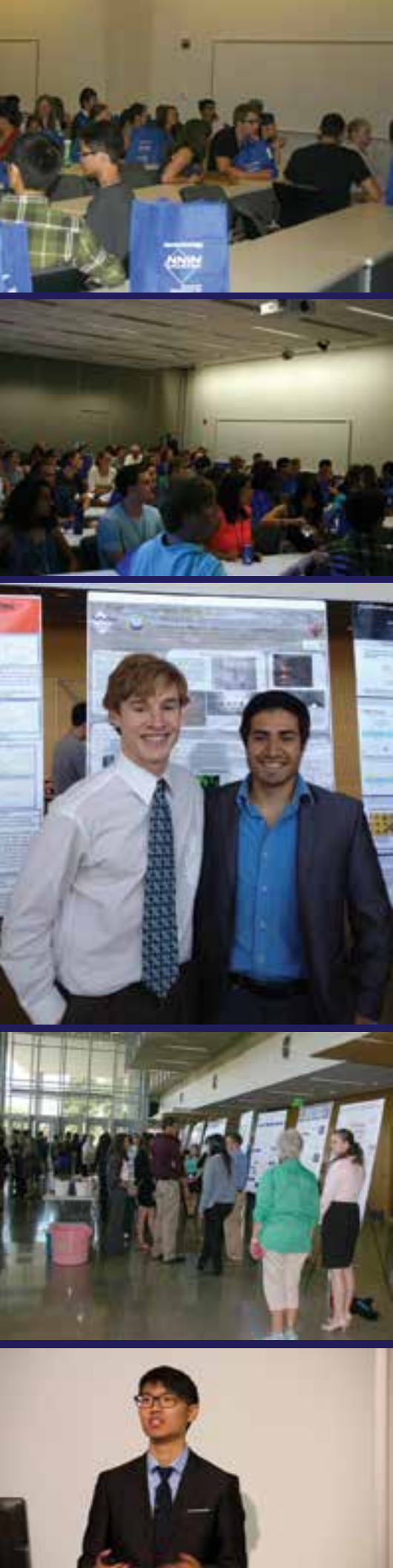
Research

Accomplishments

TABLE OF CONTENTS

2014 NNIN REU REPORTS BY SECTION	IV-XIII
2014 NNIN REU PHOTOGRAPH CREDITS	XIII
2014 NNIN REU CORPORATE SPONSORS	XIV
2014 NNIN REU DIRECTORS' INTRODUCTION	XV
2014 NNIN REU INTERNS BY NNIN SITE	
1. <i>Arizona State University, page xvi</i>	
2. <i>Cornell University, page xvii</i>	
3. <i>Georgia Institute of Technology, page xviii</i>	
4. <i>Harvard University, page xix</i>	
5. <i>Howard University, xx</i>	
6. <i>The Pennsylvania State University, page xxi</i>	
7. <i>Stanford University, page xxii</i>	
8. <i>University of California, Santa Barbara, page xxiii</i>	
9. <i>The University of Michigan, Ann Arbor, page xxiv</i>	
10. <i>University of Minnesota-Twin Cities, page xxv</i>	
11. <i>University of Washington, page xxvi</i>	
12. <i>2014 NNIN iREG, page xxvii</i>	
13. <i>2014 NNIN iREU, page xxviii</i>	
COMMONLY USED ABBREVIATIONS AND THEIR MEANINGS	XXIX-XXXVI
2014 NNIN REU RESEARCH ACCOMPLISHMENTS	1-149
INDEX OF REPORTS, BY NNIN SITE	151
INDEX OF INTERNS, MENTORS, AND PRINCIPAL INVESTIGATORS	152-156





BIOLOGICAL APPLICATIONS, PAGES 2-41

Development of PDMS Microstructures for the Investigation of Cardiac Cell Function..... 2

Allison Bosworth, Biological Engineering, Louisiana State University
NNIN REU Site: Cornell University

High-Throughput Drug Screening *in vivo* Using Droplet Microfluidics.... 4

Carlos J. Brambila, Biology-Emphasis in Bioengineering, San Diego State University
NNIN REU Site: Harvard University

Sphingosine 1-Phosphate Functionalized Nanopatterned Scaffolds for Engineering Vascularized Skeletal Muscle Tissue..... 6

Eve Byington, Biological and Environmental Engineering, Cornell University
NNIN REU Site: University of Washington

The Disruption and Control of Microbial Biofilms..... 8

Steven Ceron, Mechanical Engineering, University of Florida
NNIN REU Site: Harvard University

Regulation of the Immune System by DNA-Drug Nanomaterials 10

Samantha Renee Corber, Chemistry & Physics, Washburn University
NNIN iREU Site: NIMS, Japan

Development of Diamond-Like Carbon Deposition Processes and Microfabrication of Thin-Film Ag/AgCl Reference Electrodes.. 12

Christopher Davidson, Biological Systems Engr., University of Nebraska – Lincoln
NNIN REU Site: University of Minnesota

Microfluidic Bio-Sensing for *in vitro* Tumor Cell Proliferation..... 14

Fatima-Joyce Dominguez, Electrical Engineering, University of Portland
NNIN REU Site: Arizona State University

Developing a Novel Microfluidic Device for the Study of Molecular Communication Between Bacterial Colonies..... 16

Lucy Hu, Bioengineering, University of California, Berkeley
NNIN REU Site: Georgia Institute of Technology

A Microfluidic Approach to Stiffness Gradient Generation in Polyacrylamide-Based Cell Migration Analysis Platforms 18

Meghan Kazanski, Biomedical Engineering, University of Rochester
NNIN iREU Site: NIMS, Japan

Development of Zeolite-Based Nanofibers for the Removal of Uremic Toxins in Kidney Removal Patients..... 20

Gabriel R. López Marcial, Mechanical Eng., University of Puerto Rico at Mayaguez
NNIN iREU Site: NIMS, Japan

The Interaction of Cytotoxins with a Lipid Membrane Library 22

David Morse, Physics/Biophysics, The University of Tennessee, Knoxville
NNIN REU Site: Harvard University

Fabrication of Nanochannels for Linearization and Diffusion of DNA .. 24

Mark Pagkaliwangan, Chemical Engineering, University of Massachusetts Amherst
NNIN REU Site: University of Minnesota

Effects of Adhesion Layers in Silver Plasmonic Nanostructures for Surface Enhanced Raman Spectroscopy 26

Ashka Shah, Physics, Harvey Mudd College
NNIN REU Site: Stanford University

**Effects of Gold Nanoparticle Size and Functional Group
on Adipogenesis of Mesenchymal Stem Cells 28**

Peter Su, Chemical and Biomolecular Engineering, University of California, Berkeley
NNIN iREU Site: NIMS, Japan

**Label-Free Detection of *Escherichia coli* using
Silicon Nanophotonic Biosensors 30**

Emily Thompson, Biomedical Engineering, Arizona State University
NNIN REU Site: University of Washington

**Integration of Highly Porous Membranes
with Microfluidic Body-on-a-Chip Devices 32**

Hidetaka Ueno, Department of Biomedical Engineering, Kagawa University, Japan
NNIN iREG Site: Cornell University

**Direct Writing for Biological Applications:
Cell Patterning into Micro-fluidic Channels
and Nanoparticle Writing onto Patterned Substrate 34**

Benjamin Vizy, Biological Engineering, Purdue University
NNIN REU Site: University of Michigan

**Functionalization of 6H Highly Doped Silicon Carbide
Surfaces for Determining Cell Electrophysiology 36**

Kaleel Wainwright, Biology, Columbia University
NNIN REU Site: Howard University

**Microfabricated Cell Array Device
for Screening of Metastatic Potential 38**

James Paul Wondra, II, Biology, California State University Channel Islands
NNIN REU Site: University of Minnesota

**Controlling Biofilm Formation Through
the Use of Conducting Polymers 40**

Ashlyn Young, Biomedical Engineering, University of North Carolina at Chapel Hill
NNIN iREU Site: Centre Microélectronique de Provence, France



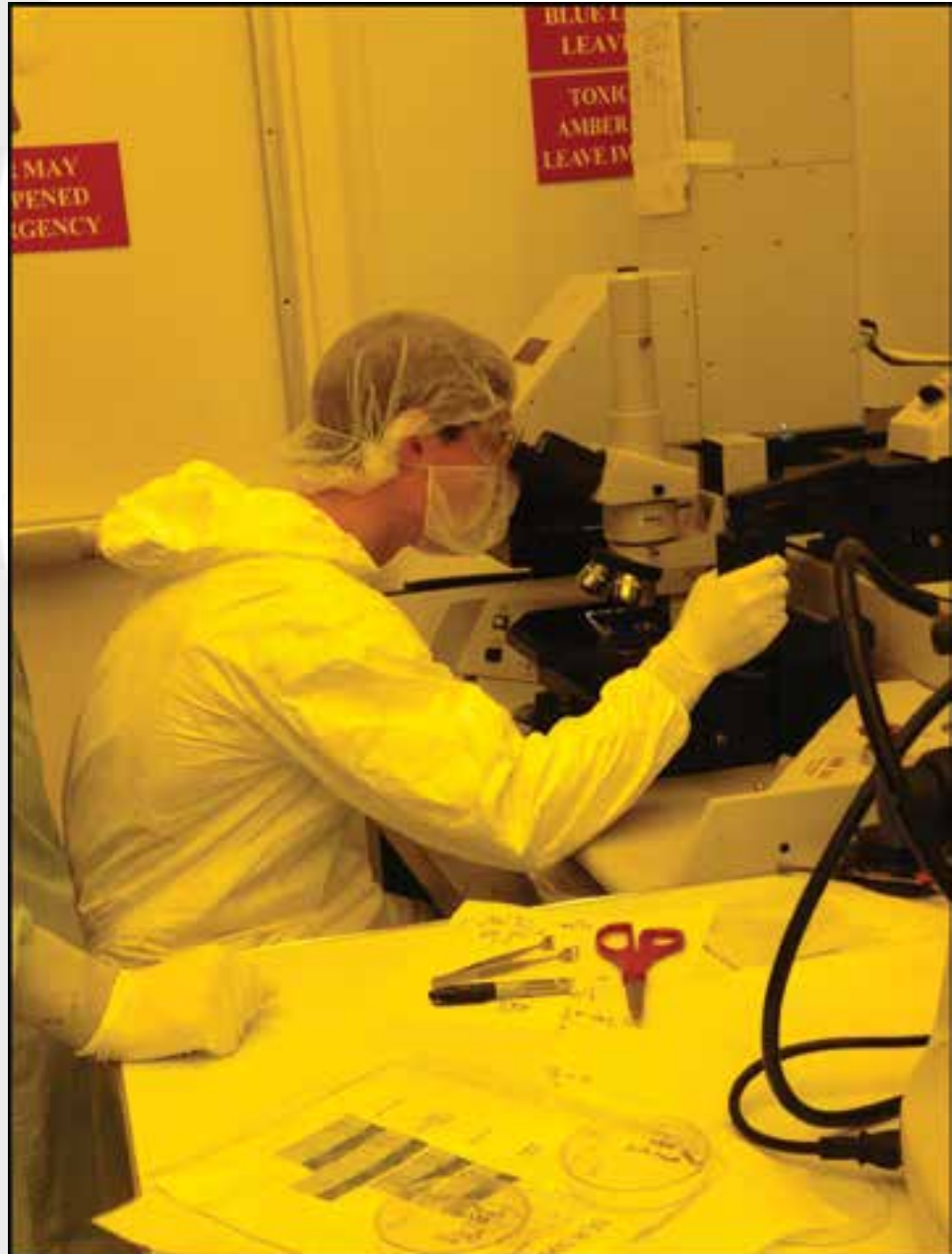
CHEMISTRY, PAGES 42-45

Self-Assembled Structures Through Triblock Terpolymers Forming Gyroid Structures 42

Shinsuke Hirata, Graduate School of Engineering, Kyushu University, Japan
NNIN iREG Site: Cornell University

Developing Methodology for Living Polymerization of Functionalized Conjugated Monomers using Nickel Catalysts with Electron-Rich Phosphine Ligands..... 44

John Ren, Chemical Engineering, Oregon State University
NNIN REU Site: University of Washington



ELECTRONICS, PAGES 46-55

Studying the Effect of Materials and Processing on the Electrical Properties of Bilayer Al / Amorphous CoTiN Metal Gates for Advanced Nanoelectronic Devices	46
<i>William Anderson, Electrical and Computer Engineering, Baylor University NNIN REU Site: Stanford University</i>	
Optimization of Hybrid Fuel Cell Designs and Materials	48
<i>Fausto Mares-Davila, Chemical Engineering, The University of Arizona NNIN REU Site: Georgia Institute of Technology</i>	
Interlayer Dielectric and Interconnect for Heterointegration	50
<i>Julie Miller, Chemical Engineering, The Pennsylvania State University NNIN REU Site: University of Michigan</i>	
Aluminum Oxide for Surface Passivation in Photovoltaics	52
<i>Tara Nietzold, Materials Science Engineering, Rutgers University NNIN REU Site: Arizona State University</i>	
Fabrication of Five-Terminal Laterally-Actuated Nano-Electro-Mechanical (NEM) Relays.....	54
<i>Shanel Wu, Physics, Harvey Mudd College NNIN REU Site: Stanford University</i>	





MATERIALS, PAGES 56-105

Applications of Atomic Layer Deposition of Tin Oxide 56

Sunny Aggarwal, Chemical Engineering, City College of New York
NNIN REU Site: The Pennsylvania State University

Bimetallic Nanocrystals and Their Optical Properties 58

Nnenna E. Dieke, Chemistry, Agnes Scott College
NNIN REU Site: Georgia Institute of Technology

Selective Area Atomic Layer Deposition: Developing Techniques that will Enable Single-nm Technologies 60

Alicia M. Elliott, Engineering Science, Stony Brook University
NNIN REU Site: Cornell University

Directed Assembly of Nanowires in AC Fields: Tuning Wire Design and Electrode Geometry to Observe Ordered Arrays 62

Robyn Emery, Biology, Northwest University
NNIN REU Site: The Pennsylvania State University

Early Hydration of Portland Limestone Cements Monitored by Raman Spectroscopy 64

Dylan J. Freas, Chemistry, Williams College
NNIN REU Site: Georgia Institute of Technology

Extent of Dopant Activation after Microwave and Rapid Thermal Anneals Using Similar Heating Profiles 66

Taliya Gunawansa, Optical Engineering, Norfolk State University
NNIN REU Site: Arizona State University

Characterizing TiN Resistivity using PEALD with TDMAT 68

Matthew Hartensveld, Microelectronic Engr., Rochester Institute of Technology
NNIN REU Site: University of California, Santa Barbara

Aluminum-Induced Crystallization of Amorphous Silicon on Patterned Substrates 70

Jon-L Innocent-Dolor, Chemical Engineering, Syracuse University
NNIN REU Site: The Pennsylvania State University

Fabrication of Low-Density Vertically Aligned CNT Forests 72

Yasuhiro Kimura, Mechanical Engineering, Tohoku University, Japan
NNIN iREG Site: Georgia Institute of Technology

Synthesis, Device Fabrication, and Characterization of Two-Dimensional Transition Metal Dichalcogenides 74

Matthew Koehler, Mechanical Engineering, The University of Saint Thomas
NNIN REU Site: The Pennsylvania State University

Growth of Boron Nitride for Two-Dimensional Applications 76

Tewa Kpulun, Physics and Math, Vassar College
NNIN REU Site: Howard University

Investigation of Nanodiamond Foil Product for H- Stripping to Support Spallation Neutron Source 78

Rachel Lim, Materials Science, Rice University
NNIN REU Site: Howard University

Characterization and Modeling of Carrier Dynamics in Thin Films of Gallium Nitride 80

Rachel Lucas, Physics/Aerospace Engineering, Purdue University
NNIN REU Site: University of California, Santa Barbara

Decreasing Contact Resistance to n-InGaAs with ALD TiN 82

Brian Markman, MSE, The Pennsylvania State University
NNIN REU Site: University of California, Santa Barbara

Using Fluid Dynamics Modeling to Guide the Fabrication of Patterned Shearing Blades for the Solution Deposition of Single-Crystalline Organic Semiconductor Thin Films 84

Geoffrey C. Martin-Noble, Chemistry and Computer Science, Haverford College
NNIN REU Site: Stanford University

Characterization of InAs/AlSb/GaSb Heterostructures When Exposed to *in situ* Plasma Cleans in an ALD Process 86

Marlee Motes, Chemical Engineering, University of Arkansas
NNIN REU Site: University of California, Santa Barbara

Cohesion and Adhesion in Thin-Film Organic Nanostructured Materials for Photovoltaic Applications 88

G. Emily Nitzberg, Mechanical Engr. & Computer Science, University of Portland
NNIN REU Site: Stanford University

Patterning Silicon Nanowire Arrays using EBL 90

Matthew Salmon, Chemical Engineering, North Carolina State University
NNIN REU Site: Georgia Institute of Technology

Mechanical Properties of Hierarchical Nanoporous Metal 92

Aki Sato, Chitose Institute of Science and Technology, Japan
NNIN iREG Site: Georgia Institute of Technology

Nanoparticle Photoresists: Synthesis and Characterization of Next-Generation Patterning Materials 94

Pavel Shapurenska, Chemical Engineering, City College of New York
NNIN REU Site: Cornell University

The Optimization of High Growth Rate GaN Thin Film Mobility 96

Bethany Smith, Materials Science and Engineering, Arizona State University
NNIN REU Site: University of California, Santa Barbara

Doping in Spray-Deposited Fe₂O₃ for Next-Generation Photovoltaics... 98

Wesley Tatum, Physics and Physical Chemistry, Whitworth University
NNIN REU Site: Arizona State University

Investigation of Straight-Edge Graphene Grown via Segregation on Ni(110) using Scanning Tunneling Microscopy.... 100

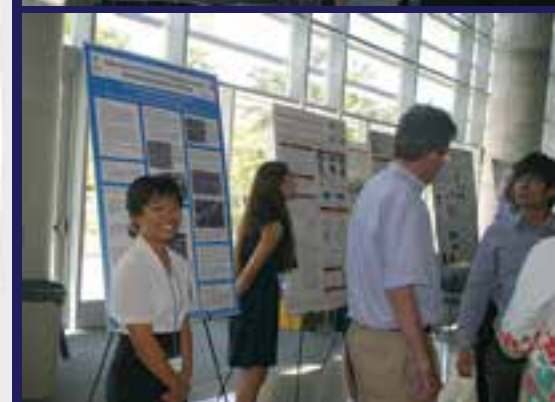
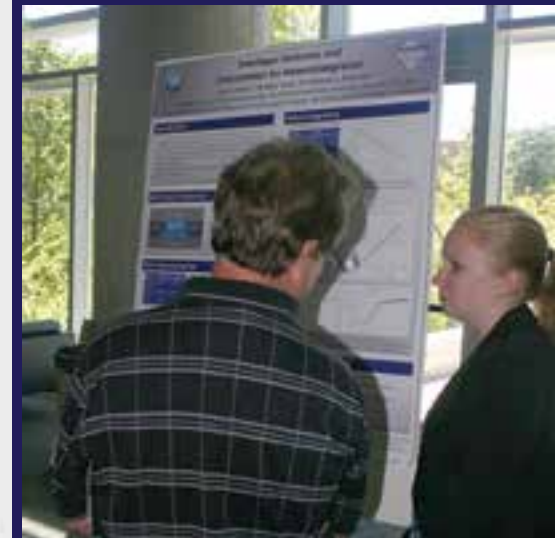
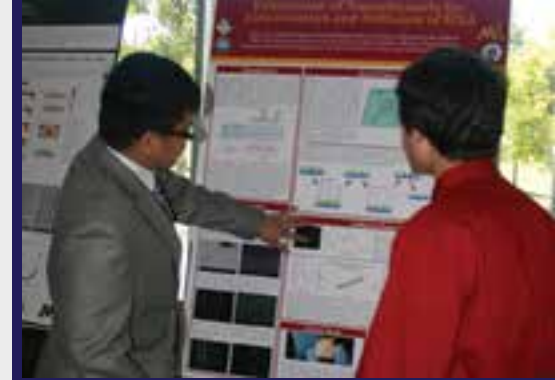
**Jill Wenderott, Physics, University of Kansas,
Materials Science and Engineering, University of Michigan**
NNIN iREU Site: NIMS, Japan

BiO(ClBr)_{(1-x)/2}I_x Solid Solutions with Controllable Band Gap Engineering as Efficient Visible-Light Photocatalysts for Wastewater Treatment 102

Connie Wu, Electrical Engineering and Economics, University of Pennsylvania
NNIN iREU Site: NIMS, Japan

Effects of Doping on Boride Thermoelectrics 104

Allison Wustrow, Chemistry, University of California Berkeley
NNIN iREU Site: NIMS, Japan





MECHANICAL DEVICES, PAGES 106-111

Design and Fabrication of a Microfluidic Device to Study Tumor Cell Mechanics During Metastasis 106

Michael Homsy, Chemical Engineering, The Ohio State University
NNIN REU Site: The Pennsylvania State University

Microfabrication and Dynamic Testing of Electromagnetic Microactuators for Endomicroscopy 108

Samantha Kang, Mechanical Engineering, University of Washington, Seattle
NNIN REU Site: University of Michigan

A Tri-Axial Angular Accelerometer for Vestibular Prostheses 110

Yu Kitamura, Graduate School of Engineering, Kobe University, Japan
NNIN iREG Site: Georgia Institute of Technology

OPTICS & OPTO-ELECTRONICS, PAGES 112-121

Photovoltaic Devices Made from Plasma-Doped Two-Dimensional Layered Semiconductors 112

Samuel Arthur, Physics, Colby College
NNIN REU Site: University of Michigan

Bio-Inspired Surface Treatments and Quasi-Ordered Nanostructures to Control Broadband IR Response 114

Lesley Chan, Chemical Engineering, University of Southern California
NNIN REU Site: University of California, Santa Barbara

Study of Cerium Doped TiG Thin Films for Magneto-Optical Applications 116

Emiliana Cofell, Physics, Scripps College
NNIN REU Site: University of Minnesota

Particle Sorting on Microfluidic Chips using Optical Forces 118

Brandon Foley, Chemical Engineering, University of Wisconsin – Madison
NNIN REU Site: Harvard University

Opto-Electronic Characterization of Narrow Band Gap Semiconductors at Cryogenic Temperatures 120

Chanud Yasanayake, Physics, Pomona College
NNIN REU Site: University of California, Santa Barbara





PHYSICS & NANOSTRUCTURE PHYSICS, PAGES 122-131

**Characterization and Solar Cell
Application of GaSb Quantum Dots 122**
Arthur Bowman, III, Physics, Wayne State University
NNIN iREU Site: NIMS, Japan

**A Coupled Dipole Approach to
Electron Energy Gain Spectroscopy 124**
Jacob Busche, Physics, Oregon State University
NNIN REU Site: University of Washington

**Fabricating Heavy Metal/Ferromagnetic Bilayers
for Spin Torque Applications 126**
Austin Little, Applied Physics, Morehouse College
NNIN REU Site: Cornell University

Fabrication of Nanoholes Smaller than 100 Nanometers 128
Luke Ness, Applied Physics and Computer Science, Bethel University
NNIN REU Site: University of Minnesota

Growth and Transfer of 2D Semiconductors and Heterostructures... 130
Nick Stone-Weiss, Physics, Juniata College
NNIN REU Site: University of Washington



PROCESS & CHARACTERIZATION, PAGES 132-149

Device Integration of Lithium Niobate Microring Resonators Patterned with a Silicon Hard Mask	132
<i>Nicolás Andrade, Electrical Engineering, Virginia Commonwealth University NNIN REU Site: Harvard University</i>	
Piezoelectric Material P(VDF-TrFE) Thin-Film Process Flow for Ultrasonic Transducers	134
<i>Mariella Arias, Biomedical Engineering, El Camino College NNIN REU Site: Cornell University</i>	
Fabrication of Diamond Microwires for Quantum Information Processing Applications	136
<i>Wu Joon Cha, Mechanical Engineering, Columbia University NNIN REU Site: Howard University</i>	
Characterization of Ionic Liquid Gels used with Conformable Conducting Polymer and Textile Electrodes used for Electroencephalography	138
<i>Dakota Crisp, Biomedical Engineering, University of Michigan NNIN iREU Site: Centre Microélectronique de Provence, France</i>	
The Effect of Low Temperature Growth & Annealing on the $\text{Al}_2\text{O}_3/\text{In}_{0.53}\text{Ga}_{0.47}\text{As}$ Interface	140
<i>Megan Hill, Materials Science and Engineering, Cornell University NNIN REU Site: University of California, Santa Barbara</i>	
Surface Micromachining of Microfluidic Devices	142
<i>Staci Hill, Chemistry, Middlebury College NNIN REU Site: University of Michigan</i>	
Fabrication and Characterization of Diamond Field-Effect Transistors	144
<i>Tiffany Huang, Electrical and Computer Engineering, Baylor University NNIN iREU Site: NIMS, Japan</i>	
Graphene Growth by Chemical Vapor Deposition	146
<i>Laura Huddleston, Electrical Engineering, Georgia Institute of Technology NNIN REU Site: Howard University</i>	
Microtensiometers with Patterned Porous Silicon.....	148
<i>Adriana Mulero, Chemical Engineering, University of Puerto Rico-Mayaguez NNIN REU Site: Cornell University</i>	

INDEXES, PAGES 151-155

The cover image of this publication was used with permission from Gabriel R. López Marcial, who performed his research at NIMS, Japan, on "Development of Zeolite-Based Nanofibers for the Removal of Uremic Toxins in Kidney Removal Patients" -- find his full report starting on page 20.

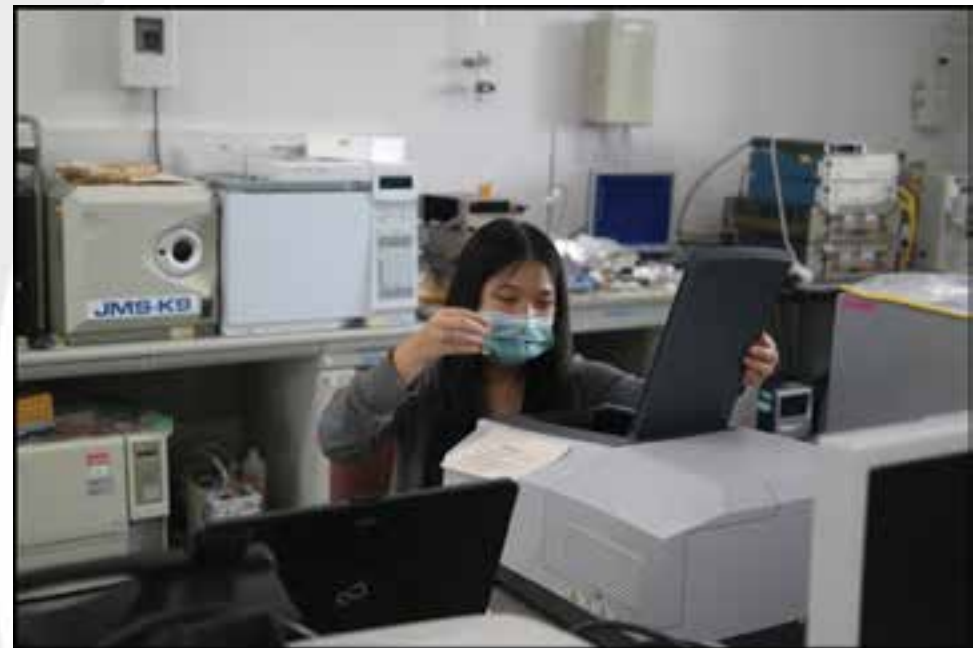
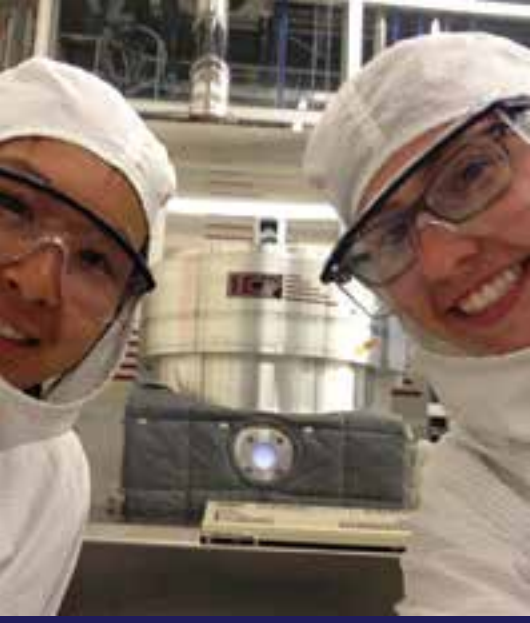
Photographs in this opening section were taken by 2014 NNIN REU & iREU interns, and NNIN staff. Melanie-Claire Mallison took the group and by site group photographs.

Full color research figures, page xxxvi, include their report page numbers.



2014 NNIN REU CORPORATE SPONSORS

Agilent Technologies • Analog Devices • Applied Materials
Canon • Daihen • Ericsson • IBM • Infineon • Intel
MERI JSC • NEC • Qualcomm • Renesas Electronics
Robert Bosch • SIX Semicondutores
STMicroelectronics • Texas Instruments
Toshiba • Ultratech





Welcome to the 2014 Edition of the NNIN REU Research Accomplishments!

This publication reflects the hard work of the undergraduate researchers, as well as the dedication and commitment of their mentors, the NNIN site staff, REU coordinators, and the principal investigators.

Our summer program brings undergraduates from colleges and universities across the U.S. into some of the nation's leading academic nanofabrication laboratories for an intensive ten-week research experience. The participants are trained in safe laboratory practices, learn the essential scientific background for their project, and then perform independent research in nanotechnology, under the guidance of their mentor. For many of the students, the NNIN REU is their first experience when the answer, or even the existence of an answer, is not yet known. The summer experience provides the students with a sample of what life for them could be like as a graduate student in applied science or engineering, both in and outside the clean room. For many, the NNIN REU Program helps them to decide to pursue a career in research and development.

During the summer of 2014, 58 students participated in our REU Program. From the previous summer's NNIN REU Program, 11 students were selected to participate in NNIN's International Research Experience for Undergraduates (iREU) Program in France and Japan. Finally, five graduate students from Japan participated in our exchange iREG program.

NNIN is committed to making all three of these programs a significant experience for the participants, by focusing on advanced research and knowledge, seeking strong mentors and staff support, exposing the students to a professional research environment, and having high expectations for the summer research projects, as well as for the presentations at the final convocation. The students' exposure to a wider variety of research conducted by their peers and the other nanofab users across diverse disciplines of science and engineering provides a significant complementary experience.

I would like to thank all of the NNIN REU staff, graduate student mentors, and faculty for their contributions to the success of this year's programs. Particular thanks are due to Ms. Melanie-Claire Mallison and Dr. Lynn Rathbun for their contributions to organizing the logistics of these programs. In addition, I am grateful to Ms. Leslie O'Neill and Dr. Nancy Healy for organizing the network-wide convocation in August at Georgia Tech in Atlanta, Georgia.

I wish all our program participants the best for their future careers, whether in science, engineering, or other disciplines. I hope you will build on this summer's experience and I look forward to hearing from you on your future successes!

Roger T. Howe, Director, NNIN
rthowe@stanford.edu



The 2014 NNIN REU Program:

ASU NanoFab, Arizona State University



Fatima-Joyce Dominguez; page 14

Taliya Gunawansa; page 66

Tara Nietzold; page 52

Wesley Tatum; page 98

The 2014 NNIN REU Program: Cornell NanoScale Science & Technology Facility, Cornell University



Mariella Arias; page 134 • Allison Bosworth; page 2

Alicia Elliott; page 60 • Shinsuke Hirata; page 42

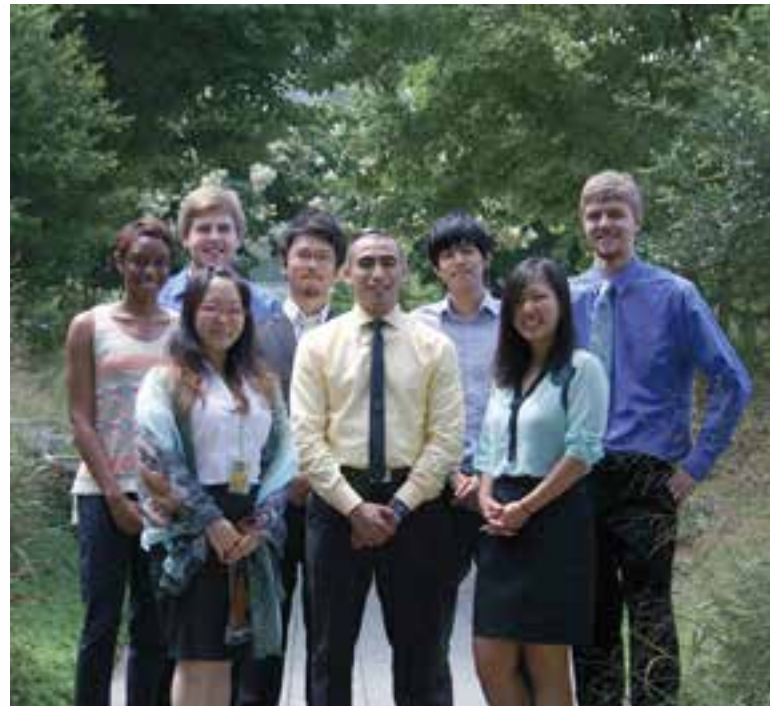
Austin Little; page 126 • Adriana Mulero; page 148

Pavel Shapurenka; page 94 • Hidetaka Ueno; page 32



The 2014 NNN REU Program:

Institute for Electronics and Nanotechnology, Georgia Institute of Technology



Nnenna Dieke; page 58 • Dylan Freas; page 64

Lucy Hu; page 16 • Yasuhiro Kimura; page 72

Yu Kitamura; page 110 • Fausto Mares-Davila; page 48

Matthew Salmon; page 90 • Aki Sato; page 92

The 2014 NNIN REU Program: Center for Nanoscale Systems, Harvard University



Nicolás Andrade; page 132

Carlos J. Brambila; page 4

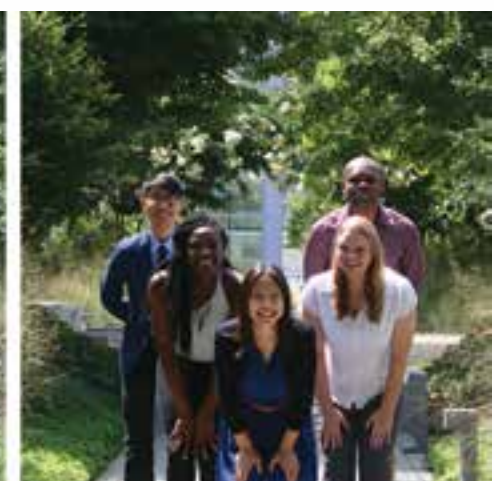
Steven Ceron; page 8

Brandon Foley; page 118

David Morse; page 22

The 2014 NNIN REU Program:

Howard Nanoscale Science & Engineering Facility, Howard University



**Wu Joon Cha; page 136 • Laura Huddleston; page 146
Tewa Kpulun; page 76 • Rachel Lim; page 78
Kaleel Wainwright; page 36**

The 2014 NNIN REU Program:

Penn State Nanofabrication Facility, The Pennsylvania State University



Sunny Aggarwal; page 56

Robyn Emery; page 62

Michael Homsy; page 106

Jon-L Innocent-Dolor; page 70

Matthew Koehler; page 74

The 2014 NNIN REU Program: Stanford Nanofabrication Facility, Stanford University



**William Anderson; page 46 • Geoffrey Martin-Noble; page 84
G. Emily Nitzberg; page 88 • Ashka Shah; page 26
Shanel Wu; page 54**

The 2014 NNIN REU Program: UCSB Nanofabrication Facility, University of California, Santa Barbara



Lesley Chan; page 114 • Matthew Hartensveld; page 68

Megan Hill; page 140 • Rachel Lucas; page 80

Brian Markman; page 82 • Marlee Motes; page 86

Bethany Smith; page 96 • Chanud Yasanayake; page 120

The 2014 NNIN REU Program:

Lurie Nanofabrication Facility, University of Michigan, Ann Arbor



Samuel Arthur; page 112

Staci Hill; page 142

Samantha Kang; page 108

Julie Miller; page 50

Benjamin Vizy; page 34 (Pictured bottom left!)

The 2014 NNIN REU Program:

Minnesota Nano Center, University of Minnesota



Emiliana Cofell; page 116

Christopher Davidson; page 12

Luke Ness; page 128

Mark Pagkaliwangan; page 24

James Paul Wondra, II; page 38



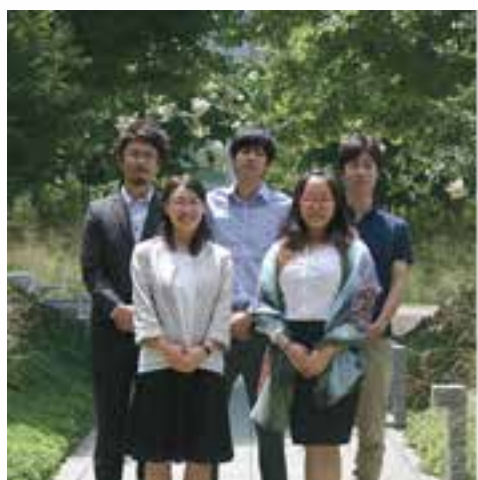
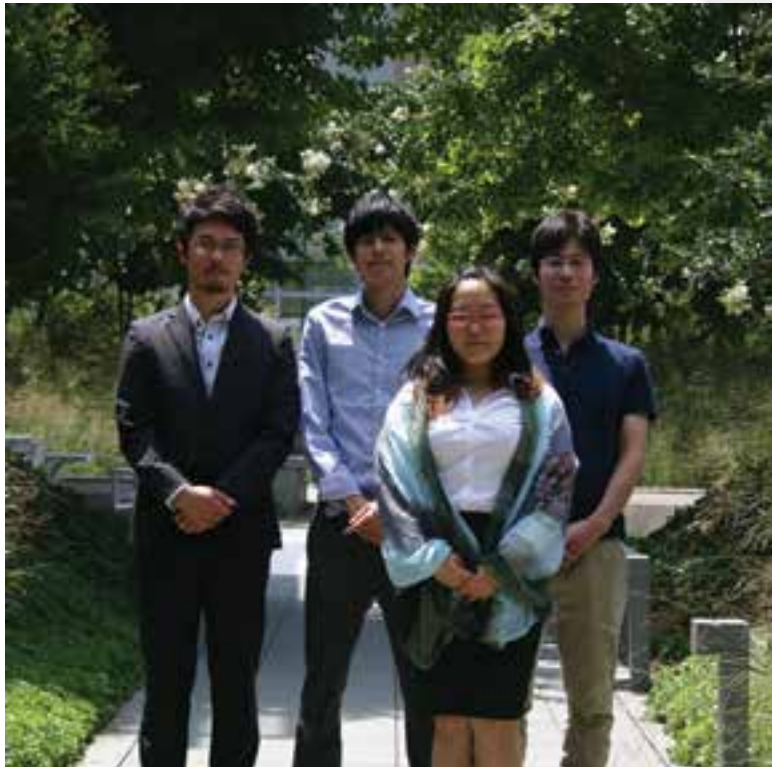
The 2014 NNIN REU Program:

Washington Nanofabrication Facility & Molecular Analysis Facility, University of Washington



**Jacob Busche; page 124 • Eve Byington; page 6
John Ren; page 44 • Nick Stone-Weiss; page 130
Emily Thompson; page 30**

2014 NNIN International Research Experience for Graduates (NNIN iREG) Program



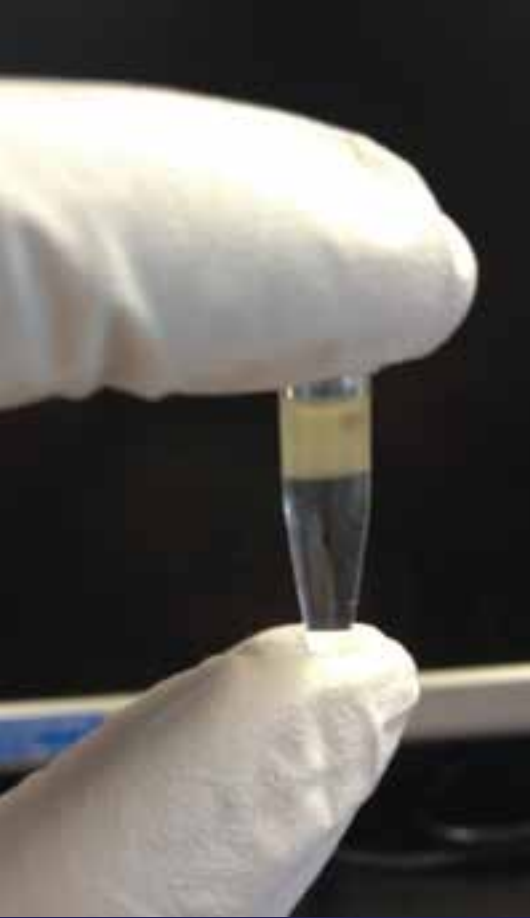
Shinsuke Hirata; page 42

Yasuhiro Kimura; page 72

Yu Kitamura; page 110

Aki Sato; page 92

Hidetaka Ueno; page 32



2014 NNIN International Research Experience for Undergraduates (NNIN iREU) Program



Arthur Bowman; page 122 • Samantha Renee Corber; page 10
Dakota Crisp; page 138 • Tiffany Huang; page 144
Meghan Kazanski; page 18 • Gabriel López Marcial; page 20
Peter Su; page 28 • Jill Wenderott; page 100
Connie Wu; page 102 • Allison Wustrow; page 104
Ashlyn Young; page 40

Commonly Used Abbreviations and Their Meanings

μl microliter
 μm micron, micrometer
 μN micro-Newton
 μs microsecond
 Ω Ohm
 $<$ is less than
 $>$ is greater than
 \sim approximately
1D one-dimensional
2D two-dimensional
3D three-dimensional
 ^4He helium-4
 $\alpha\text{-Si}$ amorphous silicon
AC alternating current
AFM atomic force microscopy/microscope
Ag silver
Al aluminum
 Al_2O_3 aluminum oxide
ALD atomic layer deposition
 AlGaN aluminum gallium nitride
Ar argon
ARC anti-reflective coating
 ArF argon fluoride
As arsenic
Au gold
AuNPs gold nanoparticles
B boron
BAM bisphenol aminomethyl
 BCL_3 boron trichloride
BHJ bulk heterojunction
Bi bismuth
BN boron nitride
BOE buffered oxide etch
Br bromine
C carbon
C centigrade
C-V capacitance-voltage
 C_3N_4 carbon nitride
 CaCO_3 calcium carbonate

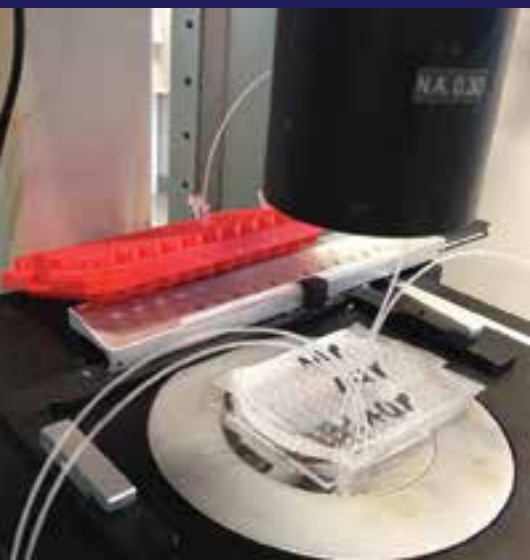




CAD computer-aided design
Cd cadmium
CdS cadmium sulfide
CdSe cadmium selenide
Ce cerium
 CF_4 carbon tetrafluoride or tetrafluoromethane
 CH_4 methane
 CHF_3 trifluoromethane
Cl chlorine
 Cl_2 chlorine gas
cm centimeter
CMOS complementary metal oxide semiconductor
CMOSFET complementary metal oxide field effect transistor
CMP chemical mechanical polishing
CNTFET carbon nanotube field-effect transistor
Co cobalt
 CO_2 carbon dioxide
Cr chromium
Cu copper
CVD cardiovascular disease
CVD chemical vapor deposition
CW continuous wave
DC direct current
DEP dielectrophoresis
DI de-ionized
DMF dimethyl formamide
DNA deoxyribonucleic acid
DNP dynamic nuclear polarization
DRAM dynamic random access memory
DRIE deep reactive ion etch
DUV deep ultraviolet
e-beam electron beam lithography
E. coli *Escherichia coli*
EBL electron beam lithography
EDS energy dispersive spectroscopy
EELS electron energy loss spectroscopy
EG ethylene glycol
Er erbium
ErAs erbium arsenide
EUV extreme ultraviolet
ex situ Latin phrase which translated literally as 'off-site' -- to examine the phenomenon in another setting than where it naturally occurs
ex vivo Latin for "out of the living" -- that which takes place outside an organism
F fluorine
Fe iron
 Fe_2O_3 iron oxide
FESEM field-emission scanning electron microscopy/microscope

FET field-effect transistor
 FIB focused ion beam
 FIR far infrared
 FTIR Fourier transform infrared spectroscopy
 Ga gallium
 GaAs gallium arsenide
 GaAsN gallium arsenide nitride
 GaInNAs gallium indium nitride arsenide
 GaN gallium nitride
 GaP gallium phosphide
 GaSb gallium antimonide
 GBLMA α -gamma butyrolactone methacrylate
 Ge germanium
 GHz gigahertz
 GI gastrointestinal
 GPa gigapascal
 h hours
 H hydrogen
 H_2O_2 hydrogen peroxide
 He helium
 HEMTs high electron mobility transistors
 Hf hafnium
 HF hydrofluoric acid
 HfO_2 hafnium dioxide
 Hg mercury
 high- κ high dielectric constant
 HMDS hexamethyldisilazane
 HSQ hydrogen silsesquioxane
 HSQ/FOx negative electron beam resist hydrogen silsesquioxane
 Hz Hertz
 I-V current-voltage
 I/O input/output
 IC integrated circuit
 ICP inductively coupled plasma
 In indium
in situ Latin phrase which translated literally as ‘in position’ -- to examine the phenomenon exactly in place where it occurs
in vitro Latin for “within glass” -- refers to studies in experimental biology that are conducted using components of an organism that have been isolated from their usual biological context in order to permit a more detailed or more convenient analysis than can be done with whole organisms.
in vivo Latin for “within the living” -- experimentation using a whole, living organism
 InAlN indium aluminum nitride
 InAs indium arsenide
 InAs NWs indium arsenide nanowires
 InGaAsN indium gallium arsenide nitride
 InP indium phosphide





IPA.....isopropyl alcohol
IR.....infrared
ITO.....indium tin oxide
 κdielectric constant
K.....Kelvin (a unit of measurement for temperature)
K.....potassium
kg.....kilogram
kHz.....kilohertz
KOH.....potassium hydroxide
L/D.....length-to-diameter ratio
La.....lanthanum
LAO.....lanthanum aluminum oxide
LED.....light-emitting diode
LER.....line edge roughness
Li.....lithium
low- κlow dielectric constant
LPCVD.....low pressure chemical vapor deposition
m.....minute
MBE.....molecular beam epitaxy
MEMs.....microelectromechanical systems
MgO.....magnesium oxide
MHz.....megahertz
micron.....micrometer, aka μm
min.....minutes
ml.....milliliter
mm.....millimeter
mM.....millimolar
 MnO_2 NPs.....manganese oxide nanoparticles
Mo.....molybdenum
MOCVD.....metal oxide chemical vapor deposition
MOS.....metal oxide semiconductor
 MoS_2molybdenum disulfide
MOSFET.....metal oxide semiconductor field effect transistor
ms.....millisecond
mTorr.....millitorr
mV.....millivolt
MVD.....molecular vapor deposition
 $\text{M}\Omega$megaohms
N.....nitrogen
 N_2nitrous oxide
nA.....nanoAmperes
NaCl.....sodium chloride
Nb.....niobium
NEMs.....nanoelectromechanical systems
 NH_4Fammonium fluoride
Ni.....nickel
NIR.....near-infrared

nL nanoliter
nm nanometer
NMP n-methyl-2-pyrrolidone
NMR nuclear magnetic resonance microscopy / spectroscopy
NNIN iREG National Nanotechnology Infrastructure Network International Research Experience for Graduates (NNIN iREG) Program
NNIN iREU National Nanotechnology Infrastructure Network International Research Experience for Undergraduates (NNIN iREU) Program
NNIN REU National Nanotechnology Infrastructure Network Research Experience for Undergraduates (NNIN REU) Program
NPs nanoparticles
NPs nanopores
ns nanosecond
NSF National Science Foundation
O oxygen
OFET organic field effect transistor
OLED organic light-emitting diode
P(VDF-TrFE) poly[(vinylidenefluoride-co-trifluoroethylene]
Pa Pascals
PAB post-apply bake
PaC Parylene-C
Pb lead
PBG photonic bandgap
PbS lead sulfide
PbSe lead selenide
Pd palladium
PD photodetector
PDMS polydimethylsiloxane
PEB post-exposure bake
PECVD plasma enhanced chemical vapor deposition
PEDOT:PSS poly(3,4-ethylenedioxythiophene):poly(styrenesulfonate)
PEG polyethylene glycol
PEI polyethyleneimine
PFM piezo-response force microscopy
PGMA poly(glycidyl methacrylate)
pH a measure of the activity of hydrogen ions (H+) in a solution and, therefore, its acidity.
Ph.D. doctorate of philosophy
PhC. photonic crystal
PL photoluminescence
pL picoliter
PMMA. poly(methyl methacrylate)
poly-Si. polycrystalline silicon
PS-*b*-PMMA polystyrene-*block*-poly(methyl methacrylate)
Pt. platinum
Pt/Ir platinum/iridium
PV photovoltaic
PVD physical vapor deposition

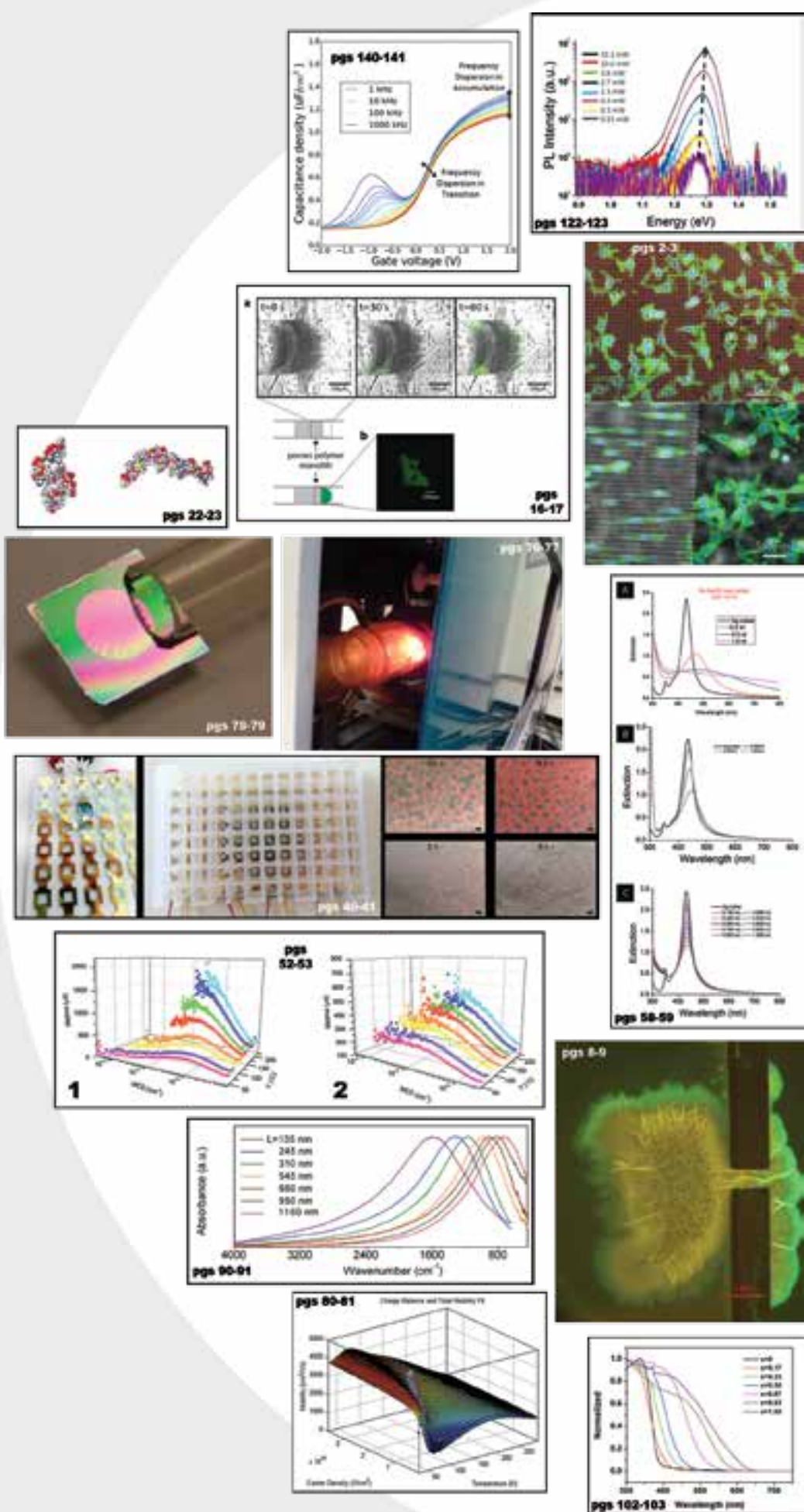




Py permalloy, $\text{Ni}_{81}\text{Fe}_{19}$
Q quality factor
QD quantum dots
QW quantum well
RF radio frequency
RF MEMS radio frequency microelectromechanical systems
RIE reactive ion etch
RMS or rms root mean square
RNA ribonucleic acid
RTA rapid thermal anneal
RTD resistance temperature device
s seconds
S sulfur
SAMs self-assembled monolayers
Sapphire $\alpha\text{-Al}_2\text{O}_3$
Sb antimony
Sc scandium
sccm standard cubic centimeters per minute
Se selenium
sec seconds
SECM scanning electrochemical microscopy
SEM scanning electron microscopy/microscope
SERS surface enhanced Raman spectroscopy
 SF_6 sulfur hexafluoride
Si silicon
 Si_3N_4 silicon nitride
SiC silicon carbide
 SiH_4 silane
SiN silicon nitride
SiNWs silicon nanowires
 SiO_2 silicon dioxide
SMS single molecule spectroscopy
Sn tin
 SnO_2 tin oxide
SNR signal-to-noise ratio
SOI silicon-on-insulator
SPR surface plasmon resonance
STEM scanning transmission electron microscopy/microscope
STJ superconducting tunnel junction
STM scanning tunneling microscopy/microscope
t-BOC *tert*-butoxycarbonyl
Ta tantalum
TaN tantalum nitride
Te tellurium
TE transverse electric
TEM transmission electron microscopy/microscope
TFT thin-film transistor

T_g glass transition temperature
THz terahertz
Ti titanium
TiN titanium nitride
 TiO_2 titanium dioxide
TM transverse magnetic
TMAH tetramethylammonium hydroxide
UHV ultra-high vacuum
UV ultraviolet
V vanadium
V voltage
vdW van der Waals
W tungsten
 WSe_2 tungsten diselenide
 XeF_2 xenon difluoride
XPS x-ray photoelectron spectroscopy
 YB_{25} yttrium boride
YBCO yttrium-barium-copper-oxide
Zn zinc
 $ZnCl_2$ zinc chloride
 ZnO zinc oxide
 $ZnO:Al$ zinc aluminum oxide
 ZnS zinc sulfide or zinc-blende
Zr zirconium
 ZrO_2 zirconium dioxide
ZTO zinc tin oxide





2014 Research Accomplishments

for the

*National Nanotechnology
Infrastructure Network
Research Experience for
Undergraduates Programs*

Development of PDMS Microstructures for the Investigation of Cardiac Cell Function

Allison Bosworth

Biological Engineering, Louisiana State University

NNIN REU Site: Cornell NanoScale Science & Technology Facility, Cornell University, Ithaca, NY

NNIN REU Principal Investigator: Prof. Jan Lammerding, Biomedical Engineering/
Weill Institute for Cell and Molecular Biology, Cornell University

NNIN REU Mentor: Dr. Patricia Davidson, Biomedical Engineering/
Weill Institute for Cell and Molecular Biology, Cornell University

Contact: allison.bosworth1@gmail.com, jan.lammerding@cornell.edu, patriciadavidson@gmail.com

Abstract and Introduction:

Polydimethylsiloxane (PDMS) is a silicone-based polymer that may serve as a flexible substrate for cell culture. The goal of this project was to microfabricate PDMS structures to study contractile forces and intracellular organization of cardiac cells. Mutations in the nuclear envelope proteins lamin A/C cause approximately 10% of inherited cases of dilated cardiomyopathy, a disease responsible for a third of all heart failures. By comparing lamin mutant and healthy cells, we can develop a better understanding of how the mutations affect cellular function, gain new insights into the origin of the disease, and identify potential treatment approaches.

We used soft lithography techniques to create thin, flexible PDMS micropillars for contractile force assessment of cardiac cells. When cells adhere to the tips of these pillars, their spontaneous contractions cause deflections in the pillars allowing for direct calculation of the contractile forces generated by the cells [1]. The deflection, δ , can be used to calculate the applied contractile force, F , using the equation $F = 3EI\delta/L^3$ where E , I , and L represent Young's modulus, moment of inertia, and length of pillar, respectively [1].

In addition, we used PDMS surfaces with equally spaced ridges to assess the organization of cells and their cytoskeleton grown on lined substrates. Because cardiac cell function depends of the organization of the cytoskeleton and previous reports had shown that lamin mutant cells have defects in mechanosensing, we were interested in using the linear ridge substrates to determine how nuclear mutations affect cytoskeletal organization [2].

For the initial studies, we cultured human and mouse fibroblasts on these two microfabricated device types, pillars and linear ridges, for preliminary testing and imaging by fluorescent microscopy.

Experimental Procedure:

Micropillar and linear microridge devices were fabricated using photolithography and SU-8 negative photoresist spun onto a silicon wafer with a thickness of 11 μm for the micropillars and 3 μm for the linear ridges. A negative PDMS mold was cast and cured from the SU-8 devices (Figure 1) [1]. This double molding approach was employed to avoid adhesion of PDMS features inside of SU-8 features during the casting and curing process. Substrates were coated with

silane between each molding steps to prevent adhesion. Finally, a drop of PDMS was placed on a glass slide, onto which the second mold was applied, and cured for 22 hours. The final devices were then carefully unmolded to obtain thin PDMS pillars and ridges.

Once fabrication was completed, the devices were prepared for fibroblast cell cultures. Fibronectin, an extracellular matrix protein, was micro-contact printed onto the micropillars to encourage cell growth on the tops of the pillars. These devices were incubated in a 0.02 g/mL Pluronic® F-127 solution to inhibit cell adhesion on the sides of the pillars and beneath the pillars. Linear ridge devices were incubated in a 50 $\mu\text{g}/\text{mL}$ fibronectin solution to obtain an even coating and encourage

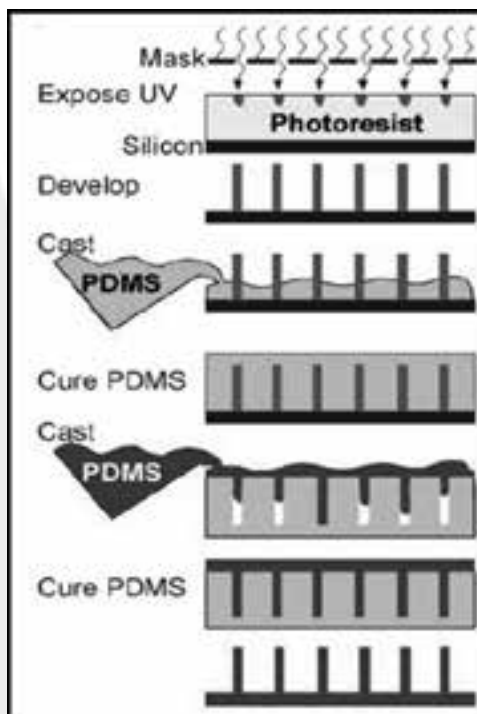


Figure 1: Overview of device fabrication process [1].

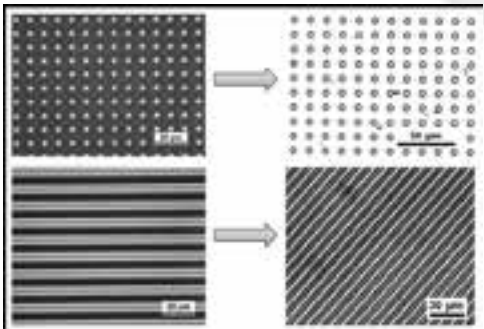


Figure 2: Optical microscope images of micropillars and linear microridges in SU-8 (left) and PDMS (right).

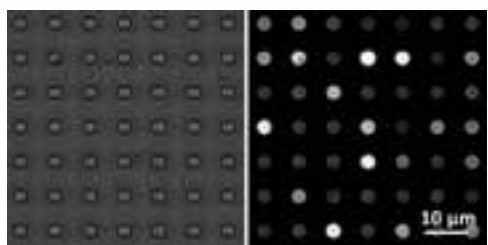


Figure 3: Micropillars stamped with fluorescent dextran to validate μ CP.

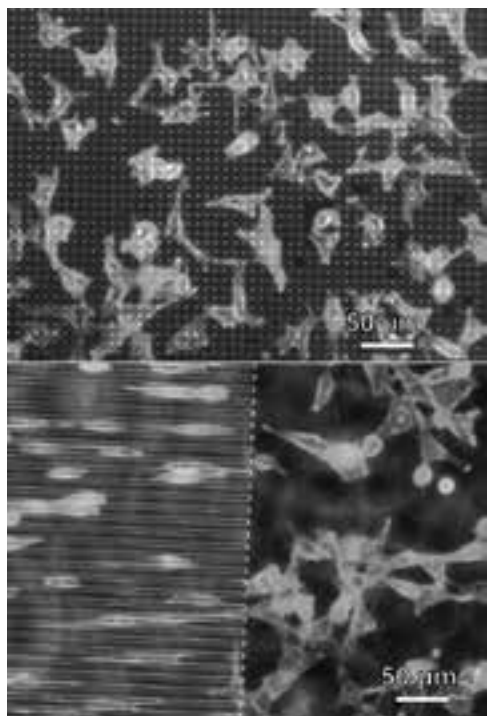


Figure 4: Fibroblasts grown on micropillars (top) and linear microridges (bottom) stained for DNA and F-actin. (See full color version on page xxxvi.)

fibroblast growth over the entire device. Fibroblasts were cultured on the devices for 24 hours, fixed, and then fluorescently stained for imaging.

Results and Conclusions:

The final PDMS micropillars were 11 μ m tall, 2 μ m in diameter and had a 9 μ m center-to-center distance. Ridges were 3 μ m tall and 5 μ m wide with 5 μ m spacing between ridges. Initial microfabrication problems with adherence of the SU-8 pillars to the silicon wafer were overcome by incorporating a flat SU-8 adherence layer and the mask design was altered to allow sufficient pillar-to-pillar distance to prevent adherence of the tall flexible pillars to themselves. SU-8 features were replicated onto PDMS molds (Figure 2), and silanization between molding steps effectively prevented adhesion of PDMS to substrate during curing process. Micro-contact printing (μ CP) techniques were verified by stamping fluorescent dextran onto pillar tops and visualization by confocal microscopy (Figure 3).

Cells successfully grew on and adhered to both device types (Figure 4); however, we were unable to observe obvious deflections of the pillars. Based on the equation above, a contractile force of approximately 15.5 nN is required to cause a 1 μ m deflection in pillars with a height of 11 μ m. The pillars may have been too stiff to see a deflection from the few nanoNewtons of forces generated by the fibroblasts in comparison to the myocytes. Another possible reason for the absence of noticeable pillar deflection is cell adherence between the pillars, rather than on top. PDMS devices may be optimized by improving cell adhesion to the top of the pillars, i.e. by soaking in Pluronic for longer or finding a better cell-repellent.

Linear ridge device images confirmed that fibroblasts aligned with the linear ridges on the substrate. In contrast, the flat PDMS surface surrounding the linear device showed cells growing in random orientations with no particular pattern. Thus, the PDMS devices worked well in providing a substrate suitable for analysis of cell function specifically aligning cells in the predicted direction.

Future Work:

Once the experimental procedures and design for the micropillar substrate are optimized, devices will be seeded with cardiac myocytes so that they can be used to compare contractile forces between healthy and lamin mutant cardiac myocytes. Linear ridges will be used to assess variations in cytoskeletal and nuclear organization in the mutant and wild-type cells. Taken together, these devices will help us to develop a better understanding of the diseases caused by mutations in the nuclear envelope proteins lamin A/C in cardiac myocytes.

Acknowledgments:

I thank the Lammerding group at Cornell University for their guidance and support, specifically Drs. Patricia Davidson and Jan Lammerding. I would like to acknowledge NNIN REU Program, NSF, and the Cornell NanoScale Science and Technology Facility for their assistance.

References:

- [1] Tan, J, et al. PNAS. 100. 1484-1489. 2002.
- [2] Bray, M, et al. Biomaterials. 31. 5241-5150. 2010.

High-Throughput Drug Screening *in vivo* Using Droplet Microfluidics

Carlos J. Brambila

Biology-Emphasis in Bioengineering, San Diego State University

NNIN REU Site: Center for Nanoscale Systems, Harvard University, Cambridge, MA

NNIN REU Principal Investigator: Dr. David A. Weitz, Physics School of Engineering and Applied Sciences, Harvard University

NNIN REU Mentors: Dr. Anindita Basu, Physics School of Engineering and Applied Sciences, Harvard University-Broad Institute;

Dr. Linas Mazutis, School of Engineering and Applied Sciences, Harvard University

Contact: carlos.brambila10@gmail.com, weitz@seas.harvard.edu, abasu@broadinstitute.org, lmazutis@seas.harvard.edu

Introduction:

High-throughput cell-based drug screenings conducted through various technologies, such as in microtiter plates, have significantly advanced drug development. However, the costs and time associated with such technologies are exorbitant. Polydimethylsiloxane (PDMS)-based microfluidic devices provide a popular *lab-on-a-chip* technique where reagents may be combined in sub-nanoliter volumes in a fast and controlled manner. PDMS is a cheap, transparent, and bio-compatible substrate that affords rapid prototyping and an efficient platform for drug screening. We used such devices to generate *water-in-oil* emulsion droplets at high throughput (~ 1000 drops per second) that efficiently encapsulated cells in the presence of drugs. Reducing the size of the reaction compartments to sub-nanoliter volumes allowed us to be parsimonious with reagents while high number of droplets ($\sim 10^6$) provided superior statistical resolution.

In this project, we designed, fabricated and used microfluidic devices to test the efficacy of cancer drugs on a human cancer cell line where the drug concentrations were systematically varied.

Experimental Procedure:

CAD Designs. We used AutoCAD (Autodesk, USA) software to design microfluidic devices. One of the designs we used was a simple co-encapsulation scheme where two reagent channels met at a junction, which were then encased in oil, generating reverse emulsion droplets (Figure 1). In order to change the drug concentration in each droplet, the respective flow rates of the reagents were changed using syringe pumps. Another design used was a double-layer device that generated a gradient of seven different drug concentrations that were then simultaneously co-encapsulated with cells in oil for a faster droplet generation without changing flow rates.

Soft Lithography. We shone UV light through a CAD mask and exposed SU-8 photoresist-covered silicon wafers to crosslink exposed areas. After development and subsequent washes, this served as a master mold to create PDMS-based microfluidic devices. Uncured PDMS was poured on this master, followed by baking. The solid PDMS layer was peeled off and covalently fused to a glass slide using plasma treatment. Finally, we coated the microchannels with Aquapel (Pittsburgh Glass Works, USA) to render them hydrophobic.

Microfluidic Emulsions. We used cancer cells from a human lymphoblast cell line that were stained using a live-dead fluorescence reporter kit (Invitrogen, USA). We used three syringe pumps (New Era Pump Systems, USA), disposable syringes and needles (BD Biosciences, USA), and polyethylene tubing to flow in drug and a fluorescent dye mix on one, cells in phosphate buffer saline on the second and an oil/surfactant mix [4] on the third channel in our microfluidic devices creating *water-in-oil* emulsion droplets. We used Geneticin, an anti-cancer drug, mixed with fluorescein (Sigma-Aldrich, USA), to estimate drug concentrations in droplets. Uniform-sized droplets with $75 \mu\text{m}$ diameter were collected in microcentrifuge tubes. The reagent flow rates were changed to generate droplets with different drug concentrations. The droplets were incubated and tested at different time points.

Data Acquisition. We used fluorescence imaging and photomultiplier tube (PMT)-based detection to interrogate the co-encapsulated droplets. We used a fluorescence microscope (IX83, Olympus, USA) for imaging and ImageJ software (NIH, USA) to analyze acquired images. A custom-built

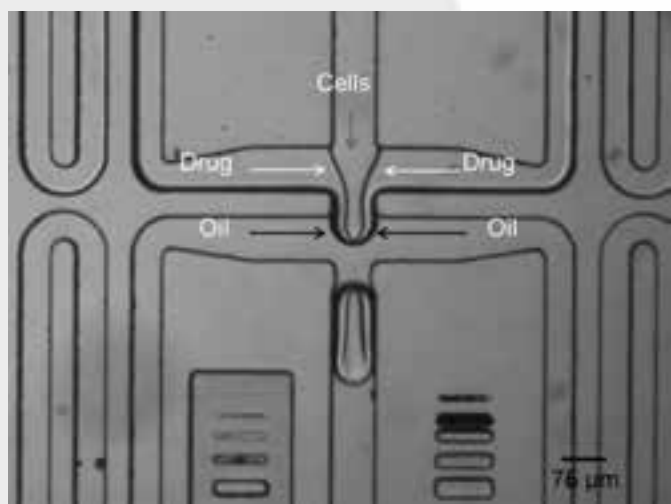


Figure 1: Generation of emulsion droplets in microfluidic co-encapsulation device.

FPGA-based (National Instruments, USA) PMT detector setup was used to detect live/dead cell state and dye concentrations in drops at high-throughput (~ 500 drops/sec).

Results and Conclusions:

We analyzed fluorescence images of cell and drug emulsions. Droplets at different light intensities (Figure 3) indicated different drug concentrations, while bright points inside the droplets marked apoptotic cells. Using ImageJ, we tracked five different fluorescein concentrations (Figure 2). Different concentrations of drug/dye detected after long period of incubation (\sim five hours) attested the absence of drug diffusion among droplets. Although fluorescence imaging was informative, it was time-consuming and difficult to analyze large amounts of data using imaging alone.

PMT-based droplet detection provided time-trace plots (Figure 4) that displayed a plateau indicating the drug concentration, superimposed with a spike that marked an apoptotic cell. This manner of detection allowed us to screen thousands of droplets in seconds.

Future Work:

The double-layer microfluidic device is still under development. Currently, only a fraction of the channels were able to generate droplets reliably. We will need to adjust the fluid-flow scheme, which require meticulous fabrication and several iterations of testing. The highest drug concentration of Geneticin used in this project (~ 60 mg/ml) was not high enough to induce appreciable levels of apoptosis in cells. We will need to increase the dosage and test several physiologically relevant concentrations. We will employ the double layer design to provide a wide array of concentrations simultaneously and will continue using the PMT detector setup to test at high throughput.

Acknowledgments:

I thank Harvard University and the NNIN REU Program, my site coordinator, Dr. Kathryn Hollar, my mentors, Anindita Basu and Linas Mazutis, my PI, Dr. David Weitz, and the Weitz group for this research opportunity, and the NSF for funding.

References:

- [1] Basu, A., et al., Developing a High-Throughput Drug Screening Platform Using Droplet Microfluidics, abstract, Controlled Release Society Annual Meeting, 2014.
- [2] Guo, Mira T., et al., Droplet microfluidics for high-throughput biological assays. 2012; Royal Society of Chemistry. (12): 2146-2148, 2154.
- [3] Mazutis, L., Single-cell analysis and sorting using droplet-based microfluidics. *Nature Protocols.* 2012 (8), 870-874.
- [4] Holtze, C., et al., Biocompatible surfactants for water-in-fluorocarbon emulsions. *Lab Chip* 2008 (8), 1632.

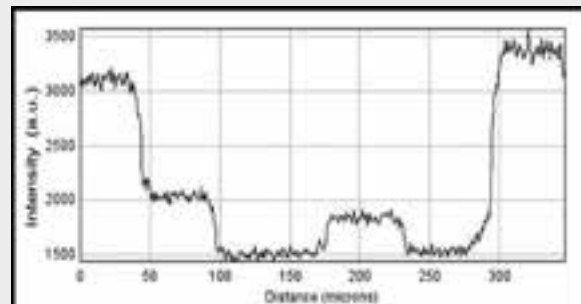


Figure 2: Plot of droplet intensities at different fluorescein concentrations.

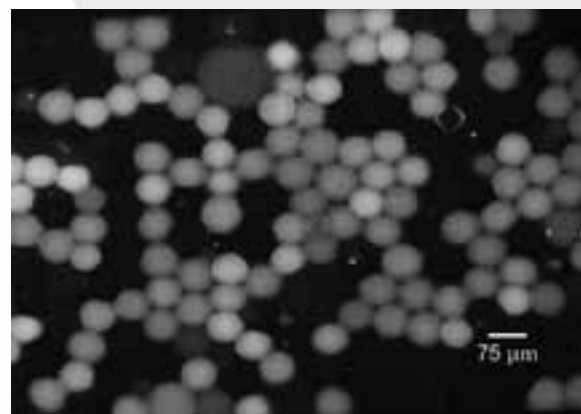


Figure 3: Image of cells and drug encased in droplets taken after five hours from co-encapsulation.

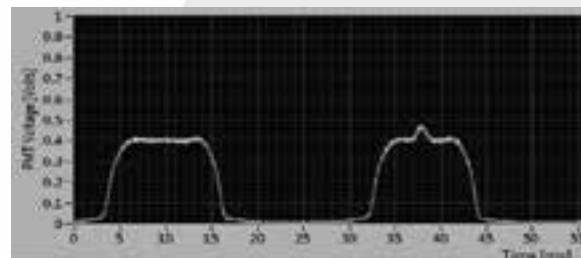


Figure 4: Time-trace snapshot of droplets detected using PMT. The plateaus indicate the fluorescein concentration in droplets, while the peak atop the second plateau indicates an apoptotic cell.

Sphingosine 1-Phosphate Functionalized Nanopatterned Scaffolds for Engineering Vascularized Skeletal Muscle Tissue

Eve Byington

Biological and Environmental Engineering, Cornell University

NNIN REU Site: Washington Nanofabrication Facility & Molecular Analysis Facility, University of Washington, Seattle, WA

NNIN REU Principal Investigator: Dr. Deok-Ho Kim, Bioengineering, University of Washington

NNIN REU Mentor: Jonathan Tsui, Bioengineering, University of Washington

Contact: emb356@cornell.edu, deokho@uw.edu, jhtsui@gmail.com

Abstract:

Duchenne muscle dystrophy (DMD) is a genetic disorder that affects one in 3,600 males, leading to early death due to a lack of dystrophin in muscle tissue [1]. Implanted primary muscle cell patches have previously been shown to increase myogenesis and dystrophin expression in DMD mouse models [2]. This project involves cultivating muscle cells on biomimetic nanopatterned poly(lactic-co-glycolic acid) (PLGA) scaffolds that are fabricated using capillary force lithography. These scaffolds mimic topographical cues presented by the aligned collagen fibers of the extracellular microenvironment in skeletal muscle. Sphingosine 1-phosphate (S1P) is a circulating lipid metabolite known to promote angiogenesis, myoblast differentiation and satellite cell proliferation. By functionalizing the nanopatterned scaffolds with S1P, we hypothesize that the muscle tissue will be more mature and vascularized prior to implantation, therefore integrating better with the host tissue to ultimately improve function in dystrophic muscles. The optimum concentration of S1P will be determined using immunostaining and qRT-PCR data regarding myogenic, endothelial and neurogenic genes.

Introduction:

Duchenne muscle dystrophy (DMD) is the most common type of muscle dystrophy, affecting one in 3,600 males. The genetic disorder results from a mutation in dystrophin, which is integral to the structural stability of muscle tissue. Dystrophin forms a protein complex that connects muscle fibers to the extracellular matrix (ECM) via the cell membrane. DMD patients therefore suffer from muscle degeneration, fibrosis and early death—living an average of only 25 years.

Current treatments for DMD are mostly limited to palliative care. Attempts to directly inject stem cells or myoblasts into DMD patients' muscles have been largely unsuccessful, resulting in poor cell survival rates and low dispersion capabilities. Our proposed solution is to use implantable tissue patches to restore muscular function. These patches can provide long-lasting dystrophin expression, due to the presence of both mature muscle cells and satellite cells that provide a pluripotent cell reservoir. They also promote neovascularization due to the presence of endothelial cells, allowing the patches to integrate easily into the host tissue.

Engineering tissue requires a cell culture environment that is as close to the tissue's native microenvironment as possible. We used nanopatterning on the biodegradable polymer poly(lactic-co-glycolic acid) (PLGA) to mimic the collagen fibers present in the skeletal muscle ECM. The patterning—aligned ridges that are 800 nm wide and 600 nm in height—is similar to the dimensions and anisotropic topography of collagen fibrils (Figure 1). We also functionalized the scaffolds

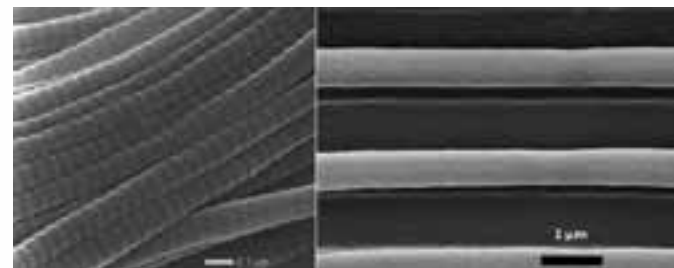


Figure 1: SEMs of collagen fibers on left (Dr. Claus Burkhardt, NMI, Reutlingen, Germany) compared to our scaffold on right, functionalized with 50 μ M S1P.

with the metabolite sphingosine 1-phosphate (S1P), which is known to promote angiogenesis, myoblast differentiation and satellite cell proliferation.

Experimental Procedure:

The PLGA scaffolds were fabricated using solvent-assisted capillary force lithography (CFL). PLGA was dissolved in chloroform at 15% w/v and deposited on glass coverslips mounted on polydimethylsiloxane (PDMS) gel. PDMS is pressed onto the solution for five minutes to absorb the solvent. The film is then left open to air for five minutes on a hot plate at 120°C. A nanopatterned polyurethane-acrylate (PUA) mold is placed on top of the film and pressure is applied for 15 minutes. The CFL process is shown in Figure 2.

The coverslips are glued onto bottomless wells using NOA83H, which is cured in UV overnight. A solution of 10 μ M Tris buffer and 3,4-dihydroxy-L-phenylalanine (DOPA) at 2 mg/mL, along with the appropriate concentration of S1P, was used to functionalize the scaffolds. Concentrations of S1P were 0 μ M, 50 μ M, 100 μ M, 175 μ M, and 250 μ M respectively.

Primary mononuclear muscle cells were isolated from mice, and were seeded at 100,000 cells per scaffold. Each [S1P] group included flat and patterned scaffolds, and there was an additional control group seeded on tissue culture plates with no S1P. The cells were cultured for ten days.

Results and Conclusions:

Quantitative reverse-transcription polymerase chain reaction (qRT-PCR) was performed to measure the relative quantities of marker genes for myogenic and endothelial differentiation. Pax7 was found to have a much higher expression on the nanopatterned scaffolds, indicating a larger population of satellite cells (Figure 3). Expression of MyoG, a marker for mature muscle cells, was also slightly higher on the nanopatterned scaffolds (Figure 3).

The expression of endothelial genes had a clear correlation with the concentration of S1P—both CD31, a marker for early endothelial differentiation, and eNOS, a marker for mature endothelial cells, were more highly expressed as the concentration of S1P on the scaffolds increased (Figure 4). This indicates that cells grown in the presence of S1P may have more angiogenic potential.

Future Work:

Data is still being analyzed for the neurogenic markers of the qRT-PCR, as well as the immunostaining results for myogenic, endothelial and neurogenic proteins. *In vivo* testing of the tissue patches in DMD mouse models is the next step, which will ultimately determine how viable this treatment is for restoring muscle function in those afflicted with DMD.

Acknowledgments:

Special thanks to my principal investigator Dr. Deok-Ho Kim and my mentor Jonathan Tsui, as well as Dr. KJ Janebodin, David Yama, Hyunsoo Lim, the NNIN REU staff and the University of Washington NTUF staff for the SEM imaging. Additionally I would like to thank the NNIN REU Program and the NSF for funding this work.

References:

- [1] A.D.A.M. Medical Encyclopedia. "Duchenne muscle dystrophy." Atlanta (GA): A.D.A.M., Inc. (2005).
- [2] Yang, H. S., et al. "Nanopatterned muscle cell patches for enhanced myogenesis and dystrophin expression in a mouse model of muscular dystrophy." *Biomaterials*, 35(5), 1478-1486 (2014).

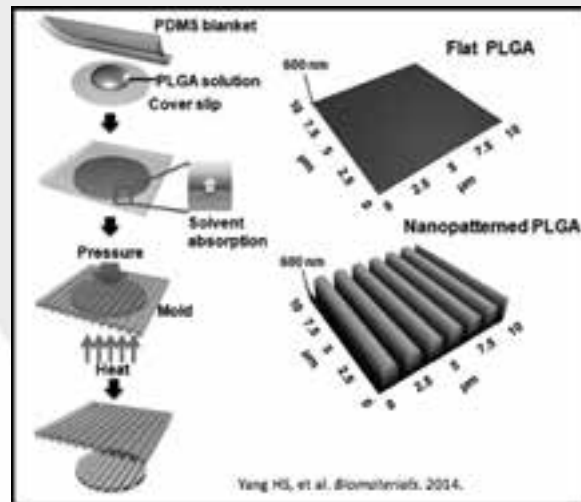


Figure 2: Fabrication technique of solvent-assisted capillary force lithography, and 3D renditions of the resulting flat and patterned films.

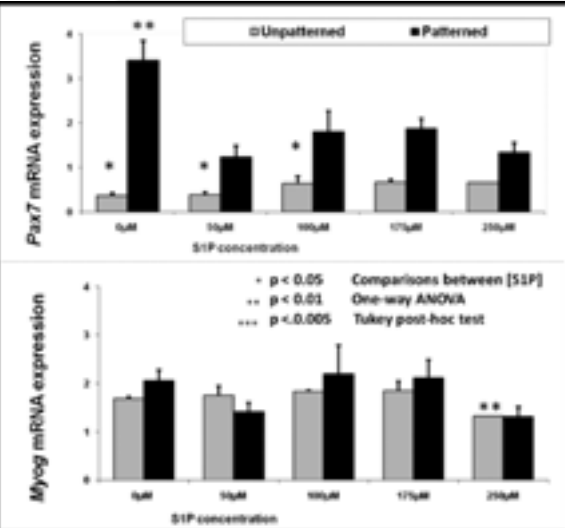


Figure 3: qRT-PCR for myogenic genes: Pax7, a marker for satellite cells, and MyoG, a marker for advanced muscle cell differentiation.

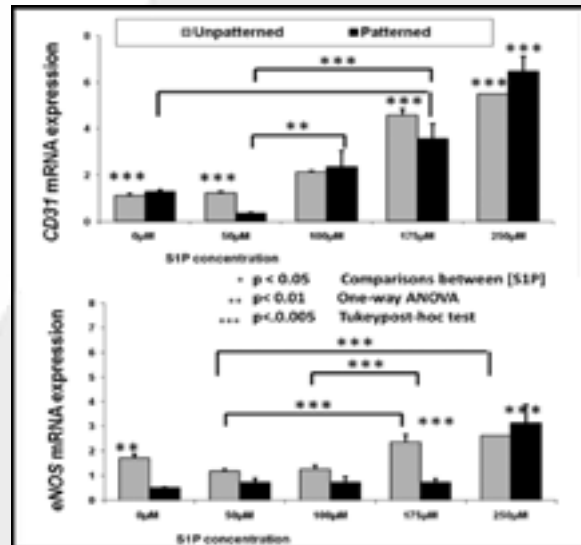


Figure 4: qRT-PCR for endothelial genes: CD31, expressed initially in differentiation, and eNOS, expressed later in differentiation.

The Disruption and Control of Microbial Biofilms

Steven Ceron

Mechanical Engineering, University of Florida

NNIN REU Site: Center for Nanoscale Systems, Harvard University, Cambridge, MA

NNIN REU Principal Investigator: Professor Shmuel Rubenstein, Applied Physics, Harvard University

NNIN REU Mentor: Gareth Haslam, Applied Physics, Harvard University

Contact: stevenceron@hotmail.com, shmuel@seas.harvard.edu, haslam@seas.harvard.edu

Abstract:

Microbial biofilms of the species *Bacillus Subtilis* were grown so that the changes in the expression of several important phenotypes could be analyzed using fluorescence microscopy. Biofilms exist in all kinds of environments; instead of acting as independent swimmers, the cells work as a community, which in turn results in a number of benefits for the colony, making it the preferred living condition for bacteria. However, the ability of biofilms to survive in harsh environments can cause serious problems in the medical and industrial fields where they lead to the spread of infection and degradation of components. Understanding the factors that lead the bacteria to change from one phenotype to another can provide insight to the best approach in solving these issues. We performed a set of novel experiments where the bacteria were presented with physical barriers that interrupted the normal expansion of the colony across the surface of the agar substrate. The barriers led to a unique response from the bacteria in respect to the growth rate along certain areas as well as the expression of a certain phenotype in a specific location.

Introduction:

Microbial biofilms were grown on a 9 mm thick piece of agar substrate in a Petri® dish with laser-cut acrylic barriers that formed channels for the biofilm to grow through. The barriers acted as walls, and as a result the bacteria could not receive nutrients from one side of barrier. The width of the channels was varied between 2 mm, 5 mm, and 10 mm, while the length of the channel was kept at a constant 3.175 mm. One half of the biofilm grew towards the barrier, and the other half grew over a flat agar substrate, serving as the control of the experiment.

Throughout the experiments, there was a noticeable correlation between the width of the channel and growth pattern of the biofilm as well as the intensity of the matrix phenotype while and after the biofilm grew through the length of the channel.

Methods:

The laser-cut barriers were put in the agar substrate by pouring agar into the Petri dish to a height of 1-2 mm and letting the substrate cool down to the point where it was no longer liquid. The acrylic barrier was then placed in the agar at 90° relative to the bottom of the Petri dish. Another amount of agar was then poured into the Petri dish, around the barrier, up to a height of 7 mm.

Throughout the whole experimental process, we inoculated the bacteria 5 mm away from the entrance to the channel.

Results and Conclusions:

The biofilms that grew through the 10 mm wide channels barely changed their regular growth while and after they grew through the length of the channel. The biofilms kept a regular gene expression and followed a fairly regular radial growth pattern, almost as if there was no barrier in place.

Figure 1 shows a triple-reporter fluorescent image of a colony that was inoculated 5 mm away from the entrance to a 2 mm wide channel, nine days after its inoculation. Although most of the biofilm had already sporulated, this image shows the growth pattern and greater matrix intensity after the biofilm had passed through the channel.

We believe that the higher raw intensity for the matrix phenotype after the biofilm had grown through the channel, shown in Figure 2a, was due to when the biofilm grew into the channel. The matrix cells at the edge of the colony could have formed higher stack of cells in the smaller surface area, thus creating a higher intensity and a higher percentage of matrix cells at the exit of the channel. The condensation along the edge of the walls could have led to the rapid spread of the cells in this area, leading to the matrix cells growing away from the lining of the wall on the second side of the barrier.

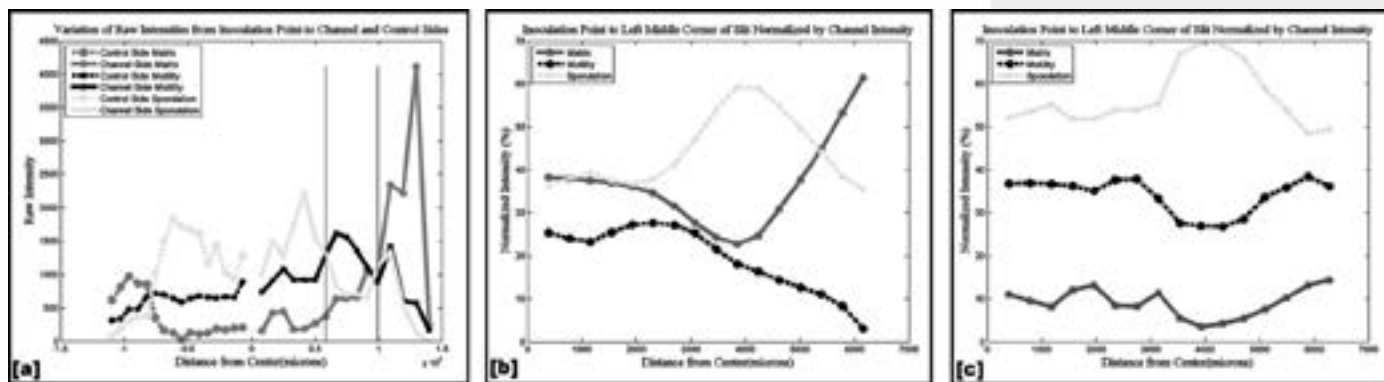
We observed a tendency for the bacteria to sporulate as the biofilm grew towards the left and right edges of the channel on the inoculation side. Unlike the second side of the barrier, the biofilm did not grow along the wall on the inoculation side.

The percentage of the peak of the sporulation intensity increased by 10% between these two instances, shown in Figures 2b and 2c. However, there was only an increase of 5% when the variation of intensities was measured from the inoculation point to the control side.

The difference in the increase of percentages of sporulation leads us to believe that the presence of the barrier increased the amount of sporulation on the inoculation side of the experiment. Unlike the second side of the barrier, where the biofilm rapidly grew along the lining of the wall and agar, the biofilm sporulated and stopped expanding along the first side of the barrier. As the biofilm expanded towards the control side, it received many nutrients that allowed the cells to continue dividing and switch between the matrix and motility phenotypes.

Acknowledgements:

I would like to thank my mentor, Gareth Haslam, and principal investigator, Shmuel Rubenstein, for all of their help throughout the process, as well as Stephan Koehler for his advice on experiments. I would also like to acknowledge the National Science Foundation for funding my research and the National Nanotechnology Infrastructure Network Research Experience for Undergraduates (NNIN REU) Program, and Kathryn Hollar, my site coordinator, for this great experience.



Regulation of the Immune System by DNA-Drug Nanomaterials

Samantha Renee Corber

Chemistry, Physics, Washburn University, Topeka, KS

NNIN iREU Site: National Institute for Materials Science (NIMS), Tsukuba, Ibaraki, Japan

NNIN iREU Principal Investigator: Dr. Nobutaka Hanagata, Nanotechnology Innovation Station, National Institute of Material Science, Tsukuba, Japan

NNIN iREU Mentor: Hiromi Morita, Biosystems Control Group, National Institute of Material Science, Tsukuba, Japan

Contact: srcorber@gmail.com, hanagata.nobutaka@nims.go.jp, morita.hiromi@nims.go.jp

Abstract:

Single stranded cytosine-phosphate-guanine oligodeoxynucleotides (ss-CpG ODN) have been shown to bind to Toll-like receptor 9 (TLR9) located in the endosome of macrophages in the immune system. This allows for regulation of both the innate and adaptive immune system that can lead to medical treatments such as cancer immunotherapy. Double stranded non-CpG ODN (ds-non-CpG ODN) are capable of regulating the innate immune system through interactions with cytosolic receptors. Our goal for this project was to investigate how the shape of different nanomaterials can affect the action of the ODN drug in macrophages. Both ss-CpG ODN and ds-non-CpG ODN were functionalized separately onto a cationic lipid DOTAP, carbon nanohorn (CNH), polyethyleneimide-coated CNH, and MoS₂ monolayer sheet. The ODN-nanomaterial solutions were transfected to macrophages and the RNA was isolated. Finally, reverse transcription and real time polymerase chain reaction were performed to measure the relative expression level of interleukin 6 (IL-6) and interferon beta (IFN- β), two proteins secreted in the adaptive and innate immune system pathways respectively. It was found that for both ss-CpG ODN and ds-non-CpG ODN, samples incubated with DOTAP had the highest level of expression IL-6 and IFN- β .

Introduction:

Ss-CpG ODN and ds-non-CpG ODN are both capable of regulating the immune system through different pathways (Figures 1 and 2). Ss-CpG ODN activates the adaptive immune system through the TLR9 in the endosome of macrophages of the immune system, which in turns produces the protein IL-6. Ds-non-CpG ODN activates the innate immune system through binding different cytosolic DNA receptors in the cytosol that produces the protein IFN- β . For this project, our goal was to investigate how the shape of the nanomaterial can affect the action of the DNA drug in macrophages. DOTAP is a cationic lipid that composes the membrane around the endosome in macrophages, which is capable of binding the drug with electrostatic interaction. Molybdenum disulfide (MoS₂) sheets are monolayer sheets similar in morphology to graphene.

Finally, CNH are similar to single walled carbon nanotubes but are around 10 to 20 nm and form a cone shape. They aggregate together to form particles around 60 nm long. For both MoS₂ and CNH, the drug is adhered to the surface of the nanomaterial. Because CNH and the ODN are both negatively charged, it is unclear what forces are adsorbing the ODN onto the surface of the CNH. Ss-CpG ODN is believed to change conformation when adhered to the nanomaterial, which in turn can affect how it interacts with TLR9, leading to either enhanced or lower the immune response. For ds-non-CpG ODN, the nanomaterial acts as a carrier for the ODN drug out of the endosome and into the cytosol.

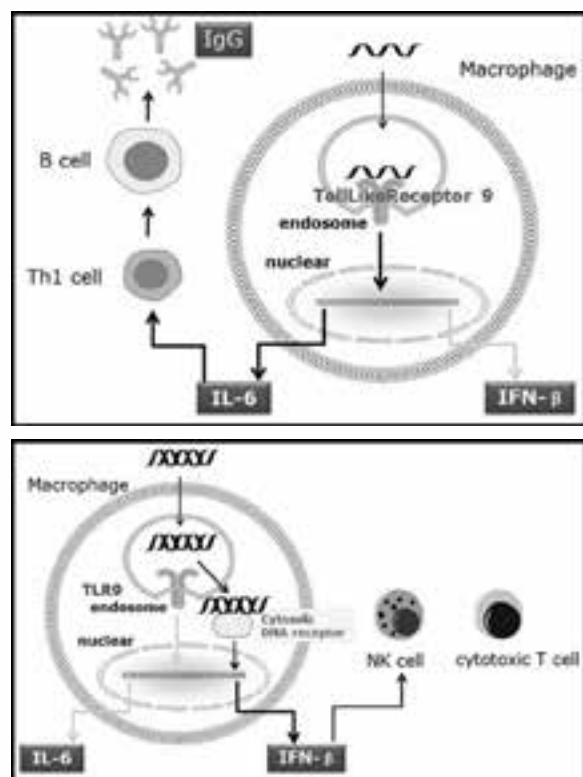


Figure 1, top: Diagram of the immune system activation pathway for ss-CpG ODN. Figure 2, bottom: Diagram of the immune system activation pathway for ds-non-CpG ODN.

Experimental Procedure:

To see if the nanomaterial drugs are activating the immune system, we measured the levels of IL-6 and IFN- β . First, we functionalized the ODN onto the nanomaterial and added it to a culture of macrophages, allowing it to incubate overnight. After loading the DNA onto the nanomaterial, except for the case of DOTAP, the material was ultracentrifuged and the supernatant collected and measured using ultra-violet/visible light spectroscopy. From this, the mass amount of DNA loaded onto the material is calculated. The ribonucleic acid (RNA) from the cell was then isolated and cleaned up to remove impurities.

Next, reverse transcription is performed to transcribe the RNA back to deoxyribonucleic acid (DNA). The amount of protein produced in the cells is inferred from the amount of DNA measured using real-time polymerase chain reaction

(q-PCR). The cellular DNA is mixed with buffer and primer that is complement to the sequence of DNA for either IL-6 or IFN- β . GAPDH, a house-keeping protein that has a stable production in cells throughout different conditions, was used as a housekeeping protein to standardize the expression level against the other samples.

Results and Conclusions:

The results of IL-6 and IFN- β for nanomaterials loaded with ss-CpG ODN are shown in Figure 3. We observed that DOTAP was the most effective nanomaterial for delivery of ss-CpG ODN to the TLR9 in the endosome. From this result, we can conclude that the ODN adsorbed onto the surface of the other nanomaterials is not able to interact with TLR9. For the ds-non-CpG ODN, only the production of IFN- β was investigated. Consequently, DOTAP also had the highest potential to induce IFN- β for the delivery of ds-non-CpG ODN (Figure 4). The biggest challenge with activating the cytosolic receptors is that the DNA must leave the endosome. Because DOTAP is composed of the same material that the endosome membrane is composed of, it can combine with the membrane, releasing the loaded drug into the cytosol while the other materials must diffuse through the membrane to deliver to the cytosolic receptors.

Future Work:

Due to the large error in the ds-non-CpG ODN experiment, more trials would need to be completed to verify the work. To investigate the effects of electrostatic interaction versus adsorption on the ODN, the same experimental steps seen here could be performed on CNH sample but coated in polyethylene imide (PEI), a positively-charged polymer, before ODN functionalization.

Acknowledgements:

I would like to thank my principal investigator, Dr. Nobutaka Hanagata and mentor, Ms Hiromi Morita, along with all the members of our group at NIMS for their guidance and expertise through this project. I would also like to thank Dr. Yudasaka (AIST, Japan) for providing the CNH and Dr. Xu (Zhejiang University, China) for providing the MoS₂. Finally, I would like to thank NNIN, especially Dr. Nancy Healy and Dr. Lynn Rathbun for two wonderful summer experiences over the past two years, and the NNIN iREU Program and NSF for funding.

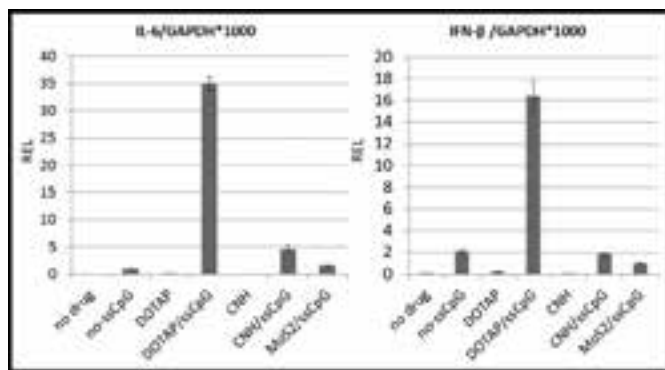


Figure 3: Relative expression level of IL-6 (a) and IFN- β (b) for ss-CpG ODN with various nanomaterials.

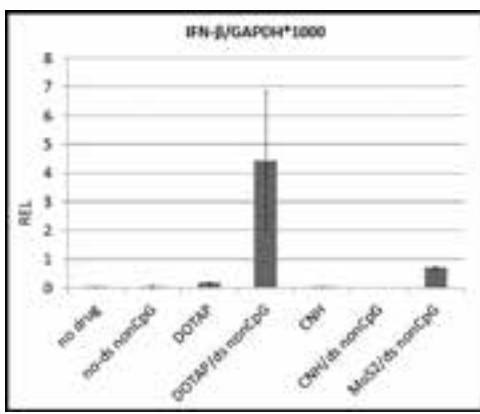


Figure 4: Relative expression level IFN- β for ds-non-CpG ODN with various nanomaterials.

Development of Diamond-Like Carbon Deposition Processes and Microfabrication of Thin-Film Ag/AgCl Reference Electrodes

B
I
O
L

Christopher Davidson

Biological Systems Engineering, University of Nebraska – Lincoln

NNIN REU Site: Minnesota Nano Center, University of Minnesota-Twin Cities, Minneapolis, MN

NNIN REU Principal Investigator and Mentor: Dr. Stephen A. Campbell,
Electrical and Computer Engineering, University of Minnesota-Twin Cities

Contact: cdavidson222@gmail.com, campb001@umn.edu

Abstract:

The ability to track neurotransmitters at a cellular level could greatly expand our understanding of the brain. To do this, however, we need to make safe, implantable devices that can sense activity at this level. This summer, two aspects of this project were focused on: a) the use of diamond-like carbon as a biocompatible coating for these devices, and b) the fabrication of thin-film silver/silver chloride (Ag/AgCl) electrodes to measure concentration of neurotransmitters. Due to its favorable properties, diamond-like carbon could reduce glial scarring and improve durability of these sensors. It was deposited using different gas mixtures by an rf-plasma enhanced chemical vapor deposition (PECVD) system. Unfortunately, only amorphous carbon was formed during this process. However, annealing at 600°C for 30 minutes in a sealed ampoule left traces of diamond-like carbon. Next, microfabrication of a Ag/AgCl thin-film electrode was completed. This electrode can be used as a reference for cyclic voltammetry to measure concentration of neurotransmitters in the brain.

Introduction:

Diamond-like carbon (DLC) has many advantageous properties, such as high wear resistance, hardness, biocompatibility, and a low coefficient of friction, that allow it to be such a promising material for biomedical applications. Radio frequency plasma enhanced chemical vapor deposition (rf-PECVD) using methane (CH_4) as a carbon precursor is one way to deposit DLC [1]. Diluting CH_4 with an inert gas, such as N_2 , He, or Ar, is believed to assist the creation of capacitive coupled plasma and to enhance the plasma density [2].

Cyclic voltammetry is the process by which voltage is swept between two values at a fixed rate, and current is measured and plotted. This plot is called a voltammogram. Voltammograms can be used to quantify neurotransmitter types and concentration. To run cyclic voltammetry, however, a stable reference electrode, such as a silver / silver chloride (Ag/AgCl) electrode, is needed. It is also necessary to microfabricate this electrode to allow for a maximum amount of these devices to be put in the brain sensing system.

Experimental Procedure:

DLC films were deposited onto bare silicon wafer pieces by different ratios of CH_4 and either N_2 , He, or Ar gas mixtures. Before deposition, there was a 5-minute chamber clean with 100 sccm of N_2 at 300 watts. During deposition, the rf-power was 150 W, and the deposition time was kept constant at ten minutes. The deposition pressure was kept at 300 mTorr. There

was a constant total gas flow of 100 sccm for all trials and a substrate temperature of 20°C. Films were then characterized using Raman spectroscopy. The spectra showed that there was a very high concentration of hydrogen in the films, so DLC was not formed. Thus, one sample was annealed with N_2 gas at 600°C in a mini-brute furnace for 30 minutes. It was necessary to seal this sample in a glass ampoule to prevent oxidation of the film.

The Ag/AgCl electrode that was fabricated was made of multiple layers. First, layers of silicon dioxide (SiO_2 , conductive layer), titanium and palladium (adhesive layer), and Ag were deposited. After this, the Ag layer was chlorinated. This was carried out through electrochemical chlorination in an HCl solution at a constant current of 1000 $\mu\text{A}/\text{cm}^2$ for 10 minutes [3].

Results and Conclusions:

The deposition rates of the DLC films, depending on the ratio of N_2/CH_4 and He/CH_4 , are shown in Figure 1. The figure shows that deposition rate increased up to about 70% N_2 or He, and then decreased. This observation is similar to that observed by Kim, et al. [2], with a gas mixture of Ar/ CH_4 . This drop most likely occurred because when the CH_4 concentration got too low, the etching rate—due to the diluting gas—became greater than the deposition rate of CH_4 .

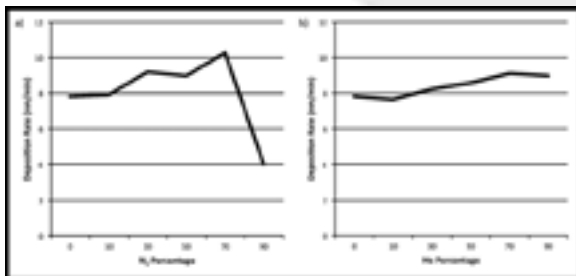


Figure 1: Variation of DLC deposition rates of the; a) N_2/CH_4 and b) He/CH_4 gas mixtures.

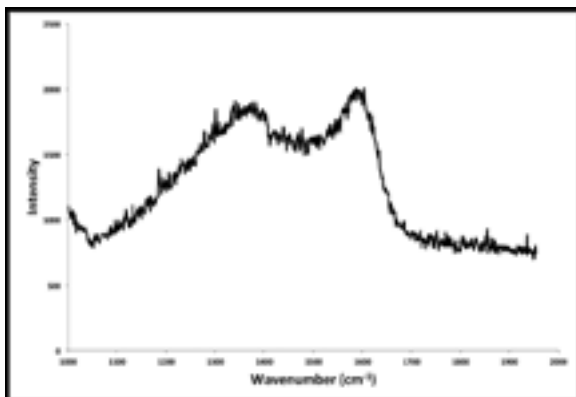


Figure 3: Raman spectra for annealed sample.

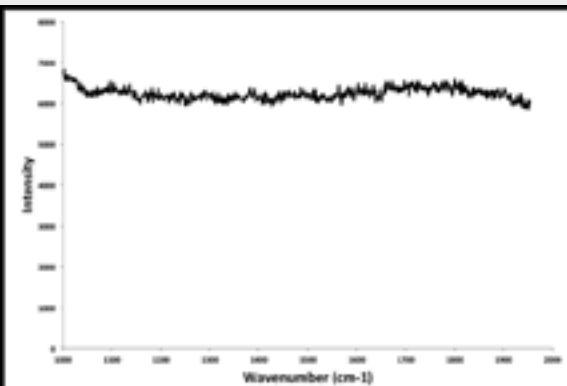


Figure 2: Raman spectra for 50% CH_4 / 50% N_2 sample.

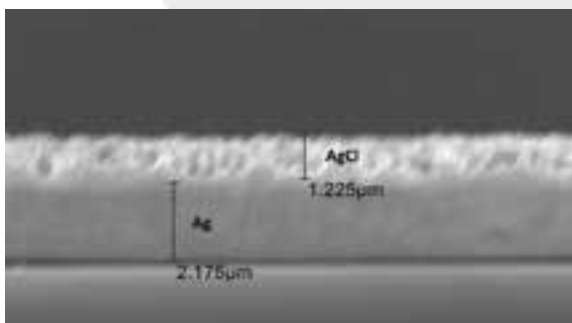


Figure 4: SEM cross-section of $Ti/Pd/Ag/AgCl$ electrode.

After characterizing the films using Raman spectroscopy, it was shown that DLC had not formed. As shown in Figure 2, the G-peak (1600 cm^{-1}) and D-peak (1350 cm^{-1}) that are representative of sp^2 and sp^3 hybridized carbon, respectively, were not present in the spectra. We believe that this was due to the high concentration of hydrogen in the films. After annealing, however, the hydrogen was removed from the film and sp^2 and sp^3 C-C bonds were formed. Figure 3 shows the spectra for this annealed sample, and both the G-peak and D-peak are present.

After this process was done, the thin-film $Ti/Pd/Ag/AgCl$ electrode was microfabricated. Figure 4 shows a scanning electron microscope (SEM) cross-section image of the final film. It shows about $1.2\text{ }\mu\text{m}$ of $AgCl$ and $2.2\text{ }\mu\text{m}$ of Ag . Therefore, about 36% of the original Ag film was converted to $AgCl$. This agrees with the work of Huang, et. al., ran the same process and had 33.3% of the Ag film converted to $AgCl$ [3].

Future Work:

Once DLC films are made, stress tests and biocompatibility tests will be done to gain further information on the material.

Next steps in work with the $Ag/AgCl$ electrode include patterning the electrode and running cyclic voltammetry tests with different neurotransmitters.

Acknowledgments:

I would like to thank the NNIN REU Program and NSF for funding this project. I would also like to thank Dr. Stephen Campbell for his help and guidance, and Dr. James Johns and the Minnesota Nano Center for providing the equipment and training necessary.

References:

- [1] Roy, R.K., and Lee K.; "Biomedical Applications of Diamond-Like Carbon Coatings: A Review"; Wiley InterScience (2007).
- [2] Kim, J., and Lee C.; "Dependence of the Physical Properties DLC Films by PECVD on the Ar Gas Addition"; Journal of the Korean Physical Society, 42, 956-960 (2003).
- [3] Huang, I., Huang, R., and Lo, L.; "Improvement of Integrated $Ag/AgCl$ Electrodes by KCl-gel Coating for ISFET Applications"; Sensors and Actuators B: Chemical, 94, 53-64 (2003).

Microfluidic Bio-Sensing for *in vitro* Tumor Cell Proliferation

Fatima-Joyce Dominguez
Electrical Engineering, University of Portland

NNIN REU Site: ASU NanoFab, Arizona State University, Tempe, AZ

NNIN REU Principal Investigator: Dr. Jennifer Blain Christen, Electrical Engineering, Arizona State University

NNIN REU Mentor: Tao Luo, Electrical Engineering, Arizona State University

Contact: domingue15@up.edu, jennifer.blainchristen@asu.edu, tluo6@asu.edu

Abstract:

We present the fabrication of a monitoring system that allows for monitoring of cells inside an incubator. The system consists of a custom cell-monitoring device, a remote gate ion sensitive field effect transistor (ISFET), an amplifier, and a BeagleBone platform. The design, fabrication, and operation of the remote gate ISFET are described. We also describe how the ISFET was used to create the autonomous, continuous-time cell monitoring system, programmed for any time interval. Finally, we present the results of monitoring cells dosed with the chemotherapy drug *Staurosporine* over a period of 38 hours.

Introduction:

Currently, chemotherapy drug testing on cultured cells is a time-consuming, tedious process. Varying doses of the drug are added to cultured cells, and cells are monitored for viability (percent of the culture flask covered in cells). To accomplish this, researchers remove cells from an incubator (causing their local temperature, humidity, and pH to drop), use a microscope to examine a small area of the flask visually (prone to error from non-uniform distribution), and return the cells to the incubator. Moreover, this long process is just one small step for the diagnosis and treatment of a cancer patient. The ability to decrease the time needed, improve the accuracy of testing, and cater to each individual patient's case is crucial to improving the chances of their survival.

ISFETs are an ideal biosensor for diagnostic testing due to their ability to accurately measure changes in a solution's acidity, such as a cancer cell's microenvironment. Cancer cells have an increased metabolism relative to healthy cells, leading to an increase in the production of lactic acid [1]. We can monitor this increase using the ISFETs as an increase in the pH of the cell culture media.

The aim of this project was to build a continuous-time, autonomous cell monitoring system, for use inside an incubator, with the ability to monitor multiple cell populations for any interval or sampling rate. The reliability of this system was to be confirmed by visually examining the cells over different intervals.

Biosensor Fabrication:

The design for the ISFET biosensor was nearly identical to the design prepared by Welch [2]. However, instead of silicon,

quartz was chosen as the substrate to allow for visualization of the cells under a microscope. The pattern for the biosensor is shown in Figure 1, with the ion-sensitive portion covered completely in silicon nitride (SiN), and the reference electrode being exposed gold (Au).

The fabrication was as follows: photolithography for resist patterning, thermal evaporation for the deposition of 30 nm of chrome and 70 nm of gold, acetone lift-off with sonication, deposition of 65 nm plasma-enhanced chemical vapor deposition (PECVD) nitride, resist patterning, reactive ion etching (RIE) etching, and finally, resist removal. The substrate was then bonded to a polydimethylsiloxane (PDMS) well through plasma cleaning.

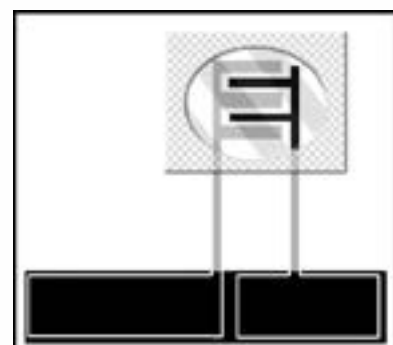


Figure 1: The areas depicted in gray are portions covered by SiN, the black areas are the exposed Au, and the checkered pattern represents the PDMS well.

Cell Treatment:

About 125 μ L of cell media containing breast cancer cells, SKBR-3, was pipetted into the PDMS well. The experimental group was treated with 5 μ L of 1 mM *Staurosporine*, a drug known to induce apoptosis in SKBR-3 cells. A control group, not treated with any drugs, was also monitored.

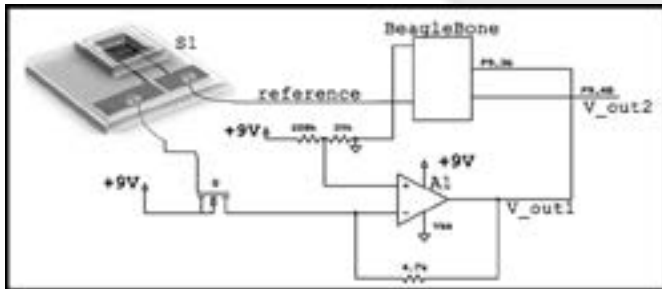


Figure 2: Schematic of the data acquisition system.

Data Acquisition System:

The biosensor's sensing region was connected to the gate of an n-channel MOSFET; while the reference electrode was connected to a BeagleBone platform's (BBP) ground. The output current of the complete ISFET was converted to a voltage by a trans-impedance amplifier before being sent to the BBP for data storage. The complete schematic for each channel is shown in Figure 2. The system, one channel each for the control and experimental group, was powered by a 9V battery, while the BeagleBone was powered by a 5V power supply. The BBP recorded the voltage of the systems in an interval of ten minutes.

Results and Conclusion:

In the first hour of cell-monitoring, the BBP crashed, causing loss of ability to monitor the control group with the data monitoring system. Furthermore, after the fourth hour, the control group evaporated due to the small amount of media the well could hold. The evaporation caused the cells to die, meaning that the control group could not be an accurate comparison to the experimental group. Imaging and data collection from the experimental group continued normally.

The results collected from the BBP are shown in Figure 3. Over a period of 38 hours, the voltage decreased from about 1.4V to 0.02V. The decrease in voltage over time shows that there was a reducing amount of cell proliferation. This agreed with the imaging of the cells shown in Figure 4, confirming that the cell-monitoring system successfully monitored the pH levels of the cells' microenvironment. However, further data will be collected to include a control group.

Further work includes optimization of the BBP to include safeguards for program failure and real-time data acquisition with visualizations over a network, and fabrication of a 2×2 sensor array on one quartz substrate for easier, cheaper monitoring of different cell populations.

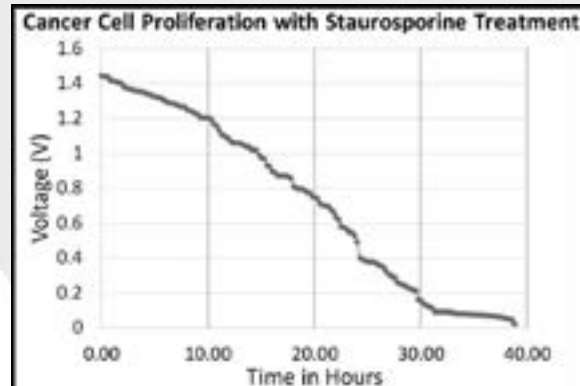


Figure 3: Voltage data collected over a period of 38 hours.

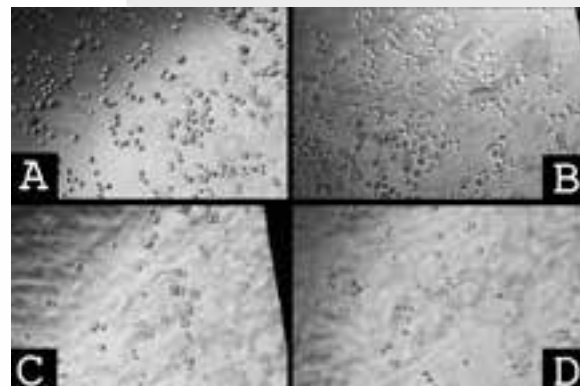


Figure 4: Imaging of the cells at (A) the initial time, (B) after 4 hours, (C) 24 hours, and (D) 36 hours.

Acknowledgements:

My utmost gratitude goes to my Principal Investigator Dr. Jennifer Blain Christen and mentor Tao Luo for all their knowledge; Hany Arafa and Dixie Kullman for help with the biological aspects; the Center for Solid State Electronics Staff, particularly Carrie Sinclair, for fabrication guidance; University of Arizona NanoFab; and finally, Arizona State University, the National Nanotechnology Infrastructure Network Research Experience for Undergraduates Program and the National Science Foundation for making all this possible.

References:

- [1] Weinberg, Robert. *The Biology of Cancer*. Garland Science, 2013.
- [2] D. Welch, "Systems Integration for Biosensing: Design, Fabrication, and Packaging of Microelectronics, Sensors, and Microfluidics", Ph.D. dissertation, Dept. Elect. Eng., ASU, Tempe, AZ, 2012.

Developing a Novel Microfluidic Device for the Study of Molecular Communication Between Bacterial Colonies

Lucy Hu
Bioengineering, University of California, Berkeley

NNIN REU Site: Institute for Electronics & Nanotechnology, Georgia Institute of Technology, Atlanta, GA

NNIN REU Principal Investigator: Craig R. Forest, Bioengineering, Georgia Institute of Technology

NNIN REU Mentor: Caitlin Austin, Bioengineering, Georgia Institute of Technology

Contact: lucyhu@berkeley.edu, craig.forest@me.gatech.edu, caitlin.austin@gatech.edu

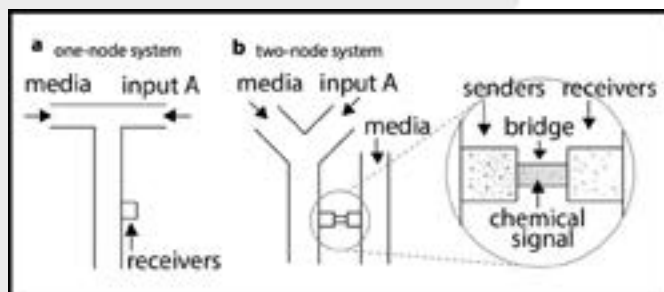


Figure 1: The concept design developed from our current one-node design into our two-node system.

Introduction:

Understanding the molecular communication between bacteria is a key component in building biosensors that utilize genetically modified bacteria for applications such as environmental monitoring. Currently, we have the capacity to study one receptor bacterial colony's response to an artificial chemical signal (i.e., a one-node system) via a microfluidic device; however, studying the communication between two bacterial colonies (i.e., a two-node system) is key to improving the robustness of biosensors. Previous studies have created devices that can pass a gaseous signal between isolated colonies [1], but devices that study aqueous signals have cross-contamination issues [2], or limited versatility of signal input [3].

This project focused on the creation of the first microfluidic device that allows for the study of various communication schemes (e.g., pulses, step functions) via an aqueous signal between sending and receiving bacterial colonies in one microfluidic chip. Our design, seen in Figure 1, is based on isolating sending and receiving colonies of bacteria in separate chambers and connecting them via a bridge that contains a porous polymer monolith that acts as a filter. Patterning the polymer monolith posed a key challenge. The chemical signal diffuses from the senders through the bridge to the receivers. However, the chemical signal doesn't entirely diffuse across the bridge, so we manipulated the geometry of our device to control the signal loss.

Experimental Methods:

Polydimethylsiloxane (PDMS) devices were fabricated using a 65g total 10:1 ratio of polymer to crosslinker (Silgard 184 Elastomer) poured onto a silanized SU-8 master mold and cured for four hours minimum at 60°C.

The device was masked off to photopattern the monolith. In fabricating the porous polymer monolith, the PDMS channels were first surface treated. A 0.25M 2,2'-dimethoxy-2-phenylacetophenone (DMPAP) in acetone solution rinse was flooded through, and then a monomer solution of a 1:1 ratio of methylmethacrylate and ethylene diacrylate was loaded in and UV exposed for 40s with an 8W of 365 nm UV. This was then flushed out and then the monolith solution—consisting of (by weight) 60% 1:1 methanol to 2-propanol solution (porogen), 20% butyl methacrylate (monomer), 20% ethylene dimethacrylate (crosslinker), and 0.4% DMPAP (photo initiator)—was flooded in and treated with 8W of 365 nm UV for 45 minutes.

Confocal microscopy of the fabricated monolith was performed with a Zeiss 510 laser scanning microscope. To test the blocking ability of the monolith, genetically engineered *Escherichia coli* (*E. coli*) that continually produced green fluorescent protein (GFP) was flown into the device against the monolith.

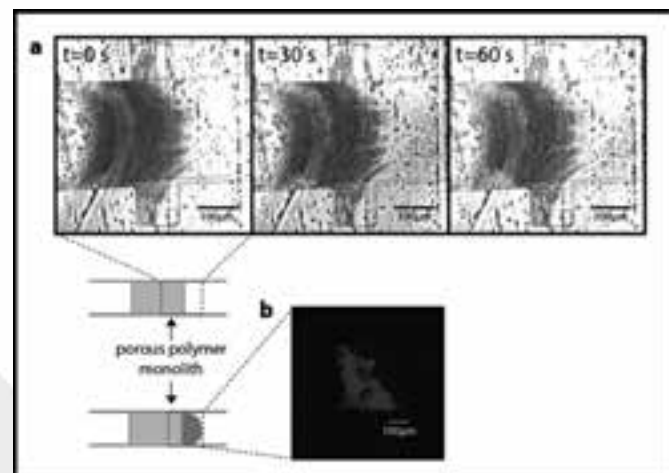


Figure 2: Microscopy images of the photopatterned monolith fabricated in an arbitrary device. (See in full color on page xxxvi.)

COMSOL Multiphysics 4.4 software was used to model theoretical chemical signal retention between the chambers in different geometries, using empirically realistic values and assuming a no flow condition in the bridge to account for biofilm buildup.

Results and Discussion:

Figure 2 depicts the confocal microscopy images of our resulting monolith. After flowing in *E. coli* that continually produced GFP, we found that the bacteria were capable of penetrating the beginning of the filter, but eventually were trapped and collect in patches, as seen in Figure 2a. In another trial of the fabrication, we imaged the bacterial plug that collected against the fabricated filter. These preliminary results show that the filter seems to be capable of preventing cross-contamination of bacterial colonies.

To manage loss of chemical signal, we engineered the device geometry to lower the velocity of the flow adjacent to the bacteria chambers by varying the channel angles. Key factors that need to be considered include the tendency for bacteria to stick to and colonize sharp turns, corners, and areas of low velocity, potentially clogging the device.

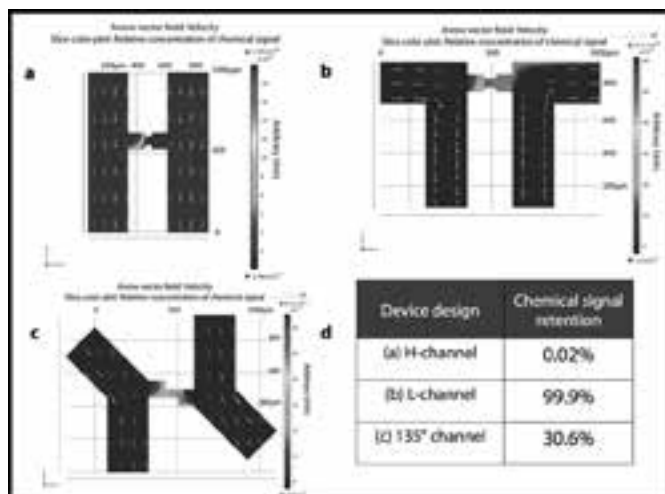


Figure 3: COMSOL plots analyzing the chemical signal retention of varying geometries.

Figure 3 shows the COMSOL plots showing the velocity vector field and concentration gradients of varying geometries. The H-channel design retained almost no signal, given the uniformity of velocity flow adjacent to the chamber. The L-channel design minimized loss of signal, but had many sharp angles areas of low flow in the corners such that clogging would occur. The 135° angled channel design allowed for a compromise between signal retention and uncontained bacterial growth. The tunable nature of the geometry offered the full range of retention percentages. We moved forward with the 135° angled channel design, because the theoretical retention of 30.6% of the chemical signal seemed sufficient.

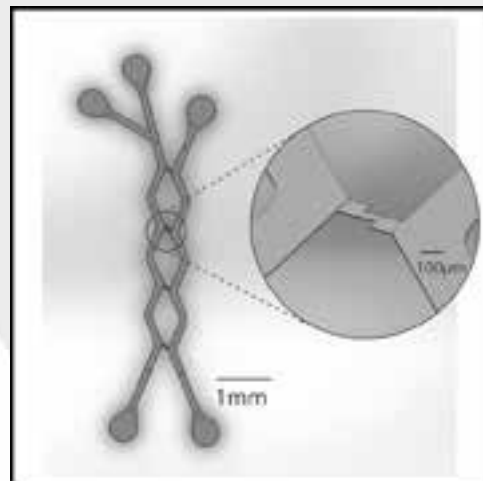


Figure 4: The final design with four chamber-pair iterations and rounded corners.

If this proves to be insufficient, one can tune the angle of the channel in the design for signal retention. Our final design is seen in Figure 4; corners are rounded to prevent bacterial adhesion.

Future Work:

Our next step is to fabricate the porous polymer monolith in the exact bridge region of our new device. We need to run experiments to see if the filter pore size provides sufficient isolation of the colonies over the time period of an experiment (~ 2 days). If insufficient, we need to adjust the recipe for the monolith to tune the pore size such that the bacteria cannot migrate through. Additionally, we need to prove that the chemical signal can freely diffuse through the monolith. With this, we will have successfully created the first microfluidic device to study an aqueous signal between two bacterial colonies.

Acknowledgements:

I would like to extend my thanks to Caitlin Austin, Prof. Craig Forest, Georgia Tech cleanroom staff, Dr. Nancy Healy, Ms. Joyce Palmer, and Ms. Leslie O'Neill. This project was made possible by the generous support of the National Nanotechnology Infrastructure Network Research Experience for Undergraduates (NNIN REU) Program and NSF.

References:

- [1] A. Prindle, et al., A sensing array of radically coupled genetic ‘biopixels’, *Nature* 481, 39-44 (2012).
- [2] S. Park, et al., Microfabricated ratchet structure integrated concentrator arrays for synthetic bacterial cell-to-cell communication assays, *Lab Chip* 12 3914-3922 (2012).
- [3] K. Nagy, et al., Interaction of Bacterial Populations in Coupled Microchambers, *Chem. Biochem. Eng.Q.*, 28 (2) 225-231 (2014).

A Microfluidic Approach to Stiffness Gradient Generation in Polyacrylamide-Based Cell Migration Analysis Platforms

Meghan Kazanski

Biomedical Engineering, University of Rochester

NNIN iREU Site: National Institute for Materials Science (NIMS), Tsukuba, Ibaraki, Japan

NNIN iREU Principal Investigator and Mentor: Dr. Jun Nakanishi, International Center for Materials Nanoarchitectonics (MANA), National Institute for Materials Science (NIMS), Tsukuba, Ibaraki, Japan

Contact: mkazansk@u.rochester.edu, nakanishi.jun@nims.go.jp

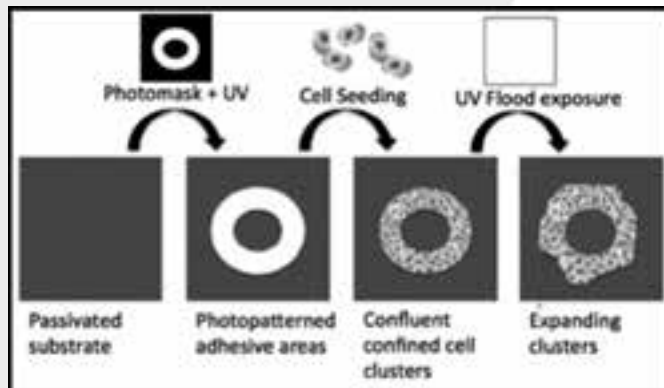


Figure 1: Passivation of substrate with PCP (2k, 5k 12h later) makes the surface nonadhesive. UV exposure of PCP-functionalized surface cleaves the PEG molecule, making exposed surfaces (photomask controlled) cell adhesive. Geometric confinement is determined by irradiation pattern. Cell spreading is initiated by non-selectively exposing the surface following cell seeding.

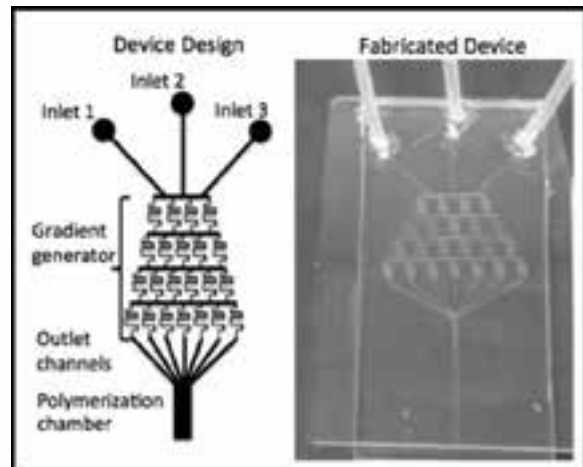


Figure 2: Device is designed for addition of 4% acrylamide in each inlet, and 0.4% bis-acrylamide in Inlets 1 and 2, and 0.04% in 3. For gradient characterization, 20 mM fluorescein was added to Inlet 1, 10 mM to 2 and milliQ H₂O to 3.

Introduction:

Collective cell migration is a critical component of physiological and pathological processes. This motility is directed by extracellular matrix (ECM) factors, including elasticity, known to profoundly affect single cell migration [1]. Less studied are the effects of mechanical compliance on collective cell migration, in which cell-cell contacts are maintained. Understanding the roles of ECM factors in collective cell migration will reveal underlying mechanisms of wound-healing, developmental, and metastatic processes [2].

Until recently, cell migration was studied on stiffness-homogenous substrates, limited in the neglect of durotaxis' stiffness gradient-directed migration [1, 3]. Gradients in niche elasticity often result from the pathological and physiological conditions involving collective cell migration, suggesting that gradients are crucial to directed colony migration.

Microfluidic gradient generation fabricates a more-appropriate substrate for comprehensive motility study, with a precise, function-defined gradient [4]. The gradient substrate is achieved by altering polyacrylamide (PAA) crosslinking density and photopolymerizing within microchannels [5, 6].

A controlled collective motility assay may be performed with surface functionalization via photo-cleavable poly(ethylene glycol) (PCP), to direct initial colony configuration and migration initiation [7, 8]. This method has successfully demonstrated collective migration trends in defined micro-environments.

The techniques of substrate formation and functionalization in this study may result in platforms with physiologically-relevant stiffness gradients and capability for light-driven alteration of cell adhesion for sophisticated motility analysis. With the fabricated device and proposed application, collective cell migration is explored to better mimic relevant pathways *in vitro*, and regulate pathways *in vivo*.

Experimental Methods:

Device Fabrication and Construction. The microfluidic device incorporated tri-inlet features, a linear gradient generator [4-5], and a gel photopolymerization chamber (Figure 2). The device was fabricated in PDMS using rapid

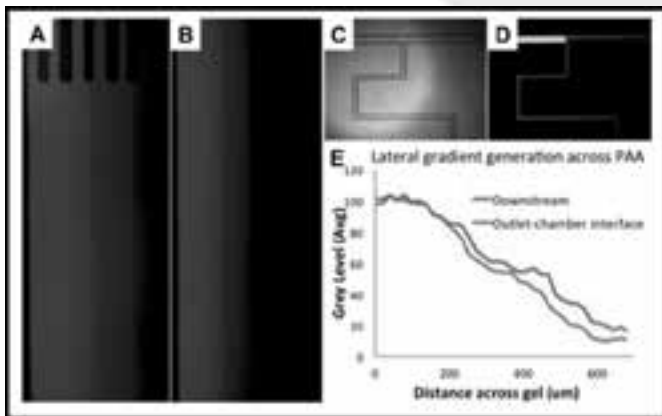


Figure 3: Fluorescent images are of gradient distribution of fluorescein across chamber width at the outlet-chamber interface (A), and downstream (B). Intensity as a function of width indicates a stepwise trend at the interface, and a linear gradient downstream (E). Adequate mixing is achieved at interfaces (C-D).

prototyping and soft lithography [9]. The PDMS component with embedded microchannels and 1.3 mm inlets, was bonded to a glass slide via O₂ plasma treatment (150 mTorr, 100 W, 1 min). Tubing (2 mm) interfaced with the inlet holes via silicon adhesive and connected to a syringe pump.

Device Characterization. Uranine fluorescent dye (MW = 332 Da) was utilized to verify gradient linearity (Figures 2-3). Fluorescent images were obtained during flow, 10-15 min after gradient establishment. Fluorescent intensities were plotted as a function of chamber width using Metamorph (Molecular Devices, CA).

Cell Micropatterning on Bulk Substrates. PAA substrates were photopolymerized on glass slides at 55 and 5 kPa [10]. Compliance measurements were performed via atomic force microscopy (AFM) and a steel bead indentation method [11]. The photopolymerization process was later modified to include methylene blue as the photoinitiator [6]. Surface functionalization via PDL and PCP was performed [7], and a patterned photomask was used in irradiation of adhesion geometries (Figures 1 and 4).

Results and Future Work:

Multiple gradient-generating devices were successfully fabricated with differing outlet dimensions approximating the design parameters. Plots of fluorescence against chamber width at the outlet-chamber interface, and downstream in chamber indicate stepwise and linear gradients, respectively (Figure 3). Thus, the substrate will be extracted at the downstream location.

Before focusing on a gradient gel study, homogeneous gels were successfully fabricated at stiffnesses of 55 kPa and 5 kPa. Stiffness measurements collected via AFM and classical measurements were accurate and comparable. Results of bulk

substrate surface functionalization correspond with previous studies [7, 8]. Irradiated regions of passivated substrate had a significantly-greater cell adhesion than non-irradiated regions (Figure 4).

Given the success of bulk substrate fabrication, characterization, and micropatterning, and substrate gradient verification with the fabricated device, we intend to proceed to fabricate stiffness-variant substrates within the device for extraction and migration study. Gradient-compliant substrate photopolymerization is proposed as described in Zaari, et al., with methylene blue [5-6].

Following substrate extraction, techniques of surface functionalization via PDL and PCP should facilitate cell micropatterning and controlled migration initiation [7-8]. The performance of this assay will be the first study of micro-controlled collective migration on a stiffness-gradient substrate with high precision. The information yielded in studies utilizing substrates fabricated with our device will well-define the role of elasticity gradients in collective migration, contributing to mimicry, alteration and understanding of biological processes.

Acknowledgements:

The author would like to thank the National Nanotechnology Infrastructure Network International Research Experience for Undergraduates Program, National Science Foundation (NSF), National Institute for Materials Science (NIMS), Dr. Jun Nakanishi, Dr. Yoshihisa Shimizu, Dr. Tomonobu Nakayama, Dr. Noni Creasey, Tomoko Ohki, and Akihiko Ohi.

References:

- [1] Lo, C., et al., *Biophysical Journal*. 2000. 79. 144-152.
- [2] Trepat, X., Fredberg, J. *Trends Cell Biol.* 2012. 21(11). 638-646.
- [3] Vincent, L., et al., *Biotechnol J.* 2013. 8(4). 472-474.
- [4] Dertinger, S., et al., *Anal. Chem.*, 2001, 73. 1240-1246.
- [5] Zaari, N., et al., *Advanced Materials*. 2004. 16, 23-24.
- [6] Lyubimova, T., et al. *Electrophoresis*. 1993. 14(1-2). 40-50.
- [7] Rolli, C., et al. *Biomaterials*. 2011. 33(8). 2409-2418.
- [8] Kaneko, S., et al. *Phys. Chem. Chem. Phys.* 2011. 13, 4051-59.
- [9] Wolfe, D B., et al. *Microengineering*. 2010. 583.
- [10] Mih, J., et al. *PLoS ONE*. 2010. 6(5). e19929.
- [11] Long, R., et al. *Biophys. Aug.* 2011, 101 (3):643-650.

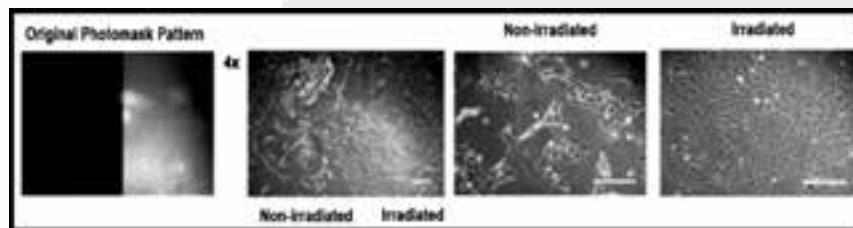


Figure 4: Selective cell patterning was demonstrated on gels with a bulk stiffness to verify process. Cell confluence corresponds with original photomask pattern, where non-irradiated surfaces demonstrate less cell adhesion.

Development of Zeolite-Based Nanofibers for the Removal of Uremic Toxins in Kidney Removal Patients

Gabriel R. López Marcial

Mechanical Engineering, University of Puerto Rico at Mayaguez

NNIN iREU Site: National Institute for Materials Science (NIMS), Tsukuba, Ibaraki, Japan

NNIN iREU Principal Investigator: Dr. Takao Aoyagi, National Institute for Material Sciences (NIMS), International Center for Materials Nanoarchitectonics (MANA), Tsukuba, Ibaraki, Japan

NNIN iREU Mentor: Dr. Koki Namekawa, National Institute for Material Sciences (NIMS), International Center for Materials Nanoarchitectonics (MANA), Tsukuba, Ibaraki, Japan

Contact: gabriel.lopez3@upr.edu, aoyagi.takao@nims.jp.go, namekawa.koki@nims.jp.go

Abstract:

Kidney failure patients in disaster areas and developing countries face the danger of having conventional hemodialysis treatments become inaccessible due to limited resources. For this reason, our goal is to develop a wearable device consisting of polymer fibers with a smart material that will selectively adsorb uremic toxins from the bloodstream, eliminating the need for more expensive treatments. The nanofibers would contain the blood compatible poly(ethylene-co-vinyl alcohol) (EVOH) as the main polymer, embedded with zeolites, a porous aluminosilicate that has the capacity to absorb toxins such as creatinine. The polymer and the zeolites were characterized separately to determine the ideal combination for the polymer meshes. This ideal combination was found to be 9 w/v% D2908 EVOH polymer fibers with a 10 wt% ratio of 940HOA zeolites. This fiber was found to absorb an impressive 57.43 mg of creatinine per gram of zeolite in the fiber. It was unusual and unexpected for the nanofiber to have a higher per gram adsorption than the free zeolites, and so further studies will be performed. These results suggest that these nanofibers could substitute for specialized equipment in removal of waste product from the bloodstream.



Figure 1: Possible application in wearable device. (Ebara, et al., Fabrication of zeolite-polymer composite nanofibers for removal of uremic toxins from kidney failure patients).

Methodology:

Fibers were first fabricated without embedded zeolites by electrospinning, which is a process in which a potential difference (voltage) is applied between a syringe with a solution and a collector, in our case a piece of aluminum paper. The voltage made the solution turn into random, solid strands that were deposited on top of the collector in the form of small fibers. To create the fibers, we first spun a PVA-water layer on top of the collector as a sacrificial layer. Then, after the EVOH

Introduction:

The final objective of this study is to develop zeolite-based polymer fibers that may be used in a wearable device to treat kidney failure patients (Figure 1). These nanofibers have two components, a polymer and a smart material, and they are intended to adsorb uremic toxins such as creatinine.

EVOH is ideal as a polymer because it is blood compatible, as well as insoluble in water, both of which are vital because the final application would involve blood being passed through EVOH-based meshes. Zeolites are porous, crystalline aluminosilicates. The microscopic pores are often called “molecular sieves,” because they can trap small molecules on their surface. There are different types and frameworks with properties varying according to pore and molecule size, as well as the orientation.

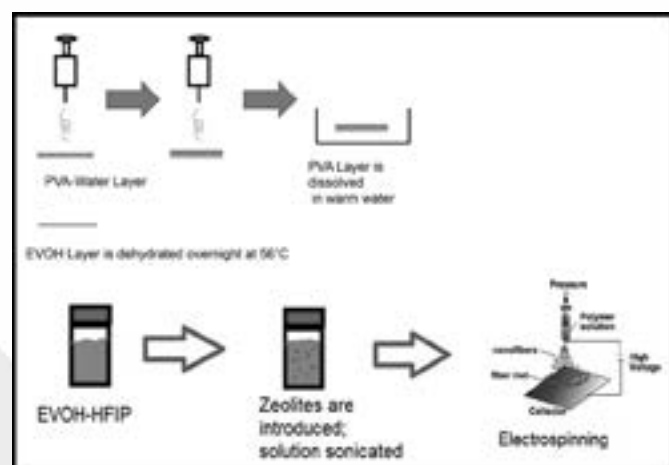


Figure 2: Fabrication techniques.

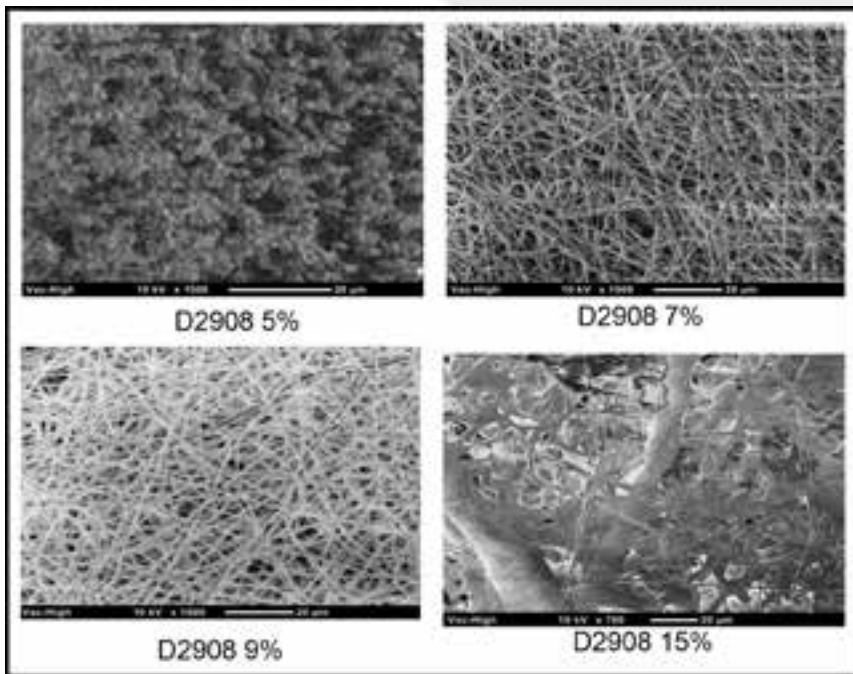


Figure 3: SEM imaging of fibers.

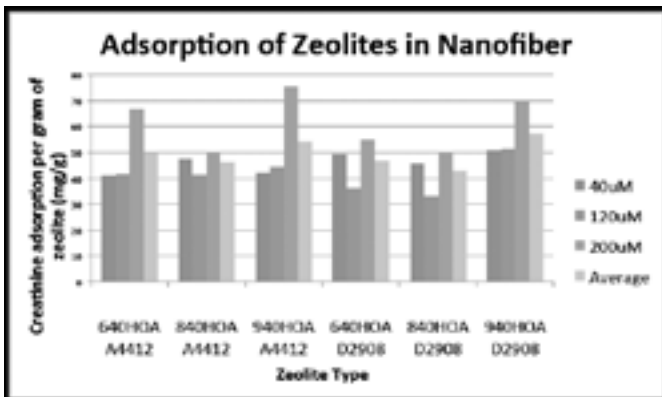


Figure 4: Adsorption capacity of zeolites in meshes.

was spun on top of it, the collector was dipped in warm water to dissolve the EVOH layer, simplifying the removal of the polymer fiber. It was then dehydrated at 56°C. This process is detailed in Figure 2. After a separate characterization of polymer fibers and zeolites, zeolites were sonicated into the EVOH solution and then electrospun to create the nanofibers.

To determine creatinine adsorption in zeolites and nanofibers, ultraviolet light (UV) absorption was used. Parting from the principle that higher concentrations of solute absorb more UV light, a calibration curve for different concentrations of creatinine-water was created. Free zeolites were introduced to a known concentration of creatinine-water and left stirring at 37°C for 24 hours, then centrifuged out of the solution. The remaining concentration was determined using UV absorption and the calibration curve. The mass of creatinine adsorbed could be obtained from the drop in concentration of the solution.

Results and Conclusions:

Different types of polymer fibers without zeolites were first characterized with a scanning electron microscope (SEM), to determine which would be better suited for the meshes. Two different EVOH polymers were selected: A4412 and D2908 (44% and 29% ethylene content, respectively). We tested 5, 7, 9, 10 and 15 w/v% and found that the lower concentrations produced “beading effects” that may affect the adherence of zeolites to the fibers. Similarly, the highest concentration (15%) produced fibers that were deformed and inconsistent in their diameter. Therefore, we chose 9 w/v% as the ideal concentration for larger, visually consistent nanofibers. The difference in ethylene content did not appear to have an effect on fiber morphology. These fibers may be observed in Figure 3.

Nine different types of zeolites were tested for their creatinine adsorption capacity UV absorption. These zeolites were 980HOA, 690HOA, 720KOA, 940HOA, 840HOA, 640HOA, 320HOA, and 500KOA. Three different experiments using varying mass of zeolites (10, 25 and 50 mg) in 200 μM concentrations gave us an idea of which zeolites adsorbed the most milligrams of creatinine per gram of zeolite. The most adsorbant zeolites were chosen for the meshes and were determined to be 940HOA, 840HOA and 640 HOA, with average adsorbance capacities of 5.56, 5.67, and 5.68 mg/g, respectively.

Six zeolite-polymer nanofibers were made, combining each of the selected zeolites and 9 w/v% solutions of both types of EVOH in a 10 w/w ratio. These fibers were also tested using UV absorption by dipping them in of 40, 120, and 200 μM creatinine-water solutions. The amount of creatinine adsorbed was adjusted to per gram of fiber and per gram of zeolite basis. These results are shown in Figure 4.

The most adsorbant zeolite polymer combinations were the ones containing the 940HOA zeolites, specifically the 940HOA-D2908 combination that had an adsorption capacity of 5.20 mg/g of fiber and 57.43 mg/g of zeolite. The ethylene content of the polymer did not seem to make any significant difference. These results are encouraging for the possible use of these fibers in a wearable device.

Acknowledgements:

I would like to thank the National Science Foundation (NSF), National Nanotechnology Infrastructure Network International Research Experience for Undergraduates (NNIN iREU) Program, and the National Institute for Material Sciences (NIMS). Special thanks go out to my mentor, Dr. Koki Namekawa, my PI, Dr. Takao Aoyagi, and everyone else at the Smart Biomaterials group at NIMS.

The Interaction of Cytotoxins with a Lipid Membrane Library

David Morse

Physics/Biophysics, The University of Tennessee, Knoxville

NNIN REU Site: Center for Nanoscale Systems, Harvard University, Cambridge, MA

NNIN REU Principal Investigator: Professor David Weitz, School of Engineering and Applied Physics, Harvard University

NNIN REU Mentor: Dr. Roy Ziblat, School of Engineering and Applied Physics, Harvard University

Contact: dmorse3@vols.utk.edu, weitz@seas.harvard.edu, rziblat@seas.harvard.edu

Abstract:

Cytotoxins are agents toxic to cells. To infect, cytotoxins must overcome the cell membrane, the primary defense of the cell. Membranes, however, are highly heterogeneous, containing many distinct domains differing by lipid content. For most cytotoxins, it is unknown if individual species differentiate between lipid compositions or if some domains act as nucleation sites for aggregation. Using microfluidic techniques, we studied the binding affinity of inert Amyloid-Beta 40 and toxic Amyloid-Beta 42, a primary suspect that exhibits neurotoxic activity leading to Alzheimer's dementia, and the membrane binding portion of the anthrax toxin, to a variety of lipid domains. By introducing the cytotoxins to a lipid domain library we were able to examine their binding propensities to lipid domains; we find this to be a selective process.

Introduction:

Bio-membranes are composed of thousands of lipid species, differing in their alkyl chains, headgroups and degree of saturation. Changes in lipid composition or even the absence of a single lipid have shown to lead to severe pathologies and death.

The leading hypothesis that explains the role of lipids in membrane functionality is that the lipids segregate into distinct domains [1]. These lipid domains can, with high specificity, incorporate or exclude proteins, hence inhibiting or accelerating biological processes at the membrane surface. Structural studies of lipid membranes have shown that the lipid packing, distances and tilt, strongly depend on the their chain length, backbone, and headgroup. This suggests that lipid complexes may have structural and chemical complementarities with proteins [2]. Knowledge of protein-domain interactions is essential to understand membrane functionality.

The complementation of lipid domains with specific proteins suggests specific binding patterns of lipid membranes with various pathogens. Our research examined the interaction of amyloid-beta (A β) peptides and the anthrax toxin with various lipid domains. A β peptides, originally the intermembrane component of the amyloid precursor protein, are found in

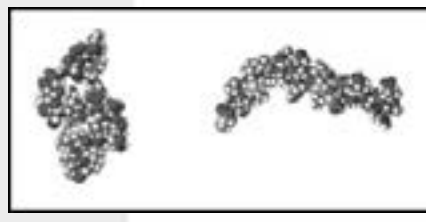


Figure 1: The inert amyloid-beta 40 peptide (left) and the toxic amyloid-beta 42 peptide (right). (See full color version on page xxxvi.)

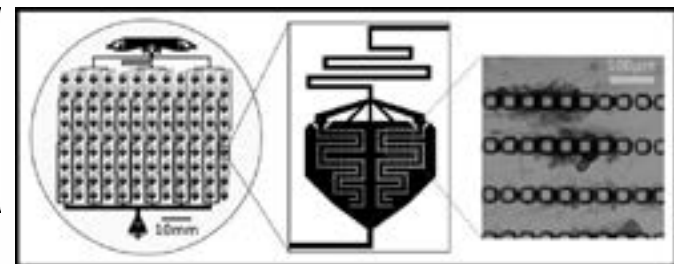


Figure 2: Magnifying from left to right: The 108 well microfluidic device; a single well; individual liposome swelling within the well.

high concentrations in the brains of Alzheimer's patients. A β_{40} and A β_{42} (Figure 1) are the two dominant forms of the A β peptide. Due to its more hydrophobic nature, the A β_{42} is the most amyloidogenic (and fibrillogenic) form of the peptide and considered the primary toxin in Alzheimer's. Using microfluidic techniques, we examined the affinity of A β_{40} and A β_{42} peptides to a lipid membrane library. In parallel with this experiment, and using similar techniques, we studied the binding of the anthrax toxin to the lipid library.

Experimental Procedure:

Using the largest lipid library in the world, consisting of 108 different lipid domains, we analyzed the binding selectivities of cytotoxins. We used a self-designed and fabricated 108 well polydimethylsiloxane (PDMS) microfluidic device (Figure 2) to introduce cytotoxins to the lipid library. The device gave

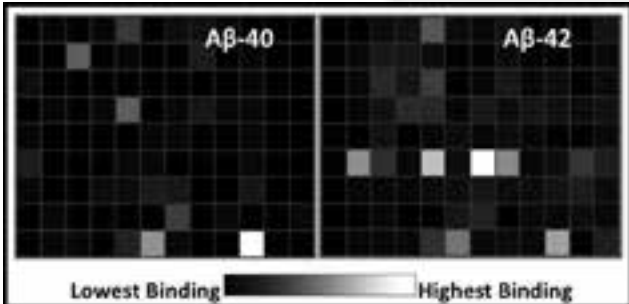


Figure 3: Amyloid-beta affinity matrices; Each square corresponds spatially to the wells on the microfluidic device. Note the distinct variations in the binding specificities the two amyloid-beta peptides.

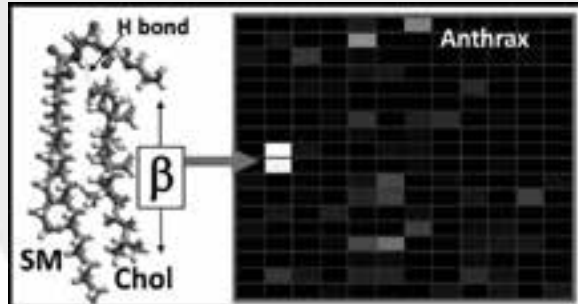


Figure 4: Anthrax affinity matrix; The toxin demonstrates high selectivity to sphingomyelin-cholesterol complexes shown left.

us tight control over small volumes, allowing us to analyze multiple samples in parallel. Liposomes were grown inside microfluidic channels by hydrating and heating lipids that were seeded within the device during fabrication. After liposome formation, fluorescently labeled cytotoxins were flushed into the device and allowed to interact with the liposomes. The liposomes were then washed and unbound cytotoxins were flushed out of the device. Using confocal microscopy and extensive image analysis, we calculated the total fluorescence per unit area of the liposomes for each well. From this information, we were able to identify the lipid domains to which the cytotoxins were bound.

Results and Conclusions:

Using microfluidics, we analyzed, in parallel, the binding preferences of a large number of lipid domains, and created affinity matrices that showed the specific binding of $\text{A}\beta$ peptides and anthrax toxin to lipid domains. These matrices show the relative fluorescence per unit area for each lipid domain. The different binding patterns of $\text{A}\beta_{40}$ and $\text{A}\beta_{42}$ (Figure 3) reveal variation in membrane binding propensities, and hence, possible differences in cytotoxicity. The binding of the peptides to cell membranes is considered the toxic step in Alzheimer's disease due to the theory that bound peptides induce neuron membrane permeability and plaque formation in the brains of Alzheimer's patients. This in mind, it is important to note that $\text{A}\beta_{42}$, considered the more toxic peptide, bound favorably to lipid domains containing cerebrosides, lipids found abundantly in the surface membranes of neural cells, while $\text{A}\beta_{40}$ bound favorably to the domains containing phosphatidylethanolamine, lipids rarely found on the surface

of neural cells.

We also created an affinity matrix for the binding pattern of the anthrax toxin (Figure 4). A series of experiments showed that the toxin had high selectivity to sphingomyelin-cholesterol complexes; these domains are considered very important for membrane functionality. This selective binding may be a useful tool, allowing scientists, for the first time, to use anthrax as a probe to label specific lipid domains.

Future Work:

To further this work, the affinity of cytotoxins to various cell lines would need to be tested. Liposomes are model membranes; the model must be proven by showing the binding selectivity of cytotoxins to various cell membranes of unique lipid compositions. Work of this nature would shed light on the toxic mechanism of Alzheimer's disease and the possibility of using anthrax as a probe for lipid rafts.

Acknowledgments:

I thank Prof. David Weitz and Dr. Roy Ziblat, my PI and mentor. I thank Dr. Kathryn Hollar, Ms. Melanie-Claire Mallison, and Dr. Lynn Rathbun for the excellent REU program. This work was supported by the NSF and the NNIIN REU Program, and took place at Harvard University.

References:

- [1] Hancock, J.F., Nature Reviews Molecular Cell Biology, 2006, 7(6), p.456-462.
- [2] Simons, K., and E. Ikonen, Nature, 1997, 387 (6633), p.569-572.
- [3] Shimizu, T., et al., Archives of Biochemistry and Biophysics, 2000, 381(2), p.225-234.

Fabrication of Nanochannels for Linearization and Diffusion of DNA

Mark Pagkaliwangan

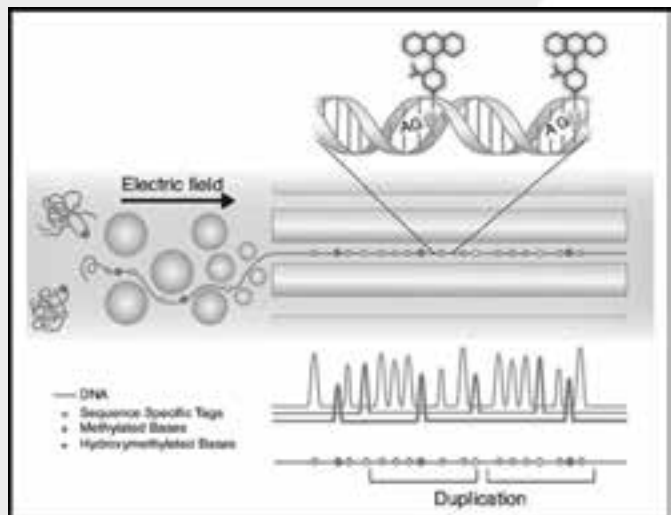
Chemical Engineering, University of Massachusetts Amherst

NNIN REU Site: Minnesota Nano Center, University of Minnesota-Twin Cities, Minneapolis, MN

NNIN REU Principal Investigator: Professor Kevin Dorfman, Department of Chemical Engineering and Materials Science, University of Minnesota-Twin Cities

NNIN REU Mentor: Damini Gupta, Chemical Engineering and Materials Science, University of Minnesota-Twin Cities

Contact: mpagkali@umass.edu, dorfman@umn.edu, gupta119@umn.edu



Introduction:

Optical mapping of deoxyribonucleic acid (DNA) has emerged as a viable alternative to help with read length restrictions in conventional sequencing. Rather than attempting whole genome sequencing, which often has errors and gaps, optical mapping uses fluorescent imaging of large (~ 10 kilobase pair - 1 megabase pair), linearly arranged, individual DNA strands in order to view large scale patterns that would be difficult to obtain by sequencing [1]. As shown in Figure 1, points of interest on the DNA are marked, and a unique barcode characteristic of the features present in the sequence is created. The optical mapping technique requires forcing the DNA to be in a linear state, which isn't preferred, as the polymer has maximum entropy in a random coil state. Nanochannel devices alleviate this problem by confining the DNA molecule to a one dimensional space, where the polymer will have no choice but to exist linearly. The focus of this project was to study the dynamic behavior of an individual, isolated DNA molecule in confinement which can be directly deduced from its diffusion properties in response to the variation of the width of the channel.

Experimental Procedure:

Four-inch fused silica wafers were used as preferred substrate for device fabrication because of their non-positive charge, to avoid sticking of negatively charged DNA backbone, and low autofluorescence, to achieve higher signal to noise ratio as compared to silicon in imaging process.

The basic structure of the device is shown in Figure 2, and consists of four DNA feeder holes (1-4) to pipet DNA dissolved in buffer solution into the device.

These holes connect to microchannels (A&B) approximately 50 μm in width, which ease the entropic jump between a bulk coil state and a linearly confined nanoscale state. The nanochannel (C&D) region of the device vary in width from wafer to wafer, as the effects of varying confinement widths on the extension and diffusivity of the DNA is desired [2]. However, despite the varying widths of the device channels, each device sought to have the same depth as its width. The nanochannels in the devices were created using electron beam lithography. A conductive layer, usually gold or aluminum, was added on top of the 950 poly(methyl methacrylate) (PMMA) e-beam resist because the substrate was nonconductive. Without a conductive layer, the electron beam spot size would be bigger than desired, leading to lower resolutions. Photolithography with AZ9260 resist was used to create the microchannel and reservoir regions, where the highest possible write resolution is not necessary. After creating patterns on the resist, reactive ion etching was used to etch the patterns into the surface of the substrate. Afterwards, fusion bonding was done at 1000°C to seal the device with a fused silica coverslip.

To study the diffusion of DNA at equilibrium, fluorescence microscopy was employed. Lambda-DNA (New England Biolabs, ~ 48 kbp) marked with YOYO dye was imaged using a laser, and a snapshot was taken every five seconds. It could be assumed that the mass at a given point was correlated to the

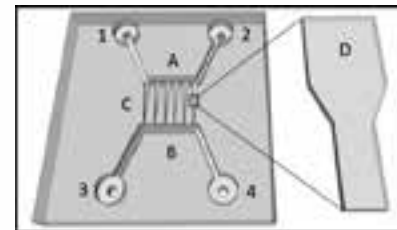


Figure 2: This figure is a basic overview of the device, with the design belonging to Gupta, et al. Reprinted with permission from [2] Gupta, D., et al. (2014). Mixed confinement regimes during equilibrium confinement spectroscopy of DNA. *J. Chem. Phys.* 140, 214901-214913.

intensity of emitted light, as the DNA was labeled with dye in even intervals, so a mass profile based on the light intensity of a given point was created. From this data, the center of mass can be established for each frame, and the movement of the center of mass was calculated. Mean squared displacement (MSD) can be found from the movement of the center of mass, and since $MSD = 2Dt$ for one dimension random walk, the diffusion coefficient D can be found by plotting MSD vs. time, t. Diffusivity was expected to decrease with the confinement size, because of the greater amount of monomer-environment interaction.

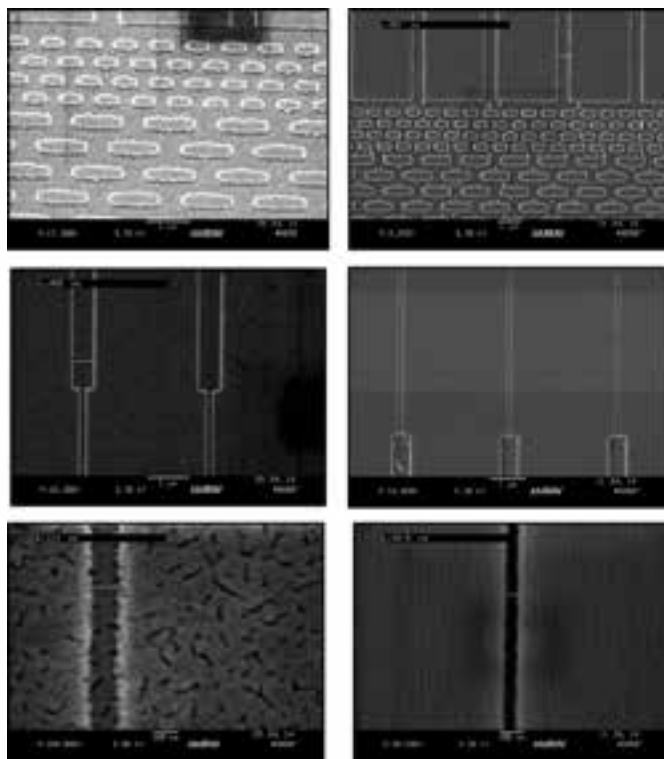


Figure 3: These devices were fabricated over the course of the project, with the nanochannel feature designs from Lam, et al. [3].

Results and Conclusions:

Figure 3 is a collection of scanning electron microscopy images that depict two different devices which were fabricated as a part of this project: a 90 nm device (left column), and a 60 nm device (right column). They show the three main features of the nanochannel region of the device. The top images show the pillar region, a gradient of hexagonally close packed protrusions which help linearize the DNA. They act like the bristles of a comb to untangle the DNA from its bulk state. The middle images show the concentration channels. These act like a funnel and collect the DNA at its interface with the nanochannels (pictured) so that more polymers will be captured in a single image. Finally, the bottom images show the nanochannels where the DNA was confined at equilibrium. Nanochannel region was based on designs used by Lam, et al. [3].

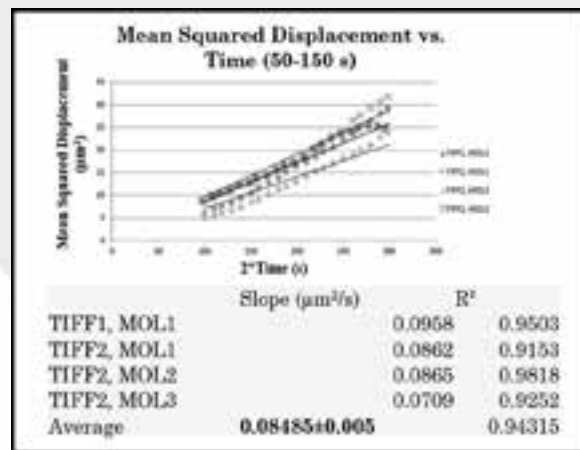


Figure 4: This graph was created by plotting the mean squared displacement of four different DNA molecules vs. $2 \times$ time while confined to a 100 nm channel.

Diffusion data was gathered with a 100×100 nm device. Our preliminary diffusion results in Figure 4 agree with the expectation that increased confinement would lead to a lower diffusion coefficient, as the diffusivity of DNA at 100 nm confinement is $0.08485 \pm 0.005 \mu\text{m}^2/\text{s}$ (E). Comparatively, $D_{\text{bulk}} = 0.46 \pm 0.03 \mu\text{m}^2/\text{s}$ [4], which is significantly higher. We can conclude that DNA does experience lower diffusivity at a much more restrictive confinement.

Future Work:

For future work, an array of devices will be made, spanning widths from 60-300 nm, and diffusion data will be gathered from all of them. This data will then be used to probe confinement regimes of DNA.

Acknowledgments:

This material is based upon work supported by the National Science Foundation under Grant No. ECCS-0335765. Special thanks to Professor Kevin Dorfman, Damini Gupta, the National Nanotechnology Infrastructure Network Research Experience for Undergraduates Program, and the Minnesota Nano Center.

References:

- [1] Levy-Sakin, M. and Ebenstein, Y. (2013). Beyond sequencing: optical mapping of DNA in the age of nanotechnology and nanoscopy. *Current Opinion in Biotechnology*. 24, 690-698.
- [2] Gupta, D., et al. (2014). Mixed confinement regimes during equilibrium confinement spectroscopy of DNA. *J. Chem. Phys.* 140, 214901-214913.
- [3] Lam, E.T., et al. (2012). Genome mapping on nanochannel arrays for structural variation analysis and sequence assembly. *Nature Biotechnology*. 30(8), 771-776.
- [4] Balducci, A., et al. (2006). Double-Stranded DNA Diffusion in Slitlike Nanochannels. *Macromolecules*. 396273-6281.

Effects of Adhesion Layers in Silver Plasmonic Nanostructures for Surface Enhanced Raman Spectroscopy

Ashka Shah
Physics, Harvey Mudd College

NNIN REU Site: Stanford Nanofabrication Facility, Stanford University, Stanford, CA

NNIN REU Principal Investigator: Robert Sinclair, Materials Science and Engineering, Stanford University

NNIN REU Mentor: Steven Madsen, Material Science and Engineering, Stanford University

Contact: shashka@g.hmc.edu, bobsinc@stanford.edu, smadsen1@stanford.edu

Abstract:

Surface enhanced Raman spectroscopy (SERS) of plasmonic nanostructures can be useful in biomedical practices, including cancer detection, because of these particles' low detection limits. Lasers at certain wavelengths excite localized plasmon resonances that enhance local electric fields and result in higher Raman intensities — this makes the particles easier to detect. Electron energy loss spectroscopy (EELS) spectra of these nanostructures taken with a transmission electron microscope (TEM) have peaks at energies corresponding to plasmon resonances. Previous work with gold nanostructures has shown that Raman wavelengths with energies corresponding to EELS energy peaks result in higher Raman enhancement. We fabricated silver plasmonic nanostructures via electron-beam lithography on silicon wafers with titanium and mercaptopropyltrimethoxysilane (MPTMS) adhesion layers. Raman spectra of the silver nanostructures revealed no enhancement with titanium layers and high enhancement with MPTMS layers, agreeing with gold results. Plasmon peaks in silver EELS spectra did not correlate with enhancement as well as gold EELS spectra. Further investigation is needed to determine a correlation between strong plasmon resonance peaks in EELS spectra and high SERS enhancement factors.

Introduction:

Metallic nanostructures that exhibit SERS properties, such as gold and silver, are coated with a Raman active dye and are injected into the bloodstream where they can then enter a tumor. The nano particles are detected by their Raman signal, which is enhanced by several orders of magnitude due to the properties of the metal. The enhanced Raman signals can be explained by the presence of surface plasmons, which are oscillating electron clouds on the surface of the metal. They can couple with electromagnetic radiation to create enhanced localized electric fields on the surface. The intensity of electric field in these regions is a superposition of the metal field and the incoming field [1].

Raman spectroscopy detects the Raman scattering process occurring at the surface of the nanostructures. Raman scattering is the inelastic scattering of light from a substrate. When the Raman dye is located in a region on the metal where there is an enhanced electric field, both the incoming and exiting photon intensities are enhanced resulting in an overall signal enhancement [1]. Factors that affect the Raman intensity are size, shape, and material of the metal nanostructures.

Another spectroscopic technique used to gain more insight into the location of surface plasmons and their contribution to enhanced Raman signals is electron energy loss spectroscopy (EELS). EELS is done in a transmission electron microscope (TEM). Electrons passing through a sample are sometimes

inelastically scattered and lose some energy. The TEM measures the energy loss of incoming electrons at each point on the sample resulting in a data cube that can be analyzed in two ways. An x,y position of an EELS data cube gives a spectrum that shows the frequency of energy loss at that point. An energy range of an EELS data cube gives an image where bright pixels indicate a higher frequency of energy loss. Bright regions correspond to the excitation of a plasmon.

Experimental Procedure:

Nanostructures were fabricated via electron-beam lithography on three-inch silicon wafers spin-coated with poly(methyl methacrylate) (PMMA) resist. The wafers were developed in a 1:3 methyl isobutyl ketone to isopropyl alcohol solution. A 2 nm layer of titanium was deposited with electron gun evaporation on one set of nanostrucrures. A monolayer of MPTMS was deposited on another set of structures with vapor deposition in a vacuum chamber. A 30 nm layer of silver was deposited with electron gun evaporation on both sets of nanostructures. For Raman spectroscopy, a Raman active substrate 4-mercaptopyridine dye was deposited by submerging the wafers in a 1 mM solution of the dye. For EELS, the same procedure was replicated on TEM silicon nitride instead of silicon wafers.

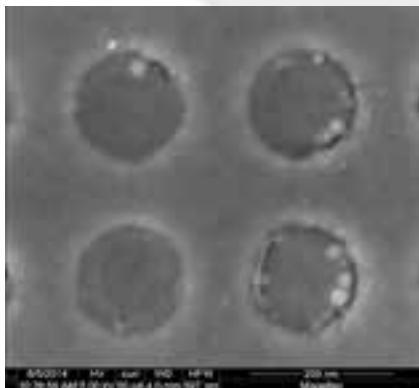


Figure 1: 144 nm diameter apertures with 100 nm spacing.

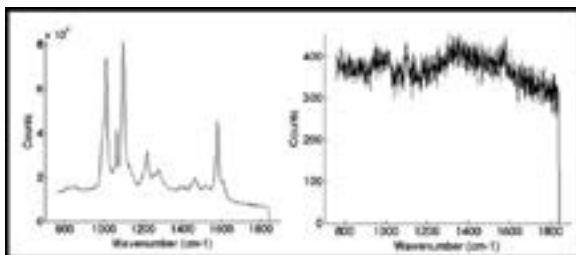


Figure 2: Raman spectra of 144 nm diameter apertures with 100 nm spacing with MPTMS adhesion layers (left) and titanium adhesion layers (right).

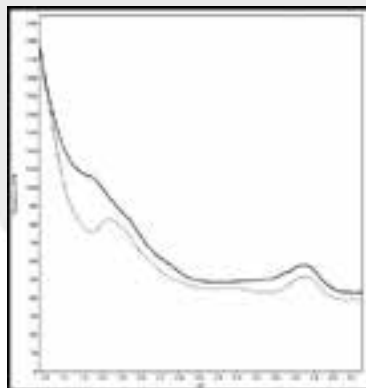


Figure 3: EELS spectra of 144 nm diameter apertures with 100 nm spacing with MPTMS adhesion layers (solid) and titanium adhesion layers (dotted).

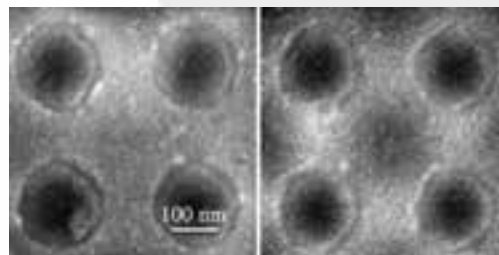


Figure 4: EELS energy slices from 1.5-1.6 eV of 144 nm diameter apertures with 100 nm spacing with MPTMS adhesion layers (left) and titanium adhesion layers (right).

We fabricated nanostructures of varying sizes, shapes and spacings to demonstrate the effects of these factors on the Raman signal enhancement and the location of surface plasmons. A scanning electron microscopy (SEM) image of nanoapertures is shown in Figure 1.

Results:

Raman spectra for silver nanostructures taken with a 785 nm (1.57 eV) laser agreed with gold results. In Figure 2, we see there was enhancement for silver structures made with MPTMS adhesion layers and no enhancement for structures made with titanium adhesion layers. These results were consistent for all silver nanostructures of various sizes, shapes and spacings.

EELS spectra of the same structures were less conclusive. For gold nanostructures, we saw strong plasmon peaks for MPTMS apertures at 1.57 eV and weak plasmon peaks for titanium apertures at 1.57 eV. Silver nanostructure EELS spectra taken in between apertures are shown in Figure 3. We see a weak plasmon peak at 1.57 eV for the MPTMS apertures and strong blue shifted plasmon peak for titanium apertures. Since MPTMS aperture peaks align better with the Raman laser energy, this may be the cause for the Raman enhancement.

Energy slices for silver nanostructures encompassing the Raman laser energy are shown in Figure 4. The brighter regions in between apertures for the titanium structure indicate

more plasmon resonance for these structures than for MPTMS structures. It appears that the correlation between strong plasmon peaks and Raman enhancement is still unclear for silver nanostructures.

Conclusion and Future Work:

Titanium adhesion layers have negative effects on Raman signals for both gold and silver nanostructures. Although strong plasmon peaks align with high enhancement for gold, further investigation is needed for silver. This includes using different laser energies for Raman spectroscopy to determine if other plasmon peaks correlate to high enhancement.

Acknowledgements:

Steven Madsen, Professor Robert Sinclair, Sinclair Group, Michael Deal, and Maureen Baran for their assistance. This research was supported by the National Nanotechnology Infrastructure Network Research Experience for Undergraduates Program and the Stanford Nanofabrication Facility. We thank the National Science Foundation for funding.

References:

- [1] Pablo G. Etchegoin and Eric C. Le Ru, Principles of Surface Enhanced Raman Spectroscopy, Chapter 1, 2009.

Effects of Gold Nanoparticle Size and Functional Group on Adipogenesis of Mesenchymal Stem Cells

Peter Su

Chemical and Biomolecular Engineering, University of California, Berkeley

NNIN iREU Site: National Institute for Materials Science (NIMS), Tsukuba, Ibaraki, Japan

NNIN iREU Principal Investigator: Dr. Guoping Chen, Tissue Regeneration Materials Unit, International Center for Materials Nanoarchitectonics, National Institute for Materials Science, Tsukuba, Ibaraki, Japan

NNIN iREU Mentor: Dr. Jasmine Li, Tissue Regeneration Materials Unit, International Center for Materials Nanoarchitectonics, National Institute for Materials Science, Tsukuba, Ibaraki, Japan

Contact: su.peter92@gmail.com, guoping.chen@nims.go.jp, li.jasmine@nims.go.jp

Introduction:

Mesenchymal stem cells (MSCs) are extremely useful in generating a multitude of cell lineages for tissue regeneration applications. The microenvironment of these MSCs is critical in regulating their differentiation, including soluble factors that bind to various cell receptors. Meanwhile, gold nanoparticles (AuNPs) have shown great potential in biological research due to their ability to interact with biomolecules. Previous work has shown AuNPs of different sizes to affect the regulation of adipogenic (fat cell) differentiation of MSCs [1]. Thus, the objective of this research was to expand on previous research by examining the effects of AuNPs of two different sizes (20 and 90 nm) and functional groups (citrate and β -mercaptopropionic acid (COOH)) on MSC growth, morphology, and degree of adipogenic differentiation.

Experimental Procedure:

Gold nanoparticles were synthesized via the citrate reduction method. Trisodium citrate was added to a 100 mL solution of 0.29 mM tetrachloroauric acid in a reflux setup, heated at 110°C, and stirred at 700 rpm for thirty minutes. AuNPs of diameters 20 nm and 90 nm were produced by varying citrate concentrations [2]. After synthesis, the AuNPs were purified via centrifugation. Then, they were characterized for size via dynamic light scattering (DLS) and ultraviolet-visible light (UV-vis) spectroscopy, charge and stability via zeta potential measurements, and morphology using scanning electron microscopy (SEM). Finally, to functionalize the AuNPs with β -mercaptopropionic acid, a ligand-exchange reaction was performed at pH 11 in dark conditions for twenty-four hours. These AuNPs were then characterized as well.

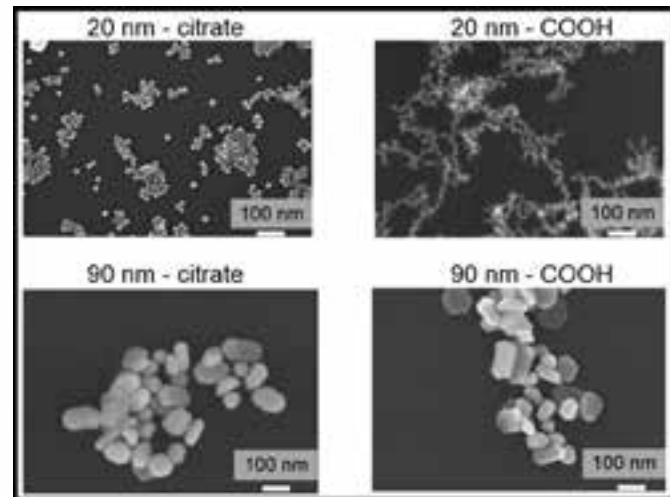


Figure 1: SEM images of the AuNPs (platinum-coated) showing morphology and size distribution.

MSCs were seeded in four 24-well plates at a density of 5×10^3 cells/cm 2 . Three biological replicates of each condition were used. After one day of culture, 1 mM of AuNPs were added in, along with adipogenesis induction media for two plates (the other two plates were negative controls). Media was changed once every three days. After seven days, growth and morphology were examined via optical microscopy, and adipogenic differentiation was quantified via an alkaline phosphatase (ALP) activity assay and an Oil Red O staining assay. ALP activity was measured using the Anaspec Sensolyte® kit. Oil Red O staining was carried out by fixing then staining the cells with Oil Red O. Cells were then imaged before the oil was eluted and measured for absorbance at 500 nm. Cells were counted using a hemocytometer under an optical microscope.

Results and Discussion:

Table 1 summarizes nanoparticle synthesis and characterization. Zeta potentials were below -20 mV, showing the AuNPs to be stable, while size and morphology of the AuNP (Figure 1) using both high and low concentrations of citrate was consistent with literature [3].

Citrate conc. (mM)	Ligand	DLS - Particle diameter after resuspension (nm)	UV-vis peak (nm)	Zeta potential (mV)
1.70	Citrate	23.4 \pm 5.0	520	-40.6 \pm 3.4
1.70	β -mercaptopropionic acid	19.7 \pm 5.6	521	-33.8 \pm 2.0
0.34	Citrate	86.8 \pm 46.3	568	-47.2 \pm 3.0
0.34	β -mercaptopropionic acid	95.8 \pm 39.9	586	-46.1 \pm 0.8

Table 1: AuNP synthesis and characterization results.

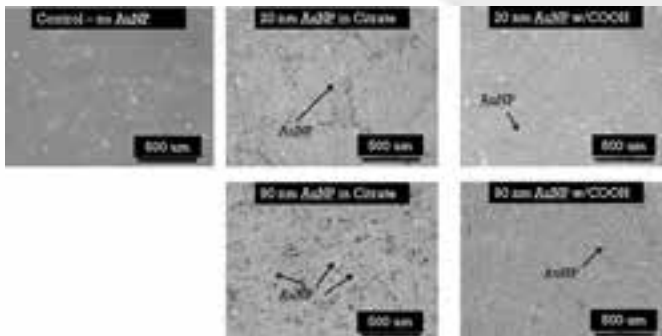


Figure 2: Undifferentiated MSCs grown in growth media after seven days. The arrows indicate AuNPs internalized by the MSCs.

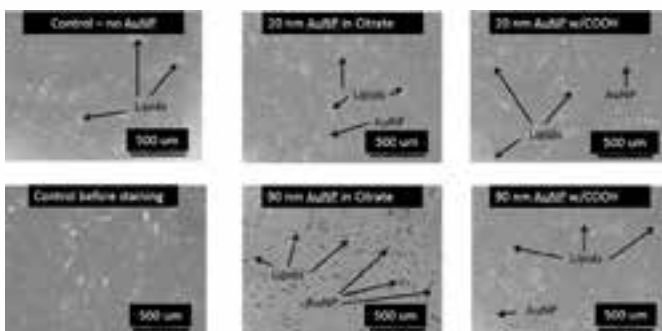


Figure 3: Oil Red O staining of MSCs cultured with adipogenic media after seven days. Arrows indicate AuNPs and lipids inside the MSCs.

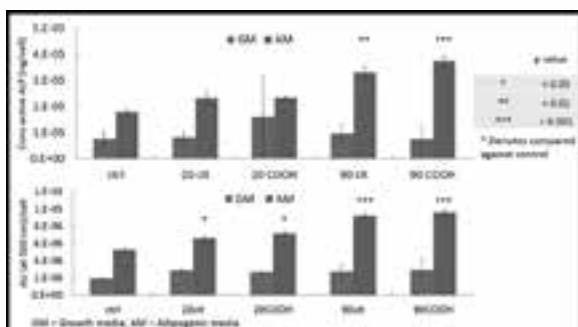


Figure 4: ALP activity assay results (top) and Oil Red O absorbance measurements (bottom) for each condition. Statistics were determined using a one way analysis of variance (ANOVA) with Tukey's Multiple Comparison Test.

Sample Conditions	Total Number of Cells/well		
	Initial	Growth Media	Adipogenic Media
Control	10000	24480	13080
20 citrate	10000	20400	10580
20 COOH	10000	21040	10240
90 citrate	10000	23280	9200
90 COOH	10000	19390	7760

Table 2: Cell number data after seven days of culture.

Figure 2 shows undifferentiated MSCs, while Figure 3 shows Oil Red O images of MSCs with adipogenic media. Adipogenesis was evident by rounding of the MSCs as well as formation of lipid droplets, but in all cases no morphological changes were visible compared to the controls. Additionally, the 90 nm AuNP-citrate condition seemed to show the most cellular uptake. Cell number data (Table 2) clearly shows that growth was inhibited by the 90 nm AuNPs functionalized with β -mercaptopropionic acid.

ALP activity results (Figure 4) demonstrated a significant increase in ALP activity for the two 90 nm AuNPs, more so for the 90 nm COOH AuNP. Additionally, Oil Red O absorbance readings showed an increase in lipid droplet formation per cell for all AuNPs, but significantly more so for 90 nm AuNPs.

These findings indicate that larger AuNPs-COOH seem to not only inhibit growth, but also favor adipogenesis simultaneously. Additionally, there was also less uptake of the 90 nm AuNPs-COOH, indicating that the functional group on this larger AuNP has strong biological implications. These AuNPs may be interacting with a variety of receptors both on the cell surface and inside the cytoplasm. One possible cause of such behavior is that the AuNPs may disrupt F-actin cytoskeleton filaments inside the MSCs, an early step in adipogenic differentiation.

Conclusions and Future Work:

We have demonstrated the successful synthesis of two different sizes and functional groups of AuNPs, and shown that larger AuNP tend to help MSCs favor adipogenesis while inhibiting growth. Although the mechanism of interaction still remains to be elucidated, these findings show interesting implications of β -mercaptopropionic acid functionalized gold nanoparticles with a diameter of around 90 nm.

For future studies, examining expression levels of genes related to adipogenesis would be useful. Additionally, a more exact concentration of AuNPs before treatment and after culture can be taken in order to quantify cellular uptake. Finally, exploration of other biologically active functional groups on the AuNP surface is already being conducted in our laboratory, which can give further information about their effects on MSC adipogenesis.

Acknowledgements:

National Institute for Materials Science, National Nanotechnology Infrastructure Network International Research Experience for Undergraduates (NNIN iREU) Program.

References:

- [1] Kohl, et al. "Effect of AuNP on adipogenic differentiation of human mesenchymal stem cells." *J Nanopart Res* (2011) 13:6789-6803.
- [2] Long, et al. "Synthesis and optical properties of colloidal AuNP." *Journal of Physics: Conference Series* 187 (2009) 012026.
- [3] Kimling, et al. "Turkevich Method for Gold Nanoparticle Synthesis Revisited." *J. Phys. Chem. B* 2006, 110, 15700-15707.

Label-Free Detection of *Escherichia coli* using Silicon Nanophotonic Biosensors

Emily Thompson

Biomedical Engineering, Arizona State University

NNIN REU Site: Washington Nanofabrication Facility & Molecular Analysis Facility, University of Washington, Seattle, WA

NNIN REU Principal Investigator: Daniel M. Ratner, Ph.D., Bioengineering, University of Washington

NNIN REU Mentors: Shon Schmidt and Pakapreud Khumwan, Bioengineering, University of Washington

Contact: ertthomp2@asu.edu, dratner@uw.edu, shons@uw.edu, pakapreud@gmail.com

Abstract:

Medical diagnostics influence 60-70% of patient treatment decisions [1], yet sophisticated, sensitive diagnostics are still largely confined to hospitals and laboratories, limiting their impact in point-of-care settings. The growing field of nanophotonic biosensors has the potential to bring clinically relevant and sensitive medical diagnostic capabilities to the patient bedside. These silicon-based sensors utilize light to detect biomolecular interactions and are compatible with today's established complementary metal-oxide-semiconductor (CMOS) foundry processes for high-volume, low-cost fabrication. The goal of this project was to demonstrate the potential application of silicon photonic biosensors to bacterial detection and compare their performance with that of a competitive technology, surface plasmon resonance (SPR). We first verified and optimized binding of *Escherichia coli* (*E. coli*) with SPR, developing an assay suitable for use on two different silicon photonic systems (transverse electric and transverse magnetic mode ring resonators). The results were compared to show the viability of bacterial detection using silicon photonic biosensors, and binding was characterized with scanning electron microscopy (SEM).

Introduction:

We employed SPR imaging to validate our bacterial binding methodology due to its well-established reputation as an optical biosensing platform [2] and its similarity to silicon photonics. In SPR, a beam of visible-spectrum light is guided through a prism onto a gold chip, and the intensity of the reflected beam is detected. Light directed at a certain resonant angle, dependent upon the refractive index of the chip, excites the surface electrons, or plasmons, causing them to oscillate. In biosensing applications, the chip is functionalized with ligands that bind to a target analyte, which shifts the resonant angle of the light [2]. This shift can be measured, enabling direct detection of analyte binding.

In silicon photonics, light is directed through a linear silicon wire known as a waveguide, which allows for coupling of the light into a resonator. Binding of bacteria at the resonator's functionalized surface changes the local refractive index and shifts the resonant wavelength, the wavelength of input light at which signal intensity is minimal due to interference [4].

The polarization of light traveling through the ring resonators determines the sensing region at the rings' surface, where binding occurs. We studied two types of ring resonators: rings using transverse electric (TE) mode light and rings using transverse magnetic (TM) mode light. The TM mode rings have a larger sensing region extending beyond their surface, so we hypothesized that TM mode rings would be better suited than TE mode rings for detection of large molecules like bacteria.

Experimental Procedure:

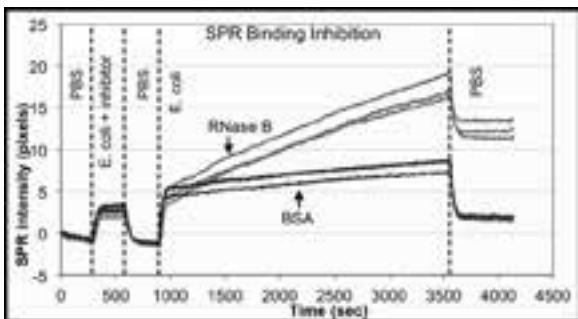
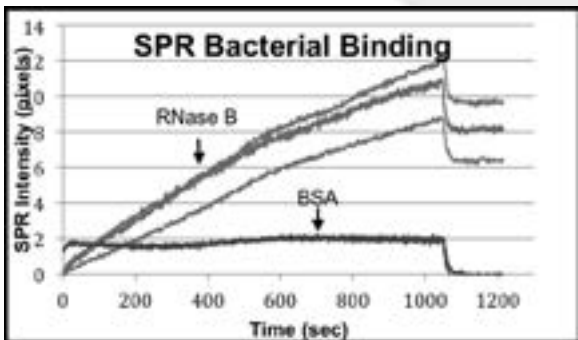
In our SPR experiment, a gold chip was spotted with RNase B, a ligand to which *E. coli* fimbriae bind [3]. The rest of the chip was blocked in bovine serum albumin (BSA), which served as a negative control. *E. coli* were flowed across the chip using a fluidic channel. To validate specific bacterial binding, we mixed the *E. coli* with alpha-phenyl mannoside, which contains the D-mannose moiety and inhibits the bacteria FimH receptors, preventing binding to RNase B.

The TE mode ring resonators were tested using the Maverick Detection System (Genalyte, San Diego, CA). Bacteria were flowed across a chip functionalized with RNase B and no shift in resonant wavelength was observed, indicating that there was no binding. We developed a custom test platform and software in order to test bacterial binding on TM mode ring resonators.

First, a phosphate buffered saline (PBS) baseline was established, after which RNase B was flowed across the chip for functionalization. Bacteria were then flowed across the chip.

Results and Conclusions:

The SPR experiment shows a shift in intensity for the RNase B regions of the chip as more bacteria are flowed across, indicating bacterial binding (Figure 1). The PBS wash at 1100 seconds removed any weakly bound molecules. Additionally, our experiment to validate specific bacterial binding was successful (Figure 2). Bacteria mixed with FimH inhibitor did



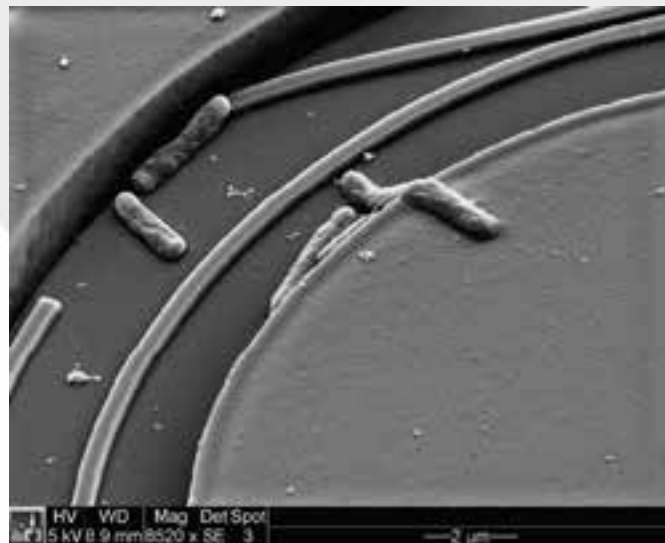
not bind to the RNase B, while bacteria without the inhibitor did bind. This verifies that the signal response detected was specific binding of *E. coli*.

The TE ring resonators showed no discernible binding, in part because of their lower level of sensitivity and their smaller resonator size relative to the large cell bacteria. This size disparity can be seen by SEM imaging of a ring resonator chip spotted directly with bacteria (Figure 3). We hypothesize that the protective fluoropolymer cladding makes binding of the bacteria to the smaller resonator difficult when the bacteria are flowed across the chip.

By comparison, the TM ring resonators did show bacterial binding (Figure 4). The shift in resonant wavelength when bacteria were flowed across the resonators indicates bacterial binding.

Future Work:

Future work with silicon photonic devices will focus on repeating and validating our results with the TM mode chips using various on-chip controls, as well as improving the devices' biocompatibility so that they can process undiluted clinical samples. Silicon photonic sensors will likely be expanded into many other diagnostic applications, especially at the point-of-care.

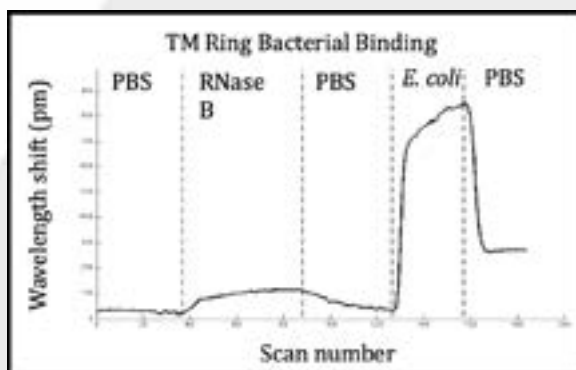


Acknowledgements:

I would like to thank Dr. Daniel Ratner, Shon Schmidt, Pak Khumwan, and the rest of the Ratner Lab, as well as Paul Neubert and the University of Washington Nanotech User Facility staff. Thanks to the National Nanotechnology Infrastructure Network Research Experience for Undergraduates Program and the National Science Foundation for funding.

References:

- [1] The Lewin Group, I. The Value of Diagnostics Innovation, Adoption and Diffusion into Health Care. (2005)
- [2] Fan, Xudong, et al. "Sensitive optical biosensors for unlabeled targets: A review." *analytica chimica acta* 620.1 (2008): 8-26.
- [3] Nilsson, Lina M., et al. "Catch Bond-mediated Adhesion without a Shear Threshold: Trimannose Versus Monomannose Interactions with the FimH Adhesion of *Escherichia coli*." *Journal of Biological Chemistry* 281.24 (2006): 16656-16663.
- [4] Washburn, Adam L., and Ryan C. Bailey. "Photonics-on-a-chip: recent advances in integrated waveguides as enabling detection elements for real-world, lab-on-a-chip biosensing applications." *Analyst* 136.2 (2011): 227-236.



Integration of Highly Porous Membranes with Microfluidic Body-on-a-Chip Devices

Hidetaka Ueno

Department of Biomedical Engineering, Kagawa University, Japan

NNIN iREG Site: Cornell NanoScale Science & Technology Facility, Cornell University, Ithaca, NY

NNIN iREG Principal Investigator: Prof. Michael L. Shuler, Department of Biomedical Engineering, Cornell University, USA

NNIN iREG Mentor: Dr. Mandy B. Esch, Department of Biomedical Engineering, Cornell University, USA

Contact: s14g507@stmail.eng.kagawa-u.ac.jp, mls50@cornell.edu, mandy.esch@cornell.edu

Abstract:

Body-on-a-chip devices are devices that contain *in vitro* tissues of multiple organs of the human body. The devices mimic part of the human body in a scaled down fashion on a silicon or polymer chip. They are used to carry out experiments in which the efficacy and safety of new drugs is tested in an inexpensive way and without the need of animal experiments. Here, we aimed to combine a barrier tissue, the gastrointestinal (GI) tract, with liver tissue within one system. Barrier tissues are important because they allow us to simulate the uptake and bioavailability of drugs. Here we microfabricated highly porous membranes that we inserted into body-on-a-chip devices for the purpose of growing GI tract epithelial cells. We also fabricated polymer chips and the corresponding housing for the devices. Finally, we carried out cell culture tests with Caco-2 cells (gastrointestinal epithelial cells) and evaluated the suitability of the devices to support the culture of these cells, providing physical stimulation through fluidic flow and enough oxygen to support cell function. The developed model will be used to test the bioavailability of drugs and nano-scale drug carriers.

Introduction:

Microfluidic body-on-a-chip systems that contain barrier tissues can be used to study the travel of drugs across such tissues and their bioavailability at the target organ. Barrier tissues consist of epithelial cells that grow on a basement membrane. The basement membrane consists of extracellular matrix components such as collagen and laminin. It is difficult to construct such natural membranes *in vitro*, making it necessary to fabricate an equivalent membrane using nanotechnology. The growth of epithelial cell on such an artificial, porous membrane allows us to access both sides of the barrier tissue during drug uptake studies.

At present, commercially available products only provide a porous area of 10% or lower. We have previously developed a fabrication protocol that allows us to microfabricate membranes that are 2-3 μm thick and up to 40% porous [1]. Here, we developed this protocol further, creating a frame around the membrane that allows us to handle it with tweezers to place the membrane into any cell culture system.

In this study, we fabricated highly porous membranes, integrated them into a GI tract/liver system, and cultured Caco-2 cells in the system to validate the proposed device.

Experiment Procedure:

Membrane Fabrication. Figure 1 shows the fabrication process of the membrane. This membrane was made of SU-8 50. SU-8 is a negative photoresist that provides biocompatibility. In this fabrication process, we first spun an SU-8 layer on Si substrate using a spin-coater. We then exposed the frame pattern. After a

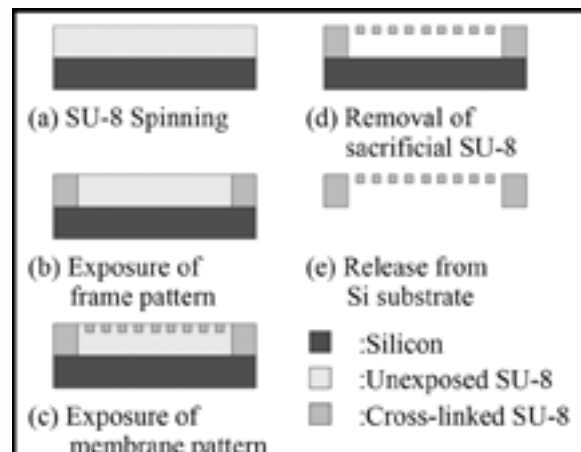


Figure 1: Fabrication process.

post exposure bake (PEB), the membrane pattern was exposed. The thickness of the membrane was about 2 to 3 μm . After the sacrificial SU-8 was removed, we released the membrane from the Si substrate. The geometry of the membrane was round with the porous area being of a diameter of 6 mm. The frame extended beyond the membrane by 3 mm. The pores were square holes of 4 μm width. The thickness of the frame was about 40 μm . The total diameter of the membrane, including the frame, was 12 mm.

Chip and Housing Construction. This cell culture device consisted of two polymer chips with 6 mm holes between

which we sandwiched the membrane. The chip was placed into a polymer housing that contained an inlet and outlet for each of the two microfluidic circuits, which allowed us to access the top and the bottom side of the membrane. The device was 3D printed using an OJBET30 Pro (ALTECH, Israel) and cleaned before adding cells for cell culture. To culture cells, we seeded them into the devices at a concentration of 100,000 cells per cm^2 . We then placed the device on a rocker platform that tilted back and forth by 12°, creating gravity-driven fluidic flow. We constructed the devices so that we would achieve the equivalent fluid residence time as seen in the GI tract and liver *in vivo*.

To achieve this, we constructed the microfluidic circuits so that we would achieve a flow rate which of 12 $\mu\text{L}/\text{min}$. We also constructed electrodes that were set into the hole of the top and the bottom parts. We used these electrodes to evaluate the condition of the Caco-2 cell layer.

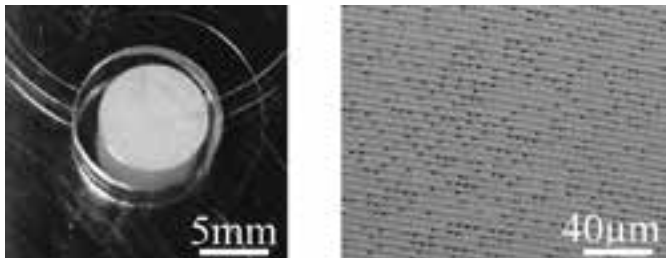


Figure 2: Fabricated membrane. (a) Photograph. (b) SEM image.

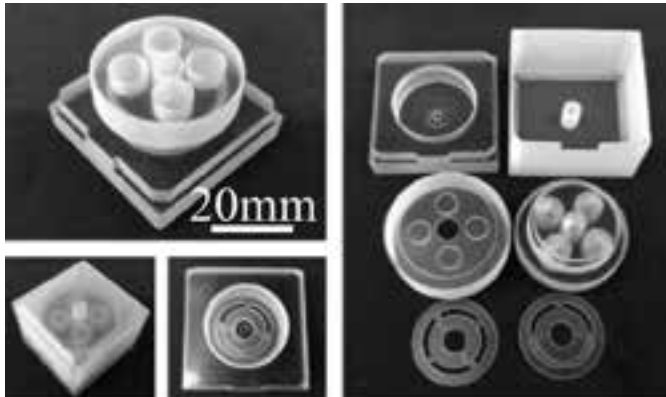


Figure 3: Fabricated device.

Results and Discussion:

Figure 2 shows a photograph and an SEM image of one of the fabricated membranes. The membrane consisted of a frame and a porous inner circle. We were able to pick up the membrane and place it in between the two polymer chips we constructed with 3D printing. The pores of the membrane, however, were only partially open, so that the overall porous area was about 10%. To achieve a greater number of open pores, we need to further optimize the fabrication protocol, balancing the exposure time, so that the membranes are thick enough to be handled, but at the same time, keeping the exposure time low to that a larger number of pores stay open.

We also printed the described polymer chips and the cell culture housing (Figure 3). We tested the volume flow rate in top and bottom fluidic circuit, finding that it was 13.55 $\mu\text{L}/\text{min}$ in the top circuit and 23.56 $\mu\text{L}/\text{min}$ in the bottom circuit.

We also seeded Caco-2 cells onto the porous membranes, cultured them for 14 days in the incubator, and then inserted the chip with membrane and cells into the cell culture device.

Figure 4 shows Caco-2 cells after the 14-day culture on the membrane, showing that the entire membrane was covered with cells.

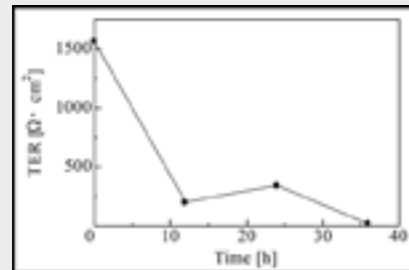


Figure 4: Time response of the resistance.

After inserting the membrane into the cell culture device, we measured the transepithelial resistance (TER). Right after the device was assembled, we measured a high resistance, confirming that the cells had established the tight junctions necessary to reliably test the uptake of drugs. However, the resistance dropped on the following day to values that indicated a damaged cell layer. Further experiments need to be done to determine the cause of this drop in resistance and to enable us to culture Caco-2 cells in the devices for more than one day.

Conclusion:

We have fabricated porous membranes with a frame that makes it possible for us to handle the membrane with tweezers and place it between two 3D printed polymer chips. The membrane supported the culture of Caco-2 cells in a Petri® dish for 14 days. Culture inside the microfluidic device was only successful for one day, as indicated by a high TER on the first day, but a subsequent drop to lower values, indicating the loss of barrier function. To extend the cell culture period of Caco-2 cells inside the devices we will conduct further experiments.

Acknowledgements:

I would like to thank deeply my PI, Prof. Michael L. Shuler, my mentor Dr. Mandy B. Esch, and my adviser Dr. Lynn Rathbun. I also appreciate CNF staff's kindly supports. This project was supported by National Science Foundation (NSF), National Nanotechnology Infrastructure Network International Research Experience for Graduates (NNIN iREG) Program, and Cornell NanoScale Science & Technology Facility (CNF).

References:

- [1] M.B. Esch, J.H. Sung, J. Yang, C. Yu, J. Yu, J.C. March, M.L. Shuler, "On chip porous polymer membranes for integration of gastrointestinal tract epithelium with microfluidic 'body-on-a-chip' devices", *Biomed Microdevices*, Vol.14, pp.895-906, 2012.

Direct Writing for Biological Applications: Cell Patterning into Microfluidic Channels and Nanoparticle Writing onto Patterned Substrate

Benjamin Vizy
Biological Engineering, Purdue University

NNIN REU Site: Lurie Nanofabrication Facility, University of Michigan, Ann Arbor, MI

NNIN REU Principal Investigator and Mentor: Pilar Herrera-Fierro, Ph.D. Lurie Nanofabrication Facility, University of Michigan
Contact: bvizy@purdue.edu, pilarhf@umich.edu

Abstract and Introduction:

Direct writing is an alternative method of patterning that is gaining popularity in many fields, particularly in biological applications. This alternative to conventional lithography can have many applications in biology, in which there are many cases where the ink, or substances to be jetted (patterned) cannot be exposed to the radiation, solvents, or temperatures needed for lithography. We will present two different applications of this technique.

Patterning cells is a practice that mimics a cell's natural environment. This allows different tests to be performed to see their natural response, such as cell-cell interactions, signals, and responses to new biotechnologies [1]. Two-phase cell patterning makes the process less harmful to cells than previous methods because it allows the cells to be patterned in a completely aqueous environment.

Two solutions of immiscible polymers, dextran and polyethylene glycol (PEG), were prepared for this experiment. Dextran was deposited onto a substrate, allowed to dry, and then rehydrated by PEG. In two-phase cell patterning, one of these solutions would contain cells, and because of PEG and dextran's interfacial tension, the cells would move to either fluid based on affinity [2]. One goal of this project was to show that dextran printed by the ink-jet method could provide similar results in microfluidic channels.

Another goal of this project was to use the ink-jet method to print fluorescent nanoparticles on a patterned substrate. Intracranial pressure (ICP) is the pressure exerted on the inside of the skull, and is generally measured after a surgery or head trauma to decrease chances of additional harm. Because this is usually measured by inserting a catheter into the brain, a more comfortable solution using microelectromechanical (MEMS) systems was recently developed [3], where quantum dots (QDs) are patterned onto small pillars and implanted in the skin. Depending on the pressure inside the head, shining infrared light on the skin will cause one layer of QDs to emit a more intense wavelength than the other, which allows ICP to be read [3]. Previous methods of patterning QDs — in which QDs were mixed into the pillar materials during lithography — were inefficient. The goal of this project was to direct-print the QDs onto the patterned pillars to increase the fluorescent signal of the pillars.

Methods:

For printing with 500 kDa dextran, 5% and 12.8% dextran by volume solutions were prepared in deionized water with a small amount of rhodamine B for fluorescence; 5% 35 kDa PEG was also used. The 12.8% solution was used to test the relationship between dextran and PEG. The 5% dextran was printed on microfluidic channels made with polydimethylsiloxane (PDMS) using the Dimatix inkjet printer (Fuji). Upon printing in the channels, the PDMS was activated and bonded to a clean glass slide. PEG was run through the channels and observations were made using the Olympus BX-51 fluorescent microscope.

For printing with QDs, a solution of toluene and rhodamine B was prepared for testing, along with a wafer covered in SU-8 pillars 250 μm in diameter. After the toluene was able to be printed on the pillars, a 1:1 solution of toluene:QDs was prepared and printed onto the pillars.

Printing on pillars also required alignment of the stage, in order to print them exactly in the center of the pillar.

Results and Conclusions:

For ink-jet printing with dextran, high voltages were used with the printer in order to get the viscous polymer to jet. Cleaning cycles on the Dimatix printer that jet fluid through the nozzles



Figure 1: Dextran's contact angle on PDMS is around 88.8 degrees.



Figure 2: Top; Dextran in microfluidic channel after PEG was introduced. Bottom; Dextran in microfluidic channel before PEG was introduced.



Figure 3: Toluene printed on 250 μm -wide pillars are around 140-180 μm in diameter.

were used before the start in order to assure jetting. Printing dots of dextran 40 μm apart in a line resulted in drops 13-17 μm in diameter, small due to the near 90 degree contact angle of dextran on PDMS (see Figure 1). Upon running PEG through the channels and using a background subtraction effect on the microscope, we were able to see that the dextran still existed in its original pattern on the channels. Larger dots were printed in the channels to further illustrate this effect (see Figure 2).

This shows that direct printing with the Dimatix Inkjet is a possible solution for two-phase cell patterning.

For toluene, a high vapor pressure liquid, printing was achieved by using low voltages. A pattern of 3x3 drops was printed on the pillars, as it contained the most area while still being somewhat consistent. Two layers were printed on the pillars, as any more did not show a significant increase in diameter. Figure 3 shows the results of toluene drops on SU-8 pillars. The diameters range from 140-180 μm . Mixing QDs in the toluene unfortunately did not achieve the desired fluorescence for this project. As shown in Figure 4, the light intensity of the QDs in toluene is around 1040 units, whereas in a previous experiments using QDs and poly(methyl methacrylate)

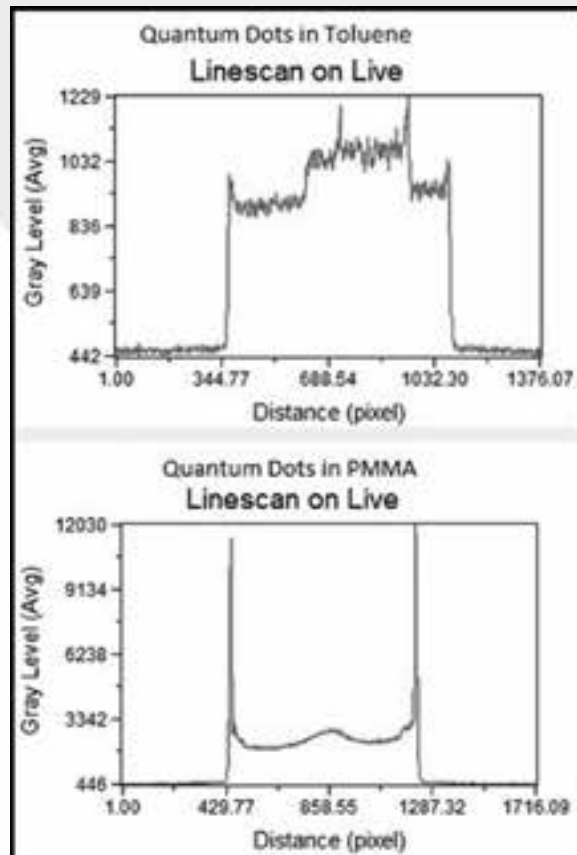


Figure 4: Top; QDs in toluene fluoresce around 1040 units. Bottom; Quantum dots in PMMA fluoresce around 3340 units.

(PMMA), fluorescence was around 3340 units. This meant that the use of Dimatix printing would not be used further in this project.

Acknowledgements:

I would like to thank the NNIN Research Experience for Undergraduates Program and the National Science foundation for giving me this opportunity, Dr. Pilar Herrera-Fierro for leading my research, Amrita Chaudhury, who was in charge of the QD project, and Brandon Lucas, Trasa Burkhardt, and the University of Michigan for coordinating this research experience.

References:

- [1] Goubko, C. A., et al. MS&E, 29 (6), 1855-1868 (2009).
- [2] Frampton, J. P., et al. Cell Co-culture Patterning Using Aqueous Two-phase Systems. J. Vis. Exp. (73) (2013).
- [3] Ghannad-Rezaie, Mostafa, et al. Journal of microelectromechanical systems 21.1: 23-33 (2012).

Functionalization of 6H Highly Doped Silicon Carbide Surfaces for Determining Cell Electrophysiology

Kaleel Wainwright
Biology, Columbia University

NNIN REU Site: Howard Nanoscale Science & Engineering Facility, Howard University, Washington, DC

NNIN REU Principal Investigator and Mentor: Dr. Tina Brower-Thomas, School of Engineering and Chemistry

Contact: kiw2103@columbia.edu, tina.browerthomas@howard.edu

Abstract:

Understanding the electrical activity of biological cells and tissue is important for medical diagnostics and bioengineering. Electrophysiology is employed to measure the electrical behavior of biological materials ranging in size from single ion channel proteins to entire organs. In order to measure the electrical properties of cells, they must be attached to a surface that is conductive and biocompatible. Silicon carbide (SiC) was used in this study because in addition to having these properties, its surface can be functionalized for protein attachment, which subsequently renders the surface amiable for cell attachment. SiC was exposed to oxygen plasma to render hydroxyl (OH) groups on its silicon (Si) face. The terminal OH groups were covalently bonded to 3-aminopropyltriethoxysilane (APTES). Raman spectroscopy measurements confirmed peaks for SiC and both oxidized and APTES functionalized SiC. The addition of APTES to SiC provided a reactive surface ready for antibody attachment and capable of supporting an antibody antigen reaction.

Introduction:

In recent years there has been an increased focus on the electrochemical properties of biological materials. Research in this field has led to significant developments in cancer, biosensor, and bioengineering research [1]. As this field of research has grown so has the need for substrates capable of greater sensitivity and selectivity. Due to its biocompatibility, electrical properties, chemical inertness, and thermal stability, SiC has proven to be an exemplary material for electrophysiological research. The process of constructing SiC-based apparatuses begins with developing an analyte-specific functionalization of SiC. In this experiment, surface chemistry of SiC was used to achieve this goal.

Experimental Procedure:

Commercially purchased 6H highly doped SiC was used in this experiment [2]. All reactions were performed on the Si face of the substrate. To begin the functionalization process, T = the samples were submerged for 5 min in trichloroethylene, succeeded by acetone, and then isopropanol. They were further cleaned using a 5:1:1 mixture of deionized water, hydrogen peroxide, and ammonium hydroxide in an 80°C environment for 10 minutes, also known as an RCA cleaning procedure.

To further remove organic contaminants and increase reactivity of the SiC surface, the substrates were then oxygen plasma cleaned using a Plasma-Therm model 790 plasma enhanced chemical vapor deposition system using a 20% oxygen/80%

argon gas mixture for a one minute period [3]. This process deposited a thin oxide layer on the surface of the SiC substrates. After oxygen plasma treatment, the substrates were placed under a fume hood and exposed to air for approximately 3 h to ensure surface chemisorption of water molecules [3]. This was done to aid APTES hydrolysis in the next step of the experiment.

APTES functionalization was performed in a class 100 clean room in a nitrogen environment. The silanol-terminated SiC samples were immersed in a 49:1 volume fraction (v/v) solution of APTES in toluene for a duration of approximately 10 minutes [3]. The substrates were then dried using N₂ gas to remove any loosely attached APTES molecules from the surface [3].

Results:

Raman spectroscopy was used in order to confirm the presence of the expected functional groups after each functionalization step. The technique has not been widely used in this fashion, though its ability to determine the presence of functional groups by detecting slight shifts in laser energy caused by interactions between the incident laser and vibrational energy levels of the molecules in the sample make it a suitable and perhaps even preferable methodology for confirming the presence of functional groups.

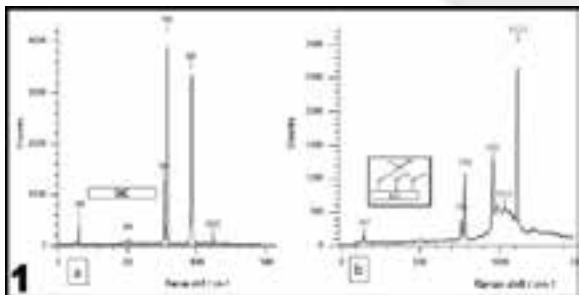


Figure 1: (a) Raman spectrum from 0 to 1500 wavenumbers of a cleaned SiC sample. (b) Raman spectrum from 0 to 1500 wavenumbers of the same sample after oxygen plasma treatment.

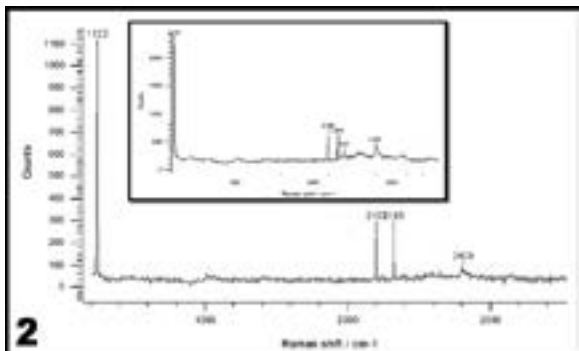


Figure 2: Raman spectrum from approximately 1100 to 2750 wavenumbers of a cleaned (refer to inset) SiC sample and the same sample after oxygen plasma treatment (larger image). A silanol terminated SiC diagram is included.

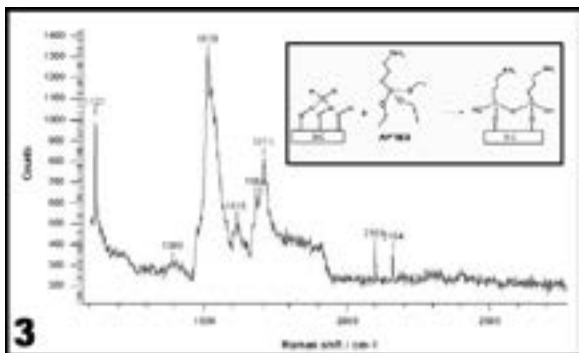


Figure 3: Raman spectrum from approximately 1100 to 2750 wavenumbers of the same sample after APTES functionalization. A diagram of the reaction is included.

In Figure 1, which displays the spectrum for the pre-oxygen treated substrate, peaks at 745 and 760 correlate to Si-C bonds, while the peak at 960 correlates to Si-Si [4]. In Figure 2, which displays the spectrum of the same sample after oxygen plasma treatment, the peak at 1120 increases significantly, indicative of the augment in Si-O bonds [4]. Figures 3 and 4 display the before and after of the APTES step, with Figure 3 corresponding to the oxygen plasma treated substrate (the

inset is the cleaned substrate) and Figure 4 corresponding to the APTES functionalized surface. After the APTES functionalization, the peaks at 1620 and 1390 reciprocal centimeters indicate the presence of amines on the surface [4].

Conclusion and Future Work:

Raman spectroscopy's ability to identify the presence of added functional groups was key to the success of this project. Now that an APTES functionalized surface has been confirmed, the focus of this project will be to determine a methodology for antibody attachment, which will either be accomplished via direct attachment using a carboxyl-amine reaction involving the constant end of the antibody and the APTES surface of SiC, or via indirect attachment by utilizing intermediate layers of compounds to achieve antibody attachment. After this, the next important benchmarks will be the selective attachment of cells and the determination of their electrical properties using scanning tunneling microscopy (STM).

Acknowledgements:

I thank Dr. Tina Brower-Thomas, our collaborators, and the Howard Nanoscale Facility Staff for their guidance and support. I also thank the NNIN REU Program for this opportunity and the NSF for their financial support.

References:

- [1] Vo-Dinh, T., et al.; *Journal of Analytical Chemistry*. 366 (6-7), 540-51 (2000).
- [2] Morkoc, H., et al.; *Journal of Applied Physics*. 76, 1363-1398 (1994).
- [3] Williams, E., et al.; *Applied Surface Science*. 258, (16), 6056-6063 (2012).
- [4] Hiraoui, M., et al.; *Materials Chemistry and Physics*. 128, 151-156 (2011).

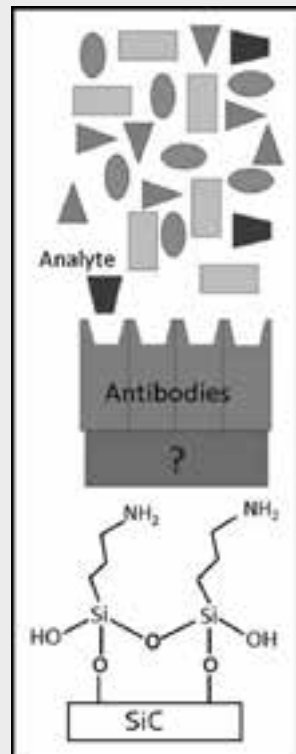


Figure 4: A schematic of the device. The region between the APTES functionalized SiC and the antibody layer depicts the uncertainty involved in how to attach the antibodies to the surface.

Microfabricated Cell Array Device for Screening of Metastatic Potential

James Paul Wondra, II
Biology, California State University Channel Islands

NNIN REU Site: Minnesota Nano Center, University of Minnesota-Twin Cities, Minneapolis, MN

NNIN REU Principal Investigator: Dr. Patrick W. Alford, Biomedical Engineering, University of Minnesota-Twin Cities

NNIN REU Mentor: Zaw Win, Biomedical Engineering, University of Minnesota-Twin Cities

Contact: james.wondra851@mci.csuci.edu, pwalford@umn.edu, winxx005@umn.edu

Abstract:

Metastasis is a complex cell migration process where a cancer cell leaves its primary tumor site to establish a secondary tumor site, causing greater than 90% of cancer related deaths. Traditionally, metastatic potentials have been quantified by individually tracking the migration of cells plated on a dish [1]. However, this method is low-throughput and requires costly live microscopy chambers. Here, we develop a high-throughput cell migration assay by employing microfabrication techniques to develop a method to capture single cells and place them in an organized array. We quantify cell migratory behavior by quantifying the disorder of the initial organized array. Migration of cancerous cells depends on the interactions between the cells and their microenvironments. Thus we validate our device by characterizing the migration of cells on substrates of varying stiffness. Upon completion of this project, the device will be usable as a diagnostic tool for rapid high-throughput analysis of the metastatic potential of biopsied tumor cells.

Experimental Procedure:

Classic Cell Migration Assay. We plated 3T3 fibroblast cells on Sylgard 184 polydimethylsiloxane (PDMS)-coated cover-slips of four different substrate moduli: 100 kPa, 300 kPa, 500 kPa, and 1000 kPa. Each substrate was then coated with fibronectin using microcontact printing [2]. The 3T3 cells were seeded onto each substrate (100 μ l; 100,000 cells/ μ l) and incubated over night at 37°C. Cells were then tracked using an Olympus IX81ZDC inverted confocal microscope by manually locating the position of cells, and obtaining images at 10 minute intervals, over 90 minutes. Celltracker [3] was used to determine the mean squared displacement of each cell, which is how far a cell has migrated from its original position.

Cell Array Device Assay. The design for the microfabricated cell array device (MCAD) was based on the work of DiCarlo, et al. [4] and was fabricated using standard soft photolithography techniques [5]. Masters were fabricated from SU-8 3025 photoresist spun on silicon wafers. PDMS (10:1 base:curing agent) was poured over the master and baked at 90°C for three hours. The MCAD was placed in conformal contact to a substrate, identical to the substrate used in the traditional cell migration assay. The MCAD (Figure 1) functioned as a microfluidic device designed with an array of cell traps (12 μ m in diameter), and bumpers used to direct cells into the traps.

A 3T3 fibroblast suspension (1 ml; 100,000 cell/ml) was flowed through the device using negative pressure, so that each trap became filled with one cell. The device was then incubated for one hour at 37°C and 5% CO₂, allowing trapped cells to attach to the fibronectin coated substrate in an organized array. Following device removal, the substrate was placed back into the incubator for three additional hours to allow for cell migration. The cells were then fixed using 4% paraformaldehyde and stained with 4',6-diamidino-2-phenylindole. Images of the cell arrays were obtained using an Olympus IX81ZDC microscope.

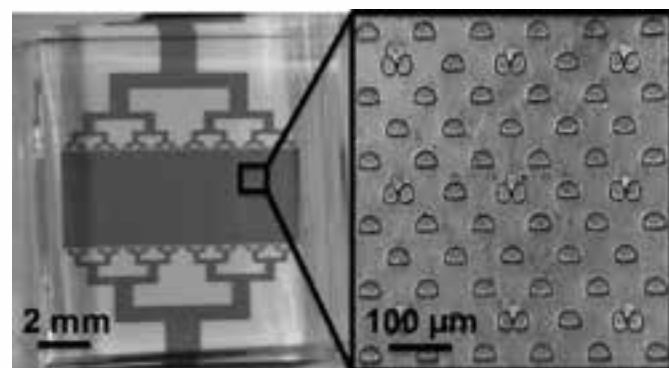


Figure 1: Microfabricated cell array device (MCAD) is a silicon microfluidic device containing an array of cell traps and bumpers.

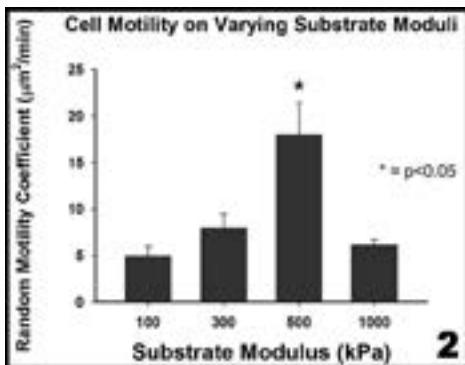


Figure 2: The traditional cell migration assay confirms that 3T3 motility on substrates of varying moduli show biphasic behavior.

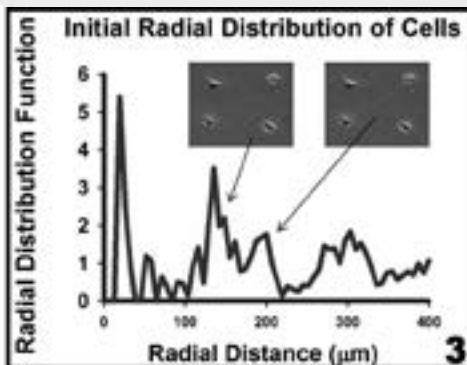


Figure 3: The radial distribution function of cells fixed immediately after MCAD removal.

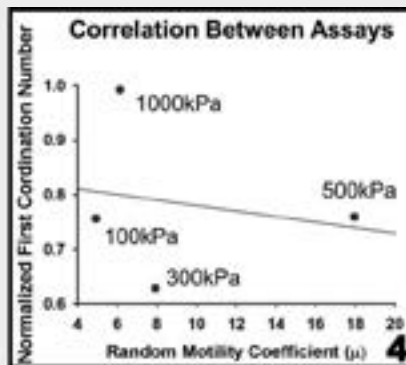


Figure 4: Correlation between the MCAD assay and the traditional cell migration assay.

Results and Conclusions:

Substrate Modulus Affects Migration. By tracking the mean squared displacement of a population of cells as a function of time, a random motility coefficient was determined for each substrate modulus by fitting a linear line through the MSD vs. time plot. The slope of the line is indicative of how migratory a population of cells is. The cells migrated significantly more on the substrate modulus of 500 kPa, shown in Figure 2. This biphasic result is consistent with previous experiments [6].

MCAD Assay. Images of cell arrays were analyzed using a custom MATLAB code to calculate a radial distribution function, shown in Figure 3. This is a way of characterizing the order of a system by calculating how the density of cells varies as a function of distance from a reference cell. The area under the second curve of the radial distribution function, corresponding to the 120 μm distance between each cell trap, is the first coordination number. A normalized first coordination number was determined for each MCAD substrate modulus and is a quantification of cell migration.

Correlation Between Assays. The results of the MCAD experiment were compared to the results of the traditional cell migration assay, as shown in Figure 4. A negative correlation between the assays would indicate agreement, as a low first coordination number corresponds to high cell migration. We see the trend that validates our device, but this data is very preliminary and inconclusive until this experiment can be repeated.

Future Work:

With further study, this device could be usable as a diagnostic tool for rapidly measuring cancer cell metastatic potential. Future work will include repeating this experiment so that a significant correlation can be obtained, and further optimizing the device.

Acknowledgements:

I would like to thank the National Science Foundation and the National Nanotechnology Infrastructure Network Research Experience for Undergraduates (NNIN REU) Program for funding this research, Jim Marti, Patrick Alford, Zaw Win, and the University of Minnesota.

References:

- [1] Dimilla, P., et al.; *J. of Cell Biology*, 122, 3, 729-737 (1993).
- [2] Tan, J., et al.; *PNAS*, 100, 4, 1484-1489 (2002).
- [3] Klingauf, M., et al.; *Biology of the Cell*, 105, 2, 91-107 (2013).
- [4] Carlo, D., et al.; *Royal Society of Chemistry*, 6, 11, 1445-1449 (2006).
- [5] Xia, Y., et al.; *Annual Review of Material Science*, 28, 152-184 (1998).
- [6] Peyton, S., et al.; *Journal of Cellular Physiology*, 204, 1, 198-209 (2005).

Controlling Biofilm Formation Through the Use of Conducting Polymers

Ashlyn Young

Biomedical Engineering, University of North Carolina at Chapel Hill

NNIN iREU Site: Centre Microélectronique de Provence, Ecole Nationale Supérieure des Mines de Saint Etienne, France

NNIN iREU Principal Investigators: George Malliaras and Róisín Owens, Department of Bioelectronics,

Centre Microélectronique de Provence, Ecole Nationale Supérieure des Mines de Saint Etienne, France

NNIN iREU Mentor: Adel Hama, Department of Bioelectronics, Centre Microélectronique de Provence,

Ecole Nationale Supérieure des Mines de Saint Etienne, France

Contact: youngat@live.unc.edu, malliaras@emse.fr, owens@emse.fr, hama@emse.fr

Introduction:

In liquid environments, microorganisms have the tendency to create complex communities on surfaces as a means of survival [1]. These microbial systems consist of a variety of organisms that thrive within a self-assembled matrix, often very resilient to the external environment. This can prove to be a serious nuisance, as biofilm accumulation commonly occurs on marine vehicles, biomedical implants, and industrial pipelines, and can be very difficult to prevent and remove [2, 3]. To combat this issue, biofouling agents have been formulated that resist and prevent unwanted biofilm growth on surfaces. These antifouling agents are commonly a pollution risk to the outside environment, as they leak biocidal agents into the surrounding marine communities or water sources. As a competitive alternative to harmful antifouling agents, the effects of the semiconductive p-doped polymer poly(3,4-ethylenedioxythiophene) polystyrene sulfonate (PEDOT:PSS) on biofilm growth has been explored under difference oxidative states [4]. A 96-well microliter plate was fabricated using photolithographic techniques, consisting of gold lines and PEDOT:PSS pixels. A continuous ± 1 V bias was applied to adjacent gold lines, which were connected via salt solution to produce different oxidative states. Prior to biasing, an *Escherichia coli* (*E. coli*) biofilm was produced *in situ* to adhere to the polymer after variable times, ranging from 0 to 22 hours. Preliminary results optically displayed that biofilms adhered better to an oxidized surface after 22 hours of constantly applied bias, with greater surface area coverage on the oxidized polymer in comparison with the reduced.

Methods:

Device Fabrication. Using soft photolithography techniques and AZ positive photoresist, clean rectangular glass slides were patterned through a 10 second UV exposure and development. Surface activation was then achieved with oxygen plasma and a 50 nm layer of chromium, followed by a 150 nm layer of gold were deposited on top of the patterned resist. Lift off was then performed with acetone and isopropanol, revealing a gold patterned device characterized by parallel conductive lines with empty square pixels to allow video microscope imaging. After gold deposition, two methods were available to attain PEDOT:PSS patterning.

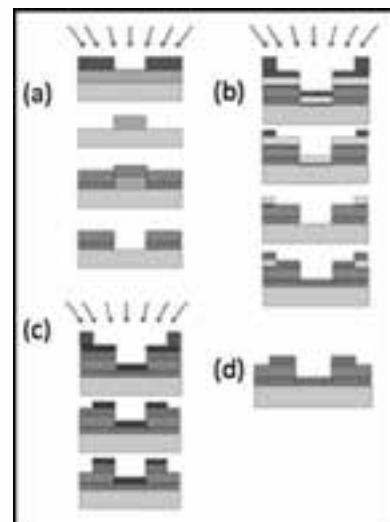


Figure 1: (a) Soft photolithography was used with positive photoresist to create Au, layered on top of Cr, conductive lines. (b) A negative photoresist was used to selectively etch a layer of soap and parylene. PEDOT:PSS polymer was spun on the parylene, which was then peeled off to create the PEDOT pixels. (c) As an alternative to parylene, orthogonal positive photoresist was used on top of PEDOT:PSS to selectively etch the pixel pattern. (d) The final device included lines of Au conductive lines with PEDOT:PSS pixels used as the active areas for *E. coli* culture.

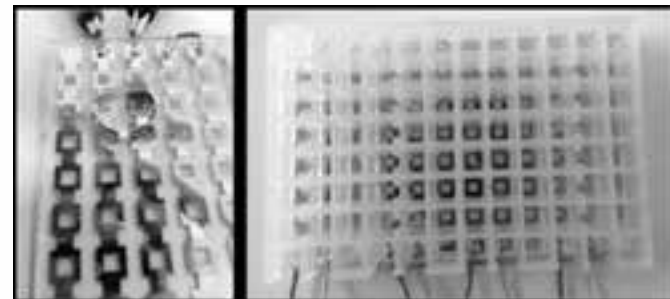


Figure 2: Three NEXTERION® MPX-96 superstructures were used atop the fabricated device. Glued together with PDMS, the top two silicon pieces were cut to allow media flow between two columns, therefore oxidizing one column of pixels and reducing the other when a ± 1 V voltage was applied to the conducting gold lines. Reduced PEDOT:PSS can be identified by a light blue color change. (See full color version on page xxxvi.)

The gold-patterned device was surface activated with oxygen plasma and spin coated at 650 rpm with PEDOT:PSS and soft baked for 60 seconds. Orthogonal negative resist was then spin coated on top of the PEDOT layer, exposed, and developed to protect square pixels of PEDOT:PSS. The unprotected PEDOT:PSS was etched through in the plasma machine, and the final photoresist was removed to reveal square pixels of PEDOT:PSS. An alternative method included a parylene peal off, though orthogonal resist was preferred. A

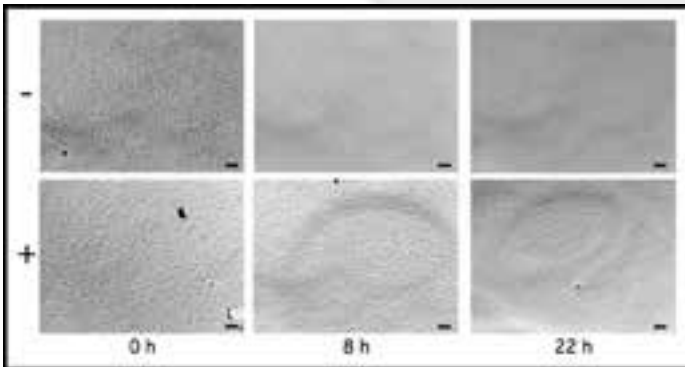


Figure 3: Biofilm growth was assessed under three different adhesion time conditions (22 hours, 8 hours, and 0 hours), and two different oxidative states (oxidized and reduced). Scale bars are 50 μ m.

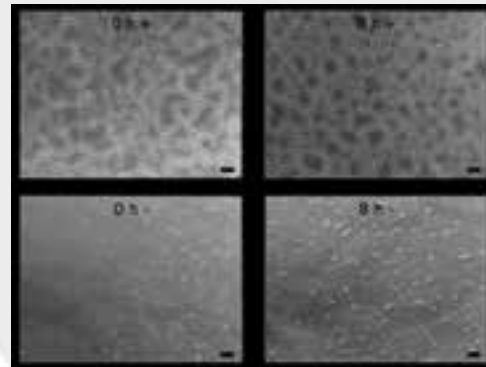


Figure 4: Biofilm was imaged with fluorescent Syto 9/Propidium Iodide live/dead dye prior to DI water washing. Red indicates dead bacteria, while green indicates living bacteria. Scale bars, 50 μ m. (Full color, page xxxvi.)

NEXTERION® MPX-96 superstructure was cut with a scalpel to allow the connection of adjacent rows with media during experimentation. The cut grid was then glued with PDMS to an in-tact grid to isolate bacteria growth on the well plate while still allowing oxidation/reduction to occur on the PEDOT:PSS. The finished device was heated to 100°C on a hotplate and the two-level grid was glued on, exposing PEDOT:PSS pixels, while preventing leakage.

Bacteria Culture. *E. coli* colonies were isolated on an agar plate and stored in the freezer for future use. A colony was selected from the agar plate for each experiment and cultured in 30 mL of LB media for 8 hr. Following three days of subculture in M63% media, 400 μ L of the *E. coli* solution was pipetted into four wells in three rows of the device (reduced, oxidized, and control) and left to grow in a humidified 30°C videomicroscope incubator for 0, 8, and 22 hr.

Experimentation. After a biofilm was formed for the determined time condition, 22 hours of ± 1 V bias were applied to adjacent rows in the videomicroscope. A time-lapse video was recorded for the 22 hour condition to observe biofilm formation under bias. Following the bias, the device was removed from the videomicroscope, supernatant fluid was removed, and each well washed twice with deionized water. Cells were then imaged in the videomicroscope. Viability of the bacteria was assessed with Syto 9/Propidium Iodide live/dead fluorescent dye post experimentation.

Results and Conclusions:

In conclusion, we found that conductive polymer oxidation affected the ability of bacteria to adhere and form biofilm, with the oxidized material displaying more biofilm growth. Through altering the oxidative state of the PEDOT:PSS, we were able to achieve a degree of control over biofilm growth. Reduced biofilm displayed a much lessened biofilm accumulation when qualitatively examined by microscopy. The preliminary images can be better quantified through surface area coverage calculations.

In a time-lapse video collected during bias, it was noted that at 0 hour, oxidized polymer displayed aggregation accumulation of bacteria in early development, a phenomenon very

characteristic of biofilm growth. Additionally, this aggregation was not observed as clearly in the reduced polymer. This was solely noted in the 0 hour condition due to the high quantity of bacteria in the samples incubated for longer times prior to bias, making changes in biofilm layer more difficult to view. Fluorescent imaging was used to determine the bacteria viability after bias and was observed under two conditions.

One condition included washing with de-ionized (DI) water; the other only included supernatant fluid removal. The justification for washing with DI water was to avoid the crystallization of media when dried. When washed with DI water prior to fluorescent imaging, it was observed that the bacteria adhered to the glass were all dead, with the only living cells in the supernatant. When avoiding the DI water step, the adhered cells were not fluorescent, possibly due to a protecting layer of fluid and cellular components formed by the biofilm. Despite the bacteria no longer appearing alive, a biofilm was existent on the oxidized polymer, while the reduced polymer did not display such. These observations facilitate the preliminary conclusion that reduced PEDOT:PSS acts as an antifouling agent for the *E. coli* bacterial species.

Acknowledgements:

Thank you to Dr. Róisín Owens, Pr. Georges Malliaras, Adel Hama, Marc Ferro, Marc Ramuz, Mary Donahue, the CMP Bioelectronics Department, and Dr. Lynn Rathbun for your mentorship, assistance, and guidance. This research was supported and funded by the National Nanotechnology Infrastructure Network Internatio NNIN iREU Program and the National Science Foundation.

References:

- [1] D. de Beer, P. Stoodley, F. Roe, Z. Lewandowski, *Biotechnology and bioengineering* 1994, 43, 1131-8.
- [2] K. Vasilev, J. Cook, H. J. Griesser, *Expert review of medical devices* 2009, 6, 553-67.
- [3] D. Pavithra, M. Doble, *Biomedical materials* (Bristol, England) 2008, 3, 034003.
- [4] G. Malliaras, R. Friend, *Physics Today* 2005, 58, 53-58.

Self-Assembled Structures Through Triblock Terpolymers Forming Gyroid Structures

Shinsuke Hirata

Graduate School of Engineering, Kyushu University, Japan

NNIN iREG Site: Cornell NanoScale Science & Technology Facility, Cornell University, Ithaca, NY

NNIN iREG Principal Investigator: Prof. Ulrich Wiesner, Materials Science and Engineering, Cornell University

NNIN iREG Mentors: Takeshi Yuasa and Dr. Hiroaki Sai, Materials Science and Engineering, Cornell University

Contact: s.hirata@mail.cstm.kyushu-u.ac.jp, ubw1@cornell.edu, ty279@cornell.edu, hs438@cornell.edu

C
H
E
M

Abstract:

Gyroid, which is one of the three-dimensional continuous network structures, is a promising structure. Gyroid structures were achieved by the use of block copolymers that show micro-phase separated structures through a self-assembly process. We fabricated a template of gyroid structures by blending triblock terpolymers and homopolymers. After self-assembled structures were prepared, homopolymers were removed by solvents, so that porous structures were obtained. Structures were evaluated by transmission electron microscopy (TEM) and scanning electron microscopy (SEM).

Introduction:

The colors of morpho butterfly's wings are derived from their wing's structure, the so called 'structural color' [1]. It has been ascertained that one of the structures is gyroid, which is a 3D continuous network structure. This structure has been and is expected to be used in many fields, for example fuel cells, solar cells, metamaterials, etc., so it is important to be able to fabricate gyroid structures easily.

Gyroid structures were achieved by the use of block copolymers. Block copolymers consist of chemically distinct components that show immiscibility due to their different chemical affinities. Since they are covalently bonded to each other, they show various micro-phase separated structures through a self-assembly process. Gyroid is one of the micro-phase separated structures, but gyroid areas on a phase diagram of diblock copolymers are generally small. We used triblock terpolymers to extend the gyroid areas because gyroid areas on a phase diagram of triblock terpolymer become larger.

Our plan to fabricate gyroid structures was to use triblock terpolymers as a template [2]. After one component of triblock terpolymer was removed by selective etching, porous structures for templates could be obtained. Our strategy for the selective etching was to blend triblock terpolymers and oligomers, which are supposed to be miscible with one component of triblock terpolymers. Because oligomers are easily removed by solvents, selective etching could be achieved. We used poly(isoprene-block-styrene-block-glycidyl methacrylate) (PI-PS-PGMA; ISG) and 1,2-polybutadiene (B), which was supposed to be miscible with polyisoprene block. And poly(glycidyl methacrylate) (PGMA) was also blended to tune the volume fractions of samples. PGMA components would keep their structure after crosslinked by acid.

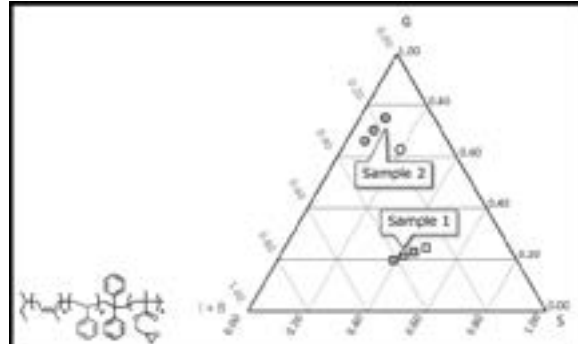


Figure 1: Chemical structure of ISG and volume fractions of each samples on phase diagram. Open square indicates ISG [1] and black squares indicate ISG [1] + B in different compositions. Open circle indicates ISG [2] and black circles indicate ISG [2] + B in different compositions.

Experimental Procedure:

ISGs (ISG [1]: $M_n(I) = 10.5$ kg/mol, $M_n(S) = 21.3$ kg/mol, $M_n(G) = 40.7$ kg/mol, ISG [2]: $M_n(I) = 4.9$ kg/mol, $M_n(S) = 6.2$ kg/mol, $M_n(G) = 13.9$ kg/mol), homopolymers B ($M_n = 3.0$ kg/mol) and/or poly(glycidyl methacrylate) (PGMA) were dissolved into tetrahydrofuran (THF) in different compositions (10 wt%) (Figure 1). Then photoacid generator (Irgacure PAG 290) was added to the solutions (1 wt% of total solute). After they were poured in aluminum dishes, they were kept overnight at 50°C during which time THF evaporated from the solutions. After light irradiation for 15 minutes to cross link the PGMA component, samples were observed by transmission electron microscopy (TEM). In preparation for TEM, specimens were

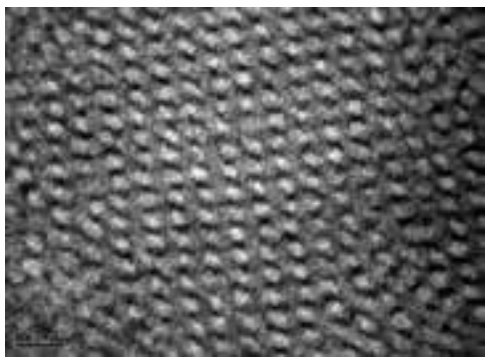


Figure 2: TEM image of Sample 1.

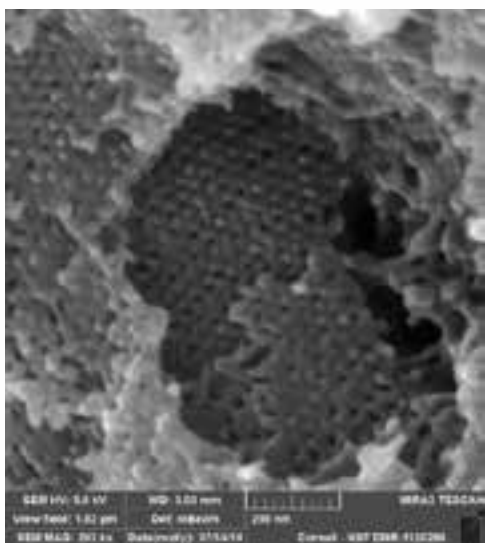


Figure 3: SEM image of Sample 1 after immersed in hexane to remove B.

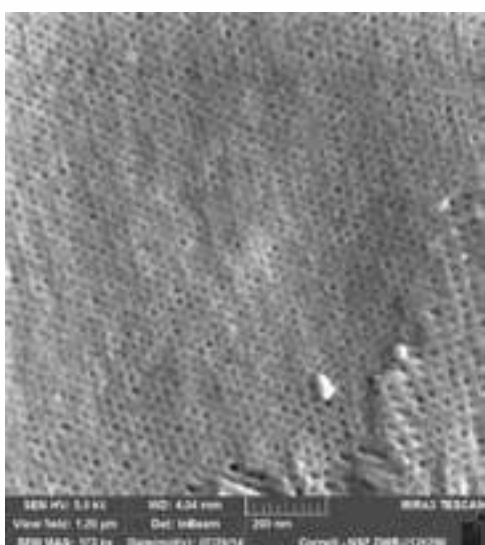


Figure 4: SEM image of Sample 2 after immersed in hexane to remove B.

cut with a cryomicrotome at -60°C, then exposed to osmium tetroxide vapor to stain I component. After samples were immersed in hexane to remove B, they were observed by SEM.

Results and Conclusions:

ISG [1] + B (square). Micro-phase separated structures were found in each sample by TEM measurement, and especially the sample shown as the middle one of black squares in the phase diagram (Figure 1) showed the most ordered self-assembled structure (Sample 1, Figure 2). This structure might be gyroid or cylinder, but it was difficult to determine its structure because the intensity of small angle x-ray scattering (SAXS) — which could identify their structures — was too weak. After it was immersed in hexane to remove B, Sample 1 was observed by SEM (Figure 3). Porous structure was found and its diameter was 15-20 nm.

ISG [2] + B + G (circle). ISG [2], B and homopolymer G were blended to fabricate samples with high G ratio. Micro-phase separated structures were found in each samples by TEM measurement, and especially the sample that is shown as the top one of the black circles in the phase diagram (Sample 2) (Figure 1) showed the most ordered self-assembled structure, which was hexagonal-packed cylinder. And then Sample 2 was immersed in hexane to remove B, followed by SEM measurements of the structure (Figure 4). Porous structure was found and its diameter was below 10 nm.

In conclusion, we could achieve the selective etching of B component from self-assembled structures. We fabricated two porous samples in different compositions and pore diameters were also different, which indicates that we could control the pore size by control the ratios of homopolymer B.

Future Work:

Future research is needed to optimize the etching conditions; temperatures, solvents, immersing time, etc. After that, porous structures will be used as a template to be replicated with functional materials by deposition of other materials.

Acknowledgments:

I would like to thank T. Yuasa, Dr. H. Sai, Prof. U. Wiesner and all the other members of Wiesner group, for their support in my summer program. And I really appreciate coordinators of this program, especially Dr. L. Rathbun. This research was supported by the National Nanotechnology Infrastructure Network International Research Experience for Graduates (NNIN iREG) Program, National Institute for Material Science (NIMS) and the National Science Foundation (NSF).

References:

- [1] R. O. Prum, et al., PNAS 2010, 107, 11676.
- [2] K. Hur, et al., Angew. Chem. Int. Ed. 2011, 50, 11985.

Developing Methodology for Living Polymerization of Functionalized Conjugated Monomers using Nickel Catalysts with Electron-Rich Phosphine Ligands

John Ren

Chemical Engineering, Oregon State University

NNIN REU Site: Washington Nanofabrication Facility & Molecular Analysis Facility, University of Washington, Seattle, WA

NNIN REU Principal Investigator: Dr. Christine K. Luscombe, Materials Science and Engineering, University of Washington

NNIN REU Mentor: Jason Lee, Chemistry, University of Washington

Contact: renjo@onid.oregonstate.edu, luscombe@uw.edu, leejason@uw.edu

C
H
E
M

Abstract:

The potential applications of polymers in the semiconductor industry have spawned further research into developing their synthetic routes. Organic semiconductors are poised to revolutionize the electronics industry because the devices made using organic semiconductors are inexpensive to fabricate when compared to their traditional silicon counterparts. One difficulty associated with polymer synthesis is molecular weight control. Living polymerization, a form of chain growth polymerization that allows for precise control of molecular weight and dispersities, has been shown to potentially solve this issue. Methods such as the Kumada Ni-Catalyzed Transfer Polymerization allow such control through the adjustment of monomer to catalyst ratios. Also problematic of polymer synthesis is the use of toxic organometallic monomers. This may be solved by involving C-H functionalization, eliminating the need for organometallic monomers, and reducing overall environmental impact. Recent reports [1] of C-H/C-O biaryl coupling of benzoxazoles via Ni(0) with electron-rich phosphine ligands have inspired our approach towards a living polymerization methodology with functionalized conjugated benzoxazole monomers. In this report, the syntheses of monomer precursors are reported.

Introduction:

Semiconductors have revolutionized human technological advancement. Used in electronics and solar energy industries, semiconductor devices made from silicon (Si) are by far the most prevalent. Despite its popularity, Si fabrication is rather expensive. Electronics-grade Si must be extremely high in purity, refined in a process that is expensive and energy intensive, both in man hours and energy used. Si production also utilizes many toxic materials, creating environmental issues that must be dealt with.

Organic semiconductors, such as conjugated polymers, have presented themselves as a viable alternative to silicon. Devices made using organic semiconductors are typically less expensive than their Si counterparts. They also utilize lower production temperatures and may have attractive properties such as transparency and flexibility that expand their range of possible uses.

Current polymer synthesis techniques pose two challenges for organic semiconductor production: molecular weight control and the use of toxic organometallic monomers. The two can be solved by utilizing living polymerization (a form of chain growth polymerization where the growing polymer chain cannot self-terminate) to solve molecular weight issues and C-H functionalization (replacing organometallic aryl

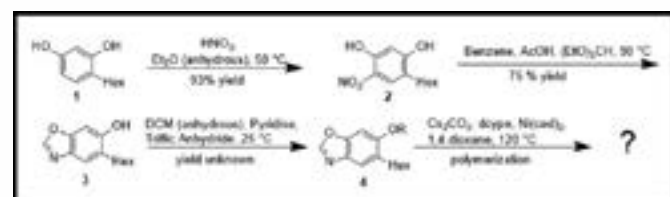


Figure 1: Reaction schemes, reactions progress in order from top to bottom.

nucleophiles/electrophiles in traditional cross-coupling with hydrogen/oxygen) to eliminate the need for organometallic reagents.

The goal of this project is to develop a methodology for the living polymerization of functionalized conjugated benzoxazole monomers using C-H functionalization. Specifically, benzoxazole monomers and monomer precursors were synthesized, and polymerizations were attempted and analyzed.

Methodology:

The synthetic steps used are shown in Figure 1.

Monomer precursors were synthesized from the starting material 4-hexylresorcinol, which was first nitrated to form

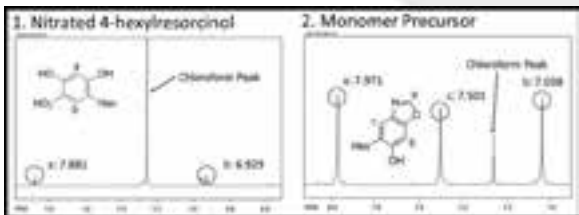


Figure 2: ^1H NMR of molecules **2** and **3**.

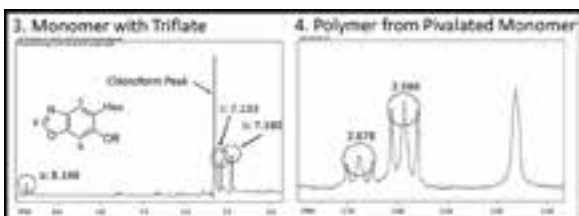


Figure 3: ^1H NMR of molecule **4** and polymerization mixture.

6-nitro-4-hexylresorcinol. A ring-closing reaction was then performed to produce 5-hydroxyl-6-hexylbenzoxazole. This monomer precursor was functionalized with either a pivalate or trifluoromethanesulfonate (triflate) to produce the benzoxazole monomer [1]. Living polymerization trials were then performed with benzoxazole monomers with either group [1, 2].

Results and Discussion:

Analysis of ^1H NMR data as well as mass spectrometry data show that the benzoxazole monomer **3** as well as precursor **2** were successfully synthesized (Figure 2). The labeled peaks strongly suggest the presence of the desired products.

In Figure 3, molecule **4** (monomer functionalized with triflate) shows a shift in peaks in comparison to the monomer precursor **3**. Note that multiple peaks have shifted both downfield and upfield. This may indicate that triflation has indeed occurred as the electronegative triflate group deshields the proton furthest away from it while shielding the two closest to it. Yields of the triflate functionalized monomer have yet to be determined. Figure 3 also shows a polymerization attempt of the benzoxazole monomer functionalized with the pivalated monomer. The presence of the two triplets in the hexyl region indicate that a dimer may have formed. This is a promising sign that biaryl coupling may have occurred, indicating that the monomer is reactive, but is not a good indication that living polymerization is successful with this monomer.

Refer to Table 1 for polymerization conditions and results.

Conclusions:

The development of a methodology for the living polymerization of functionalized conjugated benzoxazole monomers using C-H functionalization was attempted. Synthesis of

benzoxazole monomers and their precursors proved successful, but successful living polymerizations were not achieved. Benzoxazole monomers functionalized with pivalate groups show promising reactivity, as shown by dimer formation during living polymerization attempts, but further work must be done to achieve living polymerization of benzoxazole monomers. Monomers functionalized with triflate groups did not display reactivity, and further work must be performed to achieve successful polymerizations.

Future Work:

Currently, the only step of the methodology that has failed is the polymerization itself. This may be due to poor monomer quality or an unreactive C-O group. Therefore, refinement of the C-O group is required, as well as refinement of the monomer synthesis reaction. Further living polymerization attempts of the triflate monomer are also to be attempted. If proven successful, adjustments of monomer to catalyst ratios may be attempted to see if polymer chains of varying lengths may be achieved while maintaining low dispersities.

Acknowledgements:

I would like to thank Jason Lee for all his help and patience. Thanks to Lauren Kang and Lucian Suraru for supplying ^1H NMR samples and miscellaneous reagents. Acknowledgments also to Jeremy Housekeeper for use of his monomer precursors as well as inspiration for preps. I would like to thank Dr. Christine Luscombe for the opportunity to work in her lab, as well as help on presentations and papers. Lastly, the National Nanotechnology Infrastructure Network Research Experience for Undergraduates (NNIN REU) Program and National Science Foundation (NSF) for funding.

References:

- [1] Muto, K.; Yamaguchi, J.; Itami, K. Nickel-Catalyzed C-H/C-O Coupling of Azoles with Phenol Derivatives. *Journal of the American Chemical Society*. 2012, 134, 169-172.
- [2] Housekeeper, J. Laboratory Notebook Book II; University of Washington: Seattle, 2013. p 195.

Polymerization Conditions	Result
Pivalated monomer (1 equiv), CsCD_3 (1.5 equiv), dicyclopentadiene (0.2 equiv), $\text{Ni}(\text{cod})_2$ (0.1 equiv), 1,4-dioxane (4 mL)	Indication of dimer
Pivalated monomer (1 equiv), CsCD_3 (1.5 equiv), dicyclopentadiene (0.2 equiv), $\text{Ni}(\text{cod})_2$ (0.1 equiv), 1,4-dioxane (4 mL)	No indication of polymerization
Triflated monomer (1 equiv), CsCD_3 (1.5 equiv), dicyclopentadiene (0.2 equiv), $\text{Ni}(\text{cod})_2$ (0.05 equiv), 1,4-dioxane (2 mL)	No indication of polymerization

cod = 1,5-cyclooctadiene, dicyclopentadiene = 1,2-bis(cyclopentadiene)ethene

Table 1: Polymerization conditions and results.

Studying the Effect of Materials and Processing on the Electrical Properties of Bilayer Al / Amorphous CoTiN Metal Gates for Advanced Nanoelectronic Devices

William Anderson

Electrical and Computer Engineering, Baylor University

NNIN REU Site: Stanford Nanofabrication Facility, Stanford University, Stanford, CA

NNIN REU Principal Investigator: Prof. Bruce Clemens, Materials Science and Engineering, Stanford University

NNIN REU Mentor: Ranida Wongpiya, Materials Science and Engineering, Stanford University

Contact: billy_anderson@baylor.edu, bmc@stanford.edu, ranidaw@stanford.edu

Abstract:

Amorphous metal gate stacks present several advantages over traditional polysilicon gate stacks, including lower electrical resistivity and the elimination of polysilicon depletion and boron penetration effects. Recent use of amorphous metal gates in complementary metal oxide semiconductor (CMOS) integrated circuits have been shown to enhance their electrical properties by reducing work function and threshold voltage variability [1]. Additionally, amorphous metal gates are expected to exhibit enhanced diffusion barrier properties, which would stabilize the work function by preventing metal interdiffusion. However, amorphous gate mechanics have yet to be fully investigated. Understanding the effect of structure, materials, and processing on the electrical properties of transistors as well as optimizing the gate stack remain a challenge. The goal of this project was to study such effects in a bilayer metal gate structure consisting of aluminum (Al) as an upper layer and either polycrystalline titanium nitride (TiN) or partially amorphous cobalt titanium nitride (CoTiN) as a bottom layer. This would be done by comparing the diffusion barrier properties of the CoTiN gates to those of the TiN gates by measuring capacitance-voltage characteristics with varying thickness and annealing temperature. The extracted work function could then be used to determine if the amorphous gates effectively resist Al diffusion and prevent threshold voltage fluctuation, properties essential to increasing operational speed and efficiency in industrial nanoelectronic devices.

Experimental Procedure:

Several bilayer metal gate stacks consisting of a 50 nm Al upper layer and a polycrystalline TiN or amorphous CoTiN layer underneath with varying thickness (1-50 nm) were fabricated. The metals were deposited via sputter deposition onto a step-etched $\text{HfO}_2/\text{SiO}_2$ dielectric (with 2 nm of atomic layer deposited hafnium dioxide, HfO_2 , and 5-20 nm of thermally grown silicon dioxide, SiO_2) on a Si substrate.

Following deposition, the structures were etched and patterned into 200 μm diameter capacitors using standard lithography techniques. The wafers were coated with 1.6 μm of machine-spun Shipley 3612 positive photoresist, masked and patterned under high-intensity UV light, and then developed to strip away the weakened photoresist. The exposed Al was etched away using Al etchant, and the TiN or CoTiN metal underneath was dry etched with CHClF_2 (Freon 22) plasma. The remaining photoresist was then removed using a PRS3000 wet etch. Following the lithography procedure, hydrofluoric acid was used to remove the back oxide, thus improving the wafer back contact.

Inspection by optical microscope revealed that most samples sustained damage during etching and lithography procedures, possibly related to gas contamination or gas leakage in the

system as observed from the plasma color differences during etching. Damages incurred by the capacitors included over-etched capacitor boundaries as well as thread-like projections from inner and outer rings, both of which could have degraded capacitor functionality.

Fortunately, one sample of Al on 6 nm of CoTiN remained unaffected by the etching and lithography problems. This sample was used to measure the change in work function as a function of annealing temperature. Figure 1 shows the undamaged and completed sample.

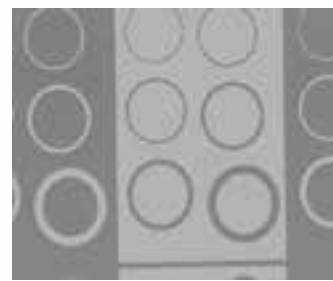


Figure 1: Salvageable Al / CoTiN (6 nm) capacitors as-deposited.

The capacitance-voltage (CV) characteristics of this sample were then measured using a bipolar bias sweep from 4V to -2.5V and back. These characteristics were used to determine several device parameters such as flatband voltage and equivalent oxide thickness, which can be used to calculate the work function as described in Reference 2.

CV characteristics for each oxide thickness of the sample were measured as-deposited and again after 300°C, 400°C, and 500°C anneals in forming gas for 20 min. Measurements were taken at 10 kHz, 100 kHz, and 1 MHz to confirm consistent device operation. Figure 2 represents CV measurements obtained from the sample after a 300°C anneal.

Flatband voltage is the voltage corresponding to the flatband capacitance; equivalent oxide thickness was derived from the maximum capacitance. Figure 3 represents a plot of flatband voltage as a function of equivalent oxide thickness.

By the equation used to calculate the metal work function, extrapolating a linear regression of flatband voltage versus equivalent oxide thickness gives the work function difference between the metal and the semiconductor. Adding the calculated work function of the semiconductor to this value yields the CoTiN work function for a particular anneal condition. Following this method, the CoTiN work function was extracted for each anneal condition and plotted with respect to annealing temperature in Figure 4.

Results and Conclusions:

The obtained results illustrate that the CoTiN metal work function nominally decreases with an increase in annealing temperature. Possible explanations include:

- Ineffective Al diffusion prevention,
- Annealing of interface defects,
- Structural changes in CoTiN during the annealing process, and,
- Interaction between dielectric and CoTiN interface.

The effectiveness of CoTiN as a diffusion barrier remains unclear. While results do indicate a change in work function of approximately 0.3 eV, this difference is relatively small compared to silicon's band gap and could be affected by any combination of the reasons cited. Further experimentation on the effects of thickness on the CoTiN work function as well as comparison to polycrystalline metals are needed to establish amorphous CoTiN barrier properties and its use as a gate material for industrial applications.

Acknowledgements:

Metal Gate Research Group: Prof. Bruce Clemens, Prof. Yoshio Nishi, Dr. Michael Deal, Dr. Jim McVittie, Ranida Wongpiya, Joanie Ouyang. REU Program Administrators: Dr. Michael Deal, Maureen Baran. Stanford Initiative for Nanoscale Materials and Processes. Stanford Center for Integrated Systems. National Science Foundation. National Nanotechnology Infrastructure Network Research Experience for Undergraduates (NNIN REU) Program.

References:

- [1] T. Matsukawa, et al. "Suppression of threshold voltage variability of double-gate fin field-effect transistors using amorphous metal gate with uniform work function." *Applied Physics Letters* 102, 162104(2013); doi: 10.1063/1.4803040.
- [2] J. Ouyang, et al. "Effect of Composition on Structural and Electrical Properties of Amorphous Ta-W-Si-C Metal Thin Films." *Electrochemical Society Solid State Letters*, 2 (10) P86-P88 (2013).

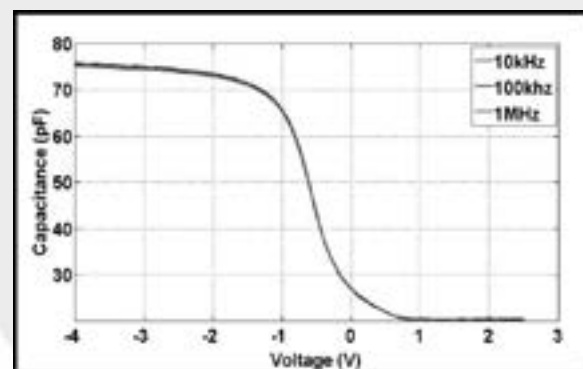


Figure 2: Capacitance-voltage characteristics of the Al / CoTiN (6 nm) sample.

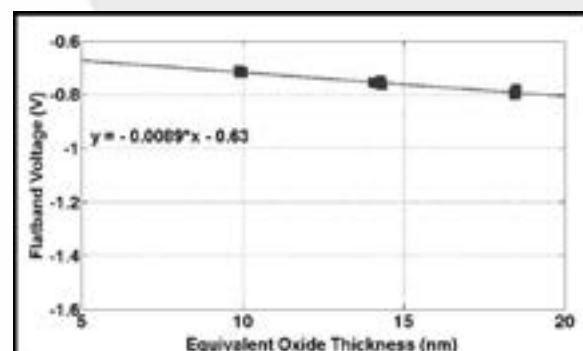


Figure 3: Plotting flatband voltage against equivalent oxide thickness is used to calculate the CoTiN work function.

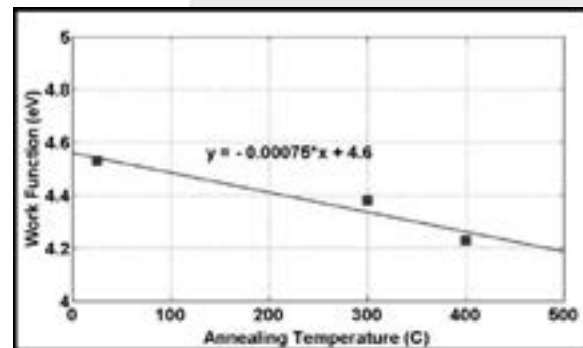


Figure 4: CoTiN work function plotted against annealing temperature shows a decrease with increasing temperature.

Optimization of Hybrid Fuel Cell Designs and Materials

Fausto Mares-Davila

Chemical Engineering, The University of Arizona

NNIN REU Site: Institute for Electronics & Nanotechnology, Georgia Institute of Technology, Atlanta, GA

NNIN REU Principal Investigator: Dr. Paul Kohl, Chemical and Biomolecular Engineering, Georgia Institute of Technology

NNIN REU Mentor: John Ahlfield, School of Chemical and Biomolecular Engineering, Georgia Institute of Technology

Contact: maresdavila@email.arizona.edu, paul.kohl@chbe.gatech.edu, john.ahlfield@chbe.gatech.edu

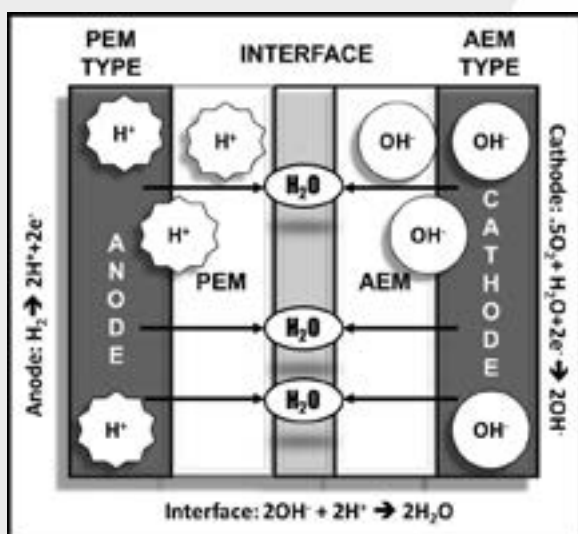


Figure 1: The membrane electrode assembly and hybrid fuel cell electrochemical reactions are shown.

Introduction:

A hybrid fuel cell (HFC) produces electricity by means of an electrochemical reaction. The membrane electrode assembly (MEA) and electrochemical reactions are shown in Figure 1. The hybrid fuel cells studied combine elements from a proton exchange membrane (PEM), which only conducts protons, and an anion exchange membrane (AEM), which only conducts hydroxides. HFCs have the potential to provide quiet, efficient, and zero emissions energy without the need for a water management system. Some problems with HFCs are expensive components such as platinum catalysts, low performance values, and AEMs that are not durable.

The main focus of this research was on the interface material that is positioned between the PEM and AEM in the fuel cell. This region is important because it provides the adhesion between the AEM and PEM, and water is created at this interface when the hydrogen and hydroxide ions combine. Two hybrid fuel cells were assembled with different interface materials. The interface material in HFC 1 was a polymer that interacts with hydrogen and hydroxide ions. The interface material in HFC 2 was a hydroxide conductive ionic liquid. Voltammetry,

impedance spectroscopy, and chronoamperometry were the electrochemical analyses performed on both cells to determine which interface material works better.

Experimental Procedure:

The cathodes and anodes were made using the recipe described in the literature, except the AEM cathode was made with toluene instead of dimethylformamide [1]. The material used as the PEM was Nafion® 117 and the material used for the AEM was Tokuyama a201. To assemble the MEA for HFC 1, the electrodes were sprayed with ionomer solution. The PEM was sprayed with neutral epoxy, ionomer interface material, which was made of polynorbornene, Nafion ionomer, and trimethylolpropane triglycidyl ether. The electrodes, PEM, and AEM were then stacked on top of each other in the order shown in Figure 1 and put into the hot press for 10 minutes at 2 MPa and 212°C to bond the layers together.

The same procedure was used to make the MEA of HFC 2 except the PEM was sprayed with ionic [bmim][OH] interface material. During the electrochemical analysis, each fuel cell was connected to a FCT 150S test station and a PARSTAT 2773, which is a combined potentiostat and galvanostat. The fuel cell test station and FC Lab V5.22 software were used to control the fuel cell temperature, relative humidity, and gas flow. The potentiostat was used to perform the voltammetry, impedance spectroscopy, and chronoamperometry. All of the electrochemical analyses were performed at 100% R.H and 55°C. At the anode, hydrogen flowed in at 10 mL/min. At the cathode, oxygen flowed in at a rate of 25 mL/min.

Results:

The voltammetry results for the HFCs are shown in Figure 2. The max current density for HFC 1 was 28 mA/cm². The max current density for HFC 2 was 38 mA/cm². HFC 1 produced 3.9 mW/cm² and HFC 2 generated 5.1 mW/cm². The power density indicates how many watts are produced per square centimeter of MEA. Chronoamperometry was performed on each HFC for five hours. The results are shown in Figure 3. HFC 1 produced a steady 0.05 A. HFC 2 produced an initial 0.13 A, then dropped to a steady 0.11 A.

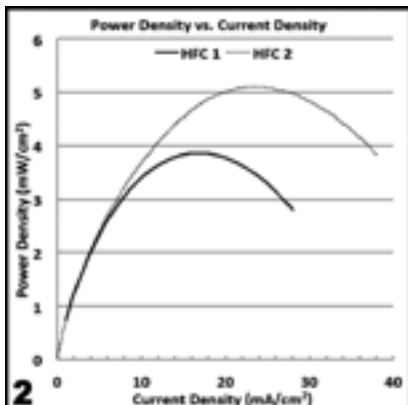


Figure 2: The results of the voltammetry experiment for HFC 1 and 2 are shown.

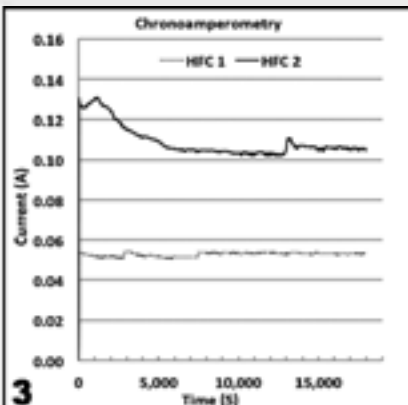


Figure 3: The chronoamperometry results of both HFCs are shown in the graph. The experiment was run for five hours.

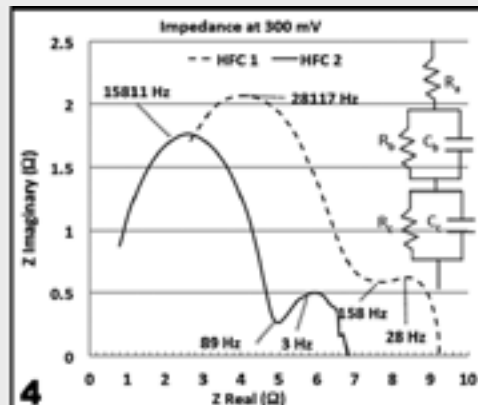


Figure 4: The chart shows the impedance spectroscopy results for both of the HFCs. The HFCs were tested at the same frequencies 0.05 Hz – 88913 Hz. Both HFCs have the same equivalent circuit shown in the graph.

It is believed that HFC 2 generated a large current because it had less resistance than HFC 1. HFC 2's low resistance can be attributed to the conductivity of the [bmim][OH].

Impedance spectroscopy measurements were taken at 300 mV from 0.05 Hz - 88914 Hz. The impedance data is shown in Figure 4. The impedance data shows the membrane, anode, and cathode resistance. The length between the first data point and the y-axis is the membrane resistance in ohms. The radius of the first peak is the anode resistance. The radius of the first valley is the cathode resistance. Both of the HFCs had the same equivalent circuit that is shown in Figure 4. An equivalent circuit may have resistors, capacitors, and inductors, but low testing frequencies eliminated the need for inductors [2]. The equivalent circuit was refined until it produced impedance values that were similar to the experimental values. The equivalent circuit and the impedance data show that HFC 2 has less resistance, which means there is less power loss to resistance.

Conclusions:

Both of the HFCs performed better than previous designs without an interface material. The ionic [bmim][OH] interface material in HFC 2 performed better than the neutral epoxy and

ionomer interface material in HFC 1 in all the electrochemical analyses. The impedance spectroscopy data indicates the [bmim][OH] decreases resistance in a HFC. It is believed the [bmim][OH] decreases resistance by conducting the incoming hydroxide ions better than a neutral interface material. The large steady current values and high power density of HFC 2 is a result of less resistance in the interface material.

In the future, it is likely that an HFC with a proton conducting interface material will be tested.

Acknowledgments:

Thank you to Dr. Paul Kohl, John Ahlfeld, Leslie O'Neill, National Nanotechnology Infrastructure Network Research Experience for Undergraduates Program, and NSF.

References:

- [1] Murat Ünlü, Junfeng Zhou, Paul A. Kohl. "Hybrid Anion and Proton Exchange Membrane Fuel Cells." *The Journal of Physical Chemistry* 113.26 (2009): 11416-11423. Print.
- [2] Monk, Paul. *Fundamentals of Electroanalytical Chemistry*. Chichester: John Wiley & Sons Ltd, 2001. Print.

Interlayer Dielectric and Interconnect for Heterointegration

Julie Miller

Chemical Engineering, The Pennsylvania State University

NNIN REU Site: Lurie Nanofabrication Facility, University of Michigan, Ann Arbor, MI

NNIN REU Principal Investigator: Prof. Rebecca L. Peterson, Electrical Engineering and Computer Science, University of Michigan

NNIN REU Mentor: Bradley Frost, Electrical Engineering and Computer Science, University of Michigan

Contact: jam6451@psu.edu, blpeters@umich.edu, bfrost@umich.edu

Introduction:

In order to vertically integrate heterogeneous electrical devices, compatible processes for interlayer dielectrics and metal interconnects are needed. The focus of this project was to study silicon dioxide (SiO_2) as an interlayer dielectric for heterointegration of two process technologies. The first step of this project was to develop and characterize a deposition process for high quality plasma enhanced chemical vapor deposition (PECVD) SiO_2 film by fabricating capacitors and testing film electrical characteristics. Once the dielectric was assessed to be viable, via etch hole and metal interconnect technologies were developed and characterized. Test structures were made to verify the electrical connection between the top contact of the bottom device and the bottom electrode of the top device. These test samples were followed by fabrication of the heterogeneously integrated devices. The ability to reliably integrate heterogeneous devices will enable new applications.

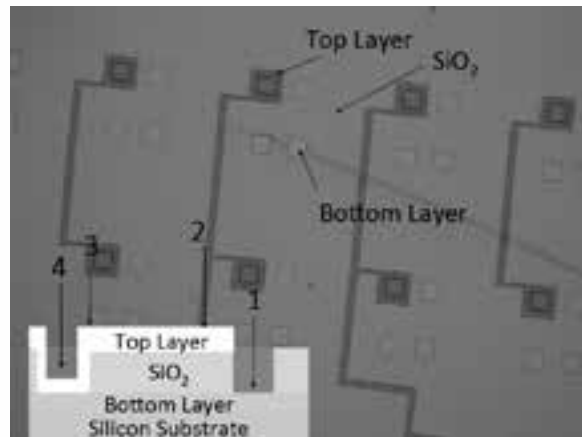


Figure 1: Structures for testing side wall coating of top metal. Numbers on the inset cross-section indicate test probe points for current-voltage measurements of Figure 3.

Experimental Procedure:

First metal-insulator-metal (MIM) capacitors were fabricated to identify a suitable dielectric film and to develop a deposition technique that would have a limited effect on previously fabricated devices existing on the substrate. Using PECVD, four different films were deposited on four 100 mm silicon wafers. Two were deposited at 200°C with thicknesses of 200 nm and 500 nm. These thicknesses were also deposited at 380°C. Tungsten was deposited using the LAB 18-02 PVD sputter tool and a shadow mask to form the top capacitor plates. Capacitance-voltage (C-V) and current-voltage (I-V) measurements were taken to determine film properties.

Once the 380°C film was determined to be a suitable dielectric, the etch rate of the film was characterized. The LAM 9400 was used for reactive ion etching (RIE) of SiO_2 with a power of 500W and gas flows of 8 sccm of SF_6 , 50 sccm of C_4F_8 , 50 sccm of He, and 50 sccm of Ar.

Next, test samples were fabricated to test the metal interconnects. A 100 nm film of aluminum (Al) was deposited on glass substrates followed by deposition of 1 μm SiO_2 . The SiO_2 was etched to create vias to the Al layer. These etch holes were covered with top metal pads as shown in Figure 1. I-V measurements were performed to determine the resistance of the metal interconnect. Finally, the optimized SiO_2 film was used as a passivation layer between two sets of transistors.

Results:

From the C-V data measured on the MIM capacitors, the experimental dielectric constants of the SiO_2 films were calculated. Its value for the 380°C film was very close to the ideal value of 3.9 [1]. This indicated that the film was dense and of a fairly high quality. I-V measurements of leakage current

were also taken, and are shown in Figure 2. The 380°C film maintained a low leakage current throughout the sweep, indicating its functionality as an insulator, while the 200°C film had significantly higher leakage current. While the 200°C oxide would be preferred for low temperature processing, the low leakage of the 380°C film makes it a better choice for heterointegration [2].

As shown in Figure 3, the resistance present between the metal pad and the side of the etch hole was approximately 23.3Ω. The resistance between the top metal pad and the bottom of the etch hole was 87.9Ω — meaning that the resistance of the side wall was about 65Ω. This large increase in resistance was due to the method used to cover the side walls of the etch holes. The sputtered metal was thin relative to the dielectric layer and thus only a very thin coating was present on the side walls.

The resistance between the top metal pad and the bottom aluminum surface was measured to be 117Ω. Thus the resistance added by the contact between the two metals was only about 20Ω. This indicates both that there was a good connection between the two metals and that there was no SiO₂ at the bottom of the etch holes. Both of these are important requirements for heterointegration of two devices.

Using the SiO₂ passivation layer, two layers of functioning transistors were fabricated. Devices in the first layer maintained their functionality even after top device fabrication, and the top devices displayed switching behavior. Figure 4 displays the results of I-V sweeps on both a bottom and a top layer transistor.

Conclusion and Future Work:

This experiment showed that SiO₂ is a suitable interlayer dielectric for the integration of two process technologies. A plasma etch was used to create openings in the SiO₂ down to the metal interconnect of the bottom device. Test samples showed that a thin metal layer could establish a reliable electrical connection through these etch holes to provide suitable vias for integrating top devices. Future work could be done to further improve the sidewall coverage and reduce via resistance. Two layers of functioning transistors were fabricated using a SiO₂ interlayer dielectric.

Acknowledgements:

I would like to thank National Science Foundation and the National Nanotechnology Infrastructure Network Research Experience for Undergraduates Program for providing the funding for this research opportunity. I would also like to thank the Lurie Nanofabrication Facility and its staff for their support. Finally I would like to thank my advisor Dr. Rebecca L. Peterson, my mentor Mr. Brad Frost, and the rest of the Peterson Lab group for their help this summer.

References:

- [1] Robertson, J. High Dielectric Constant Oxides. *Eur. Phys. J. Appl. Phys.*, 2004, (28), 265-291.
- [2] Ko, C.T., and Chen, K.N. Low Temperature Bonding Technology for 3D Integration. *Microelectronics Reliability*, 2012, (52), 302-311.

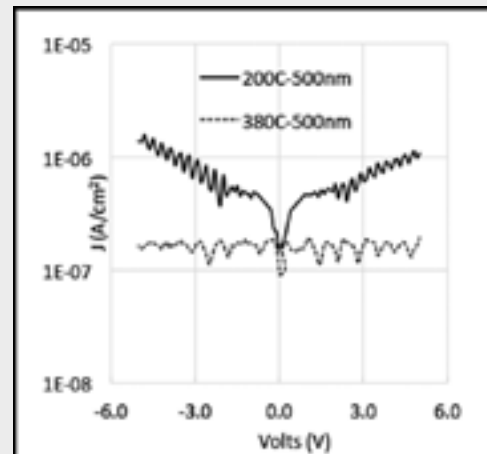


Figure 2: Average leakage current vs. voltage of 0.003 cm² SiO₂ MIM capacitors.

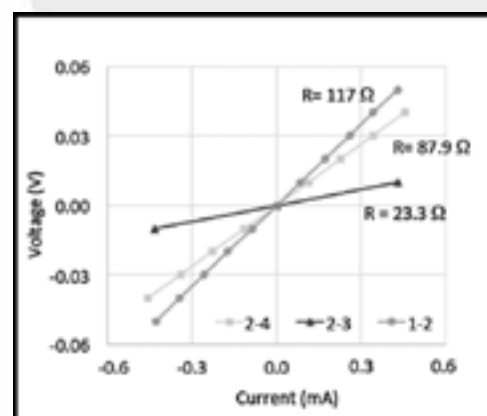


Figure 3: Resistance of metal interconnect test structures used to determine the quality of the metal vias.

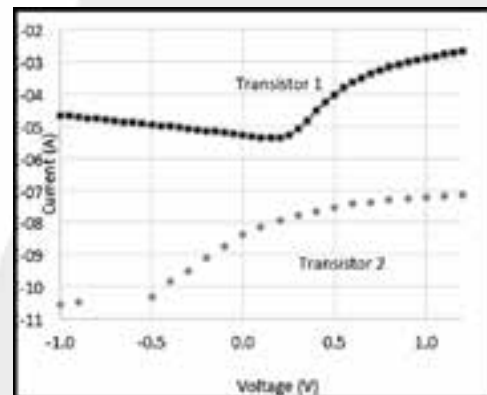


Figure 4: Measured drain current vs. gate voltage for one top layer and one bottom layer transistor. Both devices show field-effect behavior, indicating the successful heterointegration.

Aluminum Oxide for Surface Passivation in Photovoltaics

Tara Nietzold

Materials Science Engineering, Rutgers University

NNIN REU Site: ASU NanoFab, Arizona State University, Tempe, AZ

NNIN REU Principal Investigator: Mariana Bertoni, Electrical Engineering, Arizona State University

NNIN REU Mentor: Simone Bernardini, Materials Science Engineering, Arizona State University

Contact: tara.nietzold@rutgers.edu, bertoni@asu.edu, simone.bernardini@asu.edu

Abstract:

In order to study the influence of temperature and carrier injection on the surface passivation quality of p- and n-type silicon substrates, aluminum oxide thin films were deposited after cleaning as the surface passivation layer using atomic layer deposition. The minority carrier lifetime in each instance was then measured using a photoconductance lifetime tester with a variable temperature stage, both before and after annealing the samples. The results show a relationship between the increase in temperature and the increase in lifetime.

Introduction:

Conversion efficiency within silicon solar cells is limited by recombination at the surface and recombination within the bulk defects, which together limit the amount of effective carriers in the cell and therefore the current and voltage output. Reducing surface recombination is especially important as wafers become thinner in order to reduce production costs. As the thickness decreases, the surface area to volume ratio greatly increases, and surface recombination becomes a leading limiting factor in efficiency.

The equation for effective lifetime is given by Equation 1, in which the first three terms on the right of the equation represent recombination within the bulk of the material. The last term represents the effect of the surface, where $S_{front/back}$ is defined as the surface recombination velocity (SRV) in cm/s and W is the wafer thickness. As thickness decreases, this last term becomes larger and to counteract this, the SRV must be increased through surface passivation.

Experimental Procedure:

To start, 2-inch as-cut silicon wafers were cleaned using a piranha solution (sulfuric acid + hydrogen peroxide) followed by a saw-damage removal etch—both acid and alkaline chemistries were tried. The acid-based solution was a mixture of hydrofluoric acid, nitric acid, and acetic acid, and the alkaline-based solution was potassium hydroxide. Afterwards, RCA-b was used to remove any inorganic or metal contaminants on the surface. Finally, a hydrofluoric acid solution (BOE), was used to conclude the process. A BOE dip was repeated before any deposition was done in order to remove any surface oxides that may have formed.

After cleaning, atomic layer deposition (ALD) was performed using trimethyl aluminum as a precursor. This technique

$$\frac{1}{\tau_{eff}} = \frac{1}{\tau_{Auger}} + \frac{1}{\tau_{Rad}} + \frac{1}{\tau_{SRH}} + \frac{S_{front/back}}{W}$$

Eq (1)

allowed for the controlled and conformal deposition of single monolayers on the surface of the silicon wafer. After depositing approximately 30 nm of aluminum oxide on both sides, the samples were annealed in a box furnace with a nitrogen atmosphere for 30 minutes at 425°C [1]. Minority carrier lifetime was measured by photoconductance decay using a WCT-120TS lifetime tester over a temperature range of 50°C to 230°C and an injection level 1×10^{14} to 1×10^{17} cm $^{-3}$.

Results and Conclusions:

Lifetime measurements were performed for both p-type and n-type Si wafers. Figures 1 and 2 show the variation of lifetime (y-axis) with injection level (x-axis) and temperature. In both graphs, the lifetime is seen to increase parabolically as minority carrier concentration increases, with maximums around 10^{15} cm $^{-3}$. Lifetime is also seen to increase with temperature despite the wafer type involved. These results are consistent with previous observations from other authors [2-4]. The trend with increasing temperature is expected since the additional energy imparted to the samples in the form of heat helps to fill empty levels in the band gap, therefore reducing the amount of possible recombination.

The n-type wafer was analyzed in further detail, with lifetime values reaching as high as 500 μ s. The relationship between the inverse of effective lifetime and the inverse of wafer thickness taken for various wafer thicknesses at 200°C is shown in Figure 3. As depicted by Eq (1), this plot puts in evidence the

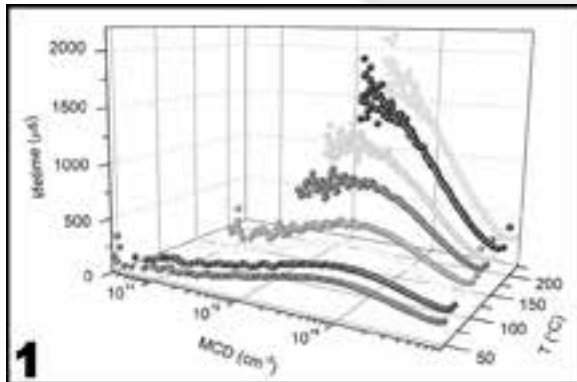


Figure 1: Lifetime versus temperature and injection level for a p-type c-Si wafer with an ALD Al_2O_3 layer. (See full color version on page xxxvi.)

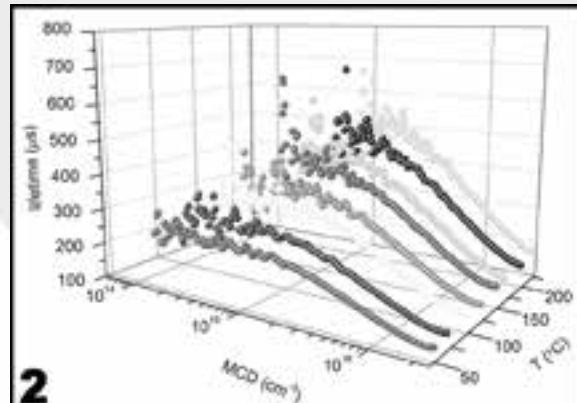


Figure 2: Lifetime versus temperature and injection level for an n-type c-Si wafer with an ALD Al_2O_3 layer. (See full color version on page xxxvi.)

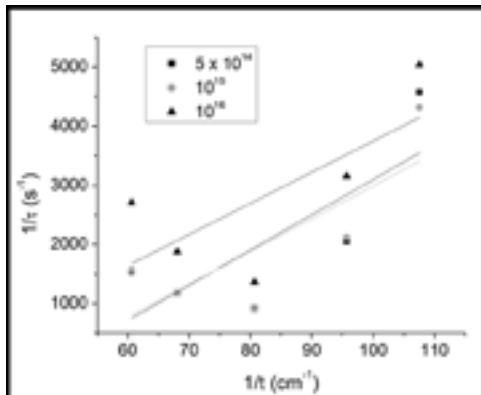


Figure 3: Inverse of lifetime versus inverse of wafer thickness measured at 200°C for n-type c-Si deposited with Al_2O_3 as wafer thickness was reduced. The slope represents the SRV.

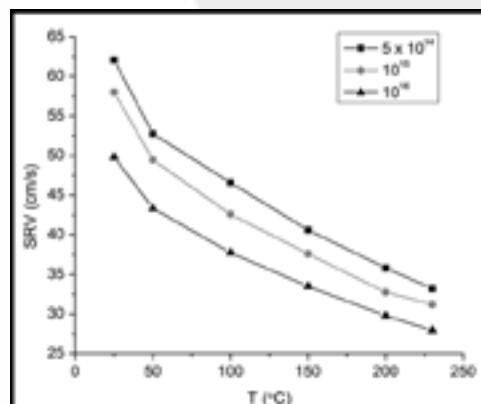


Figure 4: SRV versus temperature for n-type c-Si deposited with Al_2O_3 .

SRV achieved with this passivation layer. The temperature was then plotted against the various SRV, found for 10° intervals over the measured temperature range, shown in Figure 4. From this graph, the dependence of SRV with temperature is clear and will be the base for future modeling efforts.

Future Work:

Initially, the type of passivation (chemical or field effect) must be studied. These results will then be used to develop a model for the relationship between SRV and temperature for various passivation layers (Al_2O_3 , SiN_x , SiO_2). This will enable the subtraction of the surface effects from the effective lifetime, which ultimately will help characterize the high quality bulk silicon underneath.

Acknowledgements:

I would like to express my gratitude to my PI, Mariana Bertoni, my mentor, Simone Bernardini, as well as Laura Ding, for

all their assistance and guidance. I would also like to thank everyone at the Center for Solid State Electronics Research and MacroTechnology Works at Arizona State University for all their resources and help, as well as the NSF for making the NNIN REU Program possible.

References:

- [1] Hoex, B., Gielis, J., Van de Sanden, M., and Kessels, W. (2008). On the c-Si surface passivation mechanism by the negative-charge-dielectric Al_2O_3 . *Journal of Applied Physics*, 104 (113703), 1-7.
- [2] B. Hoex, S. B. S. Heil, E. Langereis, M. C. M. van de Sanden, and W. M. M. Kessels (2006). *APL*, 89, 042112.
- [3] G. Dingemans, R. Seguin, P. Engelhart, M. C. M. van de Sanden, and W. M. M. Kessels (2010) *Phys. Status Solidi RRL* 4, No. 1-2, 10-12.
- [4] J. Schmidt, A. Merkle, R. Brendel, B. Hoex, M. C. M. van de Sanden, and W. M. M. Kessels (2008) *Prog. Photovolt: Res. Appl.*, 16, 461-466.

Fabrication of Five-Terminal Laterally-Actuated Nano-Electro-Mechanical (NEM) Relays

Shanel Wu
Physics, Harvey Mudd College

NNIN REU Site: Stanford Nanofabrication Facility, Stanford University, Stanford, CA
NNIN REU Principal Investigator: Prof. H.-S. Philip Wong, Department of Electrical Engineering
NNIN REU Mentor: Dr. Ji Cao, Department of Electrical Engineering, Stanford University
Contact: swu@hmc.edu, jicao@stanford.edu, hspwong@stanford.edu

Abstract:

Nano-electro-mechanical (NEM) relays offer reliable alternative switches with low leakage current compared to MOSFETs. In a NEM relay, applying voltage to a gate electrode causes electrostatic force to mechanically actuate a beam, which makes contact between source and drain electrodes, allowing current to flow. One of the present drawbacks of NEM relays is that the pull-in voltage at which the switch actuates is extremely high (~20V). This project focused on a laterally-actuated (in the plane) cantilevered relay and investigated how parameters at different fabrication steps affected the relay's pull-in voltage. The body and electrodes of the relay were fabricated by first growing silicon dioxide on a silicon wafer, depositing polysilicon, and defining the physical features with electron-beam lithography. A layer of titanium nitride was then deposited and etched. Finally, the beam was released from the surface of the wafer by etching with hydrofluoric acid. Parameters such as deposition temperatures and etch times were varied in an effort to produce a durable, lower pull-in voltage relay. Lower pull-in voltages in NEM relays would be a step towards integrating the devices into ultra-low-power applications such as computing.

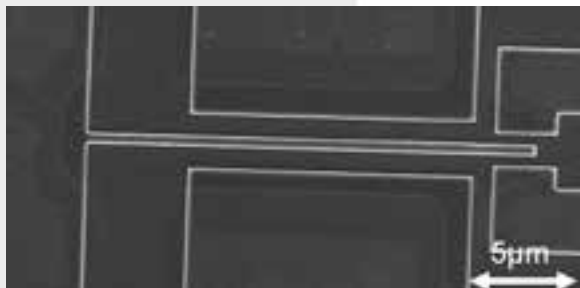


Figure 1: SEM image of a completed NEM relay. At the left is the device source, to which the beam is attached. Gates are in the middle top and bottom, and drains are at the right. Beam-to-gate gaps are 1000 nm and beam-to-drain gaps are 500 nm.

Introduction:

The most common form of logic switch today is metal-oxide-semiconductor field-effect transistors (MOSFETs). As MOSFETs are scaled down for faster computing, leakage current will flow through the device even in its “off” state. Nano-electro-mechanical (NEM) relays promise no leakage current and faster switching behavior than MOSFETs [1]. Similar to MOSFETs, a basic NEM relay requires three terminals: source, drain, and gate. Applying a sufficiently high pull-in voltage to the gate generates enough electrostatic force to move a beam, connected to the source, to contact the drain,

allowing current to flow through the device. One of the present drawbacks of NEM relays is an extremely high pull-in voltage, approximately 20V in literature [2].

In this project, we demonstrated a five-terminal NEM relay with two drains and two gates. A finished device is shown in Figure 1. The laterally-actuated beam moved in the plane of the wafer on which the device was fabricated. The goal of this project was to investigate the effects of varying certain processing steps to create a device with a lower pull-in voltage and other properties favorable for ultra-low-power application.

Procedure:

Fabrication began by growing 400 nm of silicon dioxide (SiO_2) and depositing 400 nm of polycrystalline silicon (polysilicon). The polysilicon was then patterned using electron-beam lithography (EBL) and etched anisotropically with plasma. Next, 20 nm of titanium nitride (TiN) was deposited using atomic layer deposition (ALD). The TiN was patterned with another round of EBL and etched anisotropically with plasma. This anisotropic etch removed TiN from horizontal surfaces, exposing the underlying SiO_2 , but left TiN on vertical sidewalls intact. Because we needed to determine a suitable etch recipe for TiN, we etched four separate samples for 60s, 90s, 120s, and 150s. Finally, the device was finished by etching the now-exposed oxide using 20:1 buffered oxide etch

(BOE) and drying the samples in a critical point dryer, releasing the beam. Finished devices were tested using a three-point probe measurement, with source voltage grounded, drain voltage held at 0.5V, and gate voltage varied between 0 and 25V. Devices were also imaged under a scanning electron microscope (SEM) after several fabrication steps. After examining and testing the four samples, an additional sample was prepared, with TiN etched for 150s.

Results and Discussion:

From SEM images, the 60s TiN etching samples seemed best etched, as shown in Figure 1. In contrast, the 90s, 120s, and 150s TiN etching samples (Figure 2) had unetched TiN remaining between the gates and drains. As seen in the tilted SEM image in Figure 3, underetching was apparent from tilted SEM images, but it was unclear whether the beams were fully suspended during HF etching. Measurements on the samples with 60s TiN etching revealed that current would always flow through the device. Our conclusion was that 60s was too short of an etch time, leaving a conductive layer of TiN all over the device. Measurements on the samples with 150s TiN etching were also inconclusive, as the leftover TiN between the gates and drains created a short circuit that left us unable to measure the current flowing between the source and drain. We concluded that the samples with 150s, 120s, and 90s TiN etching were unsuccessful due to problems in the TiN etching. Oddly, the second 150s TiN etch sample did not have leftover TiN for reasons yet undetermined.

Future Work:

Further investigation is needed to improve the TiN etching. Once working samples have been completed, we then need to measure pull-in voltages using the three-point probe measurement described above. Moving forward, we will further explore fabrication techniques to further decrease the pull-in voltage of these laterally-actuated NEM relays, such as varying device geometries (e.g., gaps between features, beam shape) and integrating with other technologies.

References:

- [1] R. Parsa, "Nanoelectromechanical Relays for Low Power Applications," Stanford University, dissertation, May 2011.
- [2] R. Parsa, W. S. Lee, M. Shavezipur, J. Provine, R. Maboudian, S. Mitra, H.-S. P. Wong, and R.T. Howe, "Laterally Actuated Platinum-Coated Polysilicon NEM Relays," in *Journal of MEMS*, Vol. 22, No. 3, June 2013.

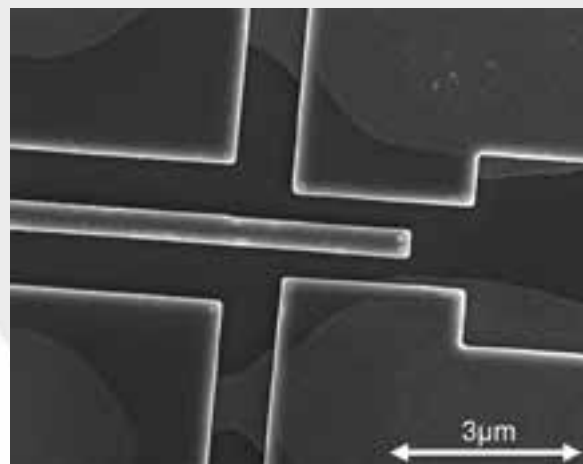


Figure 2: SEM image of a 120s TiN etching sample. TiN is visible in the lighter regions and on the reflective sidewalls. TiN remains on the surface between drains and gates.

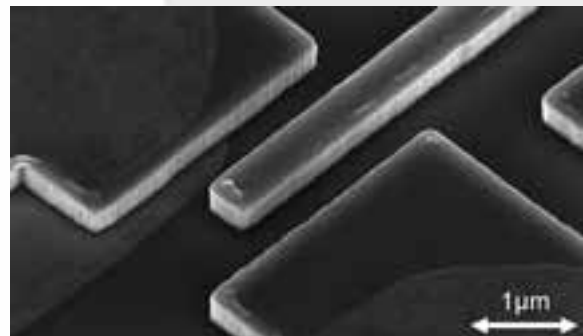


Figure 3: SEM of a 90s TiN etching sample, tilted 38°. Dark shadows under the features indicate some etching by HF.

E
L
E
C

Applications of Atomic Layer Deposition of Tin Oxide

Sunny Aggarwal

Department of Chemical Engineering, City College of New York (CUNY)

NNIN REU Site: Penn State Nanofabrication Laboratory, The Pennsylvania State University, University Park, PA

NNIN REU Principal Investigator: Dr. Suzanne Mohney, Materials Science and Engineering, The Pennsylvania State University

NNIN REU Mentors: Haila Mohammed Aldosari and Shih-Ying Yu, MSE, The Pennsylvania State University

Contact: sunnygs94@yahoo.com, mohney@ems.psu.edu

Abstract:

Atomic layer deposition (ALD) produces high-quality, low-porosity conformal nanostructures. Tin dioxide, SnO_2 , is deposited within the void space of a face-centered cubic (FCC) silica opal lattice. SnO_2 is a viable metal oxide for the formation of inverse opals due to its stability when the silica spheres are etched away. Furthermore, we explore its use as an effective interfacial layer for ohmic contacts between a metal and semiconductor. SnO_2 is deposited by ALD using tetrakis (dimethyl amino) tin and water, then 30 nm sized opals are infiltrated with varying pulse lengths of these precursors in order to attain the most depth and complete infiltration. The resulting infiltrated SnO_2 opals are characterized through field emission scanning electron microscopy (FE-SEM) and the 4-point probe to explore its filling efficiency and resistivity differences. In this work, we fill opals that are smaller than those that have been previously studied.

Introduction:

Atomic layer deposition (ALD) is a modified chemical vapor deposition technique that provides conformal, uniform monolayer-by-monolayer growth. Such advantages allow for ALD to provide opportunities in optoelectronics [1] and microelectronics. An ALD cycle follows this process: dose with first precursor, tetrakis (dimethyl amino) tin (TDMASn); purge with N_2 gas to remove any excess reactants; dose with second precursor, water (H_2O); and finally purge the remaining reactants. In this study, ALD is used for infiltration of nano-opals and electrical contacts. Opals, 30 nm in size (smaller than those typically used for self-assembled photonic crystals) [2], were fabricated using the vertical deposition method. Self-assembly of these colloids created a face-centered cubic (FCC) lattice. Its 26% void space is infiltrated with tin oxide, SnO_2 , through ALD as shown by the half reactions discussed previously by Mullings, et al. [3].

SnO_2 is selected due to ability to make good electrical contacts. It is a wide band gap semiconductor that can have a high carrier concentration and that shows strong resistance towards a variety of etching agents, including HF, which is the sole reagent that the silica templates are etched away with. Also, aggressive scaling of devices calls for low contact resistance. The use of SnO_2 in contacts between a metal and a semiconductor are being explored. Such materials lower the effective Schottky barrier height, by relieving Fermi level pinning and lowering of the conduction band offset (CBO) [4].

Experimental Procedure:

Fabrication of Opals. Nano silica colloids are dispersed in an open vial solution. Inside it, silicon substrates are placed in at a diagonal of 45°. The solution is then evaporated in a drying oven for four days, slowly, allowing for the opals to self-assemble in the FCC lattice.

Preparation of Samples. One of the opal substrates was cleaved and degreased. Degreasing included the standard 3-step procedure: sonication in acetone for five minutes, followed by sonication in isopropanol for five minutes, and a final sonication in deionized water for five minutes. The sample was then blown dry with N_2 gas for 1-2 seconds and placed in a sterile sample holder.

ALD Recipes. The prepared samples were placed in an ALD reactor (Cambridge Savannah) set at these control conditions:

- Temperature of 150°C.
- N_2 purge flow rate of 20 sccm.

Conformal deposition of SnO_2 thin films utilized saturated pulse times of 0.030 s for TDMASn and 0.015 s for H_2O . The purge times were 30 s.

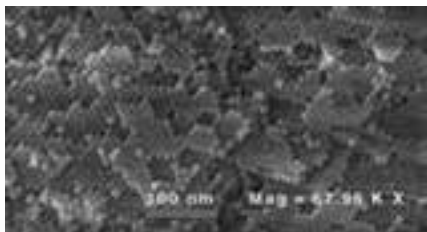


Figure 1: Empty opals; no dose of SnO_2

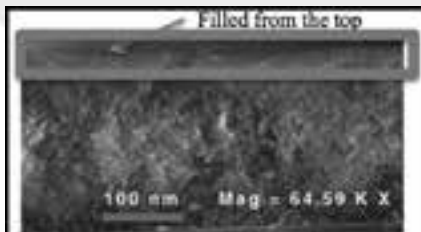


Figure 2: Infiltrated SnO_2 opal at a dose of 0.030 s of TDMASn and 0.015 s of H_2O .

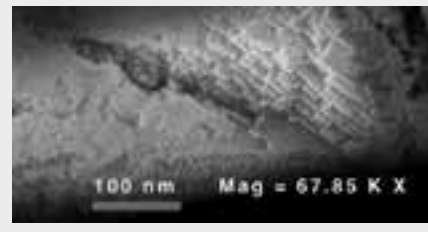


Figure 3: Infiltrated SnO_2 opal at a dose of 0.090 s of TDMASn and 0.045 s of H_2O .

Results and Conclusions:

Ellipsometry revealed that the growth rate of these films was $\sim 0.5 \text{ \AA}/\text{cycle}$. Since 5-6 nm of holes are to be filled from these 30 nm sized opals, 125 ALD cycles was used.

Figure 1 shows a FESEM image of the empty silica opal lattice, while Figure 2 demonstrates a partial filling of the opal from the saturated pulse times of the precursors. Hence, tripling the pulse times of each precursor respectively yields an almost complete infiltration as shown in Figure 3.

Further characterization of the opals done by the Keithley 2400 source-measure unit yields a variety of film sheet resistances, as shown in Figure 4.

Portrayed through the FESEM and data from the resistivity measurements, SnO_2 is shown to have deeper and a more complete infiltration into the opals as the dose increases. Such nano-scaled inverse opals can have applications in lithium ion batteries and gas sensors.

Future Works:

The silica template must be etched using ion milling (primarily to expose) and then a dilute aqueous HF solution to attain the SnO_2 inverse opals. Further characterization of these samples, such as by transmission electron microscopy, and measurement of their electronic properties can be further performed, and their applicability for batteries and sensors can be explored.

Acknowledgements:

The author thanks the support of Dr. Suzanne Mohney's lab group along with the nanofabrication staff in the Materials Research Institute of Pennsylvania State University and National Science Foundation for funding the National Nanotechnology Infrastructure Network Research Experience for Undergraduates (NNIN REU) Program.

Empty opals	
Average Voltage Measured (mV)	0.33
Current Used (nA)	5.0
Calculated Sheet Resistance (Ω)	66,000
SnO_2 Opals with 60 cycles at a dose of 0.030 s of TDMASn and 0.015 s of H_2O	
Average Voltage Measured (mV)	0.11
Current Used (nA)	5.0
Calculated Sheet Resistance (Ω)	96,100
SnO_2 on regular Si wafer at 150°C	
Average Voltage Measured (mV)	0.18
Current Used (nA)	1.0
Calculated Sheet Resistance (Ω)	829,000

Figure 4: Resistance Measurements.

References:

- [1] Niinistö, L., Nieminen, M., Päiväsaari, J., Niinistö, J., Putkonen, M. and Nieminen, M. "Advanced electronic and optoelectronic materials by Atomic Layer Deposition: An overview with special emphasis on recent progress in processing of high-k dielectrics and other oxide materials." *physics status solidi (a)* 201.7 (2004): 1443-1452.
- [2] Nishijima, Y., Ueno, K., Juodkazis, S., Mizeikis, V., Misawa, H., Tanimura, T., and Maeda, K. "Inverse silica opal photonic crystals for optical sensing applications." *Optics Express* 15.20 (2007): 12979-12988.
- [3] Mullings, Marja N. and Hägglund, Carl and Bent, Stacey F. Tin oxide atomic layer deposition from tetrakis (dimethyl amino) tin and water. *Journal of Vacuum Science & Technology A*, 31, 061503 (2013).
- [4] Yuan, Z., Nainani, A., Sun, Y., Lin, J. Y. J., Pianetta, P., and Saraswat, K. C. "Schottky barrier height reduction for metal/n-GaSb contact by inserting TiO_2 interfacial layer with low tunneling resistance." *Applied Physics Letters* 98.17 (2011): 172106.

Bimetallic Nanocrystals and Their Optical Properties

Nnenna E. Dieke
Chemistry, Agnes Scott College

NNIN REU Site: Institute for Electronics & Nanotechnology, Georgia Institute of Technology, Atlanta, GA

NNIN REU Principal Investigator: Dr. Dong Qin, School of Materials Science and Engineering, Georgia Institute of Technology

NNIN REU Mentor: Yin Yang, School of Materials Science and Engineering, Georgia Institute of Technology

Contact: ndieke@agnesscott.edu, dong.qin@mse.gatech.edu, yin.yang@mse.gatech.edu

Abstract and Introduction:

Silver nanocubes exhibit an excellent property known as localized surface plasmon resonance (LSPR) which depends heavily on the composition, size, and geometry of the nanoparticles. LSPR is useful in applications such as surface enhanced Raman scattering (SERS), making silver nanocubes an ideal material for SERS. Although silver nanocubes favor SER, it shows limited catalytic activity towards chemical reactions.

The objective of this project is to improve the catalytic behavior of silver (Ag) nanocubes, but still retain its SERS properties. This can be done by depositing a known catalyst, in this case palladium (Pd), onto the cube in order to create a Ag-Pd bimetallic nanostructure through a widely known process called galvanic replacement reaction. Galvanic replacement reaction destroys the SERS property because one Pd atom deposits onto the cube at the expense of two Ag atoms [1]. In order to combat this, galvanic is done in the presence of reducing agents that will reduce Ag⁺ back to Ag atoms to be co-deposited alongside with the palladium which will help in retaining the SERS property.

Through etching the Ag-Pd bimetallic structures with hydrogen peroxide (H₂O₂), Ag-Pd hollow nanoboxes can be created. These hollow nanostructures are more stable than Ag nanocubes, making them more ideal for SERS. The enlarged surface area should also be beneficial to their catalytic activities.

Experimental Procedure:

The way in which the Ag-Pd bimetallic nanostructure was generated was through galvanic replacement reaction alongside reducing agents, NaOH and ascorbic acid (AA). The palladium precursor, disodium tetrachloropalladate (Na₂PdCl₄), was titrated at a rate of 0.02 mL/min into a 20 mL vial that contained 1 mM of 29K polyvinyl pyrrolidone (PVP), which acted as a capping agent, NaOH, ascorbic acid, and silver nanocubes, Figure 1. The amount of NaOH introduced into the solution assisted in tuning the pH of the solution.

Once different volumes of the palladium precursor has been titrated into the mixture a ultraviolet-visible (UV-Vis) spectrum was collected to monitor the change in morphology over time, then the samples were washed three times before being prepared for TEM imaging.

Results and Discussion:

Experiments were conducted under basic and acidic conditions as well as a control experiment in which no NaOH was added to the solution. In the control experiment, the UV-Vis showed a significant shift indicating that the morphology of the cubes were changing and galvanic was taking place, Figure 1A. After taking TEM images, Figure 2, holes in the cubes were observed which also confirmed that galvanic replacement reaction did in fact take place, and a layer of palladium is present.

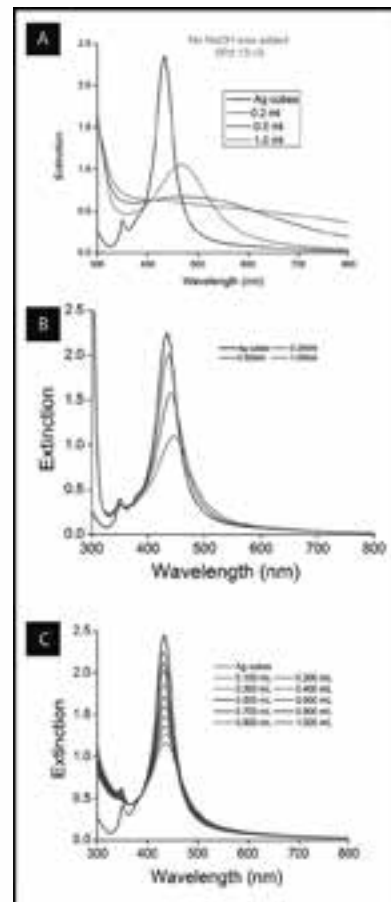


Figure 1: UV-Vis spectra of (A) the control experiment in which no NaOH was added, (B) experiment done under acidic conditions in which 200 μ L of 200 mM NaOH and 0.5 mL of 100 mM ascorbic acid were used, and (C) experiment done under basic conditions in which 90 μ L of 200 mM NaOH and 0.5 mL of 100 mM ascorbic acid were used. (See full color version on page xxxvi.)

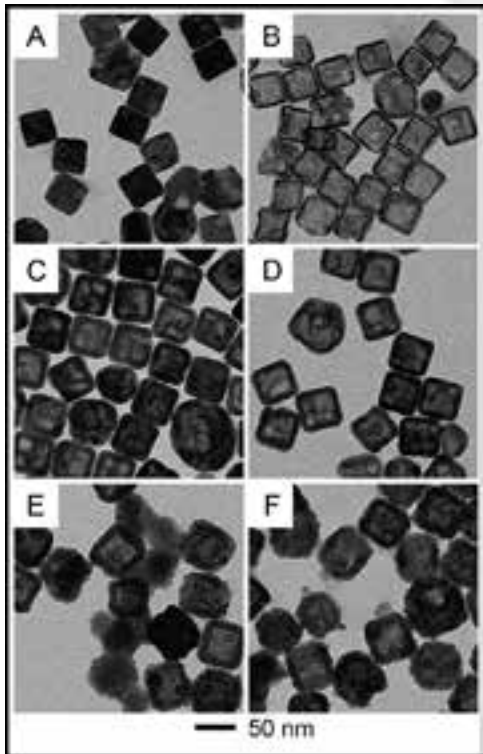


Figure 2: TEM image of control experiment where no reducing agent was added. A, C, and E are images before etching; and B, D, and F are images taken after etching with an excess amount of H_2O_2 solution.

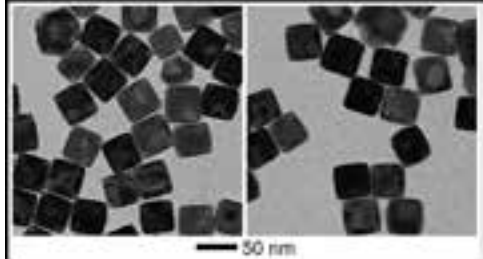


Figure 3: TEM image of sample when 200 μL of NaOH and 0.5 mL of 100 mM AA are used.

The experiment was also ran under acidic conditions with a pH of 4.83. In these samples 200 μL of 200 mM NaOH and 0.5 mL of 100 mM AA were used to tune the pH. The UV-Vis showed a shift that is characteristic of galvanic, but the shift was not as severe as in the control experiment in which no NaOH was present (see Figure 1B). The TEM images, Figure 3, showed slight holes in the cube, but in comparison with the control these holes were not as intense.

Lastly, under basic conditions with a pH of 10.86, it was noted that the UV-Vis did not have much of a shift indicating the inhibition of galvanic, Figure 1C. After taking TEM images, Figure 4, it was confirmed that the cube somewhat retained their shape, but after etching the sample with a 3% solution of H_2O_2 in order to test the quality of the cubes it was shown that the cubes were unstable, and little to no cubes were left afterwards.

The occurrence of self-nucleation was observed in Figure 1, image E. This was due to the high amount of Na_2PdCl_4 that was being injecting into the solution. Some of the precursor began to form clusters instead of depositing onto the cube which is something that negatively impacted the experiment.

Future Work:

These preliminary results can assist in furthering the study of the creation of Ag/Pd bimetallic nanostructure that possesses both excellent SERS and catalytic properties. In the future, the conditions could continue to be manipulated to determine if it is indeed possible to create these stable structures that can last under H_2O_2 etching.

Acknowledgements:

I would like to thank Dr. Dong Qin and my mentor Yin Yang for the opportunity of working in the Qin Lab this summer, Georgia Tech NNIN REU site coordinator Leslie O'Neill, as well as Joyce Allen and Dr. Nancy Healy. I would also like to thank the NSF and NNIN REU Program for their support.

References:

[1] “Galvanic replacement-free deposition of Au on Ag for core-shell nanocubes with enhanced chemical stability and SERS activity,” Y. Yang, J. Liu, Z. Fu, and D. Qin; JACS, 136, 8153-8156, (2014).

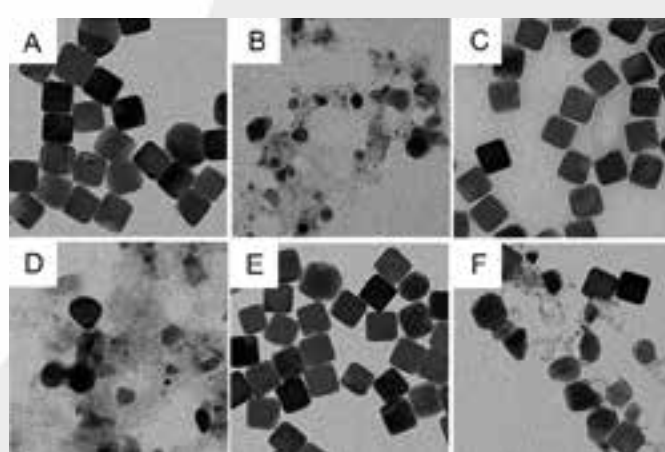


Figure 4: TEM image of product when 90 μL of NaOH and 0.5 mL of 10 mM AA is used. A, C, and E are images before etching; and B, D, and F are images taken after etching with an excess amount of H_2O_2 solution.

Selective Area Atomic Layer Deposition: Developing Techniques that will Enable Single-nm Technologies

Alicia M. Elliott

Engineering Science, Stony Brook University

NNIN REU Site: Cornell NanoScale Science & Technology Facility, Cornell University, Ithaca, NY

NNIN REU Principal Investigator: Prof. James R. Engstrom, School of Chemical and Biomolecular Engineering, Cornell University

NNIN REU Mentor: Wenyu Zhang, School of Chemical and Biomolecular Engineering, Cornell University

Contact: alicia.elliott@stonybrook.edu, jre7@cornell.edu, wz89@cornell.edu

Abstract:

Atomic layer deposition (ALD) is a chemical vapor deposition process with self-limiting growth, providing atomic level, or “digital,” control of thickness. Selective deposition extends this control to three dimensions, so 3D structures can be created without lithography. To deposit selectively, growth is promoted on one surface and prevented on another by varying deposition conditions. This project probes the intrinsic reactivity of two precursors: tetrakis-(ethylmethylamino)hafnium (TEMAH; $\text{Hf}(\text{N}(\text{CH}_3)(\text{C}_2\text{H}_5)_4$) and tris(dimethylamino)silane (3DMAS; $\text{SiH}(\text{N}(\text{CH}_3)_2)_3$). Nucleation of each precursor on a metal and dielectric substrate was studied. Saturation curves of film deposited vs. dose time were generated for TEMAH by exposing the substrates to the first half of an ALD cycle. For 3DMAS, thicker films were deposited and the growth rate was estimated using *ex situ* ellipsometry. *Ex situ* x-ray photoelectron spectroscopy (XPS) was used to determine amount of precursor deposited.

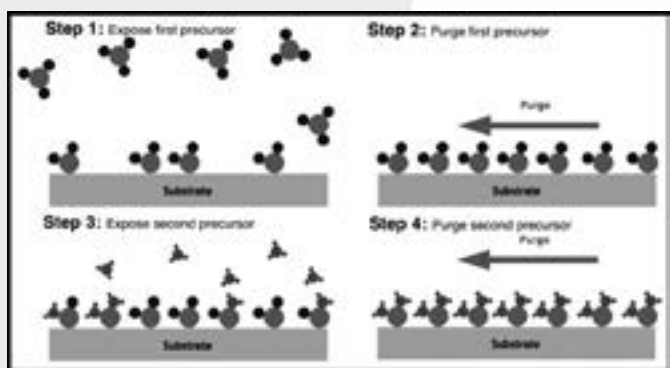


Figure 1: Schematic of the four-step ALD cycle.

Introduction:

Atomic layer deposition (ALD) is a deposition technique with a four step, self-limiting growth process (see Figure 1). Self-limiting growth allows digital control of thickness, creating highly conformal films on high aspect ratio structures.

Semiconductor devices have gone towards three dimensional (3D) features to increase speed and decrease power consumption (e.g., Intel’s tri-gate transistor). Selective deposition could be utilized to pattern in 3D using ALD. To achieve this, growth is promoted on one substrate (e.g., a dielectric) and prevented on another (e.g., a metal). If selectivity can be achieved using ALD, this precise control can be extended to three dimensions, creating 3D patterns without lithography.

As a first step to developing a process that is selective, we must first understand the intrinsic reactivity of the thin film precursor with substrates of interest.

The nucleation of each precursor on two substrates, a dielectric (SiO_2 or Al_2O_3) and a metal (Cu), must be studied to determine how to selectively prevent deposition. Precursor dose times and heater temperature should be considered. Dose times can be varied to determine when each substrate becomes saturated with the precursor.

Experimental Procedure:

Two precursors were studied: tetrakis-(ethylmethylamino)hafnium (TEMAH), the precursor for hafnia (HfO_2) films, and tris(dimethylamino)silane (3DMAS), the precursor for silica (SiO_2) films.

TEMAH was deposited onto copper (Cu) and chemical oxide (chemically grown SiO_2) substrates. Chemical oxide (SiO_2) was grown by twice exposing silicon substrates to two minutes of buffered oxide etch 6:1 and 15 minutes of Nano-Strip® heated to 70-80°C. Each sample was exposed to one half-cycle of thermal HfO_2 ALD at a heater temperature (T_s) of ~ 250°C, with the following precursor dose times: 0.0, 0.1, 0.2, 0.4, 0.7, 1.0, 2.0, 3.5, 5.0, and 7.0 seconds. Plasma SiO_2 ALD films were deposited at 200°C onto Cu and ALD-deposited alumina (Al_2O_3) substrates, varying the number of cycles as follows: 0, 10, 20, 50, and 100 cycles. The 3DMAS doses were also varied, with dose times of 0.0, 0.1, 1.0, and 4.0 seconds.

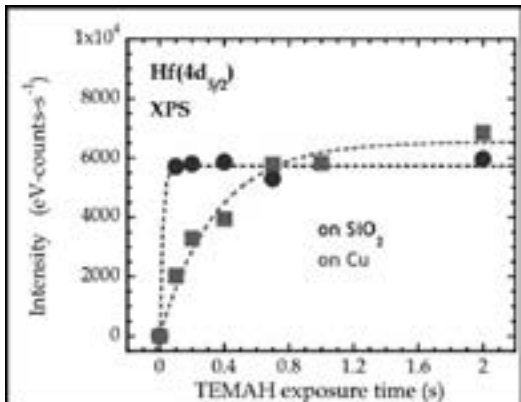


Figure 2: Integrated intensity of the Hf(4d_{5/2}) peak as a function of TEMAH dose time on SiO₂ and Cu.

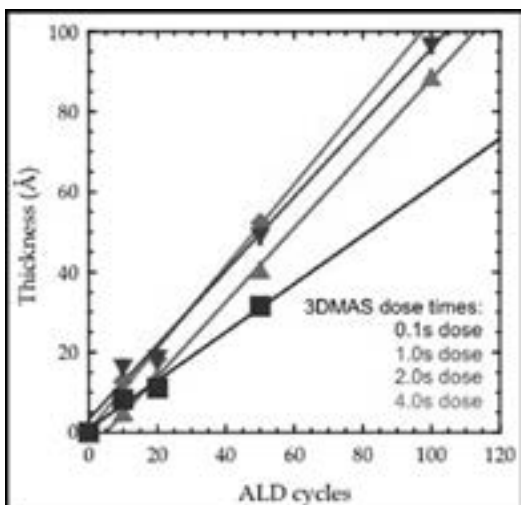


Figure 3: Estimated thicknesses of SiO₂ films (from SE) as a function of ALD cycles for four 3DMAS dose times.

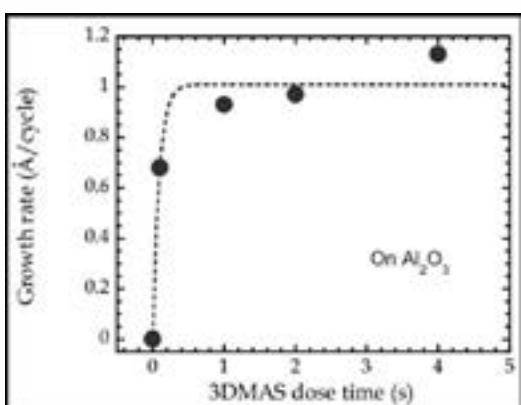


Figure 4: Estimated growth rate of SiO₂ ALD on Al₂O₃ (from SE) as a function of 3DMAS dose time.

Ex situ XPS and spectroscopic ellipsometry (SE) were used to determine how much precursor was deposited. SE was used to estimate film thicknesses for the SiO₂ ALD on Al₂O₃ and estimate growth rates. Saturation curves were generated from these analyses.

Results and Conclusions:

In Figure 2, we present the XPS integrated intensity for Hf(4d_{5/2}) against TEMAH dose time, generating a saturation curve for each substrate. These results showed that TEMAH saturated on SiO₂ substrates (~0.1s - 0.2s TEMAH dose time) much more quickly than on Cu substrates (~2s). This is most likely due to the higher concentration of hydroxyl (-OH) groups on SiO₂ surfaces, thus promoting better adsorption of the precursor on the SiO₂.

SiO₂ ALD is a plasma process (using 3DMAS and oxygen plasma), so doing half-cycle ALD like we did for Hf will not capture the important processes occurring in the oxygen plasma half-cycle. A series of thicker films were deposited for each 3DMAS dose time.

In Figure 3, we present the estimated SiO₂ thicknesses on Al₂O₃. Growth rates can be estimated using the slopes of the data points. The growth rate for 0.1s dose time is ~0.68 Å/cycle, while 1.0s, 2.0s, and 4.0s dose time growth rates ranged from ~0.93 to 1.13 Å/cycle (saturation).

A saturation curve was generated for alumina substrates from this data, as seen in Figure 4. This shows a similar shape to that for TEMAH on SiO₂. Because of the rougher substrate surface for Cu, SE cannot be used to estimate film thickness. XPS analysis will be performed and a saturation curve will be generated.

Acknowledgements:

I would like to thank the National Science Foundation for funding this work, and the NNIN REU Program and the CNF for organization. I would also like to thank Professor James R. Engstrom and Wenyu Zhang for their guidance, teaching, and reassurance. I also thank Melanie-Claire Mallison, Rob Illic, Vince Genova, and Meredith Metzler. Finally, thanks to all of the CNF staff.

Directed Assembly of Nanowires in AC Fields: Tuning Wire Design and Electrode Geometry to Observe Ordered Arrays

Robyn Emery

Biology, Northwest University

NNIN REU Site: Penn State Nanofabrication Laboratory, The Pennsylvania State University, University Park, PA

NNIN REU Principal Investigator: Prof. Christine D. Keating, Department of Chemistry, The Pennsylvania State University

NNIN REU Mentor: Sarah J. Boehm, Department of Chemistry, The Pennsylvania State University

Contact: robyn.emery13@northwestu.edu, keating@chem.psu.edu, sjb340@psu.edu

Introduction:

Nanowires form a fascinating topic of inquiry in modern research and offer material properties that are advantageous in fields such as next-generation electronics, solar cells, and optics [1]. Dense, ordered arrays of nanowires are needed to investigate potential advantages. In unregulated assembly, however, nanowires tend to become trapped in entropically unfavorable positions and orientations. This project explored the introduction of an applied current (AC) field on gold (Au) nanowires to form assemblies with observable and ultimately reproducible properties. Partially-etched nanowires were synthesized and assembled in lithographically-designed gold electrodes. Field strength was fine-tuned for specific wire designs, and the use of different electrode geometries created unique field conditions that visibly influenced resulting assemblies. Effectiveness of electrode geometries was also studied in experiments.

Wire Synthesis:

It was necessary to fabricate nanowires in large quantities while maintaining a relatively narrow size distribution. This was achieved using a porous alumina membrane that acted as a nanotemplate for the metallic wires. Multicomponent nanowires featuring segments of different metals were able to be prepared via electrodeposition into pores beginning bottom-upwards from a sacrificial silver base. Removal of both the membrane and base yielded approximately a billion monodisperse wires in solution, with a nominal diameter of 300 nm and length determined by deposition time.

The wire design chosen for experiments featured a 2 μ m gold (Au) segment and a 3 μ m etched segment (2Au-3E) (Figure 1). To achieve partially-etched nanowires, silver (Ag) metal was deposited on top of the gold segment.

A thin coating of amorphous silica retained wire shape, and selective etching of the silver segment left a hollow, solvent-filled segment in its place. Assemblies resulting from these wires were more ordered than wires featuring a longer Au segment, so experiments with the 2Au-3E wires were chosen for accurate analysis of lattice structures.

Electrode Synthesis:

Electrodes were designed featuring a central gap, micrometers in diameter, to accommodate the small wire size. Au electrodes were fabricated using standard photolithography techniques. After spinning positive photoresist onto 35 mm circular glass cover slip, projected light through a patterned mask exposed certain regions in the precise shape of electrodes. After removal of the reacted areas in a developing solution, a binding titanium (Ti) layer and a 50 nm Au layer were deposited via electron-beam evaporation. Lift-off in another developing solution removed all remaining photoresist to leave usable Au electrodes behind on the substrate surface. The two extended probes at the electrode base provided an attachment site for an external field generator.

Two types of electrodes were fabricated for assemblies (Figure 2). Bulb-stem electrodes featured alternating circular and



Figure 1: TEM of one of the 2Au-3E nanowires used in experiments.



Figure 2: The two electrode designs: bulb-stem (left) and interdigitated (right).



Figure 3: A 100 μm bulb region of the bulb-stem electrode during assembly.

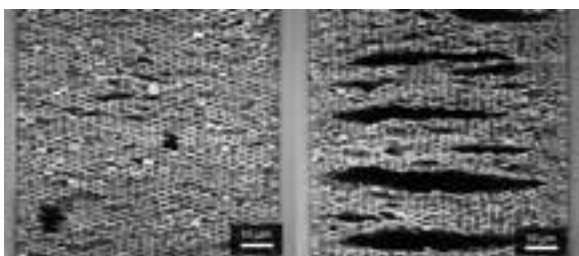


Figure 4: Annealed assemblies in the 50 μm gap of bulb-stem electrodes (left) and interdigitated electrodes (right).

rectangular regions, 100 μm at the widest and 50 μm at the narrowest. Interdigitated electrodes featured gaps of uniform widths ranging from 10 μm to 150 μm . Both electrode geometries produced unique areas of field maxima and minima that influenced final lattice structure.

Experimentation and Results:

Nanowires were appropriately diluted and placed in a silicone spacer on top of the electrode. Electrodes were attached to an external field generator using a thin Au wire and Ag epoxy binding on each probe. The cover slip with the set-up apparatus was then placed on an inverted optical microscope for real-time observation during experiments. Once wires were sedimented to the substrate surface, the field was turned on at low conditions and increased over time (Figure 3).

At low voltage and frequency, wires began to orient preferentially with Au segments in contact with the electrode edge. Particle motion occurred through a process called dielectrophoresis, where field-induced dipoles on polarizable gold segments drew wires towards the stronger field gradient at edges. Increasing voltage and frequency of the field drew in a greater number of wires and eventually allowed wires to completely bridge the electrode gap.

After the field was on for a significant amount of time, assembly structures were “annealed”—we refer to annealing as turning on and off the field to give wires the opportunity to reorient positions. The annealed structures in the 50 μm gaps of both the interdigitated and bulb-stem electrodes were compared (Figure 4). The lattices in the bulb-stem electrodes had significantly less defects, perhaps a result of “funneling” concentrating effect towards stem centers produced by larger bulbs. Since interdigitated electrodes had parallel edges, lattices did not exhibit the same density and uniformity.

A qualitative comparison of the two suggests that electrodes of alternating bulb-stem patterns are more capable of producing ideal nanowire arrangements than isometric gaps. In addition, we observed that spacing between wires was too small to accommodate the longer etched segment, suggesting that some wires had to be positioned out of plane for uniform lattices to form.

Summary:

Overall, ordered arrays of partially-etched gold nanowires were successfully produced using the 2Au-3E wire design. The bulb-stem electrodes proved to be the most effective at condensing assemblies by comparing final annealed structures to the IDE geometry.

Acknowledgements:

I'd like to thank my mentor, Sarah Boehm, for all her patience and help. I'd also like to thank my principal investigator, Christine Keating, and the entire Keating group at Penn State for allowing me to use their resources. Another *thank you* to the NNIN REU Program and NSF for the funding provided.

References:

- [1] Triplett, D. A., et al.; “Assembly of Gold Nanowires by Sedimentation from Suspension: Experiments and Simulation”; *J. of Phys. Chem. C.*, 114, 7346 (2010).

Early Hydration of Portland Limestone Cements Monitored by Raman Spectroscopy

Dylan J. Freas
Chemistry, Williams College

NNIN REU Site: Institute for Electronics & Nanotechnology, Georgia Institute of Technology, Atlanta, GA

NNIN REU Principal Investigator: Dr. Kimberly E. Kurtis, Civil and Environmental Engineering, Georgia Institute of Technology

NNIN REU Mentor: Elizabeth I. Nadelman, Civil and Environmental Engineering, Georgia Institute of Technology

Contact: dylan.j.freas@williams.edu, kimberly.kurtis@ce.gatech.edu, enadelman3@gatech.edu

Abstract:

Given its innate heterogeneity, cement hydration is a difficult process to study, and many current techniques have limited use in identifying specific chemical changes that occur during the hydration process. Raman spectroscopy has the potential to supply this information. This study was aimed at evaluating the capability of Raman spectroscopy in studying the hydration of Portland limestone cements. The consumption of many raw cement phases and the formation of major cement hydration products were detected over various time periods of hydration. This information provides insight on the nanostructural development of concrete, which can be correlated to the evolution of its macroscopic properties.

Introduction:

Globally, the cement industry accounts for approximately five percent of current anthropogenic carbon dioxide (CO_2) emissions [1]. The source of most of the CO_2 emissions during cement manufacturing is the heating of raw materials, such as limestone and clay, to form cement clinker. One method the cement industry has implemented to reduce CO_2 emissions is replacing a portion of cement clinker with filler material such as limestone. However, it is crucial to understand the effect of limestone addition on the hydration and microstructural development of cement.

Raman spectroscopy is a relatively innovative technique in the field of pure cement study. One of the most significant features of this technique is its capability for a real-time *in situ* analysis. Using this technique, researchers have characterized individual clinker components, studied the progress of timed hydration on various clinker phases, and identified products of Portland cement hydration [2]. The purpose of this present study is to extend Raman spectroscopy to the characterization of Portland limestone cements and to demonstrate its ability to characterize the formation of hydration products at the nanoscale.

Experimental Procedure:

Type I/II ordinary Portland cements containing $\sim 3\%$ limestone (“AI”) were compared to Type II Portland limestone cements containing $\sim 12\%$ limestone (“AL”). The cements were mixed with deionized water at a water-to-cement ratio of 0:4. The

cement pastes were stored in microscope well slides, and cover slips were sealed over the pastes in order to reduce the effect of carbonation.

Raman spectra were collected using a Thermo Almega XR Micro and Macro Raman Analysis Spectrometer with a 488 nm laser. A circular spot size of $50\ \mu\text{m}$ was used at 50x magnification. The Raman shift range chosen for study was $200\text{--}1200\ \text{cm}^{-1}$ with 40 seconds exposure. All instrumental configuration was systematically chosen by targeting for a high S/N ratio and statistical representativeness.

The collected data were processed using Thermo Scientific’s OMNIC Series software. The qualitative analysis of cement hydration was performed on the data normalized to the signal with the largest Raman intensity value. Baseline correction and cover slip subtraction were also applied in the data analysis.

Results And Discussion:

The Raman spectra for the two cement pastes are shown in Figures 1 and 2. Peaks were identified using values reported in the literature [3]. The results show that many major phases of commercial cement, such as limestone, gypsum, and tricalcium silicate and dicalcium silicate ($\text{C}_3\text{S} / \text{C}_2\text{S}$), can be detected, along with many major cement hydration products, including ettringite, calcium hydroxide (CH), and calcium silicate hydrate (C-S-H).

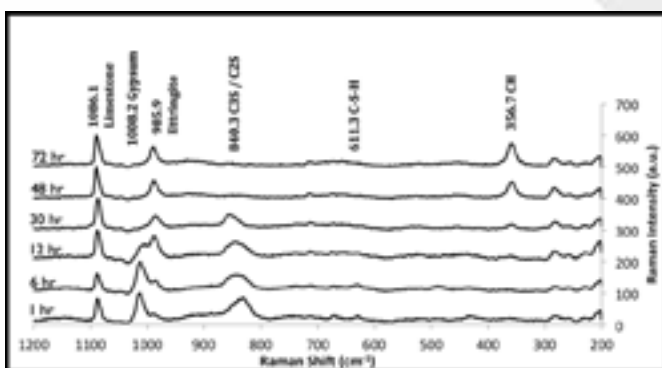


Figure 1: Time-lapsed Raman spectra of a Type II Portland limestone cement (AL).

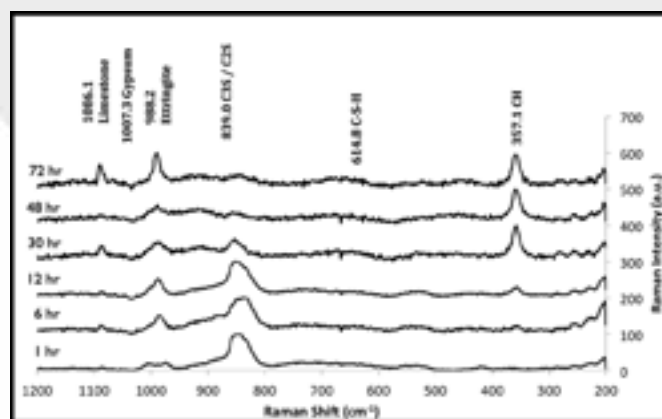


Figure 2: Time-lapsed Raman spectra of a Type I/II ordinary Portland cement (AI).

For both cement pastes, the C₃S/C₂S bands from ~800-900 cm⁻¹ become shifted toward 860 cm⁻¹ by 30 hr, which corresponds to the initial rapid hydration of C₃S, leaving primarily C₂S. By 48 hr, the C₂S signal has disappeared, indicating the consumption of both calcium silicate phases. The formation of CH (~356 cm⁻¹) is detected by 24 hr and its principal band increases in intensity through 72 hr. C-S-H was not clearly detected, but the broad C-S-H band between 600-700 cm⁻¹ is seen to increase in intensity over time as more C-S-H is produced.

The conversion from gypsum (~1008 cm⁻¹) to ettringite (~988 cm⁻¹) is illustrated as early as 6 hr and continues through 24 hr, at which point the gypsum signal has disappeared and the ettringite band continues to increase in intensity. This trend continues through 72 hr. The gypsum band is not as pronounced in the Type I/II ordinary Portland cement paste as it is for the Type II Portland limestone cement paste because the corresponding raw cement contained less gypsum prior to hydration.

Conclusions and Future Work:

This research shows that Raman spectroscopy can effectively characterize the hydration of Portland limestone cements. This nondestructive technique has been shown to provide results that are consistent with those from previous studies of cement hydration, including calorimetry and Fourier transform infrared spectroscopy studies [4]. Future work will correlate Raman spectroscopic signatures with morphological information obtained by scanning electron microscopy and specific surface area analysis, chemical composition information obtained by thermogravimetric analysis, and reaction kinetics information

provided by isothermal calorimetry, to obtain a comprehensive understanding of the nanostructural development of cement-based materials.

Acknowledgements:

This research was performed through the support of the National Nanotechnology Infrastructure Network Research Experience for Undergraduates (NNIN REU) Program and the National Science Foundation. Any opinions, findings, and conclusions or recommendations expressed in this material are those of the author(s) and do not necessarily reflect the views of the National Science Foundation. Much appreciation goes to Elizabeth Nadelman and Dr. Kimberly Kurtis for their guidance in this project.

References:

- [1] Lollini, et al. Effects of Portland Cement Replacement with Limestone on the Properties of Hardened Concrete. *Cement & Concrete Composites*, 2014, 46, 32-40.
- [2] Garg, et al. A Raman Spectroscopic Study of the Evolution of Sulfates and Hydroxides in Cement-Fly Ash Pastes. *Cement and Concrete Research*, 2013, 53, 91-103.
- [3] Potgieter-Vermaak, et al. The Application of Raman Spectrometry to Investigate and Characterize Cement, Part I: A Review. *Cement of Concrete Research*, 2006, 36, 656-662.
- [4] Ylmen, et al. Early Hydration and Setting of Portland Cement Monitored by IR, SEM, and Vicat Techniques. *Cement and Concrete Research*, 2009, 39, 433-439.

Extent of Dopant Activation after Microwave and Rapid Thermal Anneals Using Similar Heating Profiles

Taliya Gunawansa
Optical Engineering, Norfolk State University

NNIN REU Site: ASU NanoFab, Arizona State University, Tempe, AZ

NNIN REU Principal Investigator: Dr. T. L. Alford, School for Engineering of Matter, Transport and Energy, Arizona State University

NNIN REU Mentors: Ms. Zhao Zhao, School of Engineering of Matter, Transport and Energy, Arizona State University;
Dr. A. Lanz, Department of Mathematics, Norfolk State University

Contact: t.s.gunawansa@spartans.nsu.edu, ta@asu.edu, zzhao44@yahoo.com, alanz@nsu.edu

Abstract:

Many sustainability issues arise with the current manufacturing processes used for semiconductor-based solar cells. Microwave (MW) heating could be adopted as sustainable since its capital costs are less and it more efficient than conventional furnace systems. In addition, microwave heating is directly produced inside the material. This study compares the extent of dopant activation and damage repair for a MW anneal and a conventional rapid thermal anneal (RTA) with identical heating profiles. Sheet resistance measurements were used to assess the extent of dopant activation and ion channeling was used to monitor the extent of damage repair. The results showed that for identical heating profiles, MW annealing resulted in better dopant activation and damage repair.

Introduction:

When high concentrations of dopants are implanted into silicon, the surface layer becomes damaged. Large amounts of lattice damage results in increased sheet resistance. High temperature anneals are performed to repair the damage created during ion implantation and to also electrically activate the implanted dopants [1]. Rapid thermal annealing (RTA) has been used to reduce the diffusion of dopants during annealing. However, uneven heating sometime occurs due to differences in the emissivities of the various near-surface device materials. Additionally, the photons used in the RTA lamp and laser heating were not able to penetrate beyond the surface regions of the silicon [2]. However, MW of silicon allows for volumetric heating of the wafer due to the greater penetration depth of the microwave radiation [3]. In this study, we investigate the extent of dopant activation and damage repair for a MW anneal and a conventional RTA with identical heating profiles.

Experimental Procedure:

Silicon wafers received a 180 keV arsenic ion implant with one of three different doses: 1, 2 or 4×10^{15} ions cm^{-2} . A single-frequency (2.45 GHz) $2.8 \times 10^4 \text{ cm}^3$ cavity applicator microwave system with a 1300 W magnetron source was used to MW anneal the arsenic implanted silicon. A pyrometer, mounted through the cavity wall, with a spectral response of about $3.9 \mu\text{m}$, was used to monitor the near surface temper-

ature. The heating curves were then plotted in order to determine ramp up temperatures, times, and rates. A Heat Pulse 610 RTA was used to anneal each sample to obtain a similar heating curve as that of the corresponding microwave annealed sample. To monitor dopant activation, the sample surfaces were contacted with an in-line four-point-probe (FPP) equipped with a 100 mA Keithley 2700 digital multimeter. In order to determine the carrier concentration after microwave processing, Hall effect analysis was also performed. Rutherford backscattering spectrometry (RBS) was used to measure the extent of recrystallization of after each anneal.

Results and Conclusions:

Figure 1 shows the close match between the heating curves for both 50 sec MW and RTA anneals of the $2 \times 10^{15} \text{ cm}^{-2}$ sample. These results are consistent for all samples in this study. In Figure 2, sheet resistance values are shown for all three doses as a function of microwave and RTA annealing times. The MW saturation point for the dopant activation is 50 seconds. Based on this result, two set times are used for the RTA: 50s and 100s. The sheet resistances for the 50s RTA anneals are out of range (for all three doses); hence, the single hollow plotted points for the 100s RTA samples. Table 1 displays the Hall measurement results, including the carrier concentration and the sheet resistance for each MW dose.

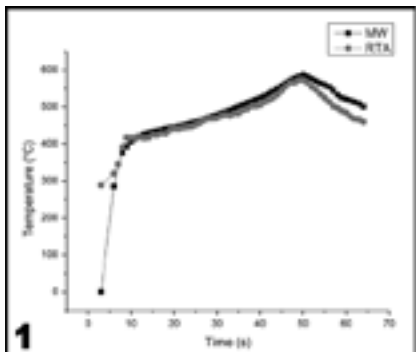


Figure 1: Illustration of the heating curve comparison between MW and RTA.

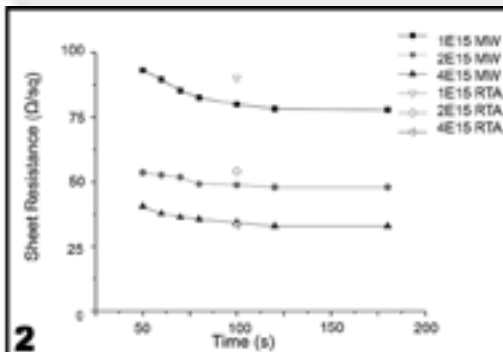


Figure 2: Comparison of the sheet resistance for MW and RTA samples.

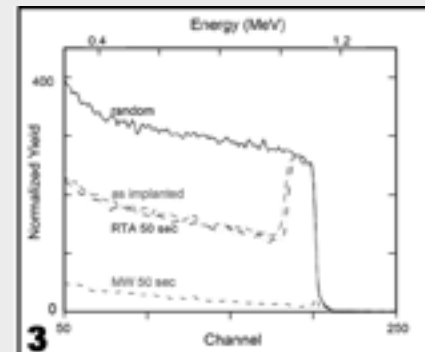


Figure 3: Represented the RBS data for four selections of samples.

Microwave annealing the samples allowed for a wider range of annealing times after the already determined saturation point. Based on the data in Table 1, it can be concluded that higher the dose and time of arsenic in the silicon, the smaller the difference in the sheet resistance between the RTA and microwave annealing. For the MW Hall measurements, the 1×10^{15} ions cm^{-2} 100s sample has a higher carrier concentration than the 2×10^{15} ions cm^{-2} 50s sample. For all three 50s doses for the RTA samples, the sheet resistance was observed to be inconclusive as a result of not reaching the saturation point.

Figure 3 illustrates the normalized yield and energy between a random, as implanted, RTA 50s, and MW 50s samples. These results showed that the MW anneals gave better dopant activation and damage repair for short times for identical heating profiles.

Future Work:

Optimize and model the microwave induced dopant activation heating process, and present findings at TMS 2015 conference.

Acknowledgments:

I sincerely thank my PI, Dr. T. L. Alford, and my mentors Ms. Zhao Zhao and Dr. A. Lanz for all of their assistance and guidance. I extend my thanks to Dr. Trevor Thornton, the National Nanotechnology Infrastructure Network Research Experience for Undergraduates Program, the National Science

Foundation, and the Center for Solid State Electronics Research at Arizona State University for providing the opportunity and funding for this research experience.

References:

- [1] K.N. Tu, J.W. Mayer, L.C. Feldman, *Electronic Thin Film Science*, Macmillan Publishing Company, New York, NY, 1992.
- [2] J.D. Plummer, M.D. Deal, P.B. Griffin, *Silicon VLSI Technology: Fundamentals, Practice and Modeling*, Prentice Hall, Upper Saddle River, NJ, 2000.
- [3] T.L. Alford, M.J. Madre, R.N.P. Vemuri, N. David Theodore. 520 4315 (2012).

Dose (cm^{-2})	Time (s)	Carrier Concentration ($\#/ \text{cm}^{-3}$)	Sheet Resistance (Ω/sq)
1.00E+15	50	9.00E+19	92.6
1.00E+15	100	1.00E+20	80.3
2.00E+15	50	1.70E+20	53.5
2.00E+15	100	1.80E+20	48.7
4.00E+15	50	3.40E+20	40.4
4.00E+15	100	4.00E+20	34.2

Table 1: Depiction of the Hall measurements obtained from the MW samples.

Characterizing TiN Resistivity using Plasma Enhanced Atomic Layer Deposition with TDMAT

Matthew Hartensveld

Microelectronic Engineering, Rochester Institute of Technology

NNIN REU Site: UCSB Nanofabrication Facility, University of California, Santa Barbara, CA

NNIN REU Principal Investigator: Mark Rodwell, Electrical and Computer Engineering, University of California Santa Barbara

NNIN REU Mentor: Robert Maurer, Electrical and Computer Engineering, University of California Santa Barbara

Contact: matthart610@yahoo.com, rodwell@ece.ucsb.edu, robdmaurer@gmail.com

Abstract:

The effects of multiple deposition parameters on the plasma enhanced atomic layer deposition (PEALD) of conductive titanium nitride (TiN) films were investigated. Specifically, effects of plasma pressure and time on TiN resistivity were characterized. Optimum growth conditions for minimum film resistivity was determined to be: plasma power of 500W, precursor gas of ammonium (NH_3), chamber pressure of 2 mTorr, and a plasma time of 30 seconds. The minimum achieved resistivity was found to be $175 \mu\Omega\text{cm}$.

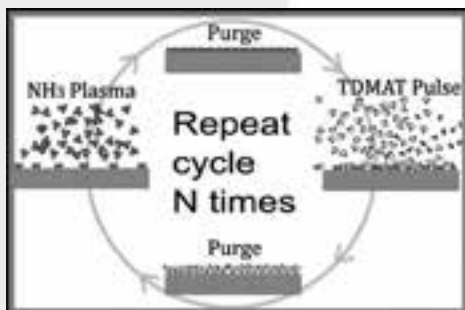


Figure 1: ALD process.

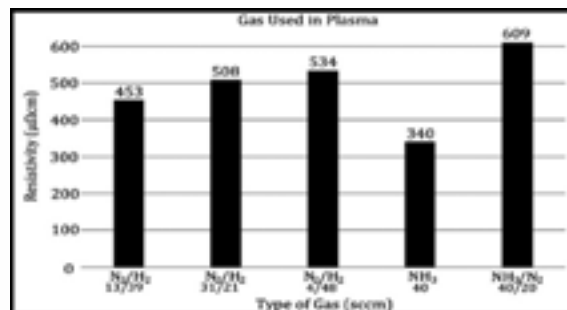


Figure 2: Plasma composition on resistivity.

Introduction:

There is a constant need for faster devices and communications. As devices are pushed to faster speeds though, frequency becomes a limiting factor. Atomic layer deposition (ALD) conducting films are used in modern electronics due to their properties of low resistivity and ability to evenly coat high aspect ratios allowing for more advanced devices. Titanium nitride (TiN) is often chosen due to its ideal properties of low resistivity. TiN is deposited by flowing tetrakis(dimethylamido) titanium (TDMAT) into the ALD chamber followed by, an argon (Ar) purge, a N_2/H_2 plasma treatment, and another Ar purge. This cycle is shown in Figure 1 and is repeated until the desired thickness is reached. This study provides an investigation of the effects of NH_3 plasma pressure on film resistivity as well as a review of these other reported variables regarding TiN.

Experimental Procedure:

The ALD system used was an Oxford FlexAL remote plasma system. Silicon <100> substrates involved were coated by an

insulating layer. The plasma parameters in the ALD cycle were varied one at a time to observe their effects on resistivity. An SEM/ellipsometer and four-point probe were used to record results.

Results and Discussion:

Plasma Power. The dependence of resistivity on plasma power was studied. Increased plasma power enhances film density by compacting layers [1] and more completely removing ligands contained in TDMAT. The denser film prevents oxygen diffusion into the material upon exposure to atmosphere [2, 3] preventing the formation of TiO_2 and other compounds that increase the resistivity [2, 4]. Plasma power increased to the maximum allowed of 500W provided the lowest resistivity.

Plasma Composition. The dependence of plasma composition was studied and results are listed in Figure 2. A stoichiometric ratio of 1:3 N:H was found to be optimal. Implementing this ratio in N_2/H_2 plasma yielded the lowest resistivity for any combination. Preserving this stoichiometric ratio, NH_3

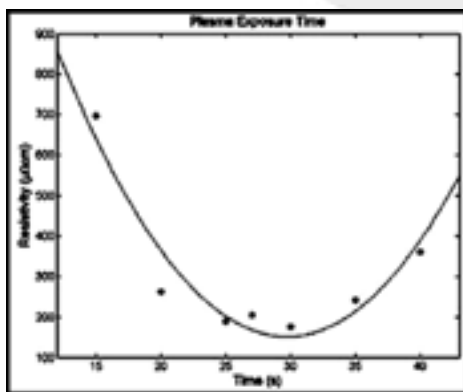


Figure 3: The effect of plasma exposure time on resistivity.

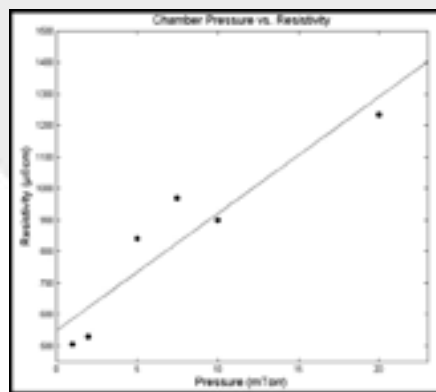


Figure 4: Chamber pressure effects on resistivity.

was also used, which yielded a lower resistivity. A possible explanation for this is that more NH_x radicals are formed [5].

Plasma Time. The duration of the plasma was found to have a significant impact on the resistivity. As Figure 3 shows, the effect of timing exhibits a parabolic like effect on the resistivity. Short timing can lead to greater carbon contamination while longer timing gives higher resistivity also, possibly due to plasma damage. An ideal time of 30 seconds was experimentally determined to give the lowest resistivity.

Chamber Pressure. For the first time, chamber pressure was varied during the plasma exposure and effect on resistivity studied. A trend was observed that has you decrease chamber pressure the resistivity is significantly lowered. This is shown in Figure 4.

Combining all optimal parameters described above, the minimum TiN film resistivity achieved was $175 \mu\Omega\text{cm}$ for a 35 nm thick film. The optimal process determined is outlined below:

1. Dose TDMAT: 2 seconds, 200 mT, 100 sccm Ar
2. Purge TDMAT: 5 seconds, 20 mT, 200 sccm Ar
3. Pump TDMAT: 5 seconds
4. Plasma Dose: 30 seconds, 2 mT, 10 sccm NH_3 , 500W
5. Purge NH_3 : 5 seconds, 20 mT, 200 sccm Ar
6. Pump NH_3 : 4 seconds
7. Repeat.

Conclusions:

The effects of chamber pressure and a review of additional plasma parameters on ALD TiN film resistivity were studied. It was found that NH_3 plasma as a precursor more effectively reacts with TDMAT. Increased plasma power and plasma exposure time ($t < 30$ seconds) decrease film resistivity due to a denser film. Combining all optimized parameters, a resistivity of $175 \mu\Omega\text{cm}$ for a 35 nm thick film was realized. Denser, less resistive, ALD TiN films have many advantages for future integration into microelectronic devices.

Acknowledgements:

This study was funded by the National Nanotechnology Infrastructure Network Research Experience for Undergraduates (NNIN REU) Program with the support of the National Science Foundation (NSF). The author thanks Robert Maurer, Prakteek Choudhary, Mark Rodwell, Bill Mitchell, and Brian Markman for their many helpful suggestions.

References:

- [1] S. Chang, et al., Surface and Coating Technology, 203, (2008).
- [2] H. Kim, JVSTB, 21, (2003).
- [3] G. Cho and S. W. Rhee, JVSTA, 31, (2013).
- [4] J. Musschoot, et al., Microelectronic Engineering, 86, (2009).
- [5] M. Hua, et al., Wear, 260, 11-12 (2006).

Aluminum-Induced Crystallization of Amorphous Silicon on Patterned Substrates

Jon-L Innocent-Dolor
Chemical Engineering, Syracuse University

NNIN REU Site: Penn State Nanofabrication Laboratory, The Pennsylvania State University, University Park, PA

NNIN REU Principal Investigator: Dr. Joan Redwing, Materials Science Department, The Pennsylvania State University

NNIN REU Mentor: Mel Hainey, Jr., Materials Science Department, The Pennsylvania State University

Contact: inohill@gmail.com, jmr31@psu.edu, melhaineyjr@gmail.com

Abstract and Introduction:

Aluminum-induced crystallization (AIC) has become an attractive method of fabricating polycrystalline silicon on insulating substrates because of its ability to produce thin films with uniform surface orientations [1], and its low process temperatures (< 500°C), which make the use of much cheaper substrates such as glass possible. One drawback of current methods is that they tend to produce films with high-angle grain boundaries. By using patterned substrates to align the grains in the films we hope to minimize the presence of high angle grain boundaries which tend to act as defects and can inhibit future device performance.

Previous studies on patterned quartz substrates made with fluorine-based reactive ion etching showed increased crystallization rate in the patterned regions, but the preferential orientation was lost. It was found that the patterned surfaces were significantly rougher than the unpatterned surfaces, which may have led to the loss of preferential orientation. This work examines the effect of surface roughness on crystallization rate and orientation.

Samples with higher and lower patterned region surface roughness were prepared by using contact lithography and fluorine and chlorine-based plasma etches, respectively. Aluminum and amorphous silicon (a-Si) layers 30 nm thick were deposited by electron-beam evaporation, and then AIC was performed by annealing the samples below the Al/Si eutectic temperature, at temperatures between 400°C

and 500°C. *In situ* and post anneal optical microscopy were used to determine the effect of patterning and roughness on crystallization and grain size. We hypothesize that the smoother surface will be better able to preserve preferential crystal orientation while maintaining the increased crystal growth rate.

Experimental Procedure:

Patterning. Fused quartz substrates were cleaned by sonication in acetone, isopropanol and de-ionized (DI) water followed by Nanostrip®. The cleaned samples were spin-coated with 3012 resist, then; contact lithography was used to produce line patterns with spacings of 100, 75, 50 and 25 μm (Figure 1). The samples were etched to a depth of 25 nm using reactive-ion plasma etch with fluorine-based etch and chlorine-based etch in order to produce samples with higher and lower surface roughness respectively. After etching, the resist was removed using acetone, isopropanol and DI water, then atomic force microscopy (AFM) was used to characterize the surface roughness of the samples and contact profilometry was used to determine the etch depth.

Deposition and Annealing. Using e-beam evaporation, 30 nm of aluminum was deposited on the etched samples, then the samples were exposed to air for 30 minutes in order to form a thin oxide layer before 30 nm of amorphous silicon was deposited onto the samples. The fused quartz substrates were diced and separated by line spacing and etch type. Anneals were performed in an annealing furnace in ambient nitrogen at 450°C for four hours on samples, and then an aluminum etchant (hydrochloric, acetic and nitric acid mixture) was used to remove the aluminum layer before optical microscopy was used to view the polycrystalline silicon layer. In order to study differences in crystallization between chlorine and fluorine etched samples, *in situ* optical microscopy was performed using a heating stage with a viewing window. Samples were again annealed at 450°C in ambient nitrogen and, images were captured every 30 seconds over the annealing period.

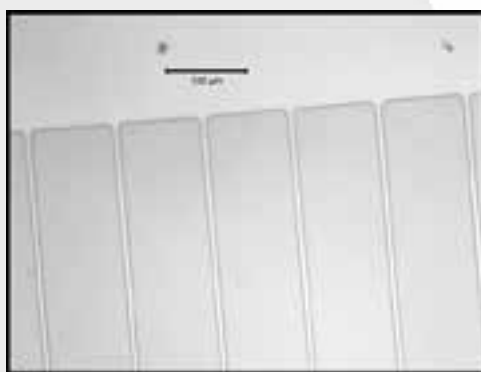


Figure 1: Optical micrograph of 100 μm patterned region.

Results:

The chlorine-based plasma etch was found to produce a surface that was much smoother (RMS 3.02 nm) than the fluorine based etch (RMS 6.88 nm) — comparable to the roughness of an unetched substrate (2.96 nm (Figure 2). For the chlorine etched samples, at a line spacing of 50 μm , there seemed to be no effect of patterning on crystallization, but 25 μm line spacing seemed to cause some grain confinement in the patterned region. Similarly, for the fluorine-based etched samples, the 25 μm -spaced line pattern had a greater effect on crystallization than the 50 μm -spaced line pattern. In both cases, however, the fluorine-based etch showed a much more dramatic effect of patterning on crystallization, with the 25 μm pattern causing almost continuous growth in the direction of the line pattern (Figure 3).

In situ optical microscopy (Figure 4) revealed that for chlorine-etched samples, nucleation began simultaneously in and out of the patterned region, but the growth rate for crystals was faster within the patterned region. Conversely, for fluorine-etched samples, nucleation occurred mainly along the lines between etched regions where there seemed to be a faster crystallization rate than the patterned region. This caused the crystals to first grow along lines, then, spread outward into the etched region, leading to the near-continuous crystals and periodicity seen in the fluorine-etched samples.

Conclusions and Future Work:

Smaller line spacing and fluorine etching seems to promote grain alignment with pattern. This result shows that patterned substrates could potentially be used to align grains. Orientation imaging microscopy will be used in order to determine the effect of surface roughness on the surface orientation. Further on, we hope to use these patterned substrates as templates for the growth of nanowires and other substances such as GaN [2].

Acknowledgements:

I would like to thank my mentor Mel Hainey, Jr. for his guidance, support and help keeping me on track with my research, my Principal Investigator Dr. Joan Redwing for welcoming me into her lab, Kathleen Gehoski for coordinating my stay at PSU and the entire Nanofab staff at PSU. I would also like to thank the NNNIN REU Program and the National Science Foundation for funding this research.

References:

- [1] M. Kurosawa, N. Kawabata, T. Sadoh, and M. Miyao, 2009. Orientation-controlled Si thin films on insulating substrates by Al-induced crystallization combined with interfacial-oxide layer modulation *Appl. Phys. Lett.* 95, 132103.
- [2] D. Tsukada, Y. Matsumoto, et al., 2009. Fabrication of (1 1 1)-oriented Si layers on SiO_2 substrates by an aluminum-induced crystallization method and subsequent growth of semiconducting BaSi_2 layers for photovoltaic application, *Journal of Crystal Growth*, 311 (14): 3581-3586.

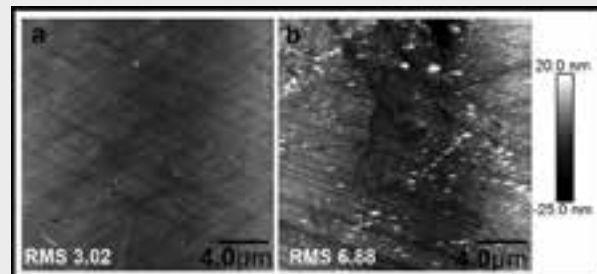


Figure 2: AFM scans; (a) chlorine-based etch, and (b) fluorine-based etch.

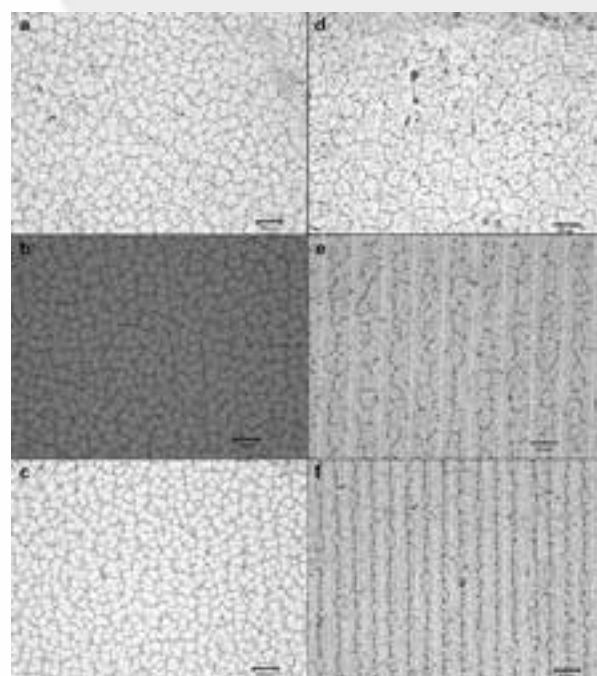


Figure 3: a) Chlorine etch unpatterned, (b) chlorine etch 50 μm pattern, (c) chlorine etch 25 μm , (d) fluorine etch unpatterned, (e) fluorine etch 50 μm , and (f) fluorine etch 25 μm .

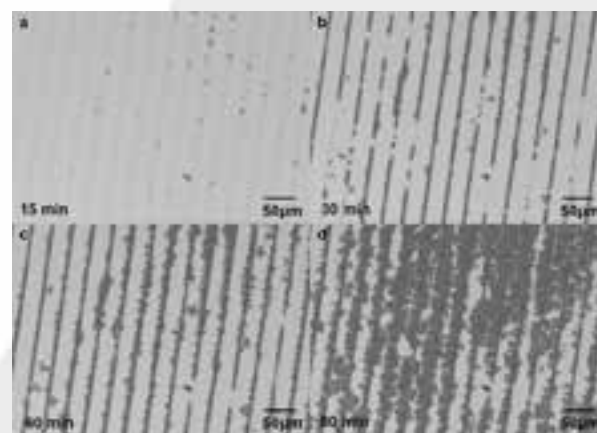


Figure 4: In situ micrographs of chlorine-etched 50 μm line patterned samples during anneal showing difference in growth rate between patterned and unpatterned region.

Fabrication of Low-Density Vertically Aligned CNT Forests

Yasuhiro Kimura

Mechanical Engineering, Tohoku University, Japan

NNIN iREG Site: Institute for Electronics & Nanotechnology, Georgia Institute of Technology, Atlanta, GA

NNIN iREG Principal Investigator: Prof. Baratunde A. Cola, Mechanical Engineering, Georgia Institute of Technology

NNIN iREG Mentor: Dr. Virendra Singh, Mechanical Engineering, Georgia Institute of Technology

Contact: kimura@ism.mech.tohoku.ac.jp, cola@gatech.edu, vsingh@gatech.edu

Abstract:

Carbon nanotubes (CNT) are a tubular nano-material made of carbon atoms and utilized by some applications due to its remarkable characteristics. The effect of growth conditions on the morphology of the CNT has been investigated for the correlation of morphology and characteristics. In the present work, the effect of growth parameters—including catalyst element, plasma properties, and the thickness of catalyst layer—on the morphology of CNT was studied to fabricate low-density CNT forests. As a result, we successfully demonstrated the fabrication of low-density CNT forests by optimizing growth parameters. The low-density CNT forests were fabricated by using 5-nm-thick nickel catalyst via low pressure chemical vapor deposition (LPCVD).

Introduction:

Carbon nanotube (CNT) is composed of one or several graphene sheets rolled into a tube and has nanoscale diameter [1]. Several noticeable characteristics of CNT, e.g. high thermal and electrical conductivity, attract increasing attention and are applied to generate the devices with outstanding performance. One of the applications of CNT is the diode array [2], which was developed by the NanoEngineered System and Transport (NEST) laboratory at the Georgia Institute of Technology. A diode array that consists of a metal-oxide-metal structure based on CNTs is capable of rectification at ultrahigh-frequencies. Conversely, this device requires low-density CNT forests for fabricating the robust device with curable resin and improving performance.

Generally, CNTs are fabricated using catalyst via chemical vapor deposition (CVD), and the morphology of CNT depends on growth conditions of CVD and surface conditions [3]. Growth conditions are plasma properties, the gases used for carbon source and facilitating CNT growth, catalyst elements, particle sizes of catalyst, structures under catalyst, etc. In this work, we focused on three parameters—catalyst element, existence of plasma, and catalyst size—for fabricating low-density CNT forests, because the listed parameters are assumed dominant to morphology of CNT and are easy to control.

The primary objective of this study was the investigation of the effect of the above parameters on the morphology of the CNT growth and fabrication of low-density CNT forests. Nickel (Ni) and iron (Fe) were used as different types of catalyst elements. LPCVD and plasma-enhanced CVD (PECVD) were used as different plasma properties. Additionally, 3, 5 and 7-nm-thick catalysts were used as different particle size of catalyst because the catalyst particle size is involved in catalyst layer thickness.

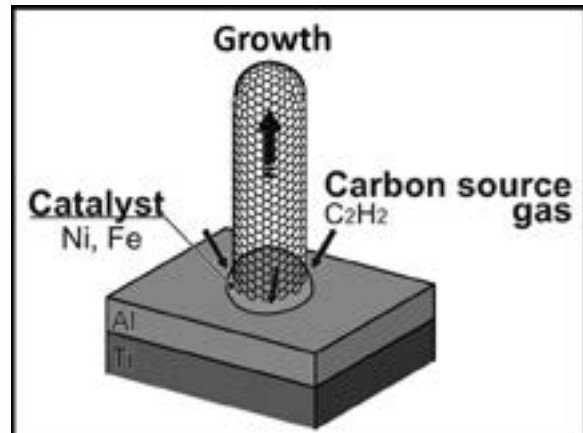


Figure 1: Schematic of CNT base-growth by CVD.

Experimental Procedure:

The fabrication process of the sample for CNT growth is given herein. Using electron-beam evaporator, 30-nm-thick Ti, 10-nm-thick Al were serially deposited as under layers onto a Si wafer. The catalyst layer, which had corresponding thickness and was composed of Ni or Fe, was formed for shaping different sizes of the catalyst particles. The CNTs were grown by using different growth conditions through CVD techniques as base-growth model, as shown in Figure 1.

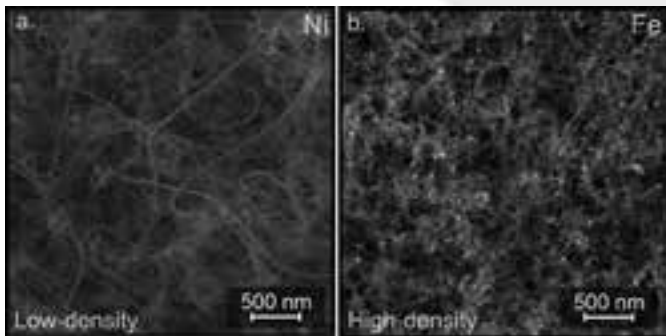


Figure 2: FE-SEM images of CNT morphology using different catalyst element; (a) Ni and (b) Fe.

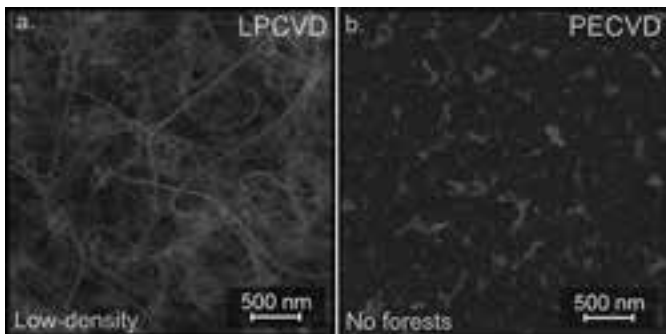


Figure 3: FE-SEM images of CNT morphology using different plasma properties; (a) LPCVD and (b) PECVD.

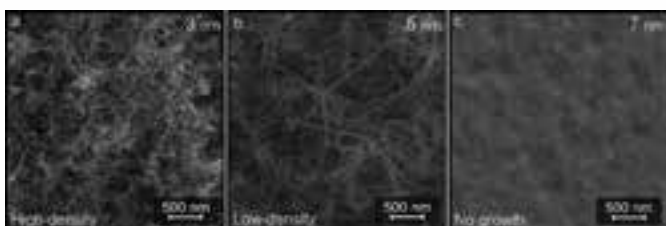


Figure 4: FE-SEM images of CNT morphology using different thickness; (a) 3 nm, (b) 5 nm and (c) 7 nm.

Results and Conclusions:

Effect of Catalyst Element. Figure 2 shows field emission scanning electron microscope (FE-SEM) images of CNT forests formed by using different catalyst elements. Other parameters of CNT growth are as follows: 10 min of growth time, LPCVD as growth technique, and 5-nm-thick of catalyst. As a result, the use of Ni catalyst contributed to fabricate low-density CNT forests. On the other hand, when Fe was utilized as a catalyst, the density of CNT forests was higher than the one using Ni catalyst.

Effect of Plasma Properties. Figure 3 shows FE-SEM images of CNT forests fabricated by using different plasma properties. Other parameters of CNT growth are as follows:

10 min of growth time, Ni as catalyst element, and 5-nm-thick of catalyst. LPCVD is suitable for growing low-density CNT forests. No CNT forests were grown using plasma, PECVD, as shown in Figure 3 (b). Normally, the plasma facilitates the CNT growth and enables CNT growth at low temperatures, but the use of plasma did not contribute to expedited CNT growth, in the case of this study. The cause of non-formation of CNT forests by using plasma is assumed that the plasma etched the catalyst particle and deposited carbon before it became a vertically aligned CNT.

Effect of Catalyst Layer Thickness. Figure 4 shows FE-SEM images of CNT forests grown by using different catalyst thicknesses. Other parameters of CNT growth are as follows: 10 min of growth time, Ni as catalyst element, and LPCVD as growth technique. The thickness of catalyst involves the particle size of catalyst as described above, and the correlation between particle size and the density of CNT is expected to be inverse proportion. In fact, the dependence between thickness involved in particle size and the density of CNT is indicated as shown in Figure 4. Nevertheless, 7-nm-thick Ni is unsuitable to fabricate low-density CNT because the film was formed with increasing thickness and particle size.

The growth and morphology of CNT were varied by different growth parameters. Consequently, the formation of low-density CNT forests can be demonstrated by using 5-nm-thick Ni catalyst via LPCVD.

Future Work:

In the future, we plan infiltrated low-density CNT forests with curable resin for the design and fabrication of CNT-based robust electronic devices.

Acknowledgements:

This work was supported by National Nanotechnology Infrastructure Network International Research Experience for Graduates (NNIN iREG) Program and National Institute for Materials Science. Part of this work was performed at the Institute for Electronics and Nanotechnology of Georgia Institute of Technology. I appreciate the support by Prof. Baratunde A. Cola, Dr. Virendra Singh, and laboratory members of NEST.

References:

- [1] Scarselli, M., Castrucci, P. and Crescenzi, M. De; *J. Phys., Condens. Matter.*, 24, 313202 (2012).
- [2] Cola, B.A., Sharma, A. and Singh, V.; U.S. Patent, WO/2014/063149, 04/24/2014.
- [3] Chhowalla, M., et al.; *J. Appl. Phys.*, 90, 5308 (2001).

Synthesis, Device Fabrication, and Characterization of Two-Dimensional Transition Metal Dichalcogenides

Matthew Koehler

Mechanical Engineering, The University of Saint Thomas

NNIN REU Site: Penn State Nanofabrication Laboratory, The Pennsylvania State University, University Park, PA

NNIN REU Principal Investigator: Professor Joshua Robinson, Department of Materials Science and Engineering, The Pennsylvania State University

NNIN REU Mentor: Brian Bersch, Department of Materials Science and Engineering, The Pennsylvania State University

Contact: koeh7692@stthomas.edu, jrobinson@psu.edu, bmb5382@gmail.com

Abstract:

Semiconducting two-dimensional transition metal dichalcogenides (TMDs), in particular molybdenum disulfide (MoS_2) and tungsten diselenide (WSe_2), have been the focus of intense research in recent years for their potential use in next-generation, scaled down electronic and optoelectronic devices due to their unique chemical, optical, and mechanical properties. TMDs are an excellent material candidate to replace silicon in digital CMOS technology, yet there still exists a need for optimized device fabrication and a scalable growth process for controllable large area, single-crystalline films. This project focused on two main objectives: WSe_2 device fabrication for Hall mobility measurements and the construction of a new metal organic chemical vapor deposition (MOCVD) system for advanced material synthesis of MoS_2 . Van der Pauw structures were fabricated by photolithography, inductively coupled reactive-ion plasma etching, and metal thin film deposition by e-beam evaporation. Devices were fabricated on several WSe_2 samples of varying morphology and were characterized by field emission scanning electron microscopy, profilometer, and Raman spectroscopy. A fully functional MOCVD system equipped with metal organic precursor “bubbler” chambers was designed and fabricated to be used for synthesis of MoS_2 .

Introduction:

Mono- and few-layered WSe_2 devices possess properties such as transparency, high flexibility, direct or indirect bandgap, high $I_{\text{ON}}/I_{\text{OFF}}$ ratio, near-perfect subthreshold swing, and high field effect mobility [1]. This material, if proven scalable and robust to conventional nanofabrication techniques, could yield a more efficient, low cost and high quality semiconductor material for industrial fabrication. We used standard photolithography to make three types of devices to test this.

Mono- or few-layered TMDs have been predominantly obtained by mechanical exfoliation from bulk crystals or powder precursor CVD. Mechanical exfoliation is not a high-throughput, scalable method while powder precursor CVD has issues precisely controlling layer thickness, uniformity, island growth, grain size, and unwanted deposition of metallic or metal oxide particulates. Modifying the currently used powder precursor CVD to a MOCVD system would greatly reduce these issues and also be compatible with existing silicon microelectronics manufacturing.

Experimental Procedure:

An exposure mask for the lithography process was designed using L-Edit, a computer aided design software, and fabricated by a laser writer. The created mask contained the layout for three devices; dual gated radio frequency field effect transistors (FET), van der Pauw structures (vdP), and transmission line measurement devices (TLM). Three successive iterations

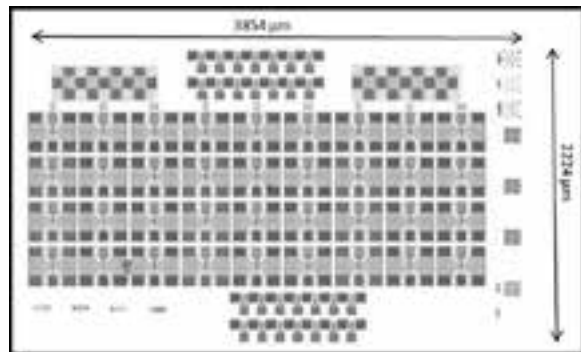


Figure 1: Exposure mask device design layout.

of photolithography were performed in order to fabricate the following layers: alignment mark layer, isolation (WSe_2 etch) layer for defining the active channel regions, and ohmic (source/drain) layer to define the contacts. A bilayer resist stack was used for lift-off of both alignment mark and contact layers. Ten nanometers of titanium (Ti) and 100 nm of gold (Au) were deposited using e-beam evaporation. A single resist layer was used for the isolation layer, and an oxygen based dry etch was successfully developed.

Constructing the MOCVD system consisted of common metal assembly tasks such as tightening bolts, joining brackets and drilling screws to assemble the frame and fasten the gas panel components. The gas lines were fully purged and evacuated

before orbital welding was performed to route the gas lines to the furnace and create a higher quality smoother weld bead. The switch box was wired by both soldering and terminal block connectors.

Results:

After each layer, devices were examined by optical microscope and field-emission scanning electron microscope (FESEM). Fortunately, WSe₂ films that are bonded to the substrate by van der Waals forces remained on the substrate even with exposure to various solvents and chemicals throughout processing, which is reassuring for future device fabrication. The majority of the devices had a visible, defined channel region shown in Figure 2. However, each device had a lack of continuous coverage in the WSe₂ channel region also shown in Figure 2, which obviates the need for more uniform, wafer-scale TMD growth.

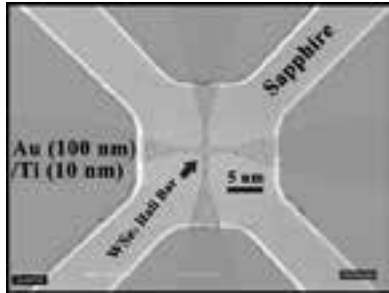


Figure 2: Finished vdP device.

A fully functional MOCVD system was designed and built, shown in Figures 3 and 4. Over 150 parts/components were ordered to create the three bubbler input system allowing multiple metal organic precursors to be used in TMD synthesis. Each bubbler has a mass flow controller and three pneumatic actuators controlled by the switchbox. Each bubbler temperature can be controlled individually by the temperature readouts on the right side of the switchbox. The user is protected by the fully ventilated sheet metal and Plexiglass® sliding door enclosure.

Conclusions:

WSe₂ proved to be a robust and compatible material for scalable device nanofabrication. In addition, it was found that WSe₂ is easily etched by an oxygen plasma and remains on the substrate throughout the fabrication process.

Even though the measurements were not taken from the vdP devices, the fabrication steps to

making the devices will help future WSe₂ research. Scientific investigators can continue to use the exposure mask and fabrication steps knowing they can achieve functioning devices if coalesced and continuous WSe₂ films are successfully grown.

The new MOCVD system will contribute to future molybdenum disulfide (MoS₂) research for many years to come. The system will allow the operator to precisely control various parameters of material synthesis to create uniform films. Readouts will give an exact flow rate for each bubbler and precursor allowing for easier repeatability and reliability. Ultimately, the new system will aid in the synthesis of uniform, large-area MoS₂, which will not only assist in device fabrication within the group, but also shed light on MoS₂ integration in manufacturing.

Acknowledgments:

I would like to thank Prof. Joshua Robinson, and Brian Bersch, along with Dr. Sarah Eichfeld and the Robinson research group for their guidance this summer. I'd also like to thank the National Nanotechnology Infrastructure Network Research Experience for Undergraduates (NNIN REU) Program and the National Science Foundation (NSF) for making this experience possible.

References:

[1] Z. Weijie, et al., "Evolution of Electronic Structure in Atomically Thin Sheets of WSe₂ and WSe₃"; arXiv. Org, Cornell University Library.



Figure 3, left: Finished MOCVD gas panel and switch box. Figure 4, right: Fully ventilated protective enclosure.



Growth of Boron Nitride for Two-Dimensional Applications

Tewa Kpulun

Physics and Math, Vassar College

NNIN REU Site: Howard Nanoscale Science & Engineering Facility, Howard University, Washington, DC

NNIN REU Principal Investigator: Dr. Gary L. Harris, Nanoscale Science and Engineering, Howard University

NNIN REU Mentor: Dr. William Rose, Nanoscale Science and Engineering, Howard University

Contact: tekpulun@vassar.edu, gharris1124@gmail.com, wbullrose@gmail.com

Abstract:

Boron nitride (BN) is an isoelectronic compound similar to carbon that is sometimes referred to as white graphene. It has several applications due to its excellent chemical properties and thermal stability. BN has weak van der Waals forces between its layers which makes it, like graphene, an excellent self-lubricant. However for certain applications, including but not limited to space applications, it is preferable to graphene. The objective of this project was to grow BN on thin substrates using a horizontal chemical vapor deposition (HCVD) system under high temperatures and pressures. Our precursors were diborane (B_2H_6) and ammonia (NH_3), while our substrates were sapphire ($\alpha-Al_2O_3$) and silicon carbide (SiC). After growth, these samples were characterized using Raman spectroscopy, atomic force microscope (AFM), and the scanning electron microscope (SEM).

Introduction:

Boron nitride (BN) is a compound that is isoelectronic to carbon; instead of carbon atoms, its lattice structure contains an equal number of boron and nitrogen atoms. It can be found in three different forms: nanosheets (BNNS), nanoribbons (BNNR), and nanomeshes (BNNM). There are four different types of BN; amorphous (α -BN), cubic (c-BN), wurtzite (w-BN), and hexagonal (h-BN).

This project mainly focused on h-BN, because it's the most stable form of BN. Its structure is similar to graphene, hence h-BN is sometimes referred to as white graphene. h-BN has strong covalent bonds between the boron and nitrogen atoms with weak van der Waals forces between its layers. This makes it an excellent lubricant with applications in cosmetics and bullet coating, and several space applications.

Using diborane and ammonia as our precursors, we attempted to grow BN on sapphire and silicon carbide substrates. Growing BN is a difficult process, thus several different methods were used to achieve our objectives.

Experimental Procedures:

First, we had to cut the $\alpha-Al_2O_3$ into smaller sizes. We used an available laser with a 1050 nm wavelength. Ideally, to cut through $\alpha-Al_2O_3$, a laser of wave length 1070 nm is required. We were unable to cut through the material, but the laser produced several striations on the back part of the whole sample. This sufficiently weaken the material allowing us to complete the cutting process with diamond tip scribes. The samples were then cleaned using standard RCA cleaning procedures.

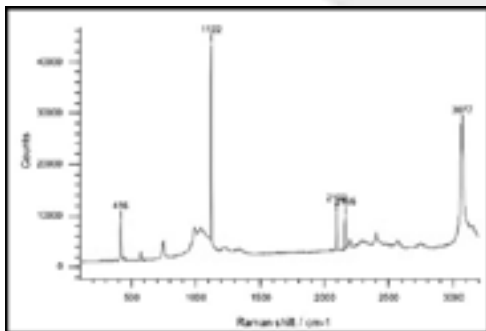


Figure 1: HCVD system. Temperatures can go as high as 1800°C and pressures as high as 400 Torr. (See full color version on page xxxvi.)

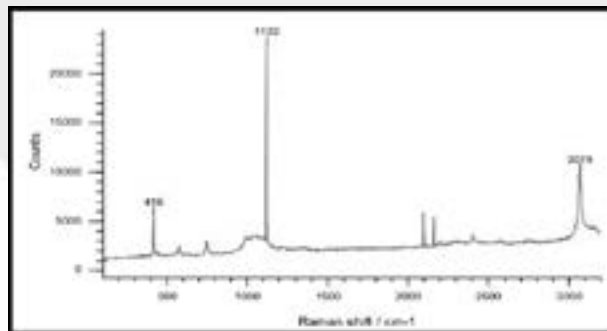
Next was the growth process where we used a horizontal chemical vapor deposition system (HCVD). The HCVD system allowed us to grow several samples on different substrates using different precursors. As you can see in Figure 1, there is a coil-like structure around the furnace that produces electromagnetic fields, which in turn creates a current that allows the device to heat up to temperatures as high as 1800°C. Pressures of about 400 Torr were also observed.

Methods and Results:

Several attempts to grow BN were made without success. We varied many of the parameters (for instance, time, amount of each precursor, and etching time) but were unable to



Graph 1: No-growth sapphire sample.



Graph 2: Sapphire growth in 1050°C.

successfully grow graphene. We used temperatures at 1000°C and 1050°C with a growth time of 15 minutes and 30 minutes. The precursor values differed from 10 sccm to 100 sccm for diborane, and 180 sccm to 200 sccm for ammonia with 9 slm for hydrogen. After each growth period, the samples were observed using Raman spectroscopy. The expected value for BN is about 1300 cm⁻¹ and our results showed Raman graphs with 1122 cm⁻¹ peaks. With this device, it was very easy to determine if the parameters we used produced expected results. Before using the Raman spectroscopy, we scanned a normal sample and compared it to that of a sample after growth; as you can see in Graphs 1 and 2.

After several attempts and additional research, we determined that having a longer growth period and higher temperatures would probably help us achieve our goal. We also characterized our samples using SEM and AFM systems. In the SEM, we used the energy dispersive spectroscopy (EDS) to determine what was on the samples' surfaces after growth. The sapphire samples showed evidence of aluminum and oxygen and the SiC showed evidence of silicon and oxygen. An AFM was used to compare the surfaces of our samples to that of previous research.

Conclusions and Future Steps:

After several attempts, there was no evidence of BN on any of the substrates. The Raman shift of a clean substrate was exactly the same as that of a substrate upon which growth had been attempted.

The next step towards growing BN on sapphire is to use other precursors instead of diborane, such as triethylboron.

Using this precursor would require using a metalorganic chemical vapor deposition system because triethylboron is a metalorganic substance. We could also continue to extend the growth period and increase the temperature.

Acknowledgments:

I would like to thank Mr. Crawford Taylor, Dr. William Rose, Dr. Gary Harris, Gurpreet Kaur, Mr. James Griffin, the Howard Nanoscale Science and Engineering Facility, and the National Nanotechnology Infrastructure Network Research Experience for Undergraduates (NNIN REU) Program.

References:

- [1] Bresnahan, S. Michael. Prospects of Direct Growth Boron Nitride Films as Substrates for Graphene Electronics. <http://arxiv.org/pdf/1310.1870.pdf>.
- [2] Cubarovs, Mihails. CVD growth of sp₂-hybridized boron nitride using aluminum nitride as buffer layer. 2011. <http://liu.diva-portal.org/smash/get/diva2:467821/FULLTEXT01.pdf>.
- [3] Ismach, Ariel. Toward the Controlled Synthesis of Hexagonal Boron Nitride Films. 18 June 2012. <http://pubs.acs.org/doi/abs/10.1021/nn301940k>.
- [4] Paduano, Qing. Self-terminating growth in hexagonal boron nitride by metal organic chemical vapor deposition. 9 June 2014. <http://m.iopscience.iop.org/1882-0786/7/7/071004/article>.
- [5] Senthilingam, Meera. Boron Nitride. 17 December 2013. <http://www.rsc.org/chemistryworld/2013/12/boron-nitride-podcast>.

Investigation of Nanodiamond Foil Product for H- Stripping to Support Spallation Neutron Source

Rachel Lim

Materials Science, Rice University

NNIN REU Site: Howard Nanoscale Science & Engineering Facility, Howard University, Washington, DC

NNIN REU Principal Investigator: Dr. Gary Harris, Electrical Engineering, Howard University

NNIN REU Mentor: Mr. James Griffin, Electrical Engineering, Howard University

Contact: rel3@rice.edu, garris@msrce.howard.edu, griffin@msrce.howard.edu

Abstract:

Diamond is an ideal material as an H- stripper foil for spallation neutron source (SNS) applications due to its high thermal conductivity, low molecular weight, and strength. Polycrystalline diamond is characterized by a high degree of internal stress, which causes the foil to curl when not supported by the substrate. Hot filament chemical vapor deposition (HFCVD) was used to grow diamond on a silicon substrate. A 1.2 cm diameter window was etched in the silicon using a 1:1:3 solution of hydrofluoric, nitric, and acetic acids, so that the diamond foil would be suspended while being supported on all sides by the silicon. Wax and diamond were used as masks to protect the outer silicon from etching. Raman spectroscopy verified a high quality diamond foil. Atomic force microscopy (AFM) revealed that the foil originally against the substrate had an average roughness of 6.7 nm while the foil away from the substrate had an average roughness of 13.2 nm. Scanning electron microscopy (SEM) revealed no cracks in the suspended foil.

Introduction:

SNS is a process that produces intense neutron beams for research. An ion source produces H- ions, hydrogen atoms with two electrons, which are injected into a linear particle accelerator. The ions pass through a foil that strips them of their electrons, yielding protons. The protons are collected in accumulator ring, then released in high energy pulses towards a liquid mercury target. Neutrons are ejected from the mercury target upon impact, which can be used for different experiments.

Currently, a carbon stripper foil is being used, but diamond would be an ideal foil. It would be able to withstand the high energy radiation because of its high thermal conductivity, low molecular weight, and strength. The foil would not have to be changed as often because diamond is more durable than just carbon.

Experimental Procedure:

A piece of <100> silicon was seeded with a nanodiamond slurry solution for ten minutes in an ultrasonic bath, then the sample was loaded into the HFCVD reactor. The working distance between the filaments and the sample was set to 20 mm, the process pressure was set to 20 torr, and the diamond heater was set to 750°C. A flow of 80.0 sccm of H₂ and 1.0 sccm of CH₄ was introduced, and when the process pressure reached 20 torr and the diamond heater temperature reached 650°C, the filament temperature was raised to 2350°C. The nanodiamond film was left to grow for 6-8 hours.

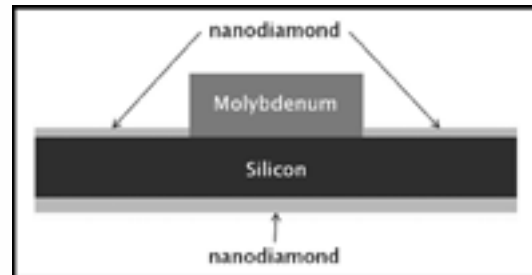


Figure 1: The circular piece of molybdenum placed in the center of the sample.

After growth of the top foil layer, the sample was flipped over, and a circular piece of molybdenum was placed in the center of the sample (see Figure 1). A diamond layer for etch masking was grown on the backside for two hours with conditions similar to the topside foil layer. The molybdenum prevented diamond from growing on part of the backside of the sample. Some of the samples were annealed at 600°C for 20 hours in a 5.0 sccm flow of N₂ at a process pressure of 20 torr in an attempt to reduce the internal stresses in the diamond foil.

The sample was placed in a 1:1:3 solution of 48% hydrofluoric, 70% nitric, and 100% acetic acids to etch a window in the silicon. The ratio of acids determined the etch rate. If the etch was too fast, the diamond came off in little pieces. If the etch was too slow, it did not etch all the way through the silicon. The backside layer of diamond protected the silicon outside of the circle from the etch, yielding a suspended diamond foil.

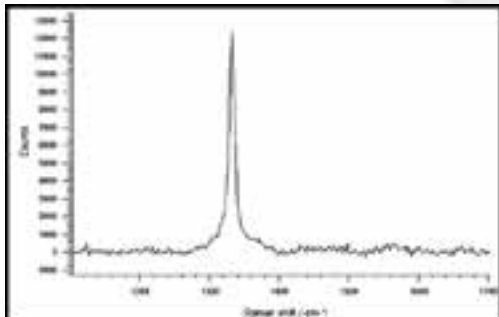


Figure 2: Raman spectroscopy verifying a high quality diamond foil with a strong diamond peak and a very weak graphite peak.

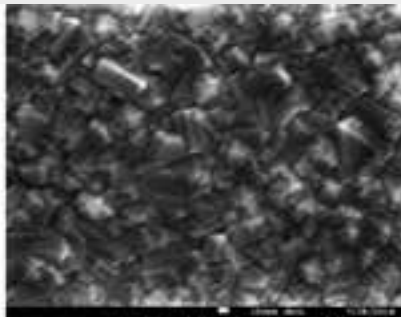


Figure 3: SEM image verifying the presence of polycrystalline diamond.



Figure 4: Optical imaging reveals no cracks in the suspended foil. (See full color version on page xxxvi.)

that was supported by the silicon. Once all of the silicon in the circle was etched away, the sample was rinsed in DI water, then allowed to air dry.

Results and Conclusions:

A high quality diamond foil was grown on a $<100>$ piece of silicon by HFCVD. Raman spectroscopy verified a high quality diamond foil with a strong diamond peak at 1333 cm^{-1} and a very weak graphite peak as seen in Figure 2. Both SEM and AFM showed the presence of polycrystalline diamond as seen in Figure 3. A 1:1:3 acid ratio was found to be ideal because it was not too fast or too slow. Using diamond as a mask to protect the silicon during etching worked better than wax by providing better mask control and greater resistance to acid etching. AFM revealed that the foil originally against the substrate had an average roughness of 6.7 nm, while the foil away from the substrate had an average roughness of 13.2 nm.

SEM and optical imaging (see Figure 4) revealed no cracks in the suspended foil. Both 6-hour diamond film growths did not crack. The annealed sample appeared to be smoother, which means that it had less internal stress. The 8-hour unannealed diamond film growth cracked, while the 8-hour annealed film growth did not. It appears that annealing the diamond foil before etching away the silicon relieves some of the stresses in the film.

Future Work:

Currently, the diamond foils that have been grown are under much internal stress. Initial results suggested that pre-etching annealing of the diamond is useful for relieving internal stress. Future work should concentrate on various anneal temperature and times for stress reduction. Another area of investigation should involve introducing argon to the gas species during

diamond growth. Depending on the argon concentration during growth, diamond grains can be reduced from poly to nanocrystalline. Smaller grains may also reduce the stress in the film. Lastly, foil testing by SNS should be performed to verify diamond foil performance.

Acknowledgements:

I would like to thank the NNIN REU Program, the NSF, and the Howard Nanoscale Facility (HNF). I would also like to thank my PI, Dr. Gary Harris, and my mentor, Mr. James Griffin, for their help and guidance, and Ms. Bokani Mtengi for training me at Howard University. Lastly, I would like to thank Dr. R.D. Vispute from Blue Wave Semiconductors for his expertise on this project.

References:

- [1] V.Kh. Liechtenstein, T.M. Ivkova, E.D. Olshanski, R. Repnow, J. Levin, R. Hellborg, P. Persson, T. Schenkel. "Advances in targetry with thin diamond-like carbon foils"; Nuclear Instruments and Methods in Physics Research A, 480 (2002) 185-190.
- [2] R.W. Shaw, D.P. Bontrager, L.L. Wilson, C.S. Feigerle, C.F. Luck, M.A. Plum. "An Electron Beam SNS Foil Test Stand"; White Paper.
- [3] T. Spickermann, M.J. Borden, R.J. Macek, R.W. Shaw, C.S. Feigerle, I. Sugai. "Comparison of carbon and corrugated diamond stripper foils under operational conditions at the Los Alamos PSR"; Nuclear Instruments and Methods in Physics Research A, 590 (2008) 25-31.
- [4] R.W. Shaw, V.A. Davis, R.N. Potter, L.L. Wilson, C.S. Feigerle, M.E. Peretich, C.J. Liaw. "Corrugated Thin Diamond Foils for SNS H- Injection Stripping"; White Paper.
- [5] R.A. Campos, V.J. Trava-Airoldi, O.R. Bagnato, J.R. Moro, E.J. Corat. "Development of nanocrystalline diamond windows for application in synchrotron beamlines"; Vacuum 89 (2013) 21-25.
- [6] RD Vispute, H.K. Ermer, P. Sinsky, A. Seiser, R.W. Shaw, G. Harris, F. Piazza. "Nanodiamond Foil Product for H- Stripping to Support Spallation Neutron Source (SNS) and Related Applications"; White Paper.

Characterization and Modeling of Carrier Dynamics in Thin Films of Gallium Nitride

Rachel Lucas

Physics/Aerospace Engineering, Purdue University

NNIN REU Site: UCSB Nanofabrication Facility, University of California, Santa Barbara, CA

NNIN REU Principal Investigator: Dr. James Speck, Materials Department, University of California, Santa Barbara

NNIN REU Mentor: Brian McSkimming, Materials Department, University of California, Santa Barbara
(2007 NNIN Intern at UCSB and 2008 NNIN iREU Intern in Tsukuba, Japan)

Contact: lucas27@purdue.edu, speck@mrl.ucsb.edu, mcskimming@gmail.com

Introduction:

Gallium nitride (GaN) is used in violet laser diodes that are used to read Blu-ray disks, as well as in light emitting-diodes ranging in color from red to ultraviolet. GaN is also employed in various wireless infrastructure applications in the form of high-electron-mobility transistors (HEMTs). GaN can operate at higher powers and temperatures than many other semiconducting materials and this makes it an excellent material for use in cell phone base stations in order to improve the distance of signal transmittance. GaN transistors use less power to convert an equivalent amount of power with less energy loss than many other semiconducting materials and because of this it has the potential to improve energy retention.

An excellent way to quantify material quality is through mobility measurements. Electron scattering from impurities as well as dislocations decreases mobility. When growth conditions of the material are varied defects and thus mobility values change. By data fitting to specific equations a value for the defect concentration can be found. We created software to do this along with plotting of raw data and the mobilities due to six scattering mechanism [1].

Methods:

Software was created to perform data fitting of carrier concentration and mobility data taken through variable temperature Hall measurements. Carrier concentration is the density of electrons in the material, while mobility is a measurement of how well these electrons move through the material while dealing with scattering events. These data values were fit to two equations, the charge balance and total mobility equations. These equations along with the variable definitions can be referenced in Figure 1. The charge balance equation is a balance confirming that the material is electrically neutral. The total mobility equation uses Matthiessen's rule in order to consolidate mobility equations for six scattering mechanisms into the overall total mobility. Each of the six component mobility equations is based off of an individual scattering mechanism, each one having a physical basis in the material.

The program began by accepting a data set and scanning in the raw data values. These values were then plotted. An example of this plot can be referenced in Figure 2. Carrier concentration increased with temperature, while mobility increased to a peak and then decreased. Mobility took this shape because as the temperature decreased from

Charge Balance Equation	
$n + N_A^- = N_D^+ =$	$\frac{N_D}{1 + \frac{gn}{N_c \exp[\frac{E_D}{k_B T}]}}$
Total Mobility Equation	
$\frac{1}{\mu_{\text{total}}} = \frac{1}{\mu_I} + \frac{1}{\mu_N} + \frac{1}{\mu_{DP}} + \frac{1}{\mu_{Piez}} + \frac{1}{\mu_{POP}} + \frac{1}{\mu_{Dis}}$	
Parameter	Symbol
g	Degeneracy of the donor state
N_c	Effective density of states
E_D	Apparent donor binding energy
n	Electron concentration
k_B	Boltzmann constant
T	Temperature
N_A	Ionized acceptor concentration
N_D^+	Ionized donor concentration
N_D	Donor concentration
μ_{total}	Total mobility
μ_I	Mobility due to ionized impurity scattering
μ_N	Mobility due to neutral impurity scattering
μ_{DP}	Mobility due to acoustic deformation potential scattering
μ_{Piez}	Mobility due to piezoelectric scattering
μ_{POP}	Mobility due to polar optical phonon scattering
μ_{Dis}	Mobility due to dislocation scattering

Figure 1: Charge balance and total mobility equations along with variable definitions [1].

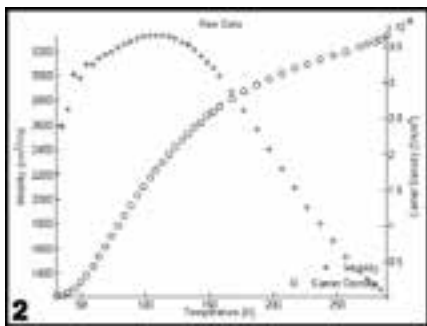


Figure 2: Raw data plot of carrier concentration and mobility data with varying temperature.

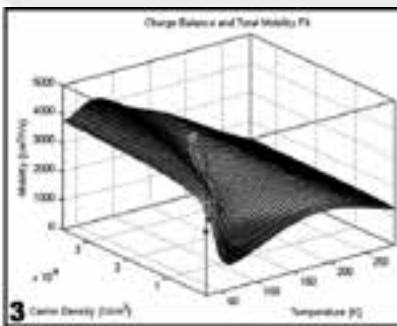


Figure 3: Fit of raw data to charge balance and total mobility equations as a surface. (See full color version on page xxxvi.)

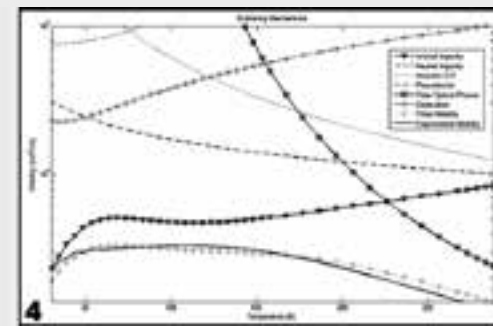


Figure 4: Mobilities due to each scattering mechanism along with total fitted and experimental mobility.

room temperature, phonons, vibrations in the lattice structure of GaN, began to lose energy and eventually freeze out. This decreased the scattering effect of polar optical phonon scattering, thus increasing the mobility. As the temperature continued to decrease, the mobility came to a peak and the effect of charge carriers themselves lost energy, and freezing out began to take over.

After the raw data values were scanned in and plotted they were fit to the charge balance and total mobility equations as a surface, which can be referenced in Figure 3. This allowed for the determination of four unknown parameter values: the acceptor concentration, N_A , which is the density of atoms in the sample that accept carriers, the donor concentration, N_D , which is the density of atoms in the material that donate carriers, the apparent donor binding energy, E_D , which is the energy required for an atom to donate a carrier, and the occupancy of traps along a dislocation, f , which is a value from 0 to 1 denoting how many traps along dislocations are occupied by a carrier. These four values can then be used in the six mobility equations for each of the scattering mechanisms as well as the total mobility equation in order to create a plot. This plot can be viewed in Figure 4.

In this plot, dominant scattering mechanisms for specific samples can be seen. Because scattering caused carriers to move more slowly, the scattering mechanism that caused the lowest mobility was the predominant scattering mechanism. In this particular sample, ionized impurity scattering was most influential up until approximately 225 K, while polar optical phonon scattering was dominant above this value.

Results and Conclusions:

Determining values for N_A , N_D , E_D , and f , along with measured mobility values, allowed for a comparison between GaN samples grown with varied conditions. N_A corresponded to

approximate defect density and defect density had a direct effect on mobility and thus sample quality. As defect density increased scattering increased, therefore decreasing mobility. Materials allowing higher mobility allowed carriers to move more easily through them and thus were a better quality material.

Future Work:

In the future, we are hoping to test the effect of different power levels of the plasma source on N_A . We are expecting to see an increase in N_A with an increase in power level as increasing the power level supplies the sample with more energy in order to create more ionized atoms and thus acceptors. We also want to test different flow rates of the plasma source and expect to see a similar correlation between it and N_A .

Acknowledgements:

Thanks to Brian McSkimming and Dr. James Speck as well as to his research group. Thank you to the National Nanotechnology Infrastructure Network Research Experience for Undergraduates Program and the NSF for funding, and thanks to the UCSB Nanofabrication Facility. Thank you also to UCSB's multiple site coordinators.

References:

- [1] Kyle, Erin C.H., Stephen W. Kaun, Peter G. Burke, Feng Wu, Yuh-Renn Wu, and James S. Speck. "High-electron-mobility GaN Grown on Free-standing GaN Templates by Ammonia-based Molecular Beam Epitaxy." *Journal of Applied Physics* 115.193702 (2014).

Decreasing Contact Resistance to n-InGaAs with ALD TiN

Brian Markman

Materials Science and Engineering, The Pennsylvania State University

NNIN REU Site: UCSB Nanofabrication Facility, University of California, Santa Barbara, CA

NNIN REU Principal Investigator: Dr. Mark Rodwell, Electrical and Computer Engineering, University of California, Santa Barbara

NNIN REU Mentor: Prateek Choudhary, University of California, Santa Barbara

Contact: brian.markman8@gmail.com, mjwrodwell@gmail.com, prateek.pc@gmail.com

Abstract:

The effects of multiple deposition parameters on the plasma enhanced atomic layer deposition (PEALD) of conductive titanium nitride (TiN) films were investigated. Specifically, effects of chamber pressure and plasma exposure time on TiN resistivity were characterized. Optimum growth conditions for minimum film resistivity was determined to be: substrate temperature of 300°C, plasma power of 500W, precursor gas of ammonia (NH₃), chamber pressure of 2 mTorr, and a plasma time of 30 seconds. The minimum achieved resistivity was found to be 176 $\mu\Omega\text{-cm}$.

Precursor Gases	Flow Rate (sccm)	ICP Power (W)	Resistivity ($\mu\Omega\text{-cm}$)
N ₂ /H ₂	13/39	400	814
N ₂ /H ₂	13/39	500	453
NH ₃	40	400	595
NH ₃	40	500	432

Table I: Resistivity relationship to plasma power for two different plasma compositions.

Precursor Gases	Flow Rates (sccm)	Resistivity ($\mu\Omega\text{-cm}$)
N ₂ /H ₂	13/39	453
N ₂ /H ₂	31/21	508
N ₂ /H ₂	4/48	534
NH ₃	40	340
NH ₃ /N ₂	40/20	609

Table II: Resistivity relation to plasma composition for combinations of N₂, H₂, and NH₃.

Introduction:

Dimensional scaling of heterojunction bipolar transistors (HBT) must be supplemented by reductions in contact resistance at the emitter and base contacts, in order to improve device performance. Specifically, the emitter contact is particularly difficult to fabricate due to the extremely high aspect ratio and high current densities required. Due to these requirements, titanium nitride is of interest because of its low resistivity and high melting temperature [1, 2]. Many deposition techniques of TiN have been explored; atomic layer deposition (ALD) is of particular interest because of its conformal coating of high aspect ratio structures and low resistivity [1, 3].

Though multiple precursors are commonly used in ALD TiN deposition, tetrakis-dimethylamido titanium (TDMAT) is attractive due to its ability to deposit at temperatures below 400°C without generating chemically aggressive, non-volatile products [1, 4, 5]. Additionally, plasma assisted processes are common due to their ability to increase deposition rate and reduce resistivity [1]. This study presents a novel investigation of chamber pressure on TiN film resistivity for low contact resistance applications as well as a review of plasma power, plasma composition, plasma exposure time, and the introduction of a hold step.

Experimental Procedure:

The ALD system used in all tests was an Oxford FlexAL remote plasma system. Substrates were prepared from doped silicon <100> wafers that were coated with an insulating layer. All samples were solvent cleaned and dehydrated before being loaded into the ALD. Sigma Aldrich 99.999% TDMAT was used. An inductively coupled plasma (ICP) system was used and operated at 500W and 13.56 MHz, unless otherwise mentioned. Substrate temperature was kept at 300°C and the TDMAT bubbler was kept at 60°C.

During tests, plasma parameters including plasma power, plasma composition, chamber pressure, and plasma exposure time were varied. Sheet resistance was then measured using a four-point probe. Film thicknesses were determined using SEM and ellipsometry.

Results and Conclusions:

To achieve the lowest TiN resistivity, the effects of plasma power, plasma composition, chamber pressure, plasma exposure time, and hold step duration were investigated.

Plasma Power. As demonstrated in Table I, as plasma power is increased, the resistivity decreases independent of the precursor oxidant.

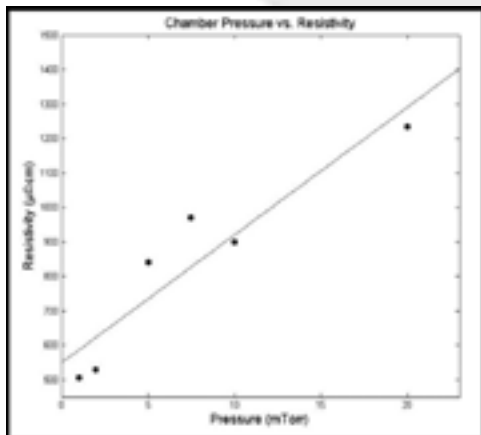


Figure 1: Resistivity as a function of chamber pressure for substrate temperature 300°C, plasma power 500W, and plasma exposure time 25 s.

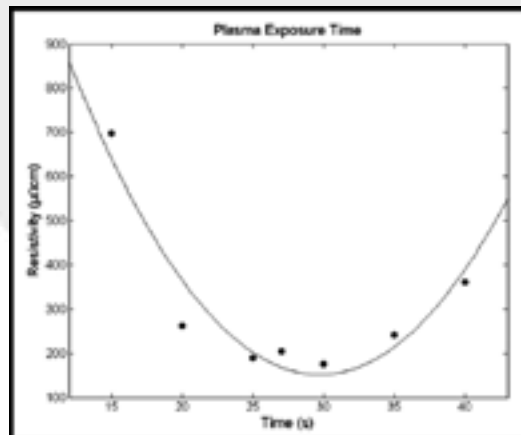


Figure 2: Resistivity as a function of plasma exposure time for substrate temperature 300°C, plasma power 500W, and chamber pressure 2 mTorr.

Plasma Composition. Both nitrogen rich and hydrogen rich plasma compositions were tested and the results are outlined in Table II. It was found that a stoichiometric ratio of N:H 1:3 is optimal for both NH₃ and N₂/H₂ precursors where NH₃ is the most favorable. This is likely due to the formation of more NH_x radicals in a NH₃ plasma than in an N₂/H₂ plasma [1, 3].

Chamber Pressure. As illustrated in Figure 1, as chamber pressure decreases, resistivity decreases. This is likely because of reduced plasma damage over time.

Plasma Time. Increasing plasma time for $t < 30$ seconds decreases the resistivity; however, when $t > 30$ seconds, resistivity increases quickly. Figure 2 demonstrates this relationship and suggests that for $t < 30$ seconds, the plasma is mostly reacting away the organic ligands contained within TDMAT. Likely after 30 seconds most of the ligands have been removed and subsequent plasma action results in plasma damage rather than defect removal.

Dose and Hold. The effect of introducing a hold step during the TDMAT dose was investigated. TDMAT was held in the chamber, allowing conformal coating of high aspect ratio structures. Further decomposition of the TDMAT also provided lower resistivity. A five second hold time was found to allow for the lowest resistivity, while an increased time realized no further improvements.

By increasing plasma power, using NH₃ as an oxidant, decreasing chamber pressure, and increasing plasma time ($t = 30$ seconds), it is possible to significantly reduce TiN film

resistivity and thus create less resistive metal contacts in many devices thus enabling next generation HBTs without having to alter the base contact as well.

Future Work:

Experimentally determined TiN has recently been incorporated into 64 nm HBTs, which are currently being processed. Transmission line models (TLM) will be fabricated to quantitatively determine the contact resistance associated with the newly developed TiN recipe. The effects of plasma power on contact resistance will be examined.

Acknowledgements:

I would like to thank Prateek, Rob, Chen-Ying, all other members of the Rodwell group, and all of the cleanroom staff for their help and support throughout the summer. Additional thanks to the NNIN REU Program, NSF, and DARPA for making this project possible.

References:

- [1] E. Gerritsen, et al., SSE, 49, (2005).
- [2] J. K. Huang, et al., Thin Solid Films, 519, (2011).
- [3] Y. Y. Chen, et al., Microelectronic Engineering, 112, (2013).
- [4] P. Caubet, et al., ECS, 155, (2008).
- [5] Atomic Layer Deposition, NNIN, UCSB.

Using Fluid Dynamics Modeling to Guide the Fabrication of Patterned Shearing Blades for the Solution Deposition of Single-Crystalline Organic Semiconductor Thin Films

Geoffrey C. Martin-Noble

Chemistry and Computer Science, Haverford College

NNIN REU Site: Stanford Nanofabrication Facility, Stanford University, Stanford, CA

NNIN REU Principal Investigator: Professor Zhenan Bao, Chemical Engineering, Stanford University

NNIN REU Mentor: Leo Shaw, Chemical Engineering, Stanford University

Contact: gmngeoffrey@gmail.com, zbao@stanford.edu, leoshaw@stanford.edu

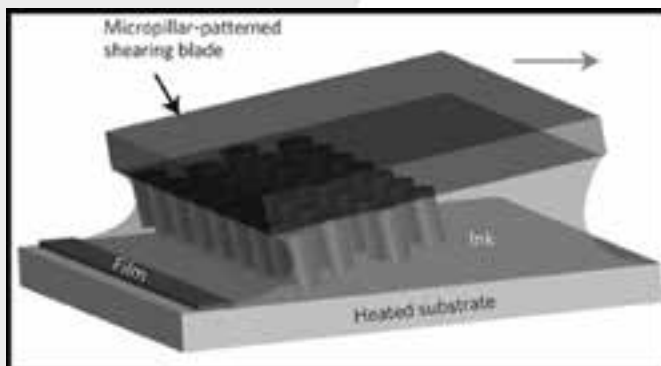


Figure 1: The solution shearing technique using a blade with micro-pillars (not to scale).

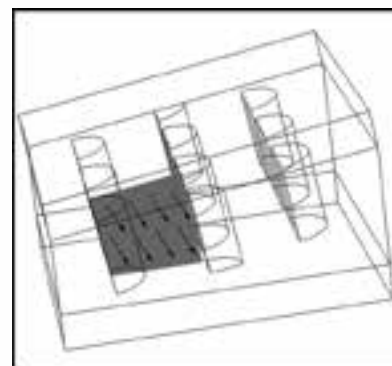


Figure 2: COMSOL model geometry. The trapezoid surface was used to measure mass flux and was not part of the model geometry.

Abstract and Introduction:

Organic semiconductors (OSCs) are promising materials for applications requiring flexible and transparent electronics and have the potential to be produced using low-cost solution processing methods [1, 2]. However, typical solution-based techniques create polycrystalline OSC thin films unable to reach the performance of single crystals grown by vapor-based deposition methods [3].

Previously, the Bao group has developed a method called solution shearing for the deposition of high quality OSC thin films for use in field effect transistors [3]. In solution shearing, the OSC is dissolved in a solvent, and the solution is spread across a heated silicon substrate by a blade moving at a constant velocity, as shown in Figure 1. The solvent evaporates as it is sheared, depositing the OSC solute as a thin film.

Using this technique to shear a solution of 6,13-bis(triisopropylsilyl)pentacene (TIPS-pentacene) in toluene resulted in thin films with field effect mobilities—the primary measure of semiconductor effectiveness—more than double the highest previously reported for TIPS-pentacene [4]. However, the films had large void spaces between crystalline ribbons. We suspected that these voids formed because as crystals grow on either side of a region, they pull solute from it, creating a zone with depleted OSC.

To eliminate these voids, micropillars were introduced to the blades [1] (see Figure 1) to induce recirculation in the solution during shearing. This modification virtually eliminated voids and resulted in mobilities double again those achieved without micropillars. Further improvement could likely be achieved by optimization of the micropillar pattern.

In order to better understand the shearing process, we used COMSOL Multiphysics to model the effects of different micropillar shapes and spacings on the solution flow during shearing. We fabricated these blades using photolithography with the aim of correlating simulated fluid flow with experimental blade performance, and thus enabling the use of modeling for future blade development.

Procedure:

Model Parameters. Figure 2 shows the model geometry used in COMSOL. Only the solvent was modeled, as the concentration of OSC is low enough to not affect viscosity. Periodic boundary conditions were used on the sidewalls to model an infinite array of pillars. The mass flux flowing through the system was set to the experimentally determined solvent evaporation rate. To simplify the calculation, the

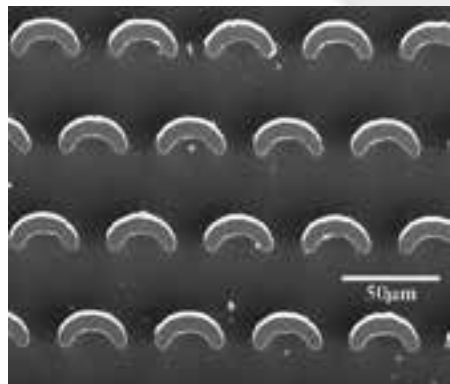


Figure 3: A scanning electron micrograph of part of a completed blade.

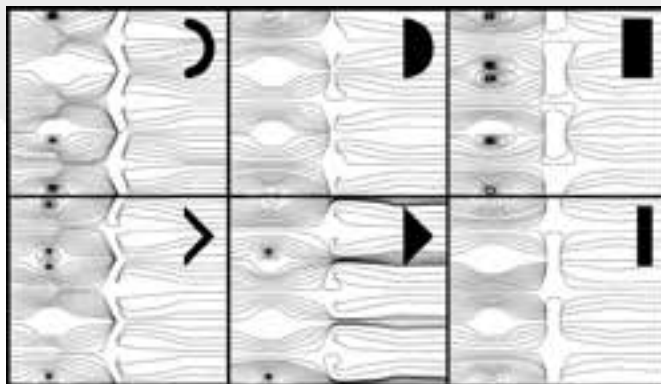


Figure 4: Velocity streamlines of simulated fluid flow. Line spacing indicates speed.

simulation was performed in the frame of reference with the blade stationary and the substrate moving to the left, but all data was adjusted back to the laboratory frame for analysis.

Fabrication of Blades. The blades were created using a standard photolithography procedure and deep reactive ion etching with sulfur hexafluoride (SF_6) on a silicon substrate.

Results and Discussion:

Figure 4 shows two-dimensional velocity streamlines of the simulated fluid flow for different pillar shapes. We also examined different pillar spacings (not shown). The flow is shown 3 μm above the substrate. To try to quantitatively evaluate the different pillar shapes, we measured the simulated lateral mass flux between two rows of pillars through the surface shown in Figure 2. We hypothesized that an increased lateral flux would be an indication of improved recirculation and therefore improved crystals. Flux measurements were 109 ng/s for the model with crescent pillars, 115 ng/s for the chevron, 115 ng/s for the thick bar, 119 ng/s for the thin bar, 123 ng/s for the semicircle, and 125 ng/s for the triangle.

Previous experimental results indicate that the chevron and crescent pillars create noticeable improvements in the TIPS-pentacene thin film, while the semicircle and bar pillars do not. However, the crescent and chevron models actually have the lowest lateral mass flux, so measuring flux across the surfaces we used does not appear to be an effective metric for evaluating the simulations. Neither can we conclude the reverse trend—lower lateral flux improves film quality—because a lateral flux of zero would result from the removal of the micropillars, which were already shown to create a significant improvement.

Summary and Future Work:

Solution shearing has already been demonstrated as an effective method for the creation of high-quality single-crystalline OSC

thin films and the addition of micropillars further improves the technique. However, we cannot use lateral flux as we have measured it in order to effectively evaluate simulation results, so we must identify another figure of merit.

To investigate this project further, we must evaluate the quality of TIPS-pentacene thin films sheared with different blades. We can examine the films optically, employ grazing incidence x-ray diffraction to calculate crystal coherence length, and measure the field-effect mobilities of the films. By correlating experimental and simulation results, we aim to find an effective metric for evaluating simulation results. With appropriate evaluation, the simulations can be used to determine optimal pillar patterning for a range of different systems.

Acknowledgements:

I would like to acknowledge the National Nanotechnology Infrastructure Network Research Experience for Undergraduates Program, the National Science Foundation, and Stanford's Center for Integrated Systems for funding. I would also like to thank the Bao Group, the Stanford Nanofabrication Facility staff, the Stanford research computing staff, Mike Deal, Maureen Baran, and my other Stanford REU interns for their support.

References:

- [1] Gao, P., et al. *Adv. Mater.* 21, 213-216 (2009).
- [2] Rogers, J. A., et al. *Proc. Natl. Acad. Sci. USA* 98, 4835-4840 (2001).
- [3] Diao, Y., et al. *Nat. Mater.* 12, 665-671 (2013).
- [4] Giri, G., et al. *Nature* 480, 504-508 (2011).

Characterization of InAs/AlSb/GaSb Heterostructures When Exposed to *in situ* Plasma Cleans in an ALD Process

Marlee Motes

Chemical Engineering, University of Arkansas

NNIN REU Site: UCSB Nanofabrication Facility, University of California, Santa Barbara, CA

NNIN REU Principal Investigator: Dr. Christopher Palmstrøm, Electrical and Computer Engineering, and Materials, University of California, Santa Barbara

NNIN REU Mentor: Borzoyeh Shojaei, Materials Science and Engineering, University of California, Santa Barbara

Contact: mjmotes@email.uark.edu, cpalmstrom@ece.ucsb.edu, borzoyeh@umail.ucsb.edu

Abstract:

The ability to control the carrier density in a semiconductor using a voltage applied to a metal gate electrode on top of a dielectric insulating layer is critical to many device applications. Gallium antimonide/indium arsenide/aluminum antimonide/gallium antimonide (GaSb/InAs/AlSb/GaSb) heterostructures have electronic properties that make them useful for electronic and optoelectronic application [1]. However, the gating efficiency has generally been low with hysteretic behavior. Surface contamination and surface oxides on the heterostructures are believed to be the cause of hysteretic gate operation. The main goal of the project is to improve gate control of group III-V antimonide based semiconductor heterostructures. An *in situ* plasma clean using both hydrogen and nitrogen was used prior to depositing of a AlN dielectric film by atomic layer deposition (ALD). Images were taken using atomic force microscopy (AFM) before and after deposition to determine if degradation of the surface occurred, and if so, the rate of degradation; also to view the atomic layers that had been deposited. Optical and atomic force microscopy images were taken between fabrication steps, as well as after fabrication was completed. The electrical properties were also measured (mobility, resistivity, carrier density via four-point probe techniques and the Hall Effect) of the full heterostructures and lone insulating buffers before and after exposure to fabrication steps. These measurements help understand the effects of surface roughness, surface contamination, and processing induced defects on gate operation of the heterostructures.

Introduction:

Compound semiconductors have applications in electronics and optoelectronics such as transistors, infrared detectors and infrared emitters. InAs is a compound semiconductor and GaSb/InAs/AlSb/GaSb heterostructures have electronic properties that make them useful for high speed, low power electronics and infra-red optoelectronic application [1]. However, their implementation in electronic devices has been limited because of difficulties in fabricating devices. Using InAs and AlSb layers, the InAs creates a channel where electrons become confined; this is called a quantum well. When processing the material to make these applications often a metal gate electrode must be fabricated onto the material that allows control of the electron density in the InAs channel by applying a voltage to the gate.

Contamination of the GaSb surface occurs very readily. It can begin to oxidize as soon as the surface is exposed to air after the growth process of the material is over [2]. It can also become contaminated when performing fabrication processes on the material. Therefore, a way to clean and protect the surface

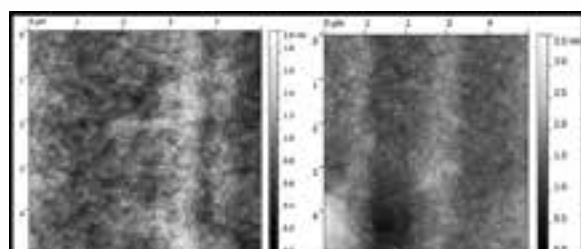


Figure 1: AFM images of the GaSb surface before and after basic photolithography process and compatible chemical clean.

without changing the material's performance is needed. The following atomic force microscopy images depict a surface immediately after growth on the right and on the left is the same sample after going through a standard photolithography process and solvent clean (see Figure 1).

Experimental Procedures:

In this experiment, two samples were tested. The first being an InAs layer 5 nm from the surface and the second being an InAs layer 55 nm from the surface. The samples were first measured for Hall mobility, sheet resistivity, and sheet carrier density by Hall measurements using four-point contacts at the corners of the samples. The samples then underwent an ALD process where in a chamber the GaSb/InAs/AlSb/GaSb heterostructure was heated to 300°C and then cleaned with hydrogen plasma and then with nitrogen plasma for a combined 10 seconds under 50W of power. Then AlN was layered in a self-limiting manor. The exposure to the nitrogen and hydrogen plasmas were repeated 1, 10, and 100 times for different ALD runs, and electronic properties were determined by Hall measurements after the combined plasma cleans and ALD process.

Results and Conclusions:

It was desired that resistivity and mobility measurements (see Figure 2 and 3) stay as close as possible to the original sample to maintain the functionality of the material. Carrier density was expected to change due to removal of surface contamination changing the surface carrier density and bulk properties changing after many cycle exposures (see Figure 4).

AlN deposition including a hydrogen and nitrogen *in situ* plasma clean was thought to be a useful agent in the passivation of GaSb/InAs/AlSb/GaSb heterostructure.

This study has shown that the electrical properties of quantum wells set back at greater distances from the structure's surface are less affected by the cleaning process while the electronic properties of quantum wells close to the structures surface were sensitive to the cleaning process.

M
A
T
S

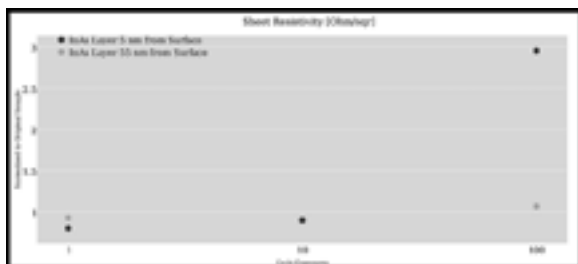


Figure 2: Plot of number of ALD cycles versus resistivity normalized to the original sample.



Figure 3: Plot of number of ALD cycles versus mobility normalized to the original sample.

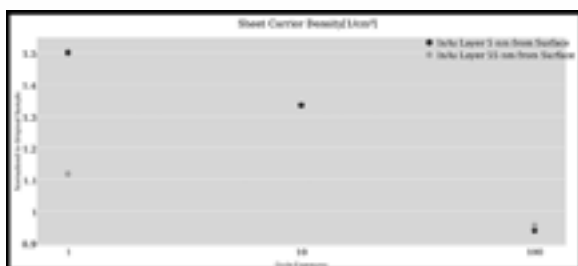


Figure 4: Plot of number of ALD cycles versus carrier density normalized to the original sample.

Future Work:

This ALD process of AlN could be a possible precursor of other treatments of the GaSb surface to prevent impurities from forming on the surface during processing as well as preventing oxidation; it is desired to use the optimal amount of cycle exposures of AlN and then also test deposition of a dielectric on top of the AlN layers to possibly improve the gating process when testing the material.

Acknowledgements:

I would like to thank Borzoyeh Shojaei, Dr. Chris Palmstrøm, and Wendy Isben for all of their help while at UCSB. I would also like to thank the NNIN staff, as well as the funding sources for this project: NNIN REU Program, NSF, and University of California at Santa Barbara.

References:

- [1] Kroemer, Herbert. "The 6.1 Å family (InAs, GaSb, AlSb) and its heterostructures: a selective review." *Science Direct Physica* 20 (2004): 196-203. Print.
- [2] Ruppalt, Laura B., Erin R. Cleveland, James G. Champlain, Sharda M. Prokes, J. Brad Boos, Doewon Park, and Brian R. Bennett. "Atomic layer deposition of Al_2O_3 on GaSb using *in situ* hydrogen plasma exposure." *Applied Physics Letters* 101.23 (2012): 231601. Print.

Cohesion and Adhesion in Thin-Film Organic Nanostructured Materials for Photovoltaic Applications

G. Emily Nitzberg

Mechanical Engineering and Computer Science, University of Portland

NNIN REU Site: Stanford Nanofabrication Facility, Stanford University, Stanford, CA

NNIN REU Principal Investigator: Reinhold Dauskardt, Materials Science and Engineering, Stanford University

NNIN REU Mentor: Christopher Bruner, Chemistry, Stanford University

Contact: nitzberg16@up.edu, rhd@stanford.edu, cbruner9@stanford.edu

Abstract:

The main focus of this project was to study the nano-mechanical properties, cohesion, and reliability of advanced thin-film architectures used in polymer organic photovoltaics. Photovoltaics are devices that convert incident light into usable energy. The cohesion of the photoactive layer, which consists of the semiconducting polymer poly(3-hexylthiophene-2, 5diyl) (P3HT) and small molecule Phenyl-C60-butyric acid methyl ester, or PC₆₀BM, are characterized using micromechanical analysis. The goal of the work was to develop an understanding of how the films adhesive/cohesive and thermo-mechanical properties are related to their nanostructure and processing conditions. In addition, we used a cross-linking agent (BABP) to minimize molecular diffusion, improving thermal stability. In particular, we were interested in how the films were affected under operating conditions; including exposure to air, solar UV irradiation, and temperature. By correlating the results to the efficiencies for our organic photovoltaics and analyzing the trends, we intend to design processing methods that will improve the mechanical reliability of these devices while maximizing thermal stability.

Introduction:

Having a finite amount of fossil fuels is one of the main reasons the development of alternative sources of energy is necessary. Additionally, the burning of said fossil fuels in such large quantities causes severe environmental alterations such as global warming. The project at hand aimed to offer a reliable alternative for fossil fuels with the use of photovoltaics.

Organic cells can be printed into very thin sheets making them weigh significantly less than inorganic based solar cells and allow for flexibility. However, organics tend to be more sensitive to air and moisture, meaning that environmental effects can severely degrade their performance. Our research also indicates that the polymers with small molecules used are relatively fragile from a mechanical perspective. This is important to note since barrier delamination of the solar cell may lead to catastrophic failure within the device. Our main concern for this project was the need for the cells to operate under severe environmental conditions.

The operational principle of an organic cell begins when light is incident upon the device, which is then followed by the absorption of the photon. This process then results in electrons

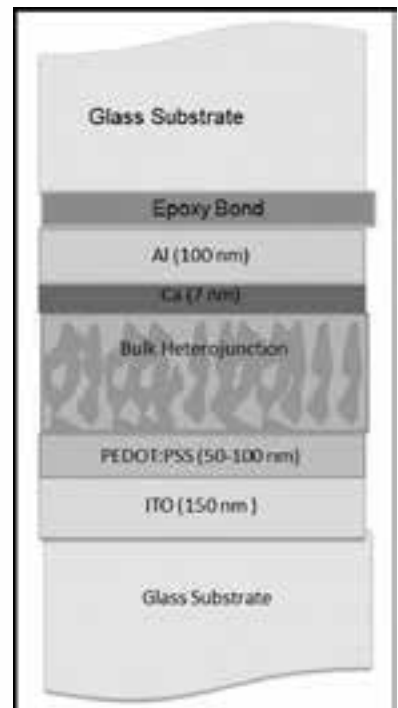


Figure 1: Organic solar cell thin film layer profile.

being excited from the highest occupied molecular orbital to the lowest unoccupied molecular orbital. Charge splitting then occurs allowing for the collection of electrons and holes.

Experimental Procedure and Results:

The organic solar cells at hand consisted of eight layers as shown in Figure 1. The core of the cell was the bulk heterojunction (BHJ) layer, which consisted of a 1:1 weight ratio of P3HT and PC₆₀BM and a particular amount of BABP ranging from 0%-10%.

First, a thin layer of BHJ solution was spin-coated onto a glass substrate and observed under a microscope after various thermal annealing times. As shown in Figure 2, BABP prevented the crystallization of PC₆₀BM with annealing time. This is important to note since it is consistent with past

literature and supports the argument that BABP allows for thermal stability of the BHJ layer via preventing the diffusion of $PC_{60}BM$ molecules.

Next, one of the most important techniques used to test the mechanical properties of the solar cell devices was the four-point bend test (4PB). The 4PB test applies an equivalent amount of force on four parallel directions on the device, two forces acting on top of the device and two on the bottom of the device, in order to propagate a crack within the cell. This technique provided a method for analyzing the cohesion values of the devices. These values are significant because if the cohesion is low failure is more likely to occur. As shown in Figure 3, the cohesion values of the devices decreased significantly when BABP was included in the BHJ layer. These results helped us understand that although BABP increased the thermal stability of the cell, it decreased the mechanical reliability by about 50%. Though the cohesion values decreased significantly, they still remained around 5 J/m^2 , which is the optimal value desired for the devices.

Finally, after analyzing the cohesive strength of the device, it was important to investigate where exactly the failure occurred. In order to do so, an x-ray photoelectron spectrometer (XPS) was used.

XPS emits an x-ray beam onto the surface of the device and utilizes the photoelectron effect to eject core shell electrons from the elements on the surface. The XPS then records peaks at specific binding energies that correspond to each element on the periodic table.

In this case, the two peaks that occurred around 200 eV corresponded to sulfur and the large peak around 300eV corresponded to carbon. XPS analysis showed that failure occurred in the (organic) BHJ layer. This was due to the prominent peaks for sulfur and carbon within the analyzed spectra (see Figure 4).

The presence of sulfur and carbon indicated failure at the BHJ since those were the two common elements of P3HT and $PC_{60}BM$. Also, the failure occurring at the BHJ did not change with BABP concentration and/or anneal time, which reinforced the conclusions made.

Conclusions:

Although organic solar cell devices have many improvements to be made, this project was able to yield a few key conclusions. First, BABP increases the thermal stability yet decreases the cohesion values of the solar cells. Next, failure occurs at the BHJ layer no matter the concentration of BABP in the device, or the anneal time it undergoes. This allows for further analysis to be done on the BHJ in order to maximize its mechanical strength. Finally, devices are able to withstand $5\text{--}11.9\text{ J/m}^2$, which are optimal values for these kinds of organic devices.

Acknowledgements:

Thank you to Professor Dauskardt, Christopher Bruner, and the 2014 Stanford NNIN REU group and staff. Also to the NNIN REU Program and National Science Foundation (NSF) for funding.

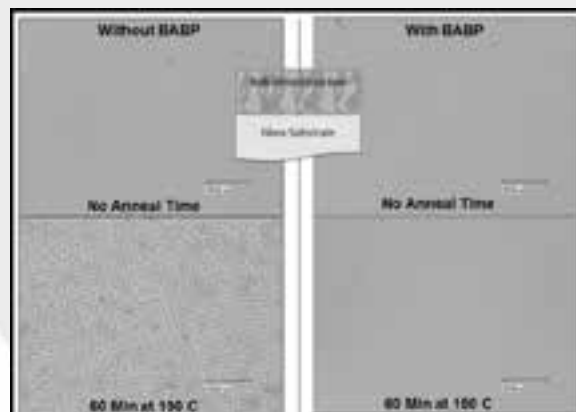


Figure 2: Microscopic images of BHJ layer on glass.

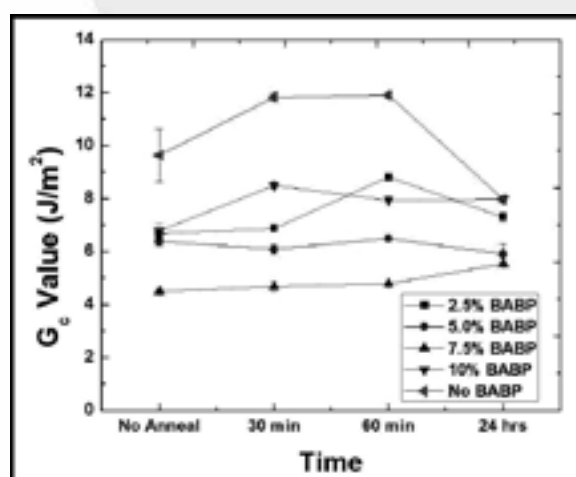


Figure 3: Cohesion values for devices with various BABP concentrations.

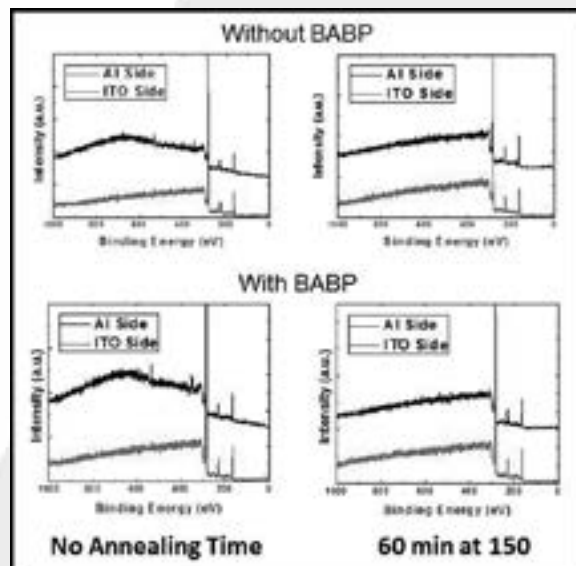


Figure 4: XPS results showed peaks at the sulfur and carbon binding energies.

Patterning Silicon Nanowire Arrays using EBL

Matthew Salmon

Chemical Engineering, North Carolina State University

NNIN REU Site: Institute for Electronics & Nanotechnology, Georgia Institute of Technology, Atlanta, GA

NNIN REU Principal Investigator: Prof. Michael Filler, Chemical and Biomolecular Engineering, Georgia Institute of Technology

NNIN REU Mentor: Ho Yee Hui, Chemical and Biomolecular Engineering, Georgia Institute of Technology

Contact: mcsalmon@ncsu.edu, michael.filler@chbe.gatech.edu, hhui3@gatech.edu

Abstract:

Silicon nanowires have applications as advanced solar energy collectors, lithium ion anodes, catalysts and biological and chemical sensors. Silicon nanowires have demonstrated superior light absorbance in photovoltaic cells. The peak wavelength of light absorbed is tunable, depending on length, doping, spacing and diameter. Length and doping control in silicon nanowires are fairly well understood. The focus of this project was to develop a method for finely controlling diameter and spacing of silicon nanowires in an array and to transfer technology from ultra-high vacuum (UHV) to more scalable systems. Electron-beam lithography (EBL) was chosen because it can pattern samples with the nanometer resolution required. Using poly (methyl methacrylate) (PMMA) as the electron-beam resist, and electron-beam evaporation to deposit gold, an array of gold catalyst nanodots was developed on the silicon substrate surface. Then silicon nanowires were grown from each gold catalyst dot through vapor-liquid-solid deposition — in which silane decomposes on the catalyst surface, creating a liquid gold silicon eutectic, and a silicon crystal grows epitaxially on the bottom of the eutectic droplet. The goal was to create arrays of nanowires with diameters as small as 20 nm.

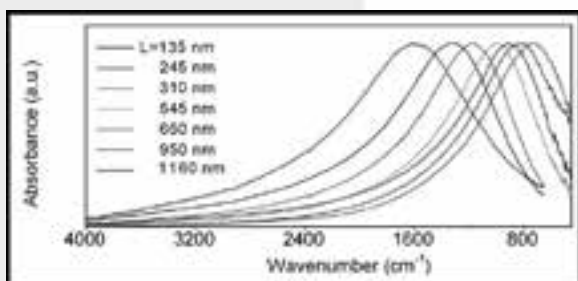


Figure 1: Surface plasmon resonance frequency varies with nanowire dimensions and spacing. (See full color version on page xxxvi.)

Introduction:

Semiconductor nanowires, also called nanopillars, are of increasing interest in scientific research. Their synthesis methods and chemical, mechanical, electronic and photonic properties have been studied. They may have use as solar cell enhancers [1]. Our research team designed silicon (Si) nanowire synthesis methods with the electronic properties in mind. Surface plasmon resonance frequency varies with nanowire dimensions and spacing (Figure 1) [2], so dimension and spacing control is critical to nanowire function.

Experimental Procedure:

A set of samples were made by cutting approximately 1 cm^2 from $<111>$ Si wafers, which are necessary — as opposed to $<100>$ Si — to produce vertical nanowires by the vapor liquid solid growth method [3]. The cut samples were then immersed in 10% hydrofluoric acid (49% HF diluted 1:4 in distilled water) for three minutes to remove silicon oxide (SiO_2), rinsed in distilled water and dried with nitrogen. They were immediately placed in an electron-beam evaporator, pumped down to 8×10^{-7} Torr and coated with 3.0 nm of gold (Au). Au-coated samples may have been stored, in clamshell sample holders in a cool dark space in the cleanroom, for as long as a week.

To grow nanowires, the reactor chamber was first vented. The reactor employed was a “CVD FirstNano Graphene Furnace” with quartz chamber, graphite susceptor, RF heating up to 2200°C , turbo pump for base pressure of 6.0×10^{-7} Torr, and fed by argon, hydrogen (H), silane and methane gas lines. An Au-coated sample was immersed in 10% HF for 15s to remove any SiO_2 that may have formed on unprotected surfaces, rinsed in distilled water and dried with nitrogen.

Immediately, the sample was placed onto the reactor susceptor and the reactor was pumped down to a base pressure below 10^{-5} Torr. The pressure was set to 7.0 Torr with only H flowing

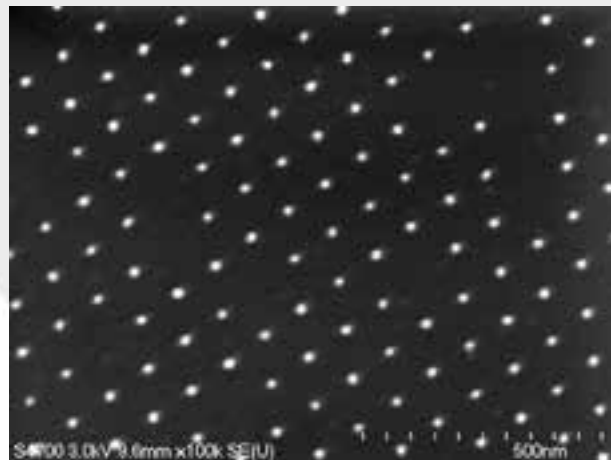
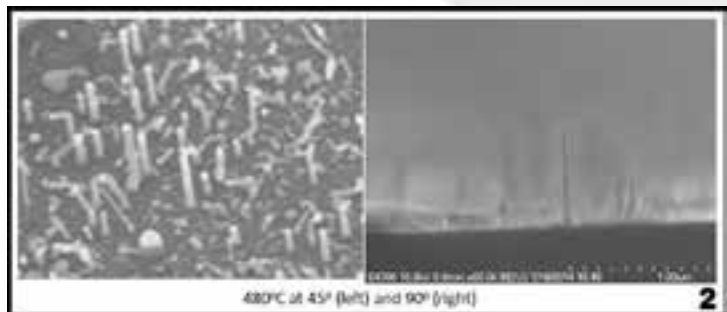
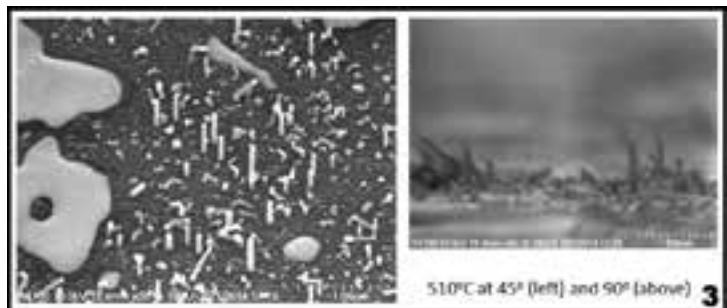


Figure 4: EBL patterning.



Figures 2, above, and 3, below: An inverse relationship was found between temperature and both nanowire kinking fraction and diameter and spacing.

at 500 standard cubic centimeters per minute (sccm). The temperature was then ramped up to 400°C over five minutes and finally, to the temperature setpoint over three minutes. After the temperature setpoint was reached, silane was flowed at 25 sccm for ten minutes and the H flow was reduced to 475 sccm to maintain a constant total flow rate. This was regarded as 350 mTorr of silane pressure for comparison to experimental results from other systems. The system was then vented and the sample removed.

The sample was then fractured for imaging by pressing with a scribe at the edge. The larger fragment of the two was placed on the 45° sample mount and the smaller fragment was placed on the 90° mount so that the fractured edge could be viewed by scanning electron microscopy (SEM).

Results, Conclusions, and Future Work:

At the tested silane pressure, an inverse relationship was found between temperature and both nanowire kinking fraction and diameter and spacing (Figures 2 and 3). There was a direct relationship between temperature and wire size uniformity at this silane pressure. Variability in the reactor controls made it difficult to draw strong correlations between temperature and nanowire morphology. More data needs to be collected, after the reactor is fixed, at higher temperatures and different silane pressures to thoroughly understand how process conditions affect nanowire morphology. Once growth conditions are optimized, EBL patterning methods can be applied to achieve

an ordered array, or more complex pattern, of nanowires by seeding the gold, or other metal, catalyst exactly where it should go (Figure 4).

Acknowledgements:

I would like to recognize my principal investigator Prof. Michael Filler and my mentor Ho Yee Hui. Dmitriy Boyuk and especially Saujan Sivaram, PhD, of the Filler group, were also a great help to me understanding our area of research and how to conduct it. Devin Brown was essential for the EBL part of the project and he did a really fantastic job patiently training Ho Yee and me on this complex tool. A number of the Georgia Tech IEN laboratory staff went the extra mile for me and were most helpful: Dean Sutter, Gary Spinner, John Pham, Thomas Averette, Scott Fowler, Claude Roney, Todd Walters, Eric Woods and Charlie Turgeon. Finally, I would thank the National Nanotechnology Infrastructure Network Research Experience for Undergraduates (NNIN REU) Program and National Science Foundation (NSF) for funding this work.

References:

- [1] Peng K, et al.; *Small*, 1, No. 11, 1062-1067 (2005).
- [2] Chou L-W, Shin N, Sivaram S, Filler M; *Journal of the American Chemical Society*, 134, 16155-16158 (2012).
- [3] Picraux S T, Dayeh S A, Manandhar P, Perea D E, and Choi S G; *JOM*, vol. 62, No. 4, 35-43 (2010).

Mechanical Properties of Hierarchical Nanoporous Metal

Aki Sato

Applied Optics, Chitose Institute of Science and Technology, Japan

NNIN iREG Site: Institute for Electronics & Nanotechnology, Georgia Institute of Technology, Atlanta, GA

NNIN iREG Principal Investigator and Mentor: Antonia Antoniou, Manufacturing Engineering, Georgia Institute of Technology

Contact: m2140050@photon.chitose.ac.jp, antonia.antoniou@me.gatech.edu

Abstract:

There is a lot of research focused on the fabrication of hierarchical nanoporous structures applicable to new devices. Also, polymer has attracted attention in the application of materials. Previous reports in the literature describe the synthesis protocols of nanoporous gold (NPG) obtained by dealloying Au/Ag foil with HNO_3 , and nanoporous copper fabricated by Cu/Si foam dealloying using HF [1]. Furthermore, it is well known that self-organized wrinkle structures are deformable anisotropic microstructures. Those wrinkle structures can be obtained by taking advantage of the difference in Young's modulus between soft and hard materials [2]. In this report, we show the preparation and measurement surface properties of a heterostructures obtained by combining metal foam and polymer. The basic surface properties of the samples will be discussed.

Introduction:

The properties of metals and polymers are quite distinct. In this project, we focused on creating heterostructures by combining polymer and metal foam structures so as to establish a new system with applications as a sensor or actuator. Metal foams can span several length scales. In this system, the porosity is in the nanometer range that offers high surface to volume ratio and allows synthesis of porous metals with unique physical properties. This structure can be obtained via a two-step process involving synthesis of a metal alloy and its controlled corrosion (dealloying) in a solution. During dealloying one element of the alloy dissolves and the remnants self-assemble into a three dimensional sponge. The elastomer used in this project is polydimethylsiloxane (PDMS). This polymer is a soft material and any curling is easy to control via Young's modulus.

One inspiration for the project involves biomimetics that is observing and replicating functional biological surfaces and replicating their functional surfaces so as to obtain superior functional materials. For example, one of the most famous biological functions is the Lotus effect. Lotus leaf surfaces have hierarchical structures ranging from nanometer to micrometer. In previous research, we fabricated a structure that mimicked shark skin by using self-organization with a sample surface made of polymer. But shark skin surface is known to have a functional drag reduction because of its riblet structure. Our intention is to fabricate the same surface with a more durable material like metal.

Periodic buckling structures, similar to the shark skin riblet, are formed by self-organization. This "wrinkle" structure formation depends on the difference in any two material's Young's modulus. Also, the period of wrinkles depends on the hard material's height — $\Lambda \propto 2\pi h(E_f/3E_s)^{1/3}$ — where Λ is the period of wrinkle, h is the thickness of hard layer, E_f equals

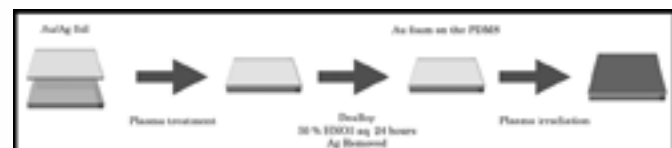


Figure 1: Gold foam on polymer process.

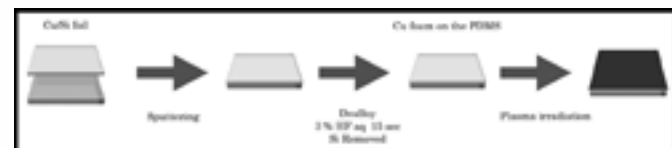


Figure 2: Copper foam on polymer process.

the hard layer's Young's modulus, and E_s is the hard layer's Young's modulus.

Experimental Procedure:

We fabricated two types of metal samples.

Gold Foam on Polymer (see Figure 1). First, we cured PDMS at 70°C for five hours. This PDMS has a Young's modulus of 1.3 MPa. We treated the PDMS surface with a plasma irradiation for 10 min, and then fixed gold (Au) and silver (Ag) complex foil (gold leaf) on top of the PDMS. NP Au foil was formed by dealloying a Au/Ag foil by using a 50% nitric acid water solution for 4, 12, and 24 hours. As a result, we obtained nanoporous gold (NPG) and polymer heterostructures. Finally, we tried using plasma irradiation to change the surface chemistry.

Copper Foam on the Polymer (see Figure 2). In the meantime, we fabricated the same structure using a different

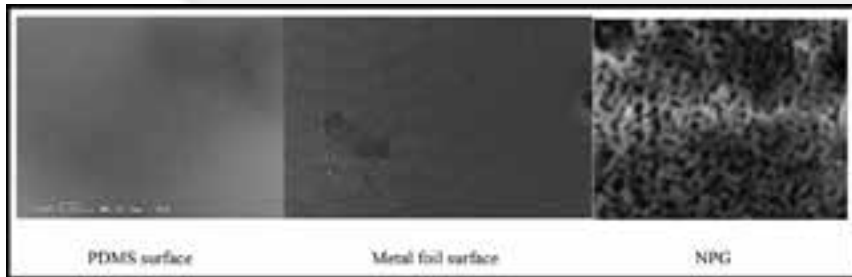


Figure 3: SEM images of surface observations.

Water contact angle	PDMS		Self standing Foil		NPG	
	No plasma	103.4	0 < 40°	48 Hours	4 Hours	
Metal : Hydrophobic Polymer : Hydrophilic	Plasma 10 min		N/A		Gradually Changed	
N = 3 Average	Plasma 30 min		N/A			

Table 1: NPG contact angles.

metal. We again cured the PDMS using the same curling condition of 2-1. After that, the PDMS surface was treated by plasma irradiation for 10 min. We then obtained copper (Cu) and silicon (Si) complex layers by sputtering, and dealloyed a Cu/Si foil using 3% HF water solution for 15 sec. After that, we obtained a nanoporous Cu and polymer heterostructure. Finally, we tried using plasma irradiation for 30 min to change the surface chemistry.

Results and Discussion:

Dealloying. Dealloying NPG for 24 hours resulted in a nanoporous structure with a pore diameter around 20 nm. According to the results of a XPS survey, NPG dealloyed by NHO_3 for 24 hours had a surface that was less than 1% Ag. However after dealloying for only four hours, the sample had 6% Ag. We concluded that this porous diameter and the Au/Ag ratio depends on dealloying time. (See Figure 3.)

Wettability. A lot of biomimetic research focuses on surface wettability. In this report we show NPG contact angle measurement data in Table 1. In general, the polymer surface showed a hydrophilic surface and the metal showed a hydrophobic surface. With no plasma treatment, the polymer surface had hydrophobicity. In contrast, after plasma irradiation, the polymer surface was hydrophilic. On the other hand, our metal form results were the reverse. Also, 24 hours of dealloying the metal foam surface showed that the contact angle was more increased than a four-hour dealloying. Surface wettability depends on surface pore diameter and chemical

metamorphic. We concluded that we could successfully make a hydrophilic metal porous surface.

Conclusions and Future Plans:

We obtained gold foam on PDMS, and we could see the difference in contact angles with this heterostructured surface. Also, we successfully obtained a nanoporous metal structure important for biomimetics. For future work, this structure has to make a clear buckling structure proven using the buckling equation, so we will need to change the thickness of the metal foam in order to obtain the periodic wrinkle structure. We can then consider sliding angle and reduction measurements. Such measurements can establish the combined properties of a complex heterostructure.

Acknowledgements:

Many thanks to Prof. Antonia Antoniou, the National Nanotechnology Infrastructure Network International Research Experience for Undergraduates (NNIN iREU) Program, and the National Institute for Materials Science (NIMS).

References:

- [1] Applied Physics Letters, 103, 241907 (2013).
- [2] T. Ohzono and M. Shimomura, Phys. Rev. B, 2004, 69(13), 132202-132206.

Nanoparticle Photoresists: Synthesis and Characterization of Next-Generation Patterning Materials

Pavel Shapurenka

Chemical Engineering, City College of New York (CUNY)

NNIN REU Site: Cornell NanoScale Science & Technology Facility, Cornell University, Ithaca, NY

NNIN REU Principal Investigator: Christopher K. Ober, Materials Science and Engineering Department, Cornell University

NNIN REU Mentor: Jing Jiang, Materials Science and Engineering Department, Cornell University

Contact: pshaptu00@citymail.cuny.edu, cko3@cornell.edu, jj453@cornell.edu

Abstract:

Hybrid metal oxide nanoparticle photoresists are prominent candidates for next-generation photolithography due to their exceptional sensitivity to extreme ultraviolet (EUV) radiation. To improve the resist's resolution, roughness, and sensitivity (RLS) performance, we explored new compositions for this nanoparticle system. In this study, a series of new nanoparticle resist compositions were synthesized and characterized by solubility and radiation dose tests, as well as deep ultraviolet (DUV) and electron-beam patterning.

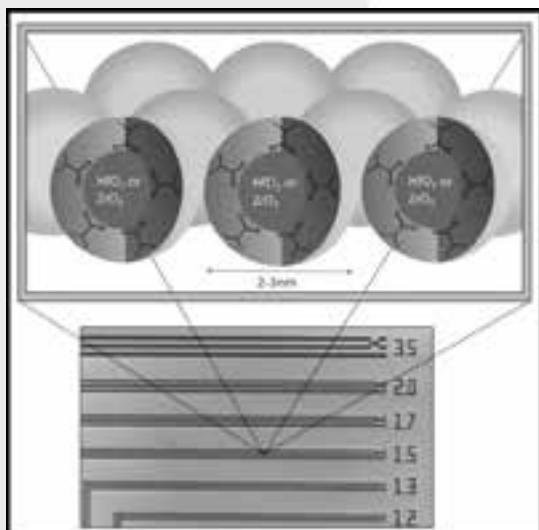


Figure 1: A schematic of the Ober group nanoparticle photoresist.

refractive index, increasing the depth of field, while the organic ligand shell defines the nanoparticle's solubility properties. It is believed that the resists' EUV sensitivity relates to the relative binding affinities of the ligand shells; however, this requires further investigation. These properties provide a unique foundation for a patterning material that can be further explored for optimal performance.

Experimental Procedure:

The nanoparticle resist was synthesized by a zirconia precursor and a carboxylic acid. The reaction workup through precipitation, resuspension, and drying yielded a nanoparticle powder. The particles were run through thermogravimetric analysis (TA Instruments) and dynamic light scattering (Zetasizer) to measure organic content and the particle size distribution.

For patterning characterization, a 10 wt% solution of particles with respect to PGMEA, with an 3 wt% addition of photoacid generator (N-hydroxy-5-norbornene-2,3-dicarboximide perfluoro-1-butan sulfonate), was prepared and spun onto a silicon wafer at 2000 RPM for 60 seconds. After a 60-second post-apply bake at 110°C, the resist was exposed with 248 or 254 nm UV light on the ASML 300C or ABM contact aligner, respectively. The JEOL 9500 e-beam lithography system was used for higher-resolution exposures.

Developing conditions were found by submerging resist samples in various developing solvents at measured durations. Solvents most commonly tried were o-xylene and 4-methyl-2-pentanol. Several developer mixtures were also attempted to more finely control developer kinetics. The ABM contact aligner was used to flood-expose adjacent regions of the wafer to test a series of doses and overall resist sensitivity. A Tencor P10 profilometer was used for film thickness measurements.

Introduction:

If the current microelectronics industry is to continue the trend set by Moore's Law, immediate solutions are required for successful next-generation patterning processes. The processes currently in development use EUV radiation at a 13.5-nanometer wavelength. However, the source for this radiation is currently too weak for industrial production throughput. The nanoparticle photoresist developed by Ober and Giannelis, et al. (Figure 1) is one prominent candidate for next-generation photolithography, helping to mitigate the light source issues with its high EUV sensitivity [1]. The inorganic metal oxide core also provides thermal stability and a higher

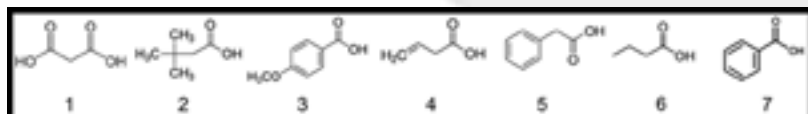


Figure 2: The attempted functional ligands for new compositions, corresponding to the numbering in Figure 3.

	Ligand	pKa	NP size (nm)	Organic content	Pattern?	Developing solvent	Optimal developing time
1	Malonic acid	2.82 5.7	—	—	No	—	—
2	3,3-Dimethylbutyric acid	4.79	4.5	47%	Yes	4-methyl-2-pentanol	30-50 s
3	4-Methoxybenzoic acid	4.47	4.0	60-65%	Yes	5:2 o-xylene:butyl acetate	45 s
4	3-Butenoic acid	4.34	—	—	No	—	—
5	Phenylacetic acid	4.31	6.7	59%	Yes	5:1 o-xylene:heptane	3-5 s
6	Butyric acid	4.82	—	55%	No	—	—
7	Benzolic acid	4.2	—	~60%	Yes	o-xylene	3-5 s

Figure 3: Results of new composition synthesis and developing conditions for each.

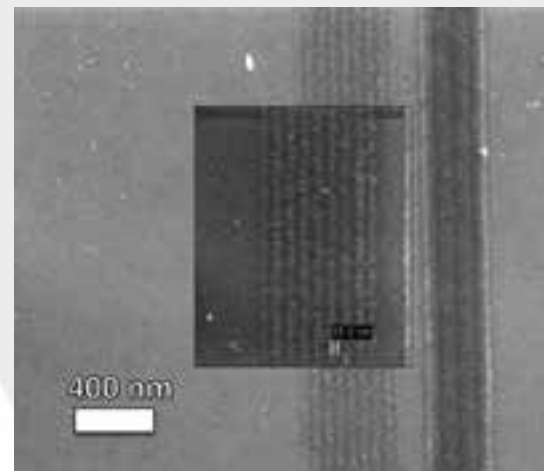


Figure 4: Electron-beam lithography result for the ZrO_2 -phenylacetic acid resist.

Results and Conclusions:

Out of the six studied compositions (compounds 1-6 in Figure 2), two synthesis products agglomerated, and one yielded insoluble particles. The three remaining syntheses were successful; two of which yielded large enough quantities to be studied in greater detail. The two successful ligands were 4-methoxybenzoic acid and phenylacetic acid.

By TGA analysis, it was found that both nanoparticle powders were 60% organic by content, and were approximately 4 to 7 nanometers in diameter. The photoresists patterned effectively under deep ultraviolet light, nearly reaching the 150-nm resolution. Electron beam exposures of 4-methoxybenzoic acid resist showed clear 100-nm features and under-developed features at 50 nm. Phenylacetic acid exposures showed clearly defined features at 80 nm, with visible 35-nm features. In order to maximize resist performance, the developing conditions need to be optimized further.

Future Work:

Having established two new patternable compositions and tailored the processing of each, further characterization is necessary for a better assessment of resist performance and optimization. Since our primary goal is to develop resists for

EUV patterning, we will study EUV exposures and compare the sensitivity with previous formulations.

We will also characterize the critical dimensions of the patterns, namely the line edge roughness and line width roughness (LER/LWR) through SuMMIT, and performing etch resistance tests for applications involving advanced process integration.

Acknowledgements:

I would like to acknowledge the National Science Foundation, the National Nanotechnology Infrastructure Network Research Experience for Undergraduates (NNIN REU) Program, and the Cornell NanoScale Science and Technology Facility for their support. A special thanks to the Ober group, my mentor Jing Jiang, Ben Zhang, Melanie-Claire Mallison, and the rest of the CNF staff for their guidance.

References:

[1] Chakrabarty, S., Sarma, C., Li, L., Giannelis, E. P., and Ober, C. K. (2014). Increasing sensitivity of oxide nanoparticle photoresists (Vol. 9048, p. 90481C-90481C-5). doi:10.1117/12.2046555.

The Optimization of High Growth Rate GaN Thin Film Mobility

Bethany Smith

Materials Science and Engineering, Arizona State University

NNIN REU Site: UCSB Nanofabrication Facility, University of California, Santa Barbara, CA

NNIN REU Principal Investigator: Professor James Speck, Materials Department, University of California, Santa Barbara

NNIN REU Mentor: Brian McSkimming, Materials Department, University of California, Santa Barbara

(2007 NNIN Intern at UCSB and 2008 NNIN iREU Intern in Tsukuba, Japan)

Contact: bbsmith5asu.edu, speck@mrl.ucsb.edu, mcskimming@gmail.com

Abstract:

We explored how n-type gallium nitride (GaN) electron mobility is affected by plasma assisted molecular beam epitaxy (PAMBE) growth conditions. The primary goal was to determine the conditions that produce the highest mobility. First, we performed a doping study to determine which carrier concentration produced the highest mobility. We then optimized mobility by varying plasma power and flow rate. All carrier concentrations and mobilities were determined using the Hall Effect. The doping study demonstrated that the optimal carrier concentration was $\sim 1.5 \times 10^{15} \text{ cm}^{-3}$. The highest mobility at this optimal carrier concentration was $\sim 550 \text{ cm}^2/\text{V}\cdot\text{s}$, thus achieving our primary goal.

M
A
T
S

Introduction:

GaN is a semiconductor of interest because of its current use in light emitting diodes (LEDs) and because of its potential future applications in high power and high frequency devices. However, there are still issues with GaN that need to be explored in order to make these exciting future applications more feasible for large scale implementation. We need to determine how to grow the best quality GaN possible. PAMBE is one prominent GaN growing method used primarily in research settings that gives the user precise control over the samples produced, though it is generally slower than other methods. However, the plasma source used in this study produced growth rates higher than any PAMBE system recorded to date [1]. We hoped to grow the highest mobility GaN possible using this new plasma source by optimizing PAMBE growth conditions. Though many different growth parameters could be varied, the two parameters focused on here were plasma power and nitrogen flow rate into the power source.

Experimental Procedure:

To optimize the PAMBE growth conditions, the experiment was broken into two parts: an optimizing carrier concentration study and an optimizing mobility study. The first part determined the optimal carrier concentration.

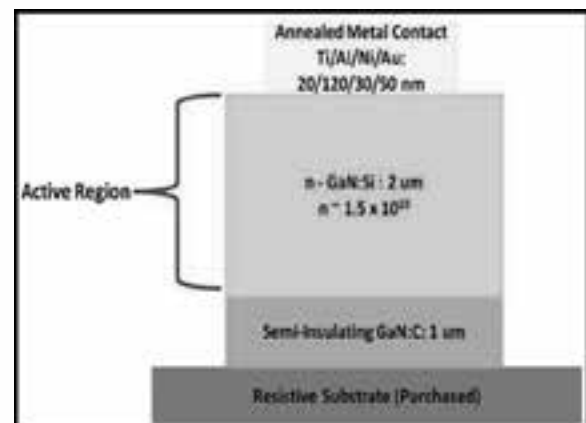


Figure 1: Cross section of a completed sample (schematic).

Various doping concentrations were tested by changing the temperature of the growth chamber. After PAMBE growth with the Nitride Gen III system onsite, each sample was characterized with atomic force microscopy (AFM) to ensure proper morphology. After checking the structure, we added many metal contacts on each sample for testing by a simple two mask contact photolithography process. The metal contacts were arranged in a Greek cross formation, and from each cross, a single Hall Effect measurement could be taken. The Hall Effect measurements determined the carrier concentrations and mobilities. Figure 1 shows a schematic of the cross-section of a completely processed sample. The measured carrier concentration that produced the highest mobility could then be matched with its corresponding doping so that way the mobility could be further optimized in part two.

After the optimal carrier concentration was determined, various plasma powers and nitrogen flow rates were tested to find the combination that produced the highest overall mobility. The samples in this series all had the carrier concentration determined in the first study. The same procedure of sample preparation and testing was used for this series as well.

Results and Conclusions:

Figure 2 is an AFM image showing typical morphology of the samples tested in both series. The step-like features present are indicative of proper PAMBE growth. This step was done as a quality check so that poor films were not processed. Figure 3 shows the results of the carrier concentration study. The two data sets presented were taken at the two plasma conditions shown. Both data sets indicate that the carrier concentration producing the greatest mobility is about $1.5 \times 10^{15} \text{ cm}^{-3}$.

Figure 4 shows the results of the optimization study. All samples presented in Figure 4 have the same carrier concentration of about $1.5 \times 10^{15} \text{ cm}^{-3}$ so that they can be fairly compared. The highest mobility recorded in this series was $\sim 550 \text{ cm}^2/\text{V}\cdot\text{s}$. The plasma power and nitrogen flow rate that produced this highest mobility were 200 W and 10 standard cubic centimeters per minute (sccm).

The results of both studies make sense. In the doping study, lower carrier concentration corresponds to lower doping. Lower doping means fewer possible scattering sites for the charge carriers in the film. Less scattering events corresponds to higher mobility, which is supported by the results of that series. The results of the optimization series also make sense because higher powers and flow rates may have the potential of damaging the film which would lower the mobility.

Future Work:

We hope to continue the optimization study for it to include other plasma powers and nitrogen flow rates so that it is more complete. Once the optimization study is fully complete, other parameters could be tested to further optimize mobility. Also, temperature dependent Hall Effect measurements should be taken so that defect concentrations can be determined. These results could be correlated to the mobilities measured for a more complete understanding of the material.

Acknowledgements:

I would like to thank Professor Speck, my mentor Brian McSkimming, the rest of the Speck group, the UCSB cleanroom staff, and my fellow intern Rachel Lucas for their support and guidance with this project. (My mentor especially deserves credit for his outstanding guidance throughout this REU experience.) Finally, I would like to thank NSF and the NNIN REU Program for their resources and for giving me this wonderful learning opportunity.

References:

- [1] B.M. McSkimming, F. Wu, T. Huault, C. Chaix, J.S. Speck. Plasma assisted molecular beam epitaxy of GaN with growth rates $> 2.6 \mu\text{m}/\text{h}$, *J. of Crystal Growth*, Volume 386, 15 January 2014, Pages 168-174 (2013).

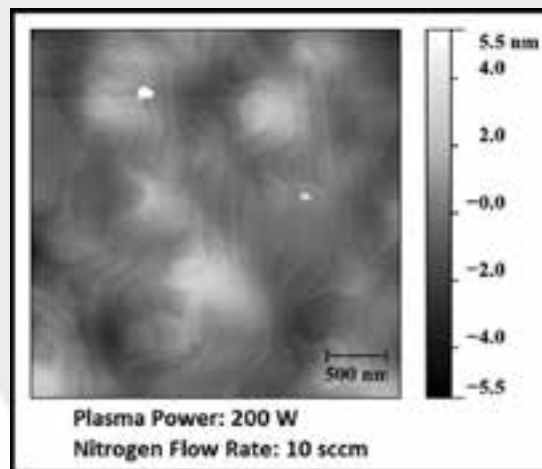


Figure 2: Typical morphology of a GaN film used in this study. All samples tested had similar morphologies.

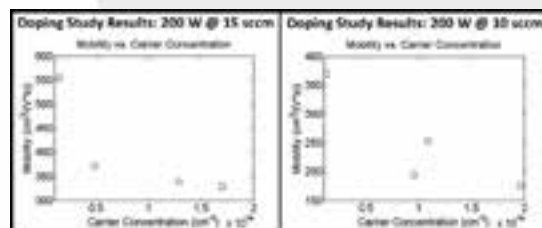


Figure 3: Mobility vs. carrier concentration for the listed growth conditions.

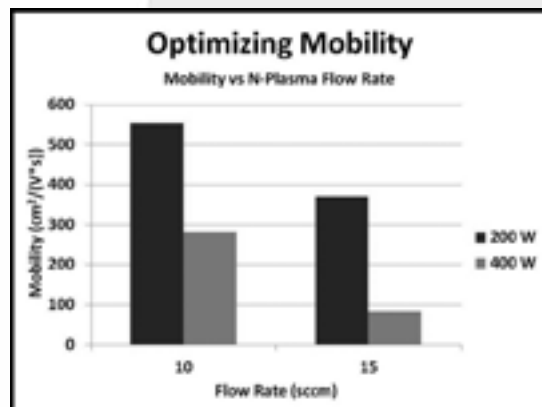


Figure 4: Mobility vs. nitrogen flow rate for plasma powers of 200 W and 400 W.

Doping in Spray-Deposited Fe_2O_3 for Next-Generation Photovoltaics

Wesley Tatum

Physics and Physical Chemistry, Whitworth University

NNIN REU Site: ASU NanoFab, Arizona State University, Tempe, AZ

NNIN REU Principal Investigator: Dr. Meng Tao, Electrical Engineering, Arizona State University

NNIN REU Mentor: Woo Jung Shin, Materials Science, Arizona State University

Contact: wtatum15@my.whitworth.edu, meng.tao@asu.edu, wshin4@asu.edu

Abstract:

The purpose of this experiment was to find optimal and simple parameters for fabrication of highly efficient solar cells with earth rich materials, which are capable of large scale deployment. Spray pyrolysis is a simple method for the creation of thin film solar cells. In this process, a solution is “atomized” into small droplets. A heated substrate evaporates the solvent, leaving behind a precipitated thin film. This technique was used to deposit a film of doped iron oxide (Fe_2O_3) onto a heated glass substrate, with a 100% ethanol solvent. The Fe_2O_3 was doped with zinc from zinc chloride (ZnCl_2). The samples were then analyzed for optimal morphology/film quality, resistivity, and transmittance using 4-point probe, SEM, and spectrophotometer. There was found to be no correlation between morphology patterns of doped and un-doped samples with the same deposition parameters. The optimal doped film structure was found to be amorphous. Optimal doping was at 9%, with a resistivity of $250 \Omega\text{-cm}$.

Introduction:

Current solar technologies are not sustainable at the terawatt scale of energy harvesting and storage. This is because they rely on either silicon (Si) or rare earth metals. Si requires massive amounts of energy for isolation, as well as notoriously harsh chemicals in the manipulation of the Si wafers, such as hydrofluoric acid or “piranha.” Rare earth metals are just that: rare. Should solar energy seek to be a main energy source for society, the materials need to be in abundance and easy to isolate and manipulate. The optimal cell would also be easily translatable to large scale production.

Experimental Procedure:

A solution was prepared with a molarity varying from 0.1-1.0 M ferric chloride (FeCl_3) in a solution of water, ethanol, or a 50/50 mixture of the two. The solution was then mixed with ZnCl_2 to be 4-20% by mass. The solution was sucked into a titanium bodied Fuso Seiki STA-5N atomizing mister (Figures 1 and 2). The solution was sprayed onto a heated substrate (glass slides). On the glass slides, a small shard of Si wafer was pinned down to cover a section of the thickest part of the film (Figure 3), so that its thickness could be measured via profilometry. As the solvent evaporated, a thin film was deposited onto the substrate [1]. Following an experimentally derived “recipe,” approximately $1 \mu\text{m}$ of film was deposited, with varying temperatures, but leaving the liquid consumption rate (LCR) and the nozzle-substrate-distance constant. This combination was used because these three variables all affect the rate at which the solvent is evaporated [1]. The sample was then allowed to cool to a temperature below 150°C before it was removed from the hotplate.

Results and Conclusions:

When the molarity of the FeCl_3 was varied, a correlation between that and film quality was found; the lower the molarity, the better the film quality [1] and the longer the deposition time was required to be. Film quality was judged by the crystallinity. In balancing these factors, 0.11 M FeCl_3 was found to be optimal [2, 3]. Solvent was varied from pure water to pure ethanol. The latter of these extremes yielded both highest film quality and shortest deposition time — 8:00 for 900 nm. Amorphous films (Figure 4) proved to have drastically lower resistivity than crystallized films, by at least two orders of magnitude.

After initial testing, continuous deposition produced lower resistivity than a pulsed deposition (rounds of :20 deposition and 1:00 re-heat period). The optimal resistivity was calculated to be $250 \Omega\text{-cm}$. This was found at 9% doping, which conflicts with literature values [2, 3]. This may be because we used an air carrier gas, rather than pure oxygen, and could also be due to a difference in spray techniques. This result is within three orders of magnitude of the goal $1-5 \Omega\text{-cm}$, which is encouraging, and this resistivity indicates that the material, still in its rudimentary stages, has the potential to be a sustainable and easily produced replacement for Si-based technologies.

Future Work:

Thermal annealing needs to be explored to see if resistivity can be lowered through that route. Sulfurization of the samples also needs to occur to tune the band gap of the film, as well as to lower the resistivity of the film. The p-type doped half of the solar cell also needs to be designed and produced.

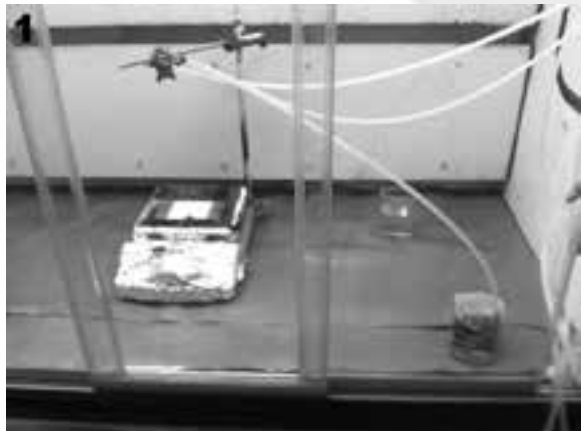


Figure 1, top left: Solution is sucked into the atomizer main body, where it is then sprayed as a mist towards the heated glass substrate.

Figure 2, bottom left: A system of valves and tubing directs pressure to the atomizer piston (controlling liquid flow), the main body (adding pressure to the solution), and to a carrier gas source (air).

Figure 3, right: Sample 7/23-2. Has lowest resistivity. Clearly visible is the section covered by the shard of silicon.

Acknowledgements:

I would like to thank my PI, Dr. Meng Tao, and my mentor, Woo Jung Shin, for all of their help, support and guidance. I would also like to thank the Center for Solid State Electronics Research. Finally, a thanks to the National Science Foundation and all of those who helped to make the NNIN REU Program possible.

References:

- [1] Hamedani, H.A. Investigation of Deposition Parameters in Ultrasonic Spray Pyrolysis for Fabrication of Solid Oxide Fuel Cell Cathode. Ph.D. Thesis, Georgia Institute of Technology, December 2008.
- [2] Ingler, W.; Baltrus, J.P.; Kahn, S.U.M. Photoresponse of p-Type Zinc-Doped Iron(III) Oxide Thin Films. *J. Am. Chem. Soc.* 2004, 126, 33.
- [3] Kumari, S.; Tripathi, C.; Singh, A.P.; Chauhan, D.; Shrivastav, R.; Dass, S.; Satsangi, V.R. Characterization of Zn-Doped hematite thin films for photoelectrochemical splitting of water. *Cur. Sci.* 2006, 91, 8.



Figure 4: Sample 7/23-2. Amorphous film allows for even distribution of the dopant. Ethanol allows for fewer surface defects (e.g., pores, cracks, etc.).

Investigation of Straight-Edge Graphene Grown via Segregation on Ni(110) using Scanning Tunneling Microscopy

Jill Wenderott

Physics, University of Kansas, Materials Science and Engineering, University of Michigan

NNIN iREU Site: National Institute for Materials Science (NIMS), Tsukuba, Ibaraki, Japan

NNIN iREU Principal Investigator: Dr. Daisuke Fujita, National Institute for Materials Science, Tsukuba, Ibaraki, Japan

NNIN iREU Mentor: Dr. Keisuke Sagisaka, National Institute for Materials Science, Tsukuba, Ibaraki, Japan

Contact: jwenderott@gmail.com, fujita.daisuke@nims.go.jp, sagisaka.keisuke@nims.go.jp

Abstract and Introduction:

Controlling the size and shape of graphene grown on metal surfaces is key to utilizing graphene in future applications. Despite having three-fold symmetry, graphene was found to grow in rectangular shapes and with straight edges on the Ni(110) surface. The focus of this project was to clarify the growth mechanism of graphene on the Ni(110) surface by observing the edges of graphene with atomic resolution. Two samples were investigated in this project: pristine Ni(110) and carbon-doped Ni(110). It is known from prior work that nickel contains a small amount of impurity sulfur that will segregate and reconstruct on the surface in a c(2×2) pattern upon annealing. This c(2×2) pattern is hypothesized to be responsible for the rectangular shape of graphene by acting as a template for graphene growth.

Graphene was grown via surface segregation by heating and then cooling the carbon-doped nickel sample. The subsequently segregated graphene was characterized with various surface characterization techniques, including scanning tunneling microscopy (STM). It was found at the atomistic level that the leading edge of graphene grows in stair-stepping fashion and the reconstructed c(2×2) sulfur on the surface of Ni(110) experiences stress during the growth of graphene, as indicated by circuitry patterns seen with STM. The density of the sulfur stress patterns changes with the size and density of graphene flakes, further confirming a direct relationship between the sulfur stress patterns and the growth of graphene.

Methods:

Carbon was doped into a nickel sample at 800°C and in high vacuum for three weeks. The sample was placed in an ultra-high vacuum chamber and heated to 1000°C for one minute and cooled to prompt segregation of graphene. The cooling rate during segregation was manipulated to determine which yielded graphene with the best crystallinity. Upon segregating graphene, the sample was moved into the ultra-high vacuum STM chamber and measured at liquid nitrogen temperature (78K). These STM measurements provided an atomistic survey of the sample.

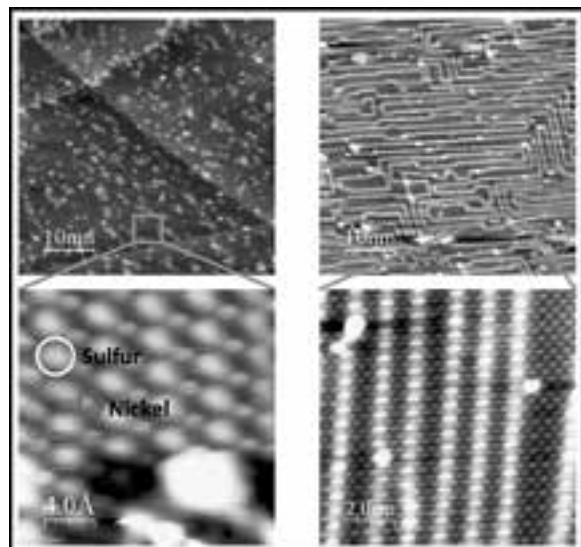


Figure 1: Sulfur on Ni(110) pristine (leftmost images), on C-doped Ni(110) (rightmost images).

The sample was also measured with low-energy electron diffraction (LEED), which showed the average crystal structure of the surface in reciprocal space, and Auger electron spectroscopy (AES), which revealed the chemical composition of the surface. Furthermore, helium ion microscopy, atomic force microscopy (AFM) and scanning electron microscopy (SEM) were used to look at the distribution and average size and shape of graphene flakes. All of these techniques allowed for a macroscopic view of the sample that, once paired with STM images, painted a more complete picture of the graphene growth mechanism on Ni(110).

Results and Conclusions:

The c(2×2) sulfur patterns on the pristine Ni(110) and the carbon-doped Ni(110) were first inspected to elucidate any differences. It was noted that STM images of the pristine Ni(110) surface confirmed the existence of sulfur arranged in

c(2×2) pattern. The carbon-doped Ni(110) STM images also showed surface sulfur, but it was observed that sulfur was stressed in such a way that it produced intricate circuitry patterns (see Figure 1). As graphene was later found on the same sample, it was inferred that the growth of graphene was straining the c(2×2) sulfur either by competing with sulfur for placement on the Ni(110) surface or effectively “pushing” sulfur out of the way during its growth.

Next, graphene and the borders between graphene and sulfur on the carbon-doped Ni(110) were investigated. Fast-Fourier transforms of STM images of graphene showed certain areas of graphene to be highly-ordered, though in several cases highly-ordered graphene bordered semi-ordered graphene (see Figure 2). It was found that decreasing the cooling rate during segregation from 10°C/sec to 3°C/sec increased the ratio of well-ordered graphene to semi-ordered graphene, but decreasing the cooling rate to 0.6°C/sec resulted in multi-layer graphene. Thus, a balance was struck between cooling slow enough to produce well-ordered graphene and not cooling so slowly that multi-layer graphene was formed.

Regarding the borders between c(2×2) sulfur and graphene, it was found that graphene grew in a stair-stepping fashion down to the atomistic scale with STM (see Figure 3). This lent support to the hypothesis that graphene is using sulfur as a template for growth. It was also confirmed that graphene segregated was composed entirely of carbon and the surface surrounding it was covered in sulfur via AES.

Finally, it was observed that as the area of graphene on the nickel surface increased, the stress patterns of the c(2×2) sulfur experienced greater compaction (see Figure 4). When multi-layer graphene was grown, the stress patterns appeared the most compacted, implying that sulfur’s presence on the surface of nickel was potentially directing the growth of graphene. It was postulated that monolayer graphene segregated laterally across the surface of nickel compacting sulfur. When sulfur could not be pushed closer together, the graphene began to grow vertically away from the surface. The use of an element such as sulfur to direct and/or quench the growth of graphene would be a breakthrough in graphene research, but more studies are needed to confirm these preliminary findings.

Future Work:

Theoretical modeling, such as density functional theory, is necessary to support experimental data collected thus far. The relative surface energies of sulfur and carbon on nickel should be considered to help clarify the mechanism of graphene growth. More experimental studies, such as segregation of graphene on nickel after sputtering sulfur from the surface, should also be conducted.

Acknowledgments:

This project would not have been possible without many parties’ support. Many thanks are owed – the National Nanotechnology Infrastructure Network International Research Experience for Undergraduates (NNIN iREU) Program and National Science Foundation, for funding; H. Guo, for helium ion microscope measurements; K. Matsushita, for atomic force microscope measurements; and T. Kusawake, for tungsten tip preparation instruction.

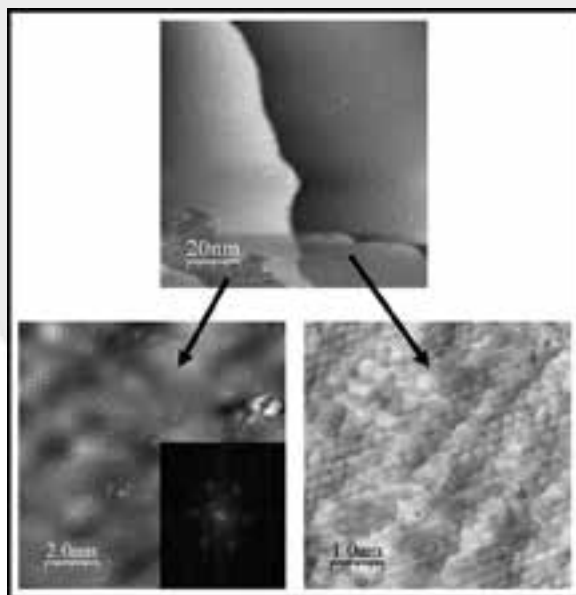


Figure 2: Well-ordered graphene (left) bordering semi-ordered graphene (right).

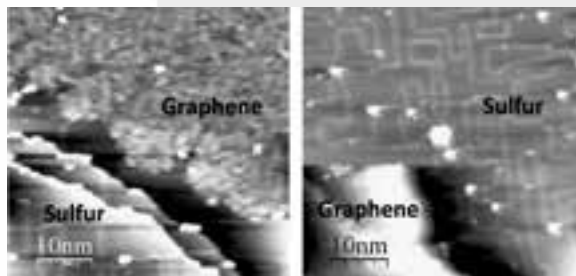


Figure 3: Borders between graphene and c(2×2) sulfur on Ni(110).

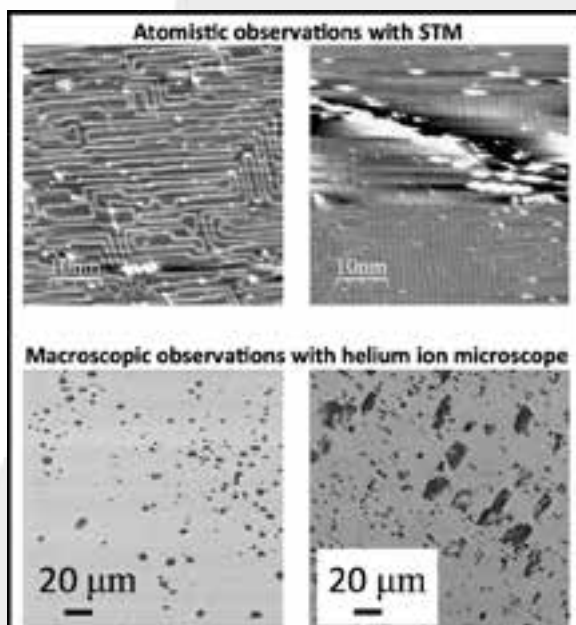


Figure 4: Comparison of sulfur stress patterns (top) to area of graphene growth (bottom), with the leftmost images corresponding to one sample and the rightmost images corresponding to another sample.

BiO(ClBr)_{(1-x)/2}I_x Solid Solutions with Controllable Band Gap Engineering as Efficient Visible-Light Photocatalysts for Wastewater Treatment

Connie Wu

Electrical Engineering and Economics, University of Pennsylvania

NNIN iREU Site: National Institute for Materials Science (NIMS), Tsukuba, Ibaraki, Japan

NNIN iREU Principal Investigator: Prof. Jinhua Ye, International Center for Materials Nanoarchitectonics (WPI-MANA), National Institute of Materials Science (NIMS), Tsukuba, Ibaraki, Japan

NNIN iREU Mentor: Guigao Liu, International Center for Materials Nanoarchitectonics (WPI-MANA), National Institute of Materials Science (NIMS), Tsukuba, Ibaraki, Japan

Contact: wuconnie@seas.upenn.edu, liu.guigao@nims.go.jp, jinhua.ye@nims.go.jp

Abstract:

The objective of this research was to find an efficient photocatalytic material for wastewater treatment. The motivation was the high cost of water treatment by oil refineries, industrial plants, and domestic waste. According to the American Society of Civil Engineers, wastewater infrastructure alone will cost around \$285 billion to build over the next 20 years [1]. As a result, BiO(ClBr)_{(1-x)/2}I_x solid solutions were investigated, because they are promising photocatalysts due to their efficient degradation capability, controllable band gap engineering, and visible light activity. The BiO(ClBr)_{(1-x)/2}I_x solid solutions were tested on water pollution proxies in the form of three dyes: methylene blue (MB), rhodamine B (RhB), and Orange II.

Introduction:

In choosing the particular material to be used, the most important requirement was that the material be visible-light reactive. The current industry standard is titanium dioxide (TiO₂). However, TiO₂ is only UV-light active, which is not ideal in terms of cost-efficiency. Similarly bismuth oxychloride (BiOCl) and bismuth oxybromide (BiOBr) are other bismuth oxyhalides that are only active under UV-light stimulation. Bismuth oxyiodine (BiOI) is visible-light active, however it has a low redox capability, which is detrimental to the degradation process in which the ability to separate electrons and holes is crucial [2]. Finally, the BiO(ClBr)_{(1-x)/2}I_x solid solution is both visible-light active and has a relatively high redox capability, and as such it provided a good basis to start our investigation into its ability to degrade wastewater liquid pollutants. Furthermore from previous research, it was also found that the photocatalyst's band gaps could be altered based on the ratio of halide composition [3]. Consequently, this allows for a method of band gap engineering that can allow for precise control of its visible-light activity.

Experimental Procedure:

The BiO(ClBr)_{(1-x)/2}I_x solutions were prepared using a solvothermal method. First, ethylene glycol was mixed with Bi(NO₃)₃•5H₂O to form a clear solution. Then the appropriate amounts of KCl, KBr, and KI salts were added with molar ratios (1-x)/2:(1-x)/2:x, where x is the percentage of KI. Next the mixture was transferred to a Teflon®-lined autoclave, which was then placed into a 160°C oven for 12 hours.

After the solution was removed from the oven, the resultant mixture was washed with water and air-dried at 70°C.

The photocatalyst was tested against the three pollutant proxies. First 100 ml of dye with a concentration of 8 mg/100 ml was mixed with 20 mg of photocatalyst. This was then placed into a liquid chamber cell and sonicated for 30 seconds before being placed under a 300W Xe arc lamp. Below was a L42 glass filter used to exclusively allow visible light and a water filter to disperse heat. Finally, 3 ml samples of the dye mixed with photocatalyst, taken in either 5-minute or 20-minute intervals depending on the characteristic degradation rate, were filtered through a syringe-driven filter unit. The samples' absorption spectra were obtained with a UV-vis spectrophotometer.

Results:

Displayed in Figure 1 are the SEM images of the solid solutions. They formed uniform crystal spheres with larger clusters as the molar ratio of iodine increased. In the UV-vis absorption spectra (Figure 2), there was a continued blue-shift of the absorption edge as x increased. The reason was that the valence band minimum (VBM) had an upward shift as x increased from the increase in orbital potential energy with the substitution of Cl 3p and Br 4p orbitals by I 5p orbitals, creating a higher VBM [4]. This narrowed the band gap. Generally, a wider visible-light absorption would be beneficial to achieving a higher photocatalytic activity.

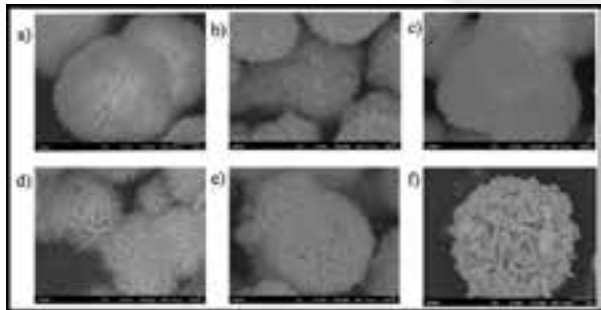


Figure 1: SEM images of the $\text{BiO}(\text{ClBr})_{(1-x)/2}I_x$ crystals.
 (a) $\text{BiO}(\text{ClBr})_{0.5}$ (b) $\text{BiO}(\text{ClBr})_{0.33}I_{0.33}$ (c) $\text{BiO}(\text{ClBr})_{0.25}I_{0.5}$
 (d) $\text{BiO}(\text{ClBr})_{0.13}I_{0.67}$ (e) $\text{BiO}(\text{ClBr})_{0.08}I_{0.83}$ (f) BiOI .

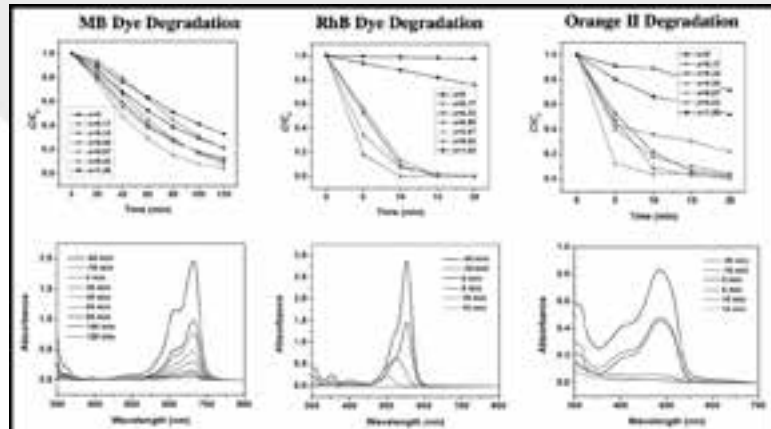


Figure 3: Degradation results.

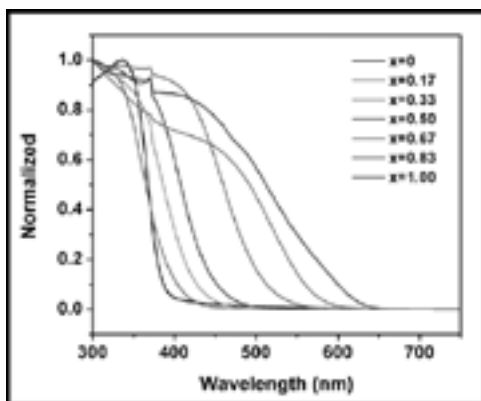


Figure 2: UV-vis absorption spectra of $\text{BiO}(\text{ClBr})_{(1-x)/2}I_x$. (See full color version on page xxxvi.)

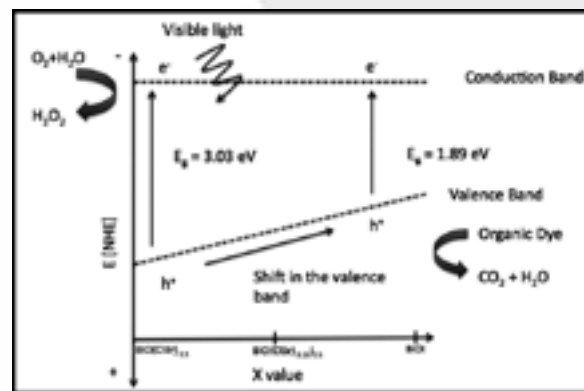


Figure 4: Band gap narrowing from shift in valence band.

Summarized in Figure 3 are the sample degradation results of the three dyes. It was found that an x value of 0.67 had the fastest degradation across all dyes. MB achieved the quickest degradation rate at 120 min, RhB at 5 min, and Orange II at 20 min.

The degradation is achieved through two differing mechanisms. When the photocatalyst was exposed to visible light, there was an excitation of electrons from the valence band to the conduction band, causing a separation of electrons and holes. Some holes reacted with water to form $\bullet\text{OH}$. The dye then reacted with either holes or $\bullet\text{OH}$ to form water and carbon dioxide, completing the degradation process.

RhB, however, degraded faster than the other two dyes due to an additional mechanism. Typically for RhB degradation there is an added mechanism in which the RhB molecules form 2-3 unstable states, which will emit an electron to form RhB^+ . This ion will then interact with holes or $\bullet\text{OH}$ to simultaneously degrade the RhB dye.

Conclusions:

$\text{BiO}(\text{ClBr})_{0.17}I_{0.67}$ exhibited the best photocatalytic properties across the dye pollutants. This is due to the tradeoff between

the increased absorption spectra inherent in the materials and the decrease in the redox capability as shown in the band gap diagram.

Future Work:

In the future, we would like to quantify hole and $\bullet\text{OH}$ generation in the photocatalytic process to confirm and characterize the reactions taking place.

Acknowledgments:

I would like to thank my principal investigator, Jinhua Ye, and my mentor, Guigao Liu, for providing the inspiration for this project. I am also thankful to the NNIN iREU Program and NSF for providing the support and funding for this research.

References:

- [1] "2013 Report Card for America's Infrastructure." American Society of Civil Engineers, n.d. Web. 30 July 2014.
- [2] Zhang, W.; Ind. Eng. Chem. Res. 2013, 52, 6740.
- [3] Zhang H. Phys. Chem. Chem. Phys. 2012, 14, 1286.
- [4] Shannon, R. Acta. Cryst. A 1976, 32, 751.

Effects of Doping on Boride Thermoelectrics

Allison Wustrow

Chemistry, University of California Berkeley

NNIN iREU Site: National Institute for Materials Science (NIMS), Tsukuba, Ibaraki, Japan

NNIN iREU Principal Investigator: Prof. Takao Mori, MANA, National Institute for Materials Science, Tsukuba, Ibaraki, Japan

NNIN iREU Mentor: Dr. Satofumi Maruyama, MANA, National Institute for Materials Science, Tsukuba, Ibaraki, Japan

Contact: wustrow@berkeley.edu, maruyama.satofumi@nims.go.jp, mori.takao@nims.go.jp

Introduction:

Approximately two thirds of the primary energy consumed by mankind is lost, with much of the loss being in the form of waste heat. Thermoelectrics can be used to recover some of that energy by converting a temperature gradient into an electrical current [1]. An ideal thermoelectric has a high Seebeck coefficient, which means it can produce many volts of potential per temperature change across the material, a low electrical resistivity, allowing for easy electronic transport across the material, and a low thermal conductivity, allowing for a temperature gradient to more easily be created across the material. The product of the Seebeck coefficient squared and electrical resistivity are referred to as a material's power factor, which is a measure of how much electrical power the thermoelectric can produce.

Thermoelectrics can be either p-type or n-type depending on whether the material's charge carriers are holes or electrons. Having matching p- and n-type thermoelectrics increases device efficiency. Borides, an attractive candidate for high temperature thermoelectrics, are mostly p-type due to a two electron deficiency in the boron icosahedra in their crystal structure [2]. However, by adding metals such as aluminum to yttrium boride (YB_{25}), one can add electrons to the valence band of the boride, transitioning the thermoelectric into n-type [3]. Doping with vanadium has been shown to improve the thermoelectric properties of another n-type boride, $YB_{22}C_2N$ [4]. In this report, vanadium (V) and manganese (Mn) were doped into yttrium aluminum boride ($YAIB_{14}$) in an attempt to add electrons to the boride valence band, improving the thermoelectric properties of the material.

Methods:

Yttrium oxide and boron powder were mixed together in a 3:8 weight ratio and heated under vacuum at 1600°C for eight hours to make YB_{25} . Samples were ground and washed in 33% nitric acid to remove impurity phases. The powder was rinsed in water, ethanol and acetone and dried. Al powder was added to the powder in a 2:1 YB_{25} to Al weight ratio. The mixture was held at 1300°C for four hours to form $Y_{0.6}Al_{0.6}B_{14}$. The pellet was ground and washed in a sodium hydroxide solution overnight to dissolve any remaining aluminum. The powder was rinsed in water ethanol and acetone.

For the V-doped sample, $Y_{0.6}Al_{0.6}B_{14}$ (0.762g) and vanadium diboride (0.042g) were heated to 1500°C for five minutes at 100 MPa using a spark plasma sintering system. The Mn-doped sample was made by adding $Y_{0.6}Al_{0.6}B_{14}$ (0.770) and manganese powder (0.036g) and heating in the same manner. Undoped $Y_{0.6}Al_{0.6}B_{14}$ pellet was made by heating the powder (0.84g) under the same conditions in the spark plasma sintering system. Seebeck coefficient and resistivity measurements were made using ZEM-2. Annealed samples were made by annealing at 1000°C for eight hours under vacuum and four hours under argon, respectively.

Results:

Doping YAIB with V and Mn improved the thermoelectric properties. Resistivity for both samples was much lower than for the undoped sample as shown in Figure 1. Both V and Mn are capable of donating some electrons to the boride electrical network. The addition of carriers to the conductive network increases the conductivity of the material. Unfortunately it also lowers the Seebeck coefficient as seen in Figure 2, as the voltage produced by a temperature difference is lower upon the addition of more carriers. However, by combining the two factors, one can see that the power factor for doping with both elements is larger than that of the undoped sample.

To further improve the power factor, the V-doped sample was annealed both under vacuum and argon. When annealed under vacuum, the Seebeck coefficient improved, suggesting removal of dopants from the material. The resistivity did not change with annealing, suggesting the removal of impurities from the material and the resulting decrease in resistivity balanced out the increase in resistivity caused by the removal of dopants. When the sample was annealed under argon, the Seebeck coefficient and resistivity both decreased, which is consistent with an increase in doping, as the extended heating assumedly allowed the vanadium to intercalate into the structure. The power factor for both annealing processes was higher than for the un-annealed sample. The sample annealed under vacuum had the highest power factor.

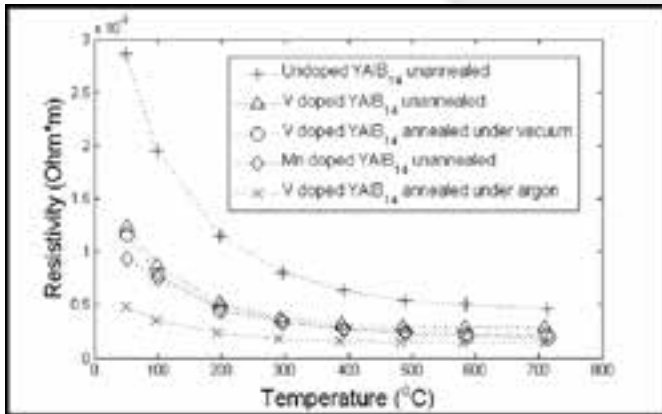


Figure 1: Resistivity of vanadium and manganese doped samples. Most samples had similar resistivities. Undoped $YAIB_{14}$ had high resistivity, and vanadium doped $YAIB_{14}$ annealed under argon had low resistivity.

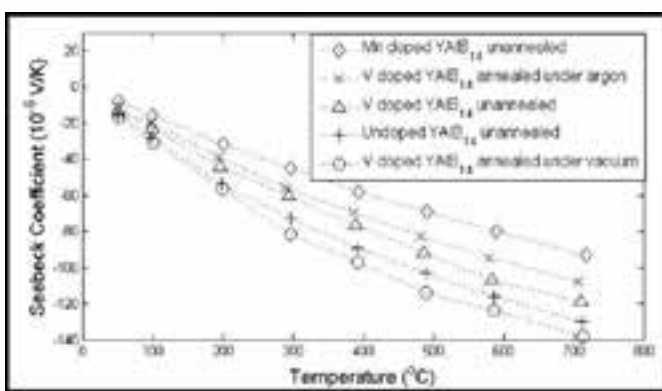


Figure 2: The Seebeck coefficient of vanadium and manganese doped samples. The lowest Seebeck coefficient belongs to manganese doped $YAIB_{14}$, and the highest is vanadium doped $YAIB_{14}$ annealed under vacuum.

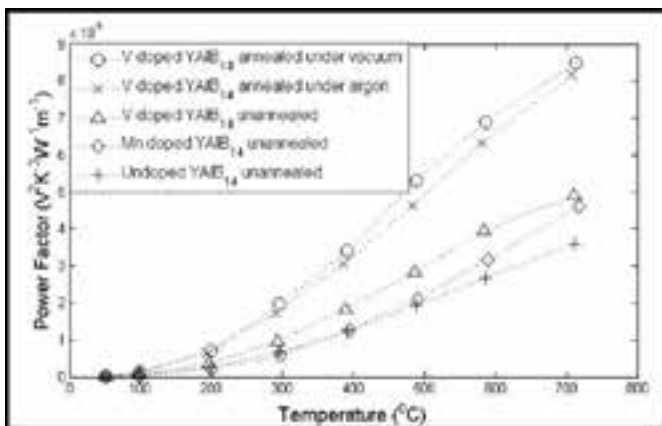


Figure 3: Power factor of vanadium and manganese doped samples. Annealed vanadium doped samples had the highest power factor.

Conclusions:

Yttrium aluminum bromide's thermoelectric properties can be enhanced by additional doping with vanadium and manganese as well as annealing the sample after doping. However the thermoelectric properties are still much poorer than the p-type boron carbide. Further research is needed to determine which dopants increase thermoelectric properties, and to discover the mechanism by which annealing changes the Seebeck coefficient. This will lead to a better understanding of how to create more efficient n-type boride thermoelectrics.

Acknowledgements:

I would like to thank Prof. Takao Mori, Dr. Satofumi Maruyama, and the entire Mori group for their guidance. I would also like to thank the NNIN iREU Program and NSF for funding this research, and the National Institute of Materials Science for hosting me.

References:

- [1] "Thermoelectric Nanomaterials", ed. K. Koumoto and T. Mori, Springer Series in Materials Science (Springer, Heidelberg, 2013) pp. 1-375.
- [2] Mori, T. "Higher Borides", in: Handbook on the Physics and Chemistry of Rare-earths, Vol. 38, ed. K. A. Gschneidner Jr., J. -C. Bünzli, and V. Pecharsky (North-Holland, Amsterdam), pp. 105-173 (2008).
- [3] Maruyama, S., Miyazaki, T., Hayashi, K., Kajitani, T., Mori, T.. Applied Physics Letter, 101 (2012) 152101.
- [4] Prytuliak, A., Maruyama, S., Mori, T.. Materials Research Bulletin, 48, (2013), 1972.

Design and Fabrication of a Microfluidic Device to Study Tumor Cell Mechanics During Metastasis

Michael Homsy

Chemical Engineering, The Ohio State University

NNIN REU Site: Penn State Nanofabrication Laboratory, The Pennsylvania State University, University Park, PA

NNIN REU Principal Investigator: Dr. Siyang Zheng, Department of Biomedical Engineering, The Pennsylvania State University

NNIN REU Mentor: Yiqiu Xia, Department of Biomedical Engineering, The Pennsylvania State University

Contact: homsy.3@osu.edu, siyang@psu.edu, yzx114@psu.edu

Abstract and Introduction:

The majority of cancer-related deaths do not result from the primary tumor, but rather, secondary tumors formed via metastasis [1]. During metastasis, a tumor cell migrates to distant organs or tissues through narrow gaps that are smaller than the size of the cell, such as pores in dense extracellular matrix networks. The characteristic mechanical properties of tumor cells that facilitate their movement through these paths are not well understood [2]. In addition, conventional methods of studying cell mechanics, such as micropipette aspiration, require specialized equipment and training [3]. On the other hand, microfluidics is an accessible alternative that is capable of simulating the *in vivo* environment of a metastasizing tumor cell [1].

To effectively explore the role of tumor cell mechanics during metastasis, a multilayer polydimethylsiloxane (PDMS) microfluidic device was designed and fabricated using soft lithography to contain narrow paths that mimic the small

gaps through which tumor cells metastasize. Specifically, the device consisted of multiple arrays of microgaps where tumor cell behavior was observed under a microscope. Furthermore, a valve feature was incorporated in the design in order to direct the flow through one channel at a time [4]. Using human breast cancer cell line MDA-MB-231, initial experiments demonstrated that our simple device is capable of conducting intricate tumor cell experiments with the purpose of developing a more complex model of the tumor cell.

Methods:

The device was designed to have three components, as shown in Figure 1. The first component contained the inlet and flow channels. The second component functioned as a valve to open or shut particular flow channels. This valve component consisted of multiple air chambers and control channels that were positioned above and perpendicular to the flow channels. The third component contained the outlet and arrays of microgaps of widths varying from 5 to 10 μm . In addition, only one microgap array could be observed under a microscope. Therefore, the valve component served to direct the flow of tumor cells through one microgap array at a time. Eventually, a microgap array became clogged with cells, and the valve component was used to switch the flow to a different microgap array, allowing multiple experiments to be performed on the same device.

In order to fabricate the device, a silicon wafer was first patterned with the outlet and microgap arrays using SU-8 photoresist. Next, AZ 4620 photoresist was used to pattern the inlet and flow channels, and the wafer was baked to produce flow channels with a rounded profile. Another silicon wafer was patterned with the valve component using SU-8. Finally, PDMS was molded over each wafer, and the two molds were bonded to each other and to a glass slide.

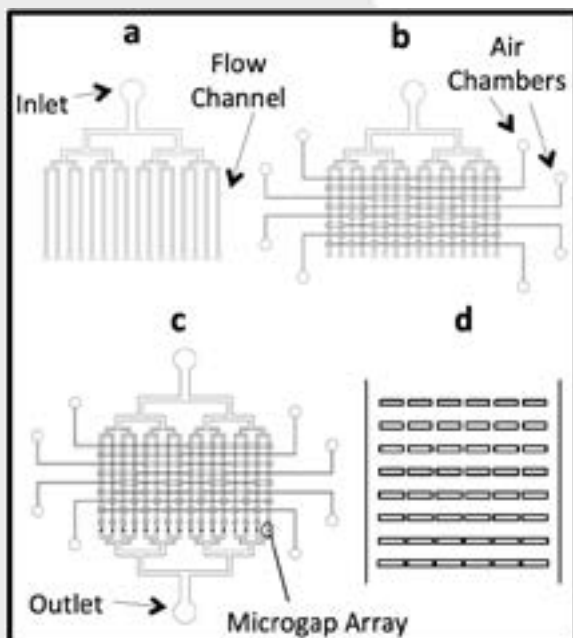


Figure 1: Design of device. (a) The first component. (b) The valve component positioned above flow channels. (c) All components. (d) Microgap array.

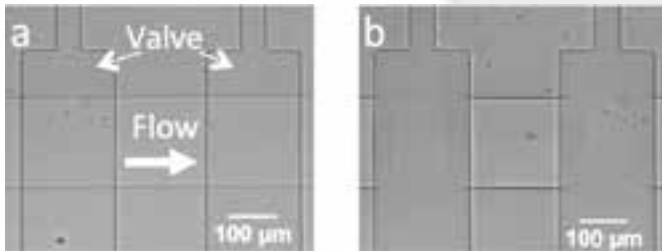


Figure 2: Valve channels (vertical) and a flow channel (horizontal). (a) Before air pressure is applied through the air chambers of the valve channels. (b) After air pressure is applied.

Results and Conclusions:

The valve component was successful in enabling and preventing flow through flow channels. Figure 2 illustrates the valve mechanism. When external air pressure was applied in air chambers, the control channels were triggered to push down and compress the flow channels below. Using a specific combination of air chambers permitted flow only through the desired flow channel.

MDA-MB-231 cells were cultured and then suspended in phosphate buffered saline (PBS). A syringe pump was used to inject the cells in suspension into the inlet at a flow rate of 1 mL per hour. Using our device, we observed tumor cell behavior at arrays of microgaps, which simulate the narrow gaps that tumor cells squeeze through during metastasis.

We observed that the extent of tumor cell deformation and success in passage through a microgap array depended on microgap width. In Figure 3, a tumor cell advanced through the first microgap with a width of 5.0 μm, but was trapped by a slightly narrower microgap with a width of 4.8 μm despite extreme deformation of the cell. Another tumor cell, in Figure 4, immediately advanced through the first microgap with a width of 6.1 μm, but took 26 seconds to pass through the next microgap with a width of 5.6 μm. These preliminary experiments indicate that our device can be used to conduct experiments to examine relationships between different factors, such as cell line and flowrate, and tumor cell behavior. In addition, different versions of the device could be designed to have altered microgap shapes and lengths. By using this device to gather data on tumor cell mechanics during metastasis, we can eventually develop a more complex model of the metastasizing tumor cell.

Acknowledgements:

I would like to thank Kathleen Gehoski, Yiqiu Xia, Dr. Zheng, the members of the Micro and Nano Integrated Biosystem Laboratory group, and the Penn State Nanofabrication Lab

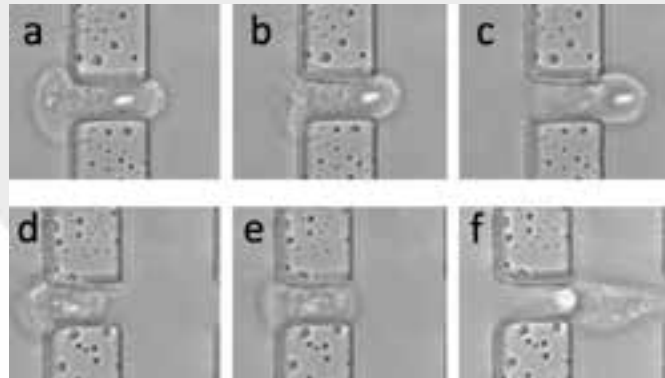


Figure 3: (a) (b) (c) A tumor cell passed through the first microgap (5.0 μm) in 18 seconds. (d) (e) (f) The same tumor cell was unable to pass through a second microgap (4.8 μm).

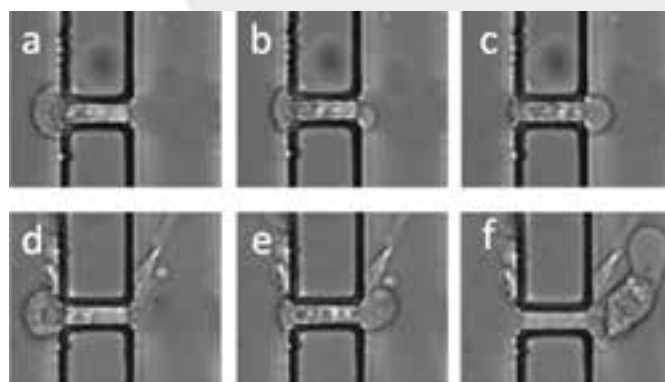


Figure 4, below: (a) (b) (c) A tumor cell passed through the first microgap (6.1 μm) in 1 second. (d) (e) (f) The same tumor cell successfully passed through a second microgap (5.6 μm) in 26 seconds.

M
E
C
H

staff. I would also like to thank the National Nanotechnology Infrastructure Network Research Experience for Undergraduates Program and the National Science Foundation for supporting this research.

References:

- [1] H. W. Hou, et al. Deformability study of breast cancer cells using microfluidics. *Biomed Microdevices*, 2009, 11, 557-564.
- [2] M. Mak, C. A. Reinhart-King, and D. Erickson. *Lab Chip*, 2013, 13, 340-348.
- [3] Q. Guo, S. Park, and H. Ma. Microfluidic micropipette aspiration for measuring the deformability of single cells. *Lab Chip*, 2012, 12, 2687-2695.
- [4] J. Melin, and S. R. Quake. Microfluidic Large-Scale Integration: The Evolution of Design Rules for Biological Automation. *Annu. Rev. Biophys. Biomol. Struct.*, 2007, 36, 213-31.

Microfabrication and Dynamic Testing of Electromagnetic Microactuators for Endomicroscopy

Samantha Kang

Mechanical Engineering, University of Washington, Seattle

NNIN REU Site: Lurie Nanofabrication Facility, University of Michigan, Ann Arbor, MI

NNIN REU Principal Investigator: Professor Kenn Oldham, Mechanical Engineering, University of Michigan, Ann Arbor

NNIN REU Mentor: Jongsoo Choi, Mechanical Engineering, University of Michigan, Ann Arbor

Contact: kangsam7@uw.edu, oldham@umich.edu, jongs@umich.edu

Abstract and Introduction:

Current endoscopic imaging, while sufficient for detecting gastrointestinal polyps, is unable to see below the tissue surface where cancer can begin [1]. Unlike conventional white light endoscopy, which is limited to horizontal (XY) planar imaging, more advanced endoscopy tools such as dual-axes confocal endomicroscopes can perform rapid optical sectioning and permit vertical (XZ) cross-sectional images of the tissue by using z-displacement scanning microactuators. Consequently, how far these endomicroscopes can see into the tissue is limited by how much z-displacement actuation can be achieved in small diameter (3-5 mm) endoscopes [2].

In this work, we successfully fabricated electromagnetic z-displacement microactuators using semiconductor micro-fabrication techniques and by characterizing the electroplating parameters of permalloy (20% iron, 80% nickel), a material that exhibits strong magnetic properties. A laser Doppler vibrometer (LDV) was used to determine the microactuator's z-displacement at different resonant frequencies.

Second generation microactuators were then designed and fabricated with the objective to exhibit greater z-displacement by using silicon dioxide (SiO_2) as the material for the bending beams in the microactuators. The testing results of the first generation devices demonstrate that electromagnetic microactuators could prove an attractive alternative to current piezoelectric, electrostatic, and thermal microactuators, which are complicated to assemble due to electrical connection requirements.

Fabrication Process:

First Generation: Seed layers—50Å of chrome (Cr) and 500Å of copper (Cu), respectively—were deposited onto a silicon (Si) wafer using electron beam evaporation. AZ-9260 photoresist was then spin-coated and patterned onto the wafer, and then inserted into a nickel-iron electroplating bath.

Our main goal was to electroplate a thin film (8-10 μm) permalloy with low residual stress since any deformation in the actuators will interfere with its performance. After characterization, we employed a pulse-reverse plating program with an anodic (forward) current density of 20 mA/cm^2 for 20 milliseconds (ms), a cathodic (reverse) current density of

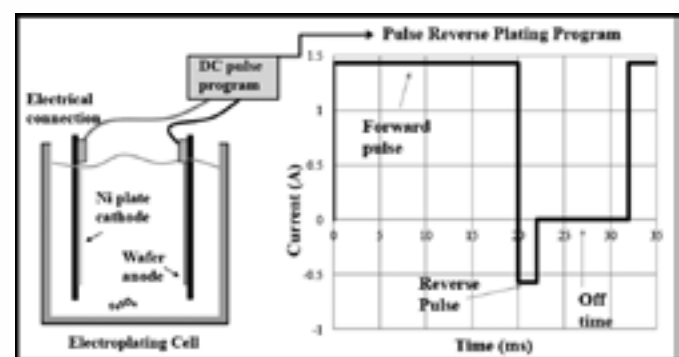


Figure 1: Electroplating set-up and program.

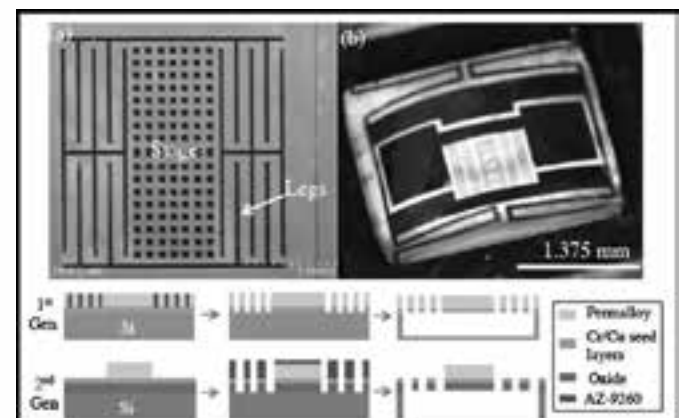


Figure 2: (a) SEM image of device. (b) Fully released 2nd generation device, process flows (below).

-8 mA/cm^2 for 2 ms, and an off time of 10 ms (see Figure 1) [3]. After 120 minutes of electroplating, 8 μm of low residual stress permalloy was deposited onto the actuators. Energy dispersive x-ray spectroscopy analysis revealed the permalloy was 88.25% nickel, 11.75% iron, and magnetic. After etching the seed layers, the wafer was processed with xenon difluoride to isotropically etch the Si and release the devices (Figure 2a).

Second Generation: To fabricate actuators with only SiO_2 as the legs, three masks were designed in AutoCAD to allow for backside etching and selective electroplating. Similar to the first generation devices, 50Å of Cr and 500Å of Cu seed

layers, respectively, were deposited onto a $2\text{ }\mu\text{m}$ SiO_2 -coated wafer via electron-beam evaporation. AZ-9260 photoresist was then spin-coated and patterned onto the wafer which was placed into the electroplating bath.

Due to a small conductive area—less than 20% total wafer area—copper sulfate initially formed instead of permalloy because of the low applied forward current (0.21A). We discovered that increasing the plating program's forward current, which is typically determined by multiplying the current density by the conductive plating area, yielded magnetic permalloy. After increasing the forward current such that the effective area was more than 80% of the total wafer area, we were able to electroplate $6.95\text{ }\mu\text{m}$ of magnetic permalloy after 20 minutes. AZ-9260 photoresist was spin-coated and patterned using the second mask; this layer also protected the permalloy structures during etching. Next, the seed layers were etched, and the oxide layer on the front side of the wafer was patterned using reactive ion etching. Finally, backside lithography, reactive ion etching, and deep reactive ion etching were completed to fully release the microactuators (see Figure 2b).

Dynamic Testing Results:

A custom made electromagnet—ferrite core wrapped with magnet wire—was placed under an actuator normal to the magnetic field generated by running current through the coil. 16 V AC peak-to-peak with 8 V offset was applied to the electromagnet such that the microactuators would generate only positive z-displacement. The effective magnetic field measured was 270 Gauss. LDV was used to measure z-displacements achieved during the frequency sweeps and to locate resonant frequencies. For testing, the LDV was focused on two parts of the actuator: the stage center and the right end of the stage. A MATLAB code was written to process the data as seen in Figure 3 (center of stage curve). Two resonant peaks at approximately 340 Hz ($300\text{ }\mu\text{m}$) and 680 Hz ($476\text{ }\mu\text{m}$) were observed. Figure 4 shows a microactuator responding to a high magnetic field gradient.

Conclusion and Future Work:

We determined a pulse reverse plating program that yielded thin film permalloy and discovered that the forward pulse has the most influence on plating. First generation prototype testing results indicate that large (more than $200\text{ }\mu\text{m}$) z-displacement was achieved at resonant frequencies. Although the current electromagnet is too large to be placed in an endoscope, this work demonstrates the exciting potential of electromagnetic actuators in endomicroscopy due to its wireless assembly.

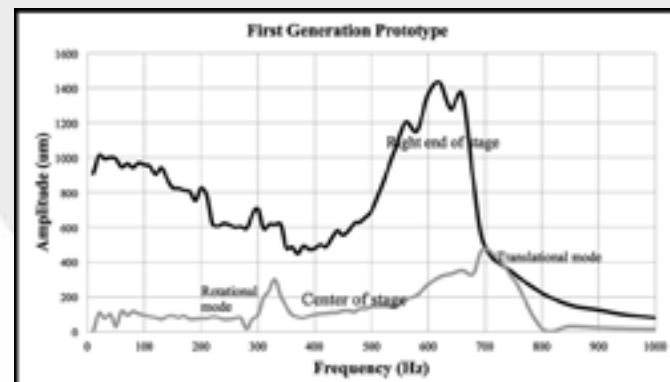


Figure 3: Results.

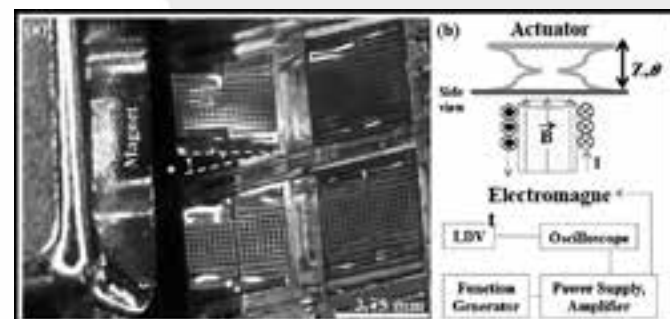


Figure 4: (a) First generation prototype tilting. (b) Testing set-up.

Future testing of second generation devices, further characterization of permalloy electroplating, and improved design of future microactuators must be done to implement electromagnetic actuators in a prototype endomicroscope.

Acknowledgements:

I owe many thanks to my mentor Jongsoo Choi, my PI Professor Oldham for his guidance, the Oldham lab group, the Lurie Nanofabrication staff, and Brandon Lucas for all of their help. I also thank the NNIN REU Program and the National Science Foundation for this great opportunity and funding.

References:

- [1] Qiu, Zhen, et al. *Gastroenterology*, V.146, Issue 3, 615-617.
- [2] Piyawattanametha, W., and T. D. Wang. *IEEE Journal of Selected Topics in Quantum Electronics* 16.4 (2010): 804-14.
- [3] Flynn, D., and M.p.y. Desmulliez. *IEEE Transactions on Magnetics* 46.4 (2010): 979-85.

A Tri-Axial Angular Accelerometer for Vestibular Prostheses

Yu Kitamura

Graduate School of Engineering, Kobe University, Japan

NNIN iREG Site: Institute for Electronics & Nanotechnology, Georgia Institute of Technology, Atlanta, GA

NNIN iREG Principal Investigators and Mentors: Professor Farrokh Ayazi and Professor Pamela T. Bhatti,

School of Electrical and Computer Engineering, Georgia Institute of Technology

Contact: 131t328t@atu.kobe-u.ac.jp, ayazi@gatech.edu, pamela.bhatti@ece.gatech.edu

Introduction:

The vestibular system is the system that informs the brain about head motion and orientation to keep stabilization of the visual axis, head and body posture. Because vestibular disorders are common and often cannot be treated by existing approaches, vestibular prostheses had been investigated [1]. A vestibular prosthesis captures angular and linear head motion using inertial sensors. This information is coded as current pulse waveforms and applied to vestibular nerves. As a result, the prosthesis provides the central vestibular system with information about head motion and orientation. For an implantable vestibular prosthesis, it is paramount to reduce system power as well as size. Especially, gyroscopic sensors, which detect angular acceleration, are key components of vestibular prostheses systems [2]. Their performance determines the performance of the whole system in terms of power consumption.

There are mainly two methods to detect angular acceleration, direct measurement and indirect measurement. Recently, gyroscopes that utilize the indirect measurement method are widely used for motion detection because of their high sensitivity. Current gyros are based on the Coriolis effect, which requires a vibratory structure in order to achieve the required sensitivity. Due to input vibratory signal, however, they consume high power. On the other hand, power consumption of angular accelerometers, which use the direct measurement method, is lower than gyroscopes, because they have a passive sensor that does not require vibratory input signal.

This summer, we focused on developing a tri-axial angular accelerometer for vestibular prostheses to take advantage of

the low power consumption of angular acceleration sensors in order to reduce battery size and extend battery life of the prosthesis device.

Table 1 summarizes the requirements angular accelerometers have to fulfill for the application of a vestibular prosthesis. The maximum detectable signal is required to be larger than 1000 r/s^2 . This is the maximum value evaluated by 700 test samples in daily activities [3]. The minimum detectable signal is required to be smaller than $1.75 \times 10^{-2} \text{ r/s}^2$, which is the same value of resolution of human vestibular systems evaluated by the deviation of the eye caused by vestibule-ocular reflex [4]. Finally, the bandwidth is required to be approximately 20 Hz.

Device Design:

To detect three axis angular acceleration, we proposed two types of devices, showed in Figure 1(a). Both of these sensors are capacitive sensors designed on a silicon-on-insulator (SOI) substrate. The Z axis sensor, called a yaw angular accelerometer, has one proof mass suspended to the anchor that is placed at

Parameter	Requirements	Device characteristics
Maximum detectable signal	$1000 \text{ [r/s}^2]$	Linear operation range $> \pm 1000 \text{ [r/s}^2]$
Minimum detectable signal	$1.75E-2 \text{ [r/s}^2]$	$TNEA < 1.75E-2 \text{ [r/s}^2]$ $TNEA = \sqrt{BNEA^2 + CNEA^2}$
Bandwidth		20 [Hz]

TNEA: Total Noise Equivalent Acceleration
BNEA: Brownian Noise Equivalent Acceleration
CNEA: Circuit Noise Equivalent Acceleration

Table 1: Specification requirements of angular accelerometer for vestibular prostheses.

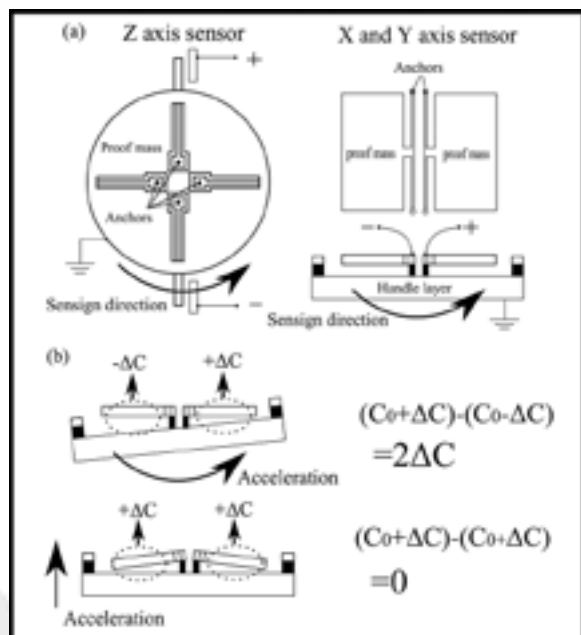


Figure 1: Schematic diagram of (a) angular accelerometers and (b) detection principle of differential design.

the center of the device by four beams. X and Y axis sensors, called roll and pitch angular accelerometers, have two proof masses that are connected to dual anchors by a torsion beam. We employed an in-plane gap of device layer to detect Z axis angular acceleration, and vertical gap between device layer and handle layer to detect X and Y axis angular acceleration. Thanks to utilizing a handle layer as bottom electrodes, these devices can be fabricated with one mask process.

In order to reduce cross axis sensitivities, we employed a differential capacitor design as showed in Figure 1(b). These devices were designed to generate capacitance change only by demanded direction of angular acceleration. In Figure 1(b), when demanded angular acceleration is applied to the device, capacitance change, detected by the differential circuit, will be generated. On the other hand, when other direction acceleration is applied to the device, for example linear acceleration, differential capacitance change will not be generated. As a result, cross axis sensitivities decrease.

Simulation Procedure:

At first, we designed each device within $1 \text{ mm} \times 1 \text{ mm}$ size and optimized to achieve high sensitivity. Although large proof mass and narrow beams are preferred to get high sensitivity, there was a concern about stiction, which happens during fabrication process. To avoid this problem, we defined the device layer thickness as $40 \mu\text{m}$ and the gap distance between electrodes as $2 \mu\text{m}$. Also we employed a beam width of $5 \mu\text{m}$ – the minimum value at which we could fabricate a $40 \mu\text{m}$ thick device layer with width:height = 1:10 aspect ratio. Then, we swept each device size and compared device specifications, such as sensitivity and maximum detectable signal.

Results and Conclusions:

Figure 2 shows the simulation results of the linear operation limit and sensitivity versus device size for the Z axis sensor, and the X and Y axis sensor. In Figure 2(a), fulfilling the

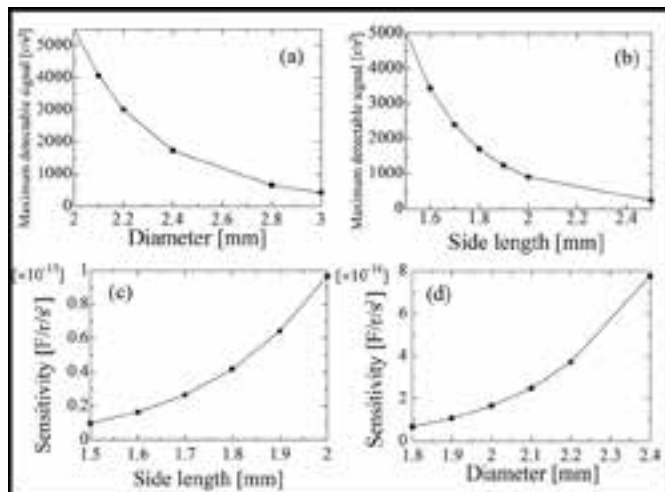


Figure 2: Simulation results of Z axis sensor's (a) maximum detectable signal and (c) sensitivity versus device diameter, X and Y axis sensor's (b) maximum detectable signal and (d) sensitivity versus device size.

requirement of the maximum detectable signal ($> 1000 \text{ rad/s}^2$), demanded that the device diameter of the Z axis sensor be smaller than 2.6 mm. In Figure 2(c), fulfilling the requirement of sensitivity calculated from the minimum detectable signal requirement, demanded that the device diameter be larger than 2.1 mm. In the same procedure, we concluded that the X and Y axis sensor's side length must be larger than 1.7 mm and smaller than 1.9 mm to fulfill both requirements. Finally, we defined the device diameter of the Z axis sensor as 2.1 mm and the device side length of X and Y axis sensor as 1.7 mm, which are the minimum values to fulfill both requirements.

Table 2 shows detailed device specifications calculated by a COMSOL simulation. These specifications fulfilled requirements for the application of vestibular prosthesis.

Acknowledgments:

This research is supported by Professor Farrokh Ayazi and Professor Pamela T. Bhatti, and Hodjat-Shamani. I would like to acknowledge the National Nanotechnology Infrastructure Network International Research Experience for Graduates (NNIN iREG) Program, the National Science Foundation, and the National Institute for Materials Science.

References:

- [1] D. M. Merfeld, et al., IEEE Trans. Biomed. Eng., vol. 54, No. 6, pp. 1005-1015, 2007.
- [2] C. M. Andreou, et al., Biomedical Circuits and Systems Conference, pp.17-20, 2013.
- [3] W. R. Bussone, et al., Thesis for the degree of Master of Science in Mechanical Engineering of Virginia Polytechnic Institute and State University, Blacksburg, Virginia, July 29, 2005.
- [4] J. J. Groen and L. B. W. Jongkees, J. Physiol. I07, I-7, 1948.

M
E
C
H

	Z axis sensor	X and Y axis sensor	Requirements
Device size	2.1mm \times 2.1mm	1.7mm \times 1.7mm	
Sensitivity [aF/rad/s ²]	248	267	200
Minimum detectable signal [rad/s ²]	1.21×10^{-2}	1.13×10^{-2}	$< 1.75 \times 10^{-2}$
Maximum detectable signal [rad/s ²]	4059	2391	>1000
Bandwidth [Hz]	500	300	>20
Cross axis sensitivity (angular)			
Z [%]	-	<<0.1	<0.1-1
X, Y [%]	<<0.1	<<0.1	<0.1-1
Cross axis sensitivity (Linear)			
Z [%]	0.01	0	<0.1-1
X [%]	0.025	<<0.1	<0.1-1
Y [%]	0.025	0.05	<0.1-1

Table 2: Detail specifications of angular accelerometers.

Photovoltaic Devices Made from Plasma-Doped Two-Dimensional Layered Semiconductors

Samuel Arthur
Physics, Colby College

NNIN REU Site: Lurie Nanofabrication Facility, University of Michigan, Ann Arbor, MI

NNIN REU Principal Investigator: Assistant Professor Xiaogan Liang, Mechanical Engineering, University of Michigan

NNIN REU Mentor: Sungjin Wi, Department of Mechanical Engineering, University of Michigan

Contact: sdarthur@colby.edu, sjwi@umich.edu, xiaoganl@umich.edu

Abstract:

Two-dimensional (2D) layered transition metal dichalcogenides (LTMDs, especially WSe_2 and MoS_2) exhibit a high absorption of visible light. For example, a LTMD monolayer (~ 0.5 nm) can absorb as much sunlight as 50-nm-thick silicon (Si) films [1]. Therefore, they are suitable for making next-generation ultrathin, flexible photovoltaic (PV) devices. However, society lacks the device physics knowledge and skills for generating built-in potentials in such emerging layered materials, which are required to separate photo-generated electron-hole pairs and create photocurrents. This REU project sought to leverage the plasma-doping method and vertically stacked LTMD heterostructures developed by Prof. Liang's group to create and optimize PV devices made from multilayer WSe_2 films with plasma-doping-induced p-n junctions. To achieve this goal, we fabricated PV devices with a vertically stacked indium tin oxide (ITO)/ WSe_2 /Au structure, using 2D layer printing, photolithography, thin-film deposition/lift-off, and plasma etching/doping. Our results provide critical information for identifying the band diagram of WSe_2 PV devices as well as optimizing their PV performance. This work provides scientific insights of the unique optoelectronic properties of 2D LTMDs at the backbone of emerging atomically layered PV devices.

Introduction:

LTMDs have a potential for making ultrathin photovoltaic (PV) devices that have great flexibility, high light-absorbing efficiency, long lifetime and low manufacturing cost. Molybdenum disulfide (MoS_2), a semiconducting LTMD, has recently been observed by Liang's group as a photovoltaic material. Tungsten diselenide (WSe_2) is another LTMD that has a similar layered structure to MoS_2 but has been anticipated to have the higher light absorption coefficients over a broader wavelength range in comparison with MoS_2 . However, the PV

response characteristics of WSe_2 -based devices still remain poorly studied. Especially, the research society needs new scientific and technical schemes to form reliable p-n junctions (or built-in potentials) in such layered semiconductors, which is expected to be very different from the junction formation schemes for conventional semiconductors.

The goal of our project was to fabricate and characterize WSe_2 -based photovoltaic cells with plasma-formed p-n junctions. In a PV process, the incident photons excite electrons from the valence band to the conduction band, creating electron-hole (e-h) pairs. The built-in field of the p-n junction can separate e-h pairs and result in a splitting of quasi-Fermi levels of electrons and holes as well as a photocurrent in the external circuit.

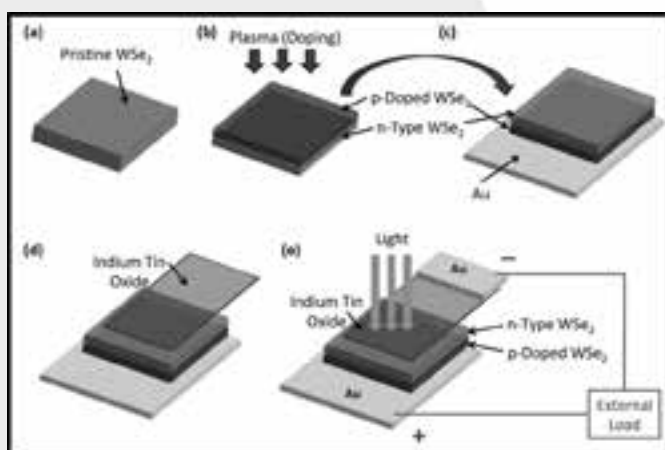


Figure 1: Schematic of the fabrication process.

Experimental Procedure:

The schematic diagram of the device fabrication process is illustrated in Figure 1. Adhesive tape squares were used to exfoliate pristine WSe_2 flakes from a bulk WSe_2 ingot (1a). The exfoliated WSe_2 flakes were then thinned by repeatedly applying them to multiple adhesive tape squares. The tape squares containing the pristine WSe_2 flakes were treated with fluoroform (CHF_3) by reactive-ion etching (1b). These flakes were subsequently bonded onto wafers containing gold

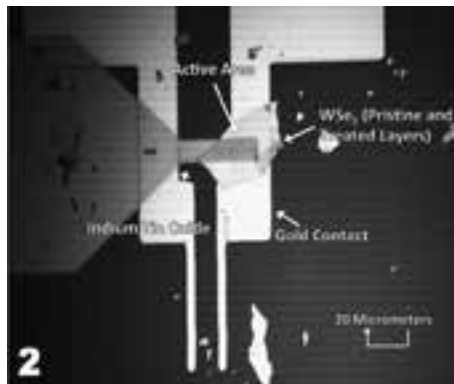


Figure 2: Completed photovoltaic cell diagram.

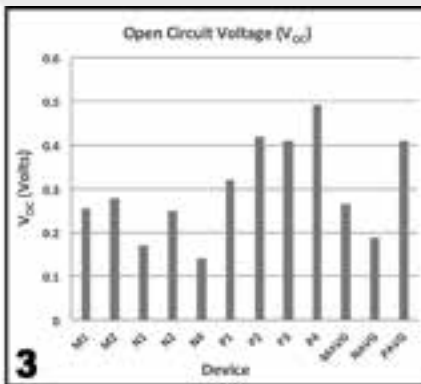


Figure 3: Open-circuit voltages for each device and averages of each device type.

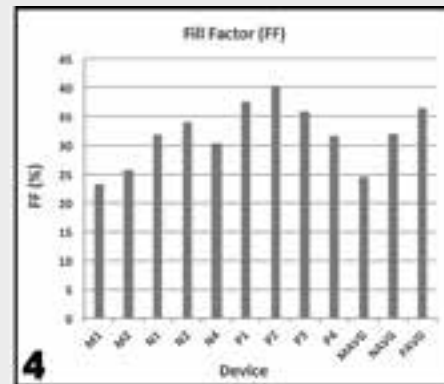


Figure 4: Fill factors for each device and averages of each device type.

(Au) contacts. Heating the wafers removed the tape residue and transferred the WSe₂ flakes onto the Au contacts of the wafers (1c). Four samples were treated with fluoroform after exfoliation and not before. Photolithography techniques were used to create a trench into which a thin film of ITO was sputtered (1d). The optical micrograph of an as-fabricated photovoltaic device made using this process is displayed in (1e) and in Figure 2.

Results and Conclusions:

A semiconductor-parameter analyzer is used for the I-V characterization of all PV devices under the illumination of 532 nm laser light. From the measured I-V characteristics, critical PV performance parameters of all devices, including open-circuit voltages (V_{oc}) (Figure 3) and fill factors (FF) (Figure 4) were determined.

“M devices” refers to MoS₂ cells previously fabricated by Liang’s group, while “N devices” refers to n-type-WSe₂/Au structured cells, and “P devices” refers to p-type-WSe₂/Au structured cells. While M cells exhibited a higher average V_{oc} (0.266 V) than N devices (0.187 V), P cells have a higher average V_{oc} (0.410 V) than both M and N devices. Furthermore, P samples exhibit the highest average FF (36.4%), followed by N samples (32.0%) and M samples (24.5%).

From these data, we can conclude that P devices (i.e., p-type-WSe₂/Au structured cells) exhibit significantly higher V_{oc} and FF parameters in comparison with M and N devices, which are crucial to ultimately obtain unprecedented PCE parameters in the future.

Future Work:

After removing the area of WSe₂ above the gold contact and not below the ITO (i.e., marginal area), power conversion efficiency (PCE), external quantum efficiency (EQE) and short circuit photocurrent density (J_{sc}) data can be obtained for further analysis and comparison. Texturing the surfaces of silicon photovoltaic cells helps contain the light in the P-N junction for a longer time and reduces surface reflections, leading to more generated carriers and a greater photocurrent [2]. This process could significantly enhance the efficiencies of the WSe₂ photovoltaic cells. Also, some LTMDs have not been examined for their efficiencies in the p-n junction of the photovoltaic cell. The same fabrication and testing processes used in this project could be employed for future investigations of newly studied LTMDs.

Acknowledgements:

I would like to thank the NNIN REU Program for selecting me to participate in their research experience. I would also like to acknowledge the National Science Foundation for their funding. Finally, I would like to offer my special thanks to my mentor, Sungjin Wi, and my PI, Xiaogan Liang, for their time and energy spent on guiding me throughout my research.

References:

- [1] Wi, S., et al.; “Enhancement of Photovoltaic Response in Multilayer MoS₂ Induced by Plasma Doping”; ACS Nano, 8, 5270-5281 (2014).
- [2] Edwards, M., et al.; “Effect of texturing and surface preparation on lifetime and cell performance in heterojunction silicon solar cells”; Solar Energy Materials and Solar Cells, 92, 1373-1377 (2008).

Bio-Inspired Surface Treatments and Quasi-Ordered Nanostructures to Control Broadband IR Response

Lesley Chan

Chemical Engineering, University of Southern California

NNIN REU Site: UCSB Nanofabrication Facility, University of California, Santa Barbara, CA

NNIN REU Principal Investigator: Prof. Michael J. Gordon, Chemical Engineering, University of California, Santa Barbara

NNIN REU Mentor: Federico Lora Gonzalez, Chemical Engineering, University of California, Santa Barbara

Contact: lesleywc@usc.edu, mjgordon@engr.ucsb.edu, floragonzalez@umail.ucsb.edu

Abstract:

Moth-eye nanostructures have been fabricated in silicon and germanium using colloidal lithography and reactive ion etching to enhance optical transmission in the near to far infrared wavelength range ($\lambda = 2\text{-}50 \mu\text{m}$). In previous reports [1, 2], high transmission was achieved using a multi-step etching process to form silicon nanostructures. Here, we demonstrate the fabrication of similar nanostructures using a simplified, single-step vertical etch by systematic modification of etch parameters that include gas flow rates ($\text{SF}_6/\text{C}_4\text{F}_8/\text{Ar}$), RF power, and etch time. Using this method, fabrication of moth eye nanostructures on germanium (Ge) was also achieved. Nanostructures were optically characterized via Fourier transform infrared spectroscopy (FTIR). High transmission was observed for Si and Ge, for both single-sided (Si: ~94% of theoretical limit, Ge: ~97% of theoretical limit) and double-sided (Si: ~88% absolute transmission, Ge: ~92% absolute transmission) moth-eye samples.

Introduction:

Recent developments in nanotechnology have shown a need for enhanced anti-reflective coatings (ARCs) for infrared (IR) devices such as thermophotovoltaics, optoelectronics, and IR detectors. These mentioned devices are typically made from high refractive index materials, such as silicon (Si), resulting in large reflective losses. Conventional ARCs are composed of vacuum-deposited thin film dielectric materials that are known to have low acceptance angles and can only enhance transmission at specific designed wavelengths. Multi-layer ARCs can overcome some of these issues, but the deposition is time consuming, expensive, and substrate dependent. Therefore, we present “bio-inspired” moth-eye (ME) nanostructures for anti-reflection, depicted in Figure 1, that operate by the introduction of a refractive index gradient, which not only provides superior broadband anti-reflection, but fabrication is both quick and simple.

Typically, ME nanostructures have been used for anti-reflection in the visible range, but our work focuses on IR wavelength ranges. ME nanostructures are also scalable and substrate-independent, which means they can be theoretically implemented for any wavelength range and any material. Furthermore, using a simplified single-step vertical etch method, as opposed to a multi-step Bosch etch plus isotropic ICP-RIE as reported previously [1, 2], we were able to make high-performance and robust ME nanostructures.

Experimental Procedure:

Fabrication of ME nanostructures was done using a simple, two-step colloidal lithography method as shown in Figure 2.

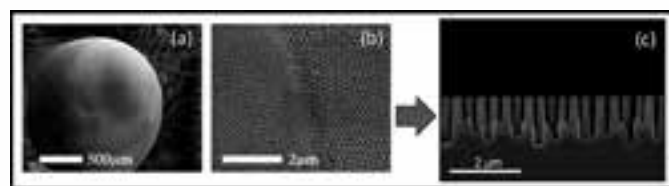


Figure 1: (a) SEM images of moth's eye showing hexagonally packed nanostructures [2]. (b) SEM image of moth-eye nanostructures fabricated on Si. (c) SEM image of moth-eye nanostructures on Ge.

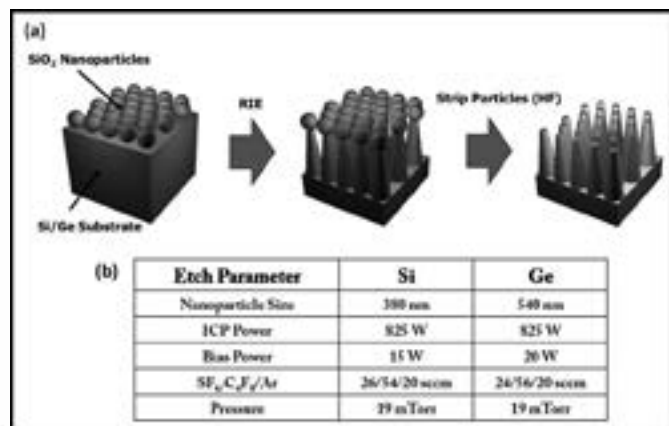


Figure 2: (a) Process scheme to create moth eye anti-reflectors: fabrication of nanostructures started with SiO_2 mask deposition using Langmuir-Blodgett, followed by reactive ion etching, and stripping of SiO_2 using HF. The process is repeated on the backside of the wafer to form double-sided nanostructures. (b) Etch parameters for reactive ion etching for both Si and Ge.

The silica nanoparticle mask was deposited on Si (University wafer, 225 μm thick, > 4000 Ohm-cm) and Ge (MTI Corp., 500 μm thick, > 50 Ohm-cm) wafers using a Langmuir-Blodgett dip coating process [1-3]. The nanoparticle sizes used were 380 and 540 nm for Si and Ge, respectively. Afterward, masked Si and Ge samples were plasma-etched (Plasma-Therm 770 SLR-RIE) using a single-step vertical etch with varying conditions for gas flow rates ($\text{SF}_6/\text{C}_4\text{F}_8/\text{Ar}$), bias power, and etch time as summarized in Figure 2.

After plasma etching, the silicon dioxide (SiO_2) nanoparticles were subsequently stripped using hydrofluoric acid (10%). The colloidal lithography process was repeated on the backside of the substrate to fabricate double-sided ME substrates. The ME nanostructures were characterized using scanning electron microscopy (SEM) for morphology and FTIR for transmission.

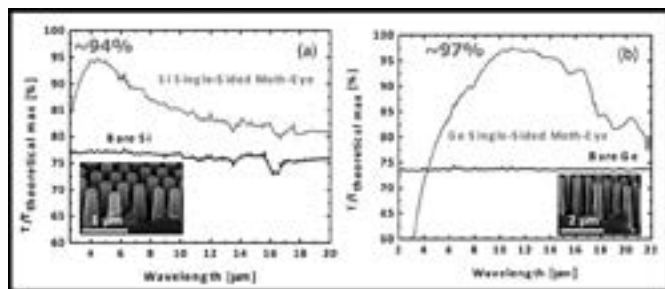


Figure 3: Normalized transmission with respect to theoretical maximum (Si: $T_{\max} \sim 70\%$, Ge: $T_{\max} \sim 64\%$) for single-sided ME nanostructures on Si and Ge and corresponding cross-sectional SEMs.

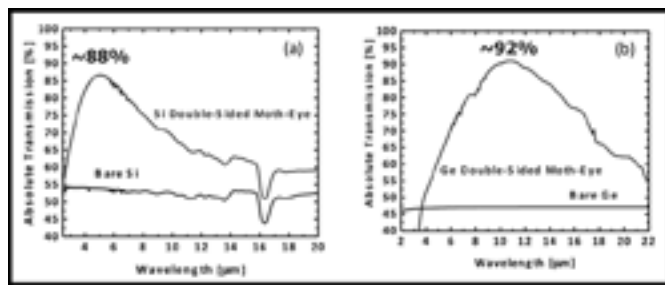


Figure 4: Absolute transmission for double-sided ME nanostructures on Si and Ge.

Results and Conclusions:

The theoretical maximum transmission was calculated to be $\sim 70\%$ for single-sided ME in Si and $\sim 64\%$ for single-sided ME in Ge. Direct transmission for single-sided Si and Ge nanostructured substrates had a peak transmission of 94% and 97% of the theoretical maximum, respectively, as shown in Figure 3. By implementing nanostructures on both sides of the substrate, the theoretical maximum increases to 100% in both materials.

Direct transmission for double-sided Si and Ge nanostructured substrates had a peak of 88% and 92% absolute transmission, respectively, as shown in Figure 4. Furthermore, by changing nanoparticle size, we were able to adjust the pitch, resulting in peak transmission wavelength shifting. For the 380 nm nanoparticle masks on Si, the resulting peak position for double-sided occurred at $\lambda = 5.5 \mu\text{m}$, while for 540 nm nanoparticle masks on Ge, the peak position for double-sided occurred at $\lambda = 10.8 \mu\text{m}$. This demonstrates the tunability of the IR response by simply modifying mask size.

Future Work:

In conclusion, using Langmuir-Blodgett and a single-step vertical etch in different materials platforms to produce ME nanostructures, we were able to achieve high optical transmission in the IR. High increases in transmission were observed for both single-sided (Si: $\sim 94\%$ of theoretical limit, Ge: $\sim 97\%$ of theoretical limit) and double-sided (Si: $\sim 88\%$ absolute transmission, Ge: $\sim 92\%$ absolute transmission) nanostructures.

With further optimization of mask deposition and etch parameters, we can achieve even better anti-reflective properties, yielding higher IR transmission and also demonstrate the ability to produce ME nanostructures in additional materials.

Acknowledgements:

I would like to thank Professor Michael Gordon, my mentor Federico Lora Gonzalez, and Professor Daniel Morse for their help and guidance this summer, as well as Alex Berry for his help in nanoparticle synthesis and mask deposition. I would also like to thank the UCSB cleanroom staff for help with the plasma etching. This work was supported by the National Nanotechnology Infrastructure Network Research Experience for Undergraduates Program, the National Science Foundation, and the Institute for Collaborative Biotechnologies.

References:

- [1] Federico Lora Gonzalez, Daniel E. Morse, Michael J. Gordon, Opt. Lett. 39, 13-16 (2014).
- [2] Federico Lora Gonzalez, Michael J. Gordon, Opt. Express 22, 12808-12816 (2014).
- [3] Federico Lora Gonzalez, Lesley Chan, Alex Berry, and Michael J. Gordon. JVST B (Submitted 2014).

Study of Cerium Doped Terbium Iron Garnet Thin Films for Magneto-Optical Applications

Emiliana Cofell
Physics, Scripps College

NNIN REU Site: Minnesota Nano Center, University of Minnesota-Twin Cities, Minneapolis, MN

NNIN REU Principal Investigator: Prof. Bethanie Stadler, Electrical and Computer Engineering, Chemical Engineering and Materials Science, University of Minnesota-Twin Cities

NNIN REU Mentor: Prabesh Dyal, Chemical Engineering and Material Science, University of Minnesota-Twin Cities

Contact: ercofell@gmail.com, stadler@umn.edu, dyal002@umn.edu

Abstract:

Thin films of magneto-optical materials are useful in optical isolators, which are devices used in photonic circuits as “optical diodes” to prevent reflected light from damaging the laser source. This is achieved by an effect called Faraday rotation, which is a rotation of the polarization of light when passing through a magneto-optic material. The material studied in this project was cerium doped terbium iron garnet ($\text{Ce:TIG}/\text{Ce}_x\text{Tb}_{3-x}\text{Fe}_5\text{O}_{12}$). The thin films were deposited on silicon and fused quartz substrates using reactive sputtering in an oxygen environment. The iron and terbium targets were sputtered at a constant power while the cerium power was varied to change the cerium concentration. The samples were annealed at 700°C, 800°C, and 900°C using rapid thermal annealing (RTA). The characterization of the samples included measuring the Faraday rotation using an optics bench setup with a 1545 nm laser. A correlation between increasing cerium content and the Faraday rotation was observed. Future work will include developing optical isolators with Ce:TIG as the magneto-optical material on a silicon platform for use in photonic circuits.

Introduction:

Optical isolators are important for use in waveguides for integrated photonic circuits; these devices prevent reflected light from damaging the laser source. Magneto-optical materials are useful for the development of optical isolators due to their ability to rotate the polarization of light through the Faraday Effect [1]. This effect, $\beta = vBd$, relates the angle of rotation of the polarization (β) to the Verdet constant (v) of the material, applied magnetic field (B), and thickness of the material (d) [2]. In this project, thin films of the magneto-optical material cerium-doped terbium iron garnet (Ce:TIG) were developed and the amount of cerium deposited in the thin films was varied in order to measure the magneto-optical properties and optimize the Faraday rotation.

Experimental Procedure:

The samples were deposited using an oxygen reactive sputtering process on silicon and fused quartz substrates. We used three targets in the sputtering chamber: iron, terbium, and cerium. The sputtering power for iron was fixed at 220 W, terbium at 110 W, and the cerium power was varied from 0-100 W in 10 W intervals. We then annealed three samples from each batch, one each at 700°, 800° and 900°C.

We were able to achieve the garnet phase from 0-50 W cerium when these samples were annealed at either 800° or 900°C. Annealing at 900°C for two minutes formed the best garnet

out of all our samples. We were also able to achieve the garnet phase from 30-50 W cerium on GGG substrates.

After checking for crystallization using x-ray diffraction (XRD), we further characterized the samples using a scanning electron microscope (SEM), vibrating sample magnetometer (VSM), energy-dispersive x-ray spectroscopy (EDS), and an optics bench setup with a 1545 nm laser to measure the Faraday rotation coefficient of the samples.

Results and Conclusions:

In observing the samples with the SEM, cracking of various sizes was noted on most samples due to a mismatch in the thermal expansion coefficients between the substrate and thin films (see Figure 1); however, this can be eradicated in actual waveguide development by patterning the samples before deposition [1].

Some challenges were encountered when measuring the atomic percentage of cerium contained in the samples with EDS, due to non-uniform composition of the samples from the sputtering process and initial technical difficulties with the EDS. The results were somewhat surprising, as increased cerium sputtering power did not always directly relate to increased atomic percent of cerium, as is shown in Figure 2. This was most likely due to variability in the bias voltage

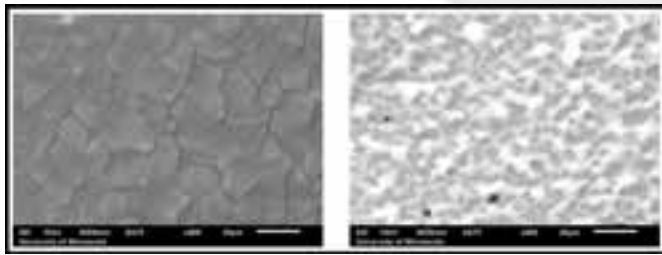


Figure 1: SEM images showing various irregularities in samples. The left image is from a sample with 30 W cerium; the right image is from a sample with 60 W cerium, which did not form garnet. Both samples are on silicon substrates.

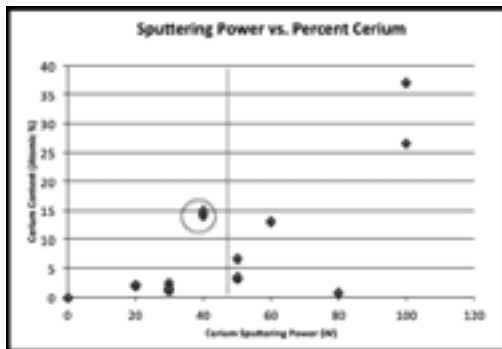


Figure 2: EDS results were slightly inconsistent — the dark grey vertical line represents the cutoff of samples that were able to form garnet. Circled data points represent the garnet sample with the highest atomic percent of cerium.

during the sputtering process, and further sample creation to gather additional data will be necessary in the future.

Measurements with the VSM were also initially challenging, as many of the hysteresis loops were slanted or did not close at one end, which did not agree with previous results from similar samples. We hypothesized that this could be explained by contributions from the silicon substrates, and were able to correct for this by subtracting readings from blank silicon for some of the measurements (see Figure 3).

The Faraday rotation measurements were promising for the samples; large negative Faraday rotations of $-2240^\circ \text{ cm}^{-1}$ and $-2620^\circ \text{ cm}^{-1}$ were observed for the two garnet samples with the largest atomic percentage of cerium. In general, a positive correlation between cerium content and Faraday rotation was observed, shown in Figure 4. However, due to irregularities in the sputtering process future characterization will be required to confirm this.

Future Work:

More sample fabrication and characterization will be necessary to determine the optimal recipe for Ce:TIG that produces the



Figure 3: VSM measurements. [Left] Initial VSM measurements for the sample with 20 W cerium. [Right] VSM measurements after subtracting silicon contributions (used in-plane loop only).

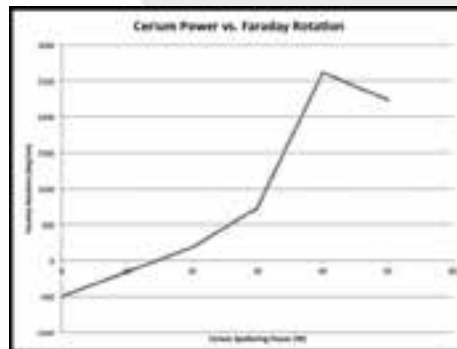


Figure 4: Faraday rotation measurement results.

greatest Faraday rotation. After this has been determined, waveguides can be fabricated and tested for eventual use in photonic circuits.

Acknowledgements:

I would like to thank Professor Beth Stadler for the opportunity to work in her lab on this project, as well as Prabesh Dulal for all his guidance and advice. I would also like to acknowledge the University of Minnesota CharFac where part of this work was carried out, which is partially funded by MRSEC. I would like to thank the NNIN REU Program and the NSF for funding this project.

References:

- [1] Dulal, P., Block, A.D., Haldren, H.A., Hutchings, D.C., Sung, S.Y., and Stadler, B.J.H. "TIG without Seedlayers on Semiconductor Substrates." *Applied Physics Letters* (to be published in 2014).
- [2] Dulal, P. "Development of Novel Iron Garnet Thin Films for Magneto-optical Applications." A proposal submitted to the ChemE and MSE faculty and the Graduate School of the University of Minnesota by P. Dulal in partial fulfillment of the requirement of the candidacy for the degree of Doctor of Philosophy.

Particle Sorting on Microfluidic Chips using Optical Forces

Brandon Foley

Chemical Engineering, University of Wisconsin – Madison

NNIN REU Site: Center for Nanoscale Systems, Harvard University, Cambridge, MA

NNIN REU Principal Investigator: Federico Capasso, Physics, Harvard University

NNIN REU Mentors: Lulu Liu and Alexander Woolf, Physics, Harvard University

Contact: brfoley@wisc.edu, capasso@seas.harvard.edu, lululiu@fas.harvard.edu, awoolf@fas.harvard.edu

Introduction:

Sorting particles using light can provide another means for particles separation. On-chip particle sorting has been used to sort particles based on size or using dielectrophoretic forces [1]. Optical forces can be used to sort particles that have similar chemical, physical, and electromagnetic properties, but different optical properties. It is especially difficult to separate particles that are enantiomers of each other, which have identical chemical and physical properties and differ only in their interactions with light. The scattering of circularly polarized light is dependent on the handedness of the chiral particle and of the circularly polarized light [2]. This difference in scattering will be used to push particles in different directions on a microfluidic chip. The microfluidic chip is a channel ending in a fork. The particles flow down the channel and are pushed either left or right, depending on the particle's handedness, causing the particles to travel the channel in the direction it was pushed. The goal of this study is to fabricate a flow chamber capable of sorting particles using optical forces.

Methods:

SU-8 Master Wafer Synthesis. The SU-8 master wafer was made using SU-8-3025 at a thickness of 20 μm using negative photoresist methods as outlined by MicroChem [3].

Flow Chamber Synthesis. The standard 10:1 monomer:cross-linking agent ratio for polydimethylsiloxane (PDMS) was mixed and degassed before pouring over the silicon master chip in a Petri® dish to a thickness of approximately 1 cm. The Petri® dish was then placed in an oven at 65°C for three hours. The PDMS was removed from the silicon wafer and plasma oxidized to adhere it to a glass slide. A 1.20 mm hole was punched in channel and a 1/16-inch O.D. tubing attached to flow the bead suspension into the microfluidic flow chamber, as shown in Figure 1.



Figure 1: A PDMS flow chamber prototype for particle sorting using optical forces.

Controlling Flow Rate. The velocity of the beads needed to be slow so there would be enough interaction time with the laser for sufficient displacement to occur. The desired flow rate was 0.02 $\mu\text{L}/\text{h}$. Gravity was used as the driving force for the flow, and was controlled by installing two needle valves to increase or reduce the friction to adjust the flow rate through the microfluidic flow chamber.

Experiment. Glass beads with a diameter of 5 μm were flowed through the flow chamber at a rate of 10-30 $\mu\text{m}/\text{s}$. A 660 nm laser was shown on the beads to the right at a power of $3.2 \times 10^{-4} \text{ mW}/\mu\text{m}^2$. The distribution of the beads at the fork were counted in the presence of the laser and compared to the distribution of the beads without the laser.

Results and Discussion:

The flow chamber successfully sorted beads using optical forces, as shown by the results in Table 1. Using Flow Chamber A, without the presence of radiation pressure, $50.8\% \pm 7.0\%$ of the beads were entering the left channel at the fork. When $3.2 \times 10^{-4} \text{ mW}/\mu\text{m}^2$ of radiation pressure was exerted on the beads towards the right, the fraction of beads travelling down

the left channel decreased to $35.7\% \pm 6.3\%$. This verifies that optical forces are capable of potentially sorting particles.

Consistency was another important measure of the flow chambers. Flow chambers with the same design should behave similarly and the same flow chambers should have consistent behavior over time. As shown in Table 1, this was not the case for these flow chambers.

Flow Chamber B had $80.2\% \pm 5.5\%$ without the presence of radiation pressure, which is significantly higher Flow Chamber A. The behavior of Flow Chamber B also changed during experiments. The fraction of beads that travelled down the left channel at the fork after the experiments was $48.3\% \pm 9.1\%$. This difference suggests that morphological changes occurred. This could have been caused by dust clogging or unclogging from the channels or from beads sticking to the PDMS walls, causing a change in the flow. An example of clogging is shown in Figure 2.

Future Work:

To resolve issues involving dust clogging of channels, a filter will be added to the flow chamber. The filter consists of diamond-shaped pillars with decreasing gap sizes designed to block any pieces of dust that may clog the channel, while letting the beads pass through freely. Currently, there is a slight attraction between the beads and the PDMS walls. With a filter consisting of PDMS pillars, bead sticking may become a more important issue. To prevent bead sticking, the PDMS will be coated with negatively charged polymer. The glass beads naturally retain a negative charge, or polystyrene beads with carboxylic acid groups on the surface can be used, giving a negative charge to the polystyrene beads. The repulsion between the like-charges of the PDMS walls and the beads will prevent the beads from sticking to the filter or anywhere along the channels.

Acknowledgements:

I would like to thank Professor Federico Capasso for allowing me to join his group this summer, my mentors Lulu Liu and Alex Woolf for their support and guidance, the rest of the Capasso group, and the Harvard site coordinators Kathryn Hollar and Sara Wenzel for helping set up the program. I would also like to thank the National Nanotechnology Infrastructure Network Research Experience for Undergraduates Program and the National Science Foundation for their financial support.

References:

- [1] K. Ahn, et al., Dielectrophoretic manipulation of drops for high-speed microfluidic sorting devices. *Appl. Phys. Lett.* 88, 024104 (2006). <http://dx.doi.org.ezproxy.library.wisc.edu/10.1063/1.2164911>.
- [2] Singham, Shermila Brito, Form and intrinsic optical activity in light scattering by chiral particles. *J. Chem. Phys.* 87, 1873 (1987). <http://dx.doi.org.ezproxy.library.wisc.edu/10.1063/1.453202>.
- [3] MicroChem. SU-8 3000 Permanent Epoxy Negative Photoresist <http://www.microchem.com/pdf/SU-8%203000%20Data%20Sheet.pdf>.

Chamber	Conditions	Left	Right	Total	Fraction Left	Error	Lower Bound	Upper Bound
A	Null	100	97	197	0.508	0.070	0.438	0.577
A	Laser Right, $3.2 \times 10^{-6} \text{ mW}/\mu\text{m}^2$	79	142	221	0.357	0.063	0.294	0.421
B	Null	162	40	202	0.802	0.055	0.747	0.857
B	Laser Right, $3.2 \times 10^{-6} \text{ mW}/\mu\text{m}^2$	164	75	239	0.686	0.059	0.627	0.745
B	Laser Left, $3.2 \times 10^{-6} \text{ mW}/\mu\text{m}^2$	138	60	198	0.697	0.064	0.633	0.761
B	Null, retrieval	56	60	116	0.483	0.091	0.392	0.574

Table 1, above: Results from preliminary experiments evaluating ability of optical forces to change distribution of beads.



Figure 2, right: Dust clogging in the flow chamber at the fork.

Opto-Electronic Characterization of Narrow Band Gap Semiconductors at Cryogenic Temperatures

Chanud Yasanayake
Physics, Pomona College

NNIN REU Site: UCSB Nanofabrication Facility, University of California, Santa Barbara, CA

NNIN REU Principal Investigator: Christopher Palmstrøm, Department of Electrical and Computer Engineering, University of California, Santa Barbara

NNIN REU Mentor: Mihir Pendharkar, Electrical and Computer Engineering, University of California, Santa Barbara

Contact: chanudn@gmail.com, cpalmstrom@ece.ucsb.edu, mihir@ece.ucsb.edu

Introduction:

Semiconductors are fundamental to modern technology, with uses ranging from scientific research to commercial applications in computing and telecommunications. There is a great deal of interest in studying these materials, both to improve their use in current technologies and to discover potential future applications in novel devices.

In this work, we focused on a characterization apparatus used for studying semiconductors (see Figure 1). This apparatus optically probed a semiconductor sample with a 532 nm Nd:YAG solid-state laser and used a monochromator and detector to generate the sample's photoluminescence (PL) spectrum. This spectrum can then be used to determine the material's band gap, an important physical property. In addition, the band gap's temperature dependence can be investigated by placing the sample in a 10 K cryostat.

The characterization apparatus was formerly only capable of optically probing semiconductors that photoluminesce visible to near infrared light. Major modifications were made to this apparatus to add to its functionality so that it could: (1) employ electrical measurements in addition to optical probing, and (2) detect narrow band gap semiconductors, which photoluminesce with mid to far infrared light. These modifications entailed both redesigning existing parts of the apparatus using the CAD software SolidWorks and incorporating new components into the setup.

Modifications:

The limitations of the apparatus were narrowed down to three major areas: the optical components, the cryostat, and the monochromator. Modifications were made to these areas to overcome their respective limitations.

The optical components were not positioned optimally, resulting in a low signal to noise ratio. This was corrected by repositioning each component individually until the signal was maximized. There was also an issue with noise from the laser; although the laser nominally lases at 532 nm, it is a frequency doubled laser that has significant lasing at 1064 nm as well. It also has significant emissions at several wavelengths near 532 nm. These two issues were resolved with the addition of two new filters, one to block light at 1064 nm and one to block light near 532 nm while still transmitting 532 nm light.

The cryostat (see Figure 2) had several distinct limitations to consider. For one, it took up to two hours to cool down from room temperature

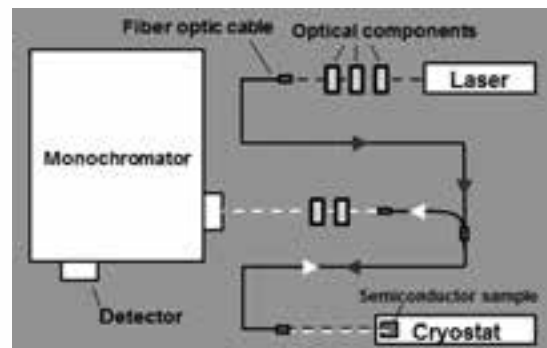


Figure 1: Characterization apparatus diagram. Laser light shown in gray, photoluminescence in white.

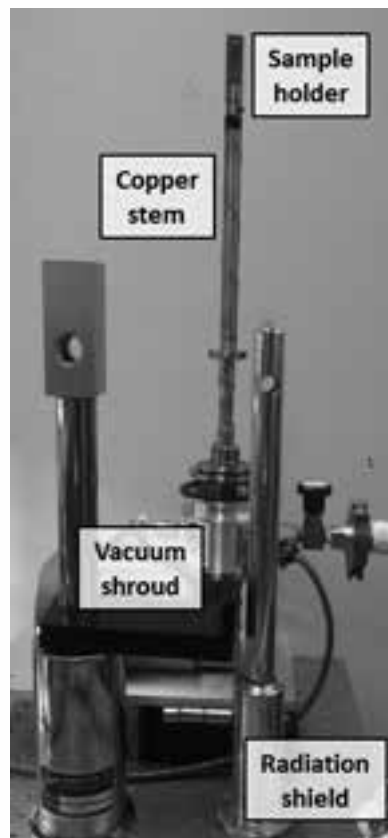


Figure 2: The former cryostat, disassembled. Labeled components were modified.



Figure 3: SolidWorks models of both versions of the new cryostat components, optical (left) and electrical (right).

to 10 K. The cryostat vacuum shroud windows absorbed mid to far infrared light, which prevented detection of the photoluminescence of narrow band gap semiconductors. The sample holder did not allow for wiring of the sample, a necessity for making electrical measurements. The modifications needed to overcome these problems yielded two sets of new cryostat components, an optical version and an electrical version (see Figure 3).

Both versions have a much shorter copper stem. This reduces cooling time since the sample holder is cooled by contact with this stem, which is in turn cooled by contact with the cryostat. The optical version has a vacuum shroud and radiation shield that accommodate new CaF_2 windows, which transmit visible to far infrared light (0.2-8 μm) and can therefore be used for narrow band gap semiconductor PL studies (i.e., InAs, InSb). The electrical version has a sample holder that supports the addition of 16 pin DIP sockets, which can be wired for electrical measurements. The electrical version also has a windowless vacuum shroud and radiation shield, which can be used when studying samples whose electrical properties are affected by ambient light.

There were four detectors that could be used with the monochromator. Two of them, an InGaAs detector and a photomultiplier tube, could be mounted onto the monochromator but could only detect light with wavelengths up to 1.8 μm , below the mid to far infrared regime. The other two detectors, InAs and HgCdTe, could detect mid to far infrared (up to 3.8 μm and up to 12 μm , respectively), but were not designed to be mounted onto the monochromator. Therefore, mounting plates were made for properly positioning the InAs and HgCdTe detectors on the monochromator where light would be focused on the detectors.

Testing:

Preliminary tests on the completed modifications suggest they are fully functional. In particular, photoluminescence spectra

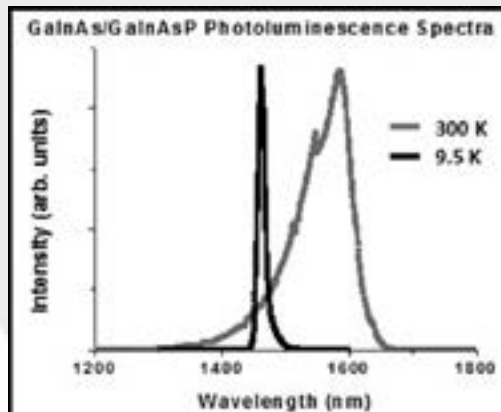


Figure 4: Photoluminescence spectra for GaInAs/GaInAsP sample at 300 K (room temperature) and at 9.5 K.

of a GaInAs/GaInAsP sample (see Figure 4) exhibited well-defined peaks both at room temperature and at 9.5 K in the cryostat, indicating that the optical alignment and new filters were yielding a satisfactory signal to noise ratio for making measurements. The signal was also clear enough to observe the peak being narrower and shifted to a smaller wavelength for the 9.5 K spectrum, an expected occurrence that shows the temperature dependence of band gap.

Future Work:

Most of the modifications have been completed and have undergone initial testing with promising results. The electrical sample holder still has to be wired for electrical measurements and the fiber optic cable will need to be replaced as it only transmits up to a wavelength of 2.5 μm . This limits the operating range of the upgraded setup, as all the modified parts function at wavelengths up to 8 μm . Further testing is required when all parts are complete and the functionality of the apparatus can be assessed as a whole.

Acknowledgements:

I would like to thank my mentor, Mihir Pendharkar, for his extensive guidance throughout this project, as well as my principal investigator Professor Chris Palmstrøm and the rest of the Palmstrøm group. The UCSB Physics Machine Shop staff were also incredibly helpful, machining the parts we designed and providing design advice. This work was supported and funded by the National Nanotechnology Infrastructure Network Research Experience for Undergraduates (NNIN REU) Program; the University of California, Santa Barbara; and the National Science Foundation.

Characterization and Solar Cell Application of GaSb Quantum Dots

Arthur Bowman, III

Physics, Wayne State University

NNIN iREU Site: National Institute for Materials Science (NIMS), Tsukuba, Ibaraki, Japan

NNIN iREU Principal Investigators: Dr. Takeshi Noda, High Efficiency Solar Cell Group, NIMS, Tsukuba, Ibaraki, Japan;
Professor Hiroyuki Sakaki, Toyota Technological Institute, Nagoya, Aichi, Japan

NNIN iREU Mentor: Dr. Martin Elborg, High Efficiency Solar Cell Group, NIMS, Tsukuba, Ibaraki, Japan

Contact: abowmaniii@wayne.edu, noda.takeshi@nims.go.jp, elborg.martin@nims.go.jp

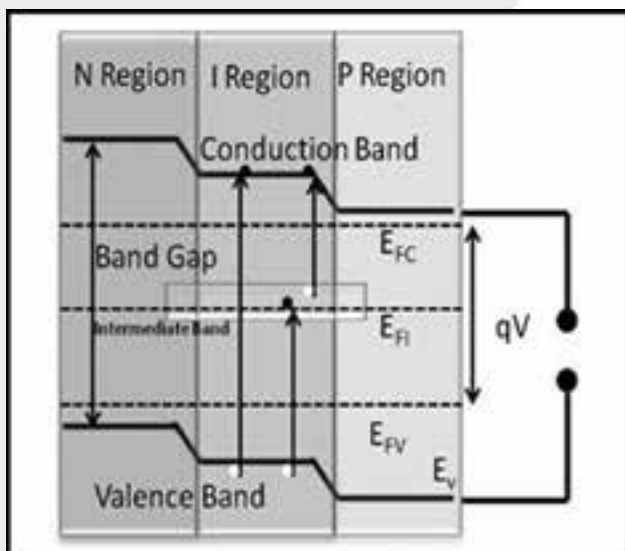


Figure 1: Ideal band diagram of the intermediate band solar cells.

Introduction:

Intermediate band solar cells (IBSC) can potentially overcome the Shockley-Queisser (SQ) conversion efficiency limit of photovoltaic devices. In addition to photocurrent generated by photons above the band gap, IBSC can utilize a “two-step” photocurrent, wherein sub-bandgap photons excite carriers from the valence to intermediate band, then intermediate to conduction band, depicted schematically in Figure 1.

Quantum dot heterostructures (QDs) are one method of realizing intermediate energy states within the band gap. Our interest is in structures with type II band alignment. In contrast to commonly used type I structures, in which both electrons and holes are confined in the narrow bandgap material, radiative recombination can be largely suppressed in type-II structures, which would be preferable for solar cell application, because losses due to radiative recombination can be reduced.

QD solar cells realized from gallium antimonite (GaSb) embedded in gallium arsenide (GaAs) are of interest as an example of type-II band solar cells. By changing the GaAs barrier to aluminum gallium arsenide (AlGaAs), we expect the dot energy levels will be situated deeply enough to achieve

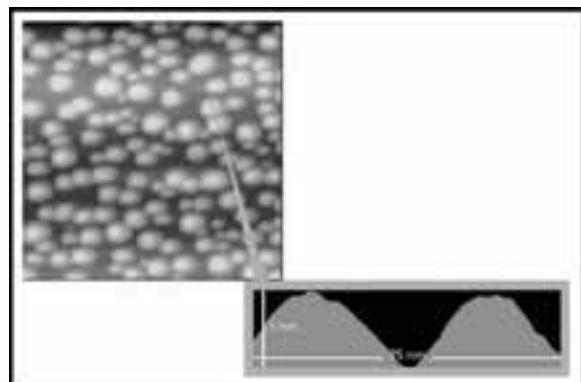


Figure 2: AFM micrograph of GaSb/AlGaAs QDs.

transition energies nearly matching the ideal IBSC configuration for highest efficiency proposed by Luque, et al. [1].

GaSb/GaAs QDs and GaSb/AlGaAs QDs were grown, and IBSC were fabricated using them. In this work, we determined the band alignment of GaSb/AlGaAs QDs, and then studied their solar cell applications.

Fabrication Procedure:

GaSb QDs embedded in GaAs and AlGaAs were grown on n-type GaAs $<100>$ substrates using molecular beam epitaxy. We employed the Stranski-Krastanov growth mode, wherein growth is first layer by layer until the thickness reaches a critical value and growth continues through the coalescence of three-dimensional “islands.” Ten layers of QDs were separated by 20 nm thick barrier layers to decouple adjacent electronic states. We fabricated QD solar cells using photolithography and sputtering. A phosphoric acid, hydrogen peroxide, and water etch was used to electrically decouple the devices. Gold wires were then bonded from the device to a serial package.

Results:

Atomic force microscopy (AFM) revealed the average height of GaSb QDs (Figure 2) was 5 nm, regardless of barrier material. The density of GaSb/GaAs QD layers was $2.9 \times 10^{10}/\text{cm}^2$ and $5.6 \times 10^{10} / \text{cm}^2$ for GaSb/AlGaAs QDs. Photoluminescence

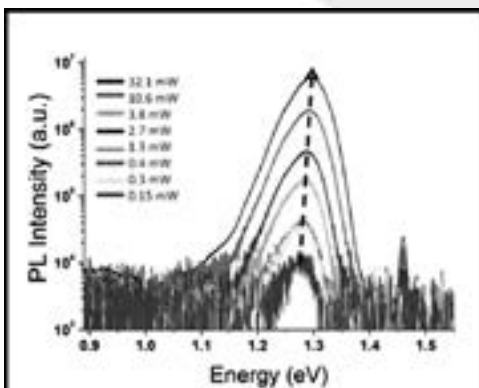


Figure 3: Blueshift of PL from GaSb/AlGaAs QDs with increasing laser power. (See full color version on page xxxvi.)

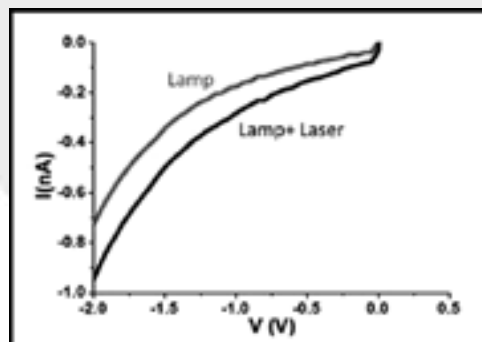


Figure 4: Two-step photocurrent generated by GaSb/AlGaAs QD solar cell.

(PL) measurements at 10 K revealed transitions at 1.09 eV for GaSb/GaAs QDs and 1.29 eV for GaSb/AlGaAs QDs from carriers occupying the QD layers. Hodgson, et al. [2] showed that increasing laser power results in a blueshift of the peak position of PL from type II QD heterostructures. PL from GaSb/GaAs QDs was blueshifted. Figure 3 shows this blueshift occurring in PL from GaSb/AlGaAs QDs. This revealed that GaSb/AlGaAs QDs has type II band alignment.

QD solar cells fabricated with GaSb/AlGaAs QDs revealed higher open circuit voltage and smaller short circuit current compared to that with GaSb/GaAs QD solar cells. This is explained by the higher band gap of AlGaAs and poor escape of photogenerated holes from the QDs due to an increase in the confinement energy.

Photocurrent spectroscopy at room temperature demonstrated the absorption of photons with energies below the band gaps of GaAs (1.5 eV) and AlGaAs (1.8 eV) corresponding to the QDs and wetting layers. The photocurrent decreased with increasing voltage, presumably due to the bias dependence of the escape efficiencies of holes from the QDs.

To observe two-step photocurrent, we used a 600 nm (2.1 eV) halogen lamp and a 1.55 μ m (0.8 eV) laser. The lamp creates electron-hole pairs, whereas the 1.55 μ m laser generates no carrier. Upon illumination with the laser, an increase in photocurrent, ΔI , was observed in solar cells fabricated from GaSb/GaAs QDs and GaSb/AlGaAs QDs (see Figure 4).

Conclusions and Future Work:

We successfully fabricated solar cells with ten layers of GaSb QDs embedded in GaAs and AlGaAs. We determined that GaSb/AlGaAs QDs has type II band alignment. We observed photocurrent generated from the QDs and wetting layers in

both GaSb/GaAs QDs and GaSb/AlGaAs QDs, and analyzed the current-voltage characteristics. We observed two-step photocurrent generation, the key operating mechanism for IBSCs. We observed reduced photocurrent by changing the barrier from GaAs to AlGaAs, which is explained by strong confinement in GaSb/AlGaAs QDs. These results demonstrate the potential of GaSb/AlGaAs QD solar cells in realizing ideal IBSC and overcoming the SQ limit.

Future work includes investigating the dependence of the two-step process on incident laser power among other experiments to study the fundamental physics of GaSb/AlGaAs QD solar cells.

Acknowledgements:

I would like to thank my principal investigators, Drs. Noda and Sakaki, mentor, Dr. Elborg, and the High Efficiency Solar Cell/Quantum Nanostructures Group for their great assistance and patience; and the National Institute of Materials Science, National Nanotechnology Infrastructure Network International Research Experience for Graduates (NNIN iREG) Program, and National Science Foundation for making this research possible.

References:

- [1] A. Luque and A. Martí. "Increasing the Efficiency of Ideal Solar Cells by Photon Induced Transitions at Intermediate Levels"; *Physical Review Letters*, v. 78, p. 5015-5017 (1997).
- [2] P.D. Hodgson, et al. "Blueshifts of the Emission Energy in Type II Quantum Dot and Quantum Ring Nanostructures"; *Journal of Applied Physics*, v. 114, p.1-6 (2012).

A Coupled Dipole Approach to Electron Energy Gain Spectroscopy

Jacob Busche

Physics, Oregon State University

NNIN REU Site: Washington Nanofabrication Facility & Molecular Analysis Facility, University of Washington, Seattle, WA

NNIN REU Principal Investigator: Dr. David J. Masiello, Department of Chemistry, University of Washington

NNIN REU Mentors: Nichloas W. Bigelow and Steven C. Quillin, Department of Chemistry, University of Washington

Contact: buschej@onid.orst.edu, masiello@u.washington.edu, bigelow@u.washington.edu, quills@u.washington.edu

Abstract:

Electron energy gain spectroscopy (EEGS) is a spectroscopic technique designed to provide high-resolution imaging of metal nanoparticles and their collective electronic oscillations called plasmons. The EEGS procedure involves pumping a plasmon with a continuous or pulsed light source from a laser, passing a high-energy (~ 100 keV) electron beam generated within a scanning transmission electron microscope (STEM) near the nanoparticle, and observing the energy lost or gained by the electron as a result of its interaction with a plasmon. The primary directive of this project is to produce a numerical model of an EEGS experiment to simulate and predict the new spectral and spatial information content contained within it. A plasmon resonance peak was observed during simulations using this technique, suggesting electron energy gain can provide a viable, zero-loss peak independent method for probing the electronic behavior of metal nanoparticles.

Introduction and Procedure:

An EEGS simulation is conducted by using a coupled dipole or discrete dipole approximation (DDA) method that assumes the target nanoparticle is composed of a large number of individual polarizable points that interact with external electric fields. The nanoparticle is then driven by both a laser and a STEM in a numerical simulation, and the induced or scattered electric field of the nanoparticle is calculated as the matrix of dipole moments in the target is allowed to relax into a energy-favorable self-consistent state. The electric field of the laser is approximated by a monochromatic plane-wave, and at the sub-wavelength scale of the nanoparticle target, is taken to be constant.

A second order interaction between the photon field of the laser light and the electron beam from the STEM becomes possible due to the plasmon oscillation coupling with both forms of radiation. A probability of photon energy transfer is generated that is proportional to the product of the electric fields and polarizations due to both the plane-wave and electron beam interactions [1], and a plot can be generated for each target arrangement to determine the normalized loss probability for each photon of energy gained by a passing electron. The numerical experiment can produce energy-gain spectra for particles of varying geometry between ~ 10 nm and ~ 100 nm in length along any given axis, providing a tool for probing interesting nanoparticle arrangements.

EEGS was developed from: (1) earlier simulations performed by B. T. Draine [2] that used the DDA to determine plasmon resonance peaks under excitation from plane-wave monochromatic light only, and (2) electron energy loss spectroscopy (EELS) simulations performed by N. W. Bigelow and A. Vaschillo, which described the energy loss probability of

passing electrons to an unexcited target. EEGS is designed to probe the plasmon-electron interaction probabilities at specific energies given by the plane-wave excitation of the system, thus freeing the results from uncertainty derived from the zero-loss-peak of a STEM [3].

Results:

The preliminary numerical experiments performed in this study modeled a spherical silver nanoparticle with a 15 nm diameter and dipole moments spaced at 1 nm. A typical plasmon peak was observed at 3.42 eV, which agreed well with the plasmon resonance spectrum generated by DDA and EELS simulations. The expression determining the gain probability was incomplete at the time of the simulation, although the data shown in the figure are correct up to a scaling factor. However, the large degree of qualitative agreement between the EEGS results and those of DDA and EELS show that electron energy gain spectroscopy can produce accurate and interesting new results in metal nanoparticle systems.

Future Work:

The energy gain probability expression in EEGS will be further refined, and the energy gain spectra from new simulations will be compared with known results from DDA and EELS methods to determine the accuracy of the technique. Numerical experiments on targets of interesting geometry will follow, probing the natural plasmon frequencies of nanoparticle systems that appear in active research.

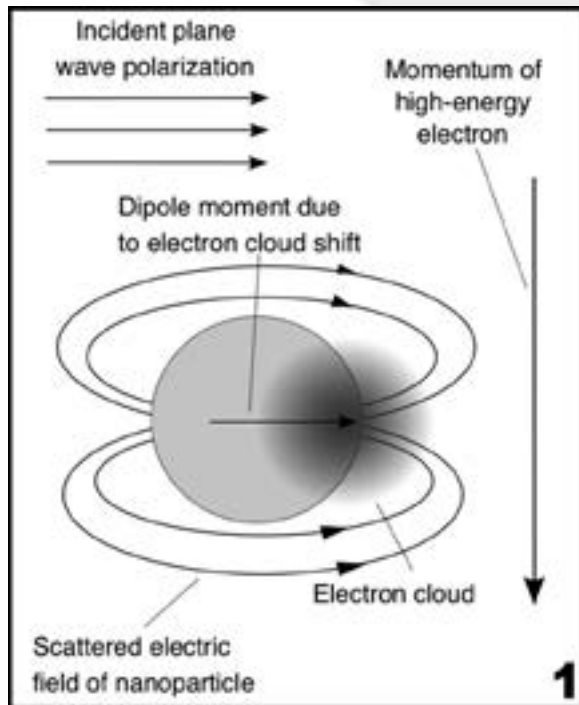
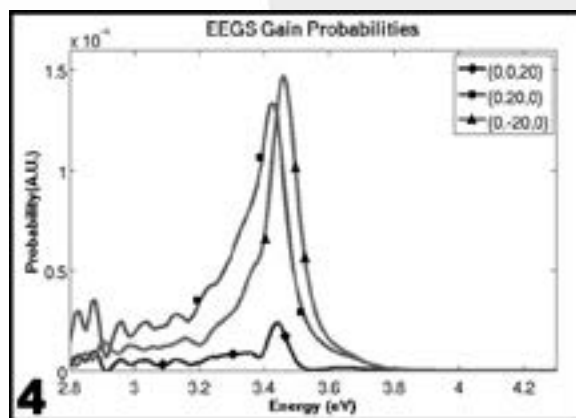
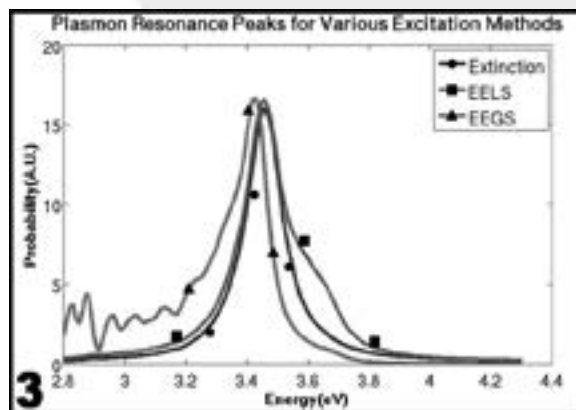
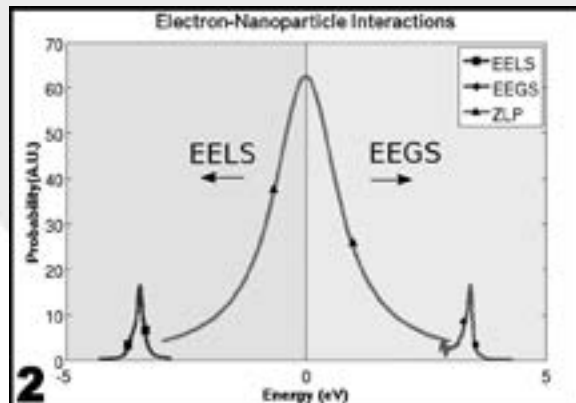


Figure 1, above: Experimental setup used to construct a typical EEGS simulation.

Figure 2, top right: The probability of energy loss or gain of a high energy electron passing a nanoparticle. The central zero-loss peak is described by a Lorentzian distribution.

Figure 3, middle right: Typical plasmon resonance peaks are shown in DDA, EELS, and EEGS spectroscopies computed via the DDA.

Figure 4, bottom right: The energy gain probability at several locations using EEGS. Both electrons and light propagate in the positive x-direction, with light polarized in the positive y-direction.



Acknowledgments:

I would like to thank Dr. David Masiello for welcoming me into his group and teaching me so much in such a short period of time. I would also like to thank Steven Quillin and Nicholas Bigelow for introducing me to their research and mentoring me through the rough patches, Niket Thakkar and Dr. Charles Cherqui for showing me how much fun the pursuit of knowledge can be, Paul Newbert for his instrumental assistance in life outside of research at this program, and the NNIN REU Program and the NSF for their support and funding of this great opportunity.

References:

- [1] Arseño-Garcia, A. and García de Abajo, F. J.; "Discrete-dipole approximation for scattering calculations"; New Journal of Physics 15, 103021, 16 pp (2013).
- [2] Draine, B. T. and Flatau, P. J.; "Discrete-Dipole Approximation for Scattering Calculations"; Journal of the Optical Society of America A Vol.11, No. 4, 1491-1499 (1994).
- [3] Bigelow, N. W.; Vaschillo, A.; Iberi, V.; Camden, J. P.; Masiello, D. J.; "Characterization of the electron-and photon-driven plasmonic excitations of metal nanorods"; ACS Nano Vol.6, No. 8, 7497-7504 (2012).

Fabricating Heavy Metal/Ferromagnetic Bilayers for Spin Torque Applications

Austin Little

Applied Physics, Morehouse College

NNIN REU Site: Cornell NanoScale Science & Technology Facility, Cornell University, Ithaca, NY

NNIN REU Principal Investigator: Prof. Daniel Ralph, Department of Physics, Cornell University

NNIN REU Mentor: Alex Mellnik, Department of Physics, Cornell University

Contact: austinlittle@gmail.com, arm282@cornell.edu, dcr14@cornell.edu

Abstract:

Magnetic devices are leading contenders for future non-volatile memory and logic implementations. Applications for magnetic devices will require the development of efficient mechanisms for reorienting their magnetization. Spintronic devices use spin currents to exert a torque on the ferromagnetic layer, causing its magnetization to reorient. When a charge current flows through a metal with a strong spin-orbit coupling, the Spin Hall Effect creates a spin current transverse to the charge current direction. This spin current applies a torque to an adjacent ferromagnet. Topological insulators, which have surface states with large in spin-orbit coupling effects, are promising options for spin current sources. Previous research has shown that the topological insulator bismuth selenide (Bi_2Se_3) efficiently generates spin currents. However, due to the high resistivity of Bi_2Se_3 , much of the charge current in a Bi_2Se_3 /Permalloy devices flows through the low resistivity Permalloy (Py) and does not contribute to the torque. This issue can be resolved by using an insulating ferromagnet. We are working to develop a new method capable of measuring spin torques acting on insulating ferromagnets by using waveguide spin pumping and a Magneto-Optical-Kerr-Effect (MOKE) microscope. We will present initial measurements of Pt/Py test devices from the MOKE microscope.

Introduction:

In previous research [1], samples consisted of 8 nm of Bi_2Se_3 and 8 nm of Py patterned into strips 10-80 μm long and 2.5-24 μm wide, with an oxidized aluminum cap to prevent oxidation of the Py layer. Although the sample geometry produced measureable spin torques, on average Bi_2Se_3 was twenty-five times more resistive than Py. As a result, much of the current shorted through the Py layer and did not contribute to the spin torque.

Our current research involved new sample geometry where we deposited a hafnium oxide insulating ferromagnetic layer in addition to transmission waveguides. The hafnium oxide insulating ferromagnetic layer should prevent the current from shorting the Py layer, while the transmission wave guides should provide a general spin torque measurement.

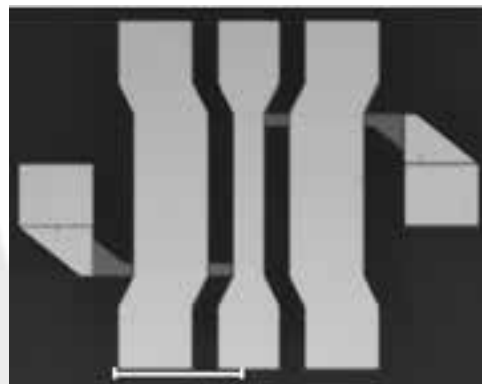


Figure 1: Device schematic.

To measure the vector components (\parallel , “in-plane”) and (\perp , “perpendicular”) of the spin torque, we also fabricated MOKE devices. The polarized light reflecting from our magnetic sample will image the scanned area and provide these vector components.

Experimental Procedure:

To make these devices, we began by depositing 6 nm of Pt and 6 nm of Py on a two-inch sapphire wafer. We also deposited 2 nm of aluminum oxide to prevent the Py from oxidizing. We then employed optical lithography and ion milling techniques to pattern the Pt/Py bilayers. We made electrical contacts from 3 nm of Ti and 150 nm of Pt in a symmetrical geometry, so that when samples were contacted using a ground-signal-ground high-

frequency probe, the currents travelling in the contacts did not produce a net Oersted field acting on the sample.

To pattern the transmission waveguide devices, we used atomic layer deposition to deposit 18 nm of hafnium oxide to prevent current from entering the ferromagnetic layer, and deposited 3 nm of Ti and 150 nm of Pt for the actual waveguide devices.

Results and Conclusions:

Preliminary resistance measurements were taken on the devices to test the sample geometry. From these measurements, the sample geometry will be reconstructed where needed in order to prevent the current from shorting through the Permalloy layer and not contributing to the spin-torque.

Future Work:

In the near future, more measurements will be taken on the devices. One set of measurements will use radio frequencies to measure the components of the spin torque produced while the MOKE will measure an overall spin torque for the device.

Acknowledgements:

I would like to acknowledge my principal investigator Dan Ralph as well as mentor Alex Mellnik. I would also like to acknowledge Jonathan Gibbons for his extensive efforts in helping with the research this summer. I thank the National Nanotechnology Infrastructure Network Research Experience for Undergraduates (NNIN REU) Program and NSF for funding. Lastly, I would like to thank Melanie-Claire Mallison and the CNF staff for their support.

References:

- [1] Spin-transfer torque generated by a topological insulator; A. R. Mellnik, J. S. Lee, A. Richardella, J. L. Grab, P. J. Mintun M. H. Fischer, A. Vaezi, A. Manchon, E.-A. Kim, N. Samarth, and D. C. Ralph. *Nature* 511, 449-451, (24 July 2014). doi:10.1038/nature13534.

P
H
Y
S

Fabrication of Nanoholes Smaller than 100 Nanometers

Luke Ness

Applied Physics and Computer Science, Bethel University

NNIN REU Site: Minnesota Nano Center, University of Minnesota-Twin Cities, Minneapolis, MN

NNIN REU Principal Investigator: Dr. Sang-Hyun Oh, Electrical and Computer Engineering, University of Minnesota-Twin Cities

NNIN REU Mentors: Daehan Yoo and Xiaoshu Chen, Electrical and Computer Engineering, University of Minnesota-Twin Cities

Contact: lan77962@bethel.edu, sang@umn.edu, yooxx094@umn.edu, chenx604@umn.edu

Abstract:

Nanohole arrays patterned in noble metal films can function as optical biosensors, because the extraordinary optical transmission through the nanoholes changes sharply with refractive index changes near the metal surface. Smaller nanoholes have sharper resonance peaks, making a better sensor. At the same time, smaller nanoholes have lower transmission efficiency. Template-stripped silver (Ag) nanohole arrays of varying diameters were used in combination with an ultra bright white light source to look at the difference in the optical response of nanoholes with diameters below 100 nm.

Experimental Procedure:

To achieve the resolutions needed for the nanohole arrays, electron-beam lithography was used to pattern thermally grown silicon dioxide (SiO_2) on a silicon wafer. The cost and speed of using electron-beam lithography limited the arrays size to be too small for practical biosensing applications. After the electron-beam resist was patterned and developed, a reactive ion etcher was used to etch through the SiO_2 layer. Images of the mold were taken to measure the hole size using a scanning electron microscope (SEM) before metal deposition, as shown in Figure 1. The SiO_2 layer was then used as a mask for etching into the Si wafer creating a mold for nanohole arrays; 100 nm of Ag was then deposited onto the mold using an electron-beam evaporator. The use of electron-beam deposition was important because the sides of the nanoholes in the silicon mold cannot have metal deposited on them otherwise they would close up and the nanoholes would not appear.

The deposited Ag was adhered to a glass slide with epoxy. The glass slide was then peeled off the silicon mold, creating template-stripped Ag nanohole arrays with ultra-smooth metallic surface. The Ag nanohole arrays were then imaged again with a SEM, as shown in Figure 2. The diameters of the nanohole arrays were found to be 53 and 105 nm.

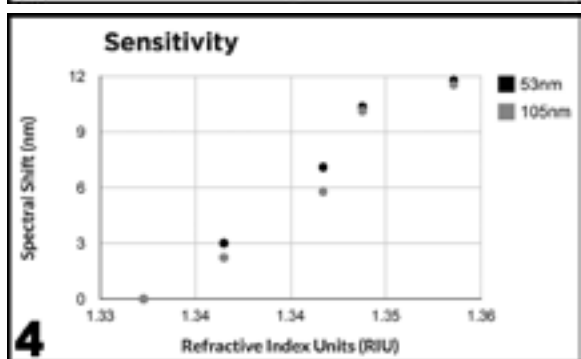
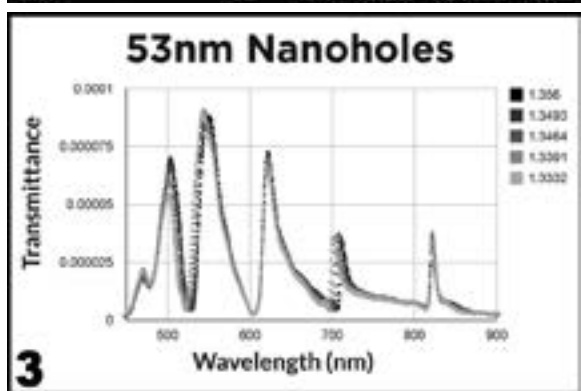
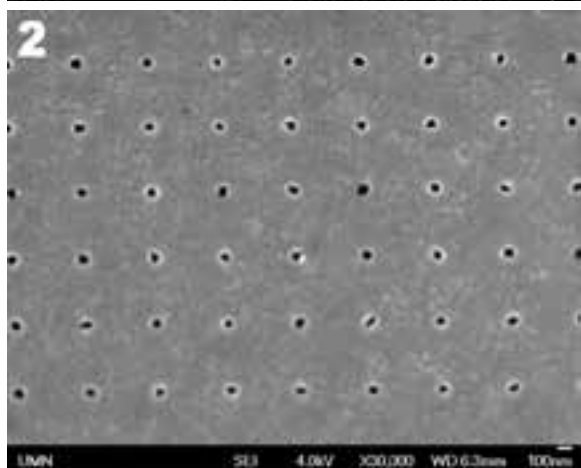
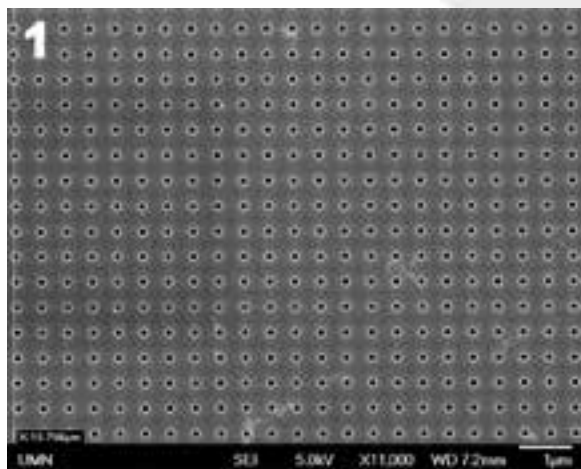
Using a broadband fiber-coupled, laser-driven light source with a 300 mm focal length imaging spectrometer, the spectrums emitted by both nanohole arrays were recorded as shown in Figure 3. The spectrums from the nanohole arrays were normalized with the spectrum of light transmitted through the glass slide. Mixtures of glycerol and water were used to measure the sensitivity of the nanohole arrays to the change to the refractive index on the exposed side of the array.

Results and Discussion:

The percent of transmitted light dropped by half an order of magnitude for the 53 nm holes compared to the 105 nm holes. The spectrums then had an eighth order polynomial fitted to them. This equation was used to find the maximum value of the fourth peak and the spectral shift was plotted for each refractive index as shown in Figure 4. The sensitivity of the two arrays was 517.33 nm/RIU for the holes with a diameter of 53 nm and 505.89 nm/RIU for the holes with a diameter of 105 nm. The data in Figure 4 was expected to be linear and was with the exception of the fourth data point in both of the data sets. The cause behind this abnormality was not able to be rectified because of time constraints.

Full width at half maximums (FWHMs) were approximated to evaluate the sharpness of the fourth peaks. The FWHMs was about 10 nm for the holes with a diameter of 53 nm and about 16 nm for the holes with a diameter of 105 nm. Making nanohole arrays with a smaller hole size is an easy way to improve the sensitivity and sharpness of the resonant peaks. Making holes below 100 nm is only a useful technique if you have an ultra bright light source, such as the laser driven light source that was used in this experiment. This is because of the extremely low transmittance through these nanohole arrays.

The improved sensitivity and sharpness of holes below 100 nm can allow for biosensing experiments that need higher precision.



Future Works:

The next step for nanohole arrays with diameters below 100 nm is to create them on a larger scale with methods such as nanoimprinting. This will allow the arrays can be used as an actual sensor. The uniformity of the nanoholes also increase by a considerable degree from the silicon molds to the template-stripped Ag nanohole arrays. Using electron beam lithography to make smaller initial holes while depositing less metal could improve these sensors as well.

Acknowledgements:

I would like to thank Dr. Sang-Hyun Oh for allowing me to be a part of his lab throughout this summer and the guidance that he gave for my research. I would also like to thank Xiaoshu Chen and DaeHan Yoo for teaching me the techniques in the cleanroom that I used throughout the summer as well as the basics behind nanoplasmonic devices. This project would have not been possible without the support of the Minnesota Nano Center and the National Nanotechnology Infrastructure Network Research Experience for Undergraduates (NNIN REU) Program. Finally I would like to thank the National Science Foundation for funding this research.

Figure 1, top left: SEM image of bare silicon with 117 nm holes in it.

Figure 2, upper left: SEM images of template-stripped Ag with 53 nm holes in it created from the silicon mold with 117 nm holes.

Figure 3, lower left: Plot of the spectrum of light emitted from the 53 nm holes.

Figure 4, bottom left: Shows the change in the resonant frequency of the fourth peak against the change of the refractive index of the fluid.

P
H
Y
S

Growth and Transfer of 2D Semiconductors and Heterostructures

Nicholas Stone-Weiss
Physics, Juniata College

NNIN REU Site: Washington Nanofabrication Facility & Molecular Analysis Facility, University of Washington, Seattle, WA

NNIN REU Principal Investigator: Xiaodong Xu, Department of Physics, University of Washington

NNIN REU Mentor: Genevieve Clark, Department of Materials Science and Engineering, University of Washington

Contact: stonenm11@juniata.edu, xuxd@uw.edu, gcl4rk@gmail.com

Abstract:

Physical vapor transport (PVT) was utilized to grow two-dimensional (2D) semiconductors that can be used in devices such as transistors, LEDs, and solar cells. Molybdenum diselenide (MoSe_2), which is in the transition metal dichalcogenide (TMDC) family, was the main semiconductor grown during this study. Limited numbers of papers have been released in which MoSe_2 monolayer crystals have been grown via PVT. In this study, MoSe_2 and other TMDC thin flakes are grown onto a SiO_2 on silicon substrate in a high-temperature furnace using PVT. Monolayer crystals were distinguished and characterized by optical imaging, photoluminescence measurements, and atomic force microscopy. By spin-coating poly(methyl methacrylate) (PMMA) onto the growth substrate, we were able to transfer the as-grown samples successfully. The PVT methods explored in this study can be further developed to create either lateral or vertical heterostructures between different monolayers.

Introduction:

Two-dimensional (2D) semiconductors have been studied extensively in recent years, as their 2D nature can make semiconductor properties easier to control. Along with their unique characteristics, 2D semiconductors are more flexible and cheaper to produce than traditional semiconductors [1]. Following the exfoliation of graphene that won the Nobel Prize in 2010, further methods of creating 2D semiconductors were developed to improve semiconductor yield and accelerate production of viable results [1]. Graphene, lacking a naturally existing band gap, began to be looked past for use in electronic devices due to the necessity of a band gap [1, 2]. Transition metal dichalcogenides (TMDCs) are 2D materials with an existing band gap having electrical properties that can improve upon graphene. Exfoliation via the Scotch tape method has proven successful for the creation of monolayer TMDCs, however the process is also time-consuming and yields few viable 2D semiconductors quickly [2]. PVT has emerged as a new technique for synthesizing 2D materials in a more time-efficient manner.

PVT involves the use of a high-temperature furnace to deposit crystalline monolayer materials onto a substrate. TMDCs have a hexagonal lattice with the form MX_2 ("M" being a transition metal and "X" a chalcogenide) [3]. Molybdenum diselenide (MoSe_2) and tungsten diselenide (WSe_2) are two TMDCs explored due to their ideal band gap for electronic circuit applications. MoSe_2 in particular has a direct band gap of 1.5 eV as well as a drastic photoluminescence change when in monolayer form, making it suitable for use in LEDs and solar cells [2]. Finding a consistent method for creating monolayer TMDCs can have various useful electronic applications.

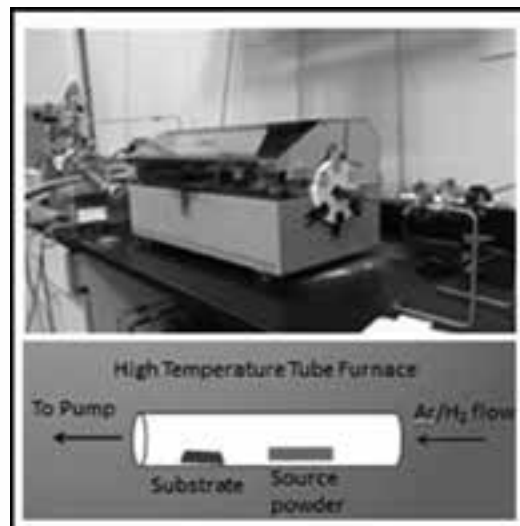


Figure 1: (a) PVT furnace setup used to grow TMDCs.
(b) Diagram of setup within furnace

Methods:

Using the setup shown in Figure 1, monolayer MoSe_2 was grown. A mixture of MoSe_2 and MoO_3 powder was placed inside the furnace as the source. SiO_2 on an Si substrate was placed upstream from the source powder in a temperature gradient. The furnace was steadily heated to a growth temperature of between 830 and 900°C at 100 millitorr. Once the maximum

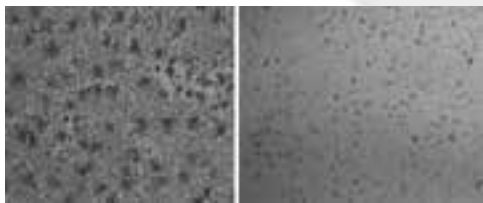


Figure 2: (a) Monolayer and bilayer MoSe_2 growth. (b) Monolayer triangular growth.

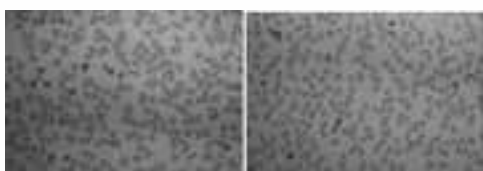


Figure 3: (a) Pre-transferred growth. (b) Post-PMMA transferred growth on new substrate.

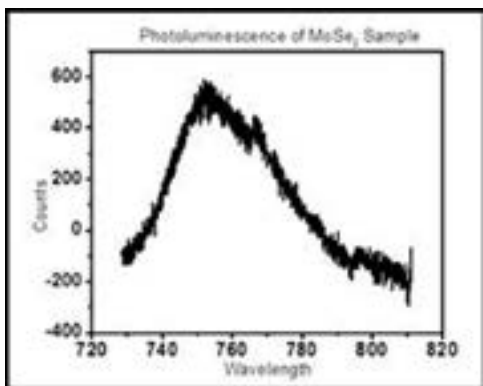


Figure 4: PL Spectrum of MoSe_2 sample.

temperature was reached, argon and hydrogen gas were flown for five minutes at 70-100 sccm and 10-27 sccm, respectively. Following the growth period, the furnace was steadily cooled to room temperature.

Monolayer MoSe_2 was successfully grown, however results were inconsistent. Photoluminescence (PL) measurements verified the presence of monolayer crystals; however the PL peak was shifted from an expected MoSe_2 peak. Crystalline triangles of monolayer MoSe_2 were found at multiple parameters, but results were not repeatable. We attributed the PL peak difference to crystalline impurity due to growth parameters not being optimized.

Improving upon growth parameters will lead to more reliable results that can vastly improve upon exfoliation with regard to

monolayer yield. Increasing the triangle size will also improve our ability to use monolayer MoSe_2 in devices.

Monolayer TMDC growth was transferred off the growth chip by spin-coating PMMA and etching in 1 M KOH solution. A thin film of PMMA containing growth was transferred onto a new substrate and cleaned with a series of solvent baths. Although optical microscopy verified the success of PMMA transfer, AFM images exposed impurities in transferred growth. In the future, dry transfer methods will be explored that cause less damage to the growth.

Conclusions and Future Directions:

Monolayer MoSe_2 was successfully grown, however results need to be replicated to make these 2D semiconductors viable. Triangular crystals need to be optimized so that they are large enough for utilization in devices, as MoSe_2 has highly attractive electronic properties. With the development of successful monolayer growth, establishment of an effective dry transfer technique can help create vertical heterostructures between TMDC monolayers that are necessary for devices. Similarly, using PVT and known parameters for other TMDCs, lateral heterostructures may be grown between 2D materials with similar lattice structures [3], which would create a 1D quantum wire with interesting electronic properties [4].

Acknowledgements:

Genevieve Clark, Xiaodong Xu, Marie Scott, Kyle Seyler
Xu Lab Group, Nanodevice Physics Lab Group, National
Nanotechnology Infrastructure Network Research Experience
for Undergraduates (NNIN REU) Program, National Science
Foundation, and University of Washington.

References:

- [1] Editorial, Graphene is not alone, *Nature Nanotechnology*, 7, 2012, 683.
- [2] Xia, J., Huang, X., Liu, L., Wang, M., Huang, M., Zhu, D., Li, J., Gu, C., and Meng, X., CVD synthesis of large-area, highly crystalline MoSe_2 atomic layers on diverse substrates and application to photodetectors, *Royal Society of Chemistry*, 2014, 6, 8949-8955.
- [3] Huang, C., et al., Lateral heterojunctions within monolayer semiconductors, 1-26 (2014) at <<http://arxiv.org/ftp/arxiv/papers/1406/1406.3122.pdf>>
- [4] Sone, J., Electron transport in quantum wires and its device applications, *Semiconductor Science and Technology*, 7, B210 (1992).

Device Integration of Lithium Niobate Microring Resonators Patterned with a Silicon Hard Mask

Nicolás Andrade

Electrical Engineering, Virginia Commonwealth University

NNIN REU Site: Center for Nanoscale Systems, Harvard University, Cambridge, MA

NNIN REU Principal Investigator: Dr. Marko Lončar, School of Engineering and Applied Sciences, Harvard University

NNIN REU Mentor: Cheng Wang, School of Engineering and Applied Sciences, Harvard University

Contact: andradenm@vcu.edu, loncar@seas.harvard.edu, chengwang@seas.harvard.edu

Introduction:

Nonlinear optical devices are powerful tools for controlling the propagation, phase, and polarization of light. Lithium niobate (LN) is a promising candidate for integrated optical devices due to its combination of strong electro-optical and nonlinear optical properties. Ring resonators made of LN with reduced device size allow for nonlinear applications such as optical storage, second harmonic generation, telecommunication, and sensors. In order for these devices to function, the ring resonator needs to have a sufficiently high quality factor (Q -factor) so as to achieve high gain at its resonant frequency. There have been numerous attempts to fabricate high Q -factor LN optical resonators by utilizing advanced manufacturing techniques including photolithography, ion-beam enhanced etching, and reactive ion etching using either chromium or nickel masks deposited on the device [1].

There are numerous advantages to the techniques listed above; nevertheless, these usually result in rough sidewall profiles, high surface roughness, reduced etch depth, and non-ideal sidewall angles. These process non-uniformities, especially surface roughness, scatter light leading to poor confinement in the waveguides and resonators.

This project highlights work done to address two significant issues, the first part seeks to improve fabrication process non-uniformities and roughness by using a silicon hard mask, and the second part of the project deals with device integration with SU-8 waveguides. The device coupling efficiency, which is essential in nonlinear optics experiments, may be enhanced by improving the coupling between the waveguide and fiber by overlaying and polishing SU-8 waveguides. These methods make the fabrication and optical test of LN devices more robust and increase the device performance by improving modal confinement and tunability.

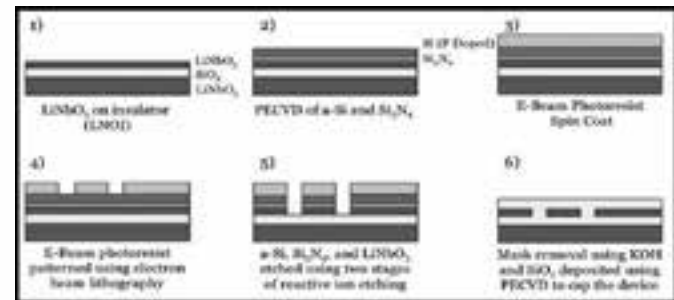


Figure 1: The fabrication process using a Si mask.

Methods:

The current process uses a FOX-16, hydrgoen silsequioxane (HSQ) electron-beam resist, as an etch mask. However, HSQ is not crystalline and is physically soft; therefore, selectivity to LN is low, approximately 0.5, which leads to non-uniform lateral etching. To address the poor selectivity of the FOX-16 process, we tested a silicon mask, as shown in Figure 1, patterned by HSQ e-beam resist and a standard silicon (Si) dry etch process. The key points of this process were the testing of different thicknesses of amorphous silicon and e-beam resist, and the patterning of LN by a physical argon (25 sccm Ar⁺) etch in a NEXX reactive ion etch (RIE) tool with an RF power of 250W and a pressure of 5 mTorr.

For the device integration portion, prior to a silicon dioxide (SiO₂) cap, SU-8 waveguides were overlaid on the sample and attached to existing waveguides to act as coupling pads for a lensed fiber. The key process was the cleaved sample polish using an Allied Polisher with 30 μ m, 6 μ m, 1 μ m, 0.3 μ m, and 0.05 μ m lapping films; the first three pads were diamond and the remaining aluminum oxide.

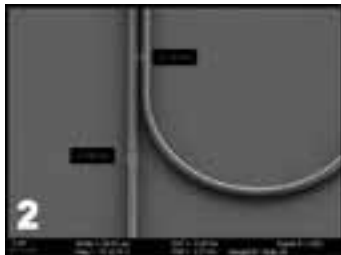


Figure 2: FESEM image of an Si mask demonstrating low surface roughness.

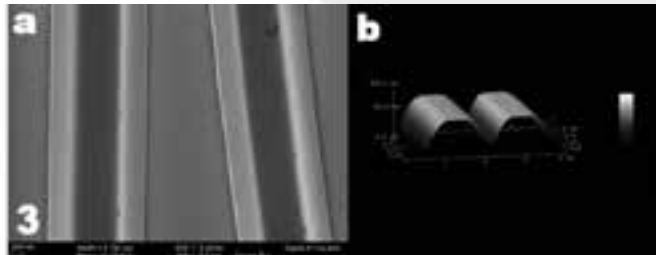


Figure 3: a) SEM image after silicon mask removal of a waveguide and ring resonator with noticeably low surface roughness and sidewall profile. b) AFM 3D image of the waveguide.

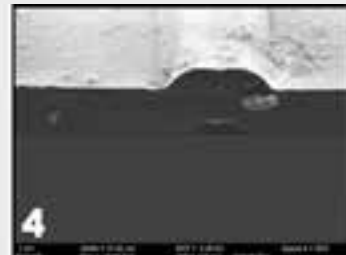


Figure 4: SU-8 waveguide after polishing.

Results:

The silicon mask, shown in Figure 2, has an acceptable sidewall profile and low surface roughness making it a promising hard mask. FOX-16 e-beam resist yielded the most favorable process for the two mask thickness based on field-emission scanning electron microscope (FESEM) images. The thicker resist layer protected the mask from being damaged by the RIE process.

The LN etch resulted in a smooth sidewall, which is important for the confinement of light in the waveguide, see Figure 3. The surface roughness of the structure (Figure 3) was a root mean square (rms) of 0.549 nm surface and 3.52 nm profile as measured with a Vecco NanoMan atomic force microscope. These values represent a relatively low surface roughness compared to results obtained using other fabrication methods. Based on these results, it may be concluded that the silicon mask thickness played an important role on surface roughness. The 800 nm silicon mask yielded a smoother sidewall profile and surface than the 600 nm mask due to better resistance to RIE damage.

Following the fabrication and optimization process, device integration using the SU-8 waveguides appeared to be greatly improved. The waveguides clearly extended to the edge of the sample, and are available to couple in light. The polished ends, as shown in Figure 4, will also be sufficient to not scatter the coupled laser light.

Conclusions:

Fabrication of LN devices with smooth sidewalls and a high aspect ratio has been demonstrated by using a silicon hard mask and RIE. This method has been used to show the potential to fabricate both ring resonators as well as a photonic crystal cavity structures using a silicon mask accompanied by RIE. The next step for the silicon mask process will be to optimize the mask thickness and the LN RIE process to create a steeper sidewall by tuning the RF power [1]. After the LN etch has been optimized, the quality factor, coupling coefficient between the resonator and the waveguide, and the laser coupling coefficient for the SU-8 will be tested. The design process can then be modified to deposit electrodes in order to electrically tune the resonator so as to create a fully functional and tunable modulator for potential use in telecommunications.

Acknowledgments:

I would like to thank my mentor Cheng Wang and Professor Marko Lončar, as well as the staff at the Center for Nanoscale Systems (CNS) for all their assistance. I would also like to acknowledge the NSF and the NNIN REU Program for funding and coordinating this research.

References:

- [1] S. Benchabane, L. Robert, J. Rauch, A. Khelif, V. Laurde, "Highly selective electroplated nickel mask for lithium niobate dry etching," J. of Applied Physics, Vol. 105, pp (094109-1)-(094109-6) (2009).

A Piezoelectric Material P(VDF-TrFE) Thin-Film Process Flow for Ultrasonic Transducers

Mariella Arias

Biomedical Engineering, El Camino College

NNIN REU Site: Cornell NanoScale Science & Technology Facility, Cornell University, Ithaca, NY

NNIN REU Principal Investigator: Amit Lal, Electrical and Computer Engineering, Cornell University

NNIN REU Mentors: Jason Hoople and Po-Chen Cheng, Electrical and Computer Engineering, Cornell University

Contact: ariasmariella.brn@gmail.com, amit.lal@cornell.edu, jth5610@gmail.com, pc445@cornell.edu

Abstract:

Thin-film high-frequency ultrasonic transducers are a good candidate for generating high frequency ultrasound into various materials. The time-of-arrival, dispersion, amplitude, and phase of transmitted and reflected wave pulses can be used to characterize materials such as biological tissue. Piezoelectric polymer transducers are attractive in interrogating biological materials because of good acoustic impedance matching, leading to low voltage drive and higher bandwidth. For these reasons, we developed a microfabrication process for P(VDF-TrFE)-based ultrasonic transducers. The low acoustic impedance of the semi-crystalline copolymer (4.32 MRayls), allows for a better acoustic impedance matching to tissue/water (1.5 MRayls), resulting in increased coupling efficiency. All materials used in this process are CMOS-compatible, which allows for fabrication of transducers directly with CMOS, greatly improving system complexity and integration. Layers in this process were defined using standard contact lithography. The ultrasonic transducers fabricated by this process showed ultrasonic pulse transmission within the frequency range of 400-600 MHz. Signals with amplitudes of 2 Vpp resulted in receive signal amplitudes of 50 mVpp.

Introduction:

There are a plethora of biological applications that would benefit from large scale ultrasonic transducer phased array systems, such as ultrasonic imaging, neural stimulation, and cell trapping. It is of interest to develop a process which will allow the integration of ultrasonic transducers directly with the drive circuits fabricated in a complementary metal-oxide semiconductor (CMOS) process. This could greatly reduce the size and power of the phased array system. Such a system could be utilized to address sensory feedback issues in prosthesis.

Piezoelectric materials, such as bulk lead zirconate titanate and aluminum nitride, are frequently used due to their high coupling coefficient and commercial availability. However, a copolymer of poly[(vinylidenefluoride-co-trifluoroethylene], or P(VDF-TrFE), presents excellent physical characteristics that make it a great candidate for a range of biological applications. The low acoustic impedance (Z_o) (4.32 MRayls) of P(VDF-TrFE) makes this material a good acoustic match

with water/tissue, resulting in more effective ultrasonic energy propagation. The copolymer also presents relatively small dielectric constant (4.0), easing transducer drive circuit design.

Device Fabrication:

All materials used in this process are CMOS-compatible, which allows for fabrication of transducers directly with CMOS, greatly improving system complexity and integration. Figure 1 illustrates left and right cross-sections of a transducer. Layers in this process were defined using standard contact lithography. The process began with an insulating layer of 500 nm PECVD of silicon dioxide (SiO_2) on a 500 μm thick 4-inch wafer. Aluminum bottom and top electrodes, of 210 nm and 250 nm respectively, were evaporated onto the substrate, and defined by wet etching. P(VDF-TrFE), dissolved in 2-butanone (7.00%w/v), was deposited by spin-coating to create a 1 μm thin layer, which was patterned using SPR 220-3.0 photoresist and etched by dry oxygen plasma etch.

After fabrication, an *in situ* electrical poling method was performed to induce piezoelectricity on the P(VDF-TrFE) film. An electrical field of 60 V/ μm was applied on the transducer under 130°C for one hour. The applied voltage was chosen in accordance with the work done by Li, et al. [1] on their fabrication of a piezoelectric tactile sensor using P(VDF-TrFE).

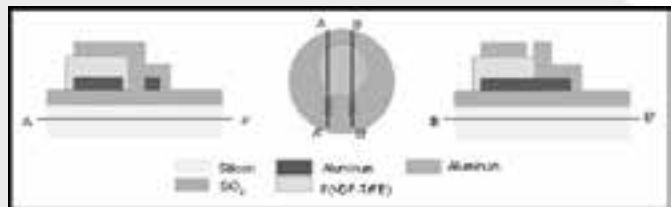


Figure 1: Schematic of fabrication process.

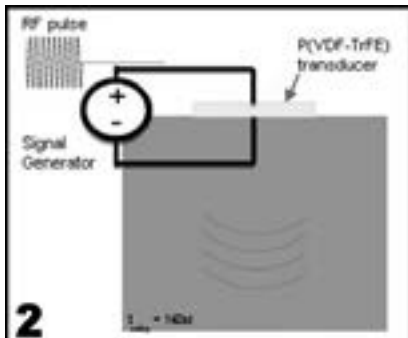


Figure 2: Experimental setup-wave propagation in silicon.

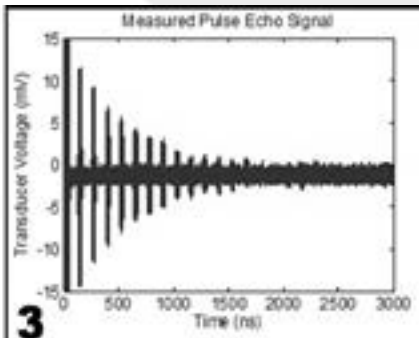


Figure 3: Pulse-echo signals.

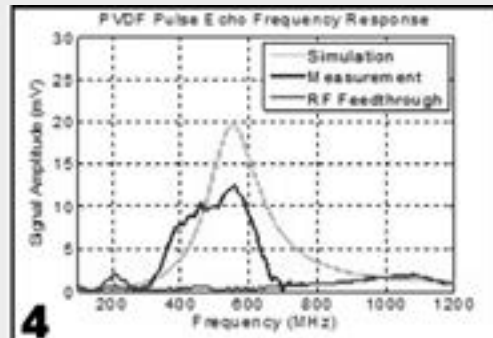


Figure 4: First echo as a function of RF.

Experimental Procedure:

A 40-nanosecond radio frequency (RF) pulse of fixed frequency was applied to the transducer through an RF switch. After approximately 130 ns, a signal was read on an oscilloscope. This signal corresponded to the time of flight of the ultrasound pulse in silicon traveling to the bottom surface, reflecting, and travelling back to the top surface (Figure 2). At the top, the ultrasonic pulse reflected again and made the journey back into the silicon. These repeated reflections were reflected in the captured signals with the same time delay corresponding to the time of flight in silicon (Figure 3).

It was of interest to investigate which signal frequencies allowed for efficient generation of ultrasound. By changing the frequency of the RF signal source, and looking at the amplitude of the first echo, the transducer's frequency response was characterized and plotted on Figure 4. Since the RF switches are not perfect isolators, there existed a small RF feed-through signal at the frequency of interest. The frequency response agreed with the simulation. Discrepancies between the two can be investigated further by considering the acoustic properties of the silicon dioxide layer, as well as considering the radiation pattern losses as opposed to the one dimensional model used for these experiments. The maximum amplitude level detected throughout the samples was 50 mVpp, though the sample here demonstrated a peak value of 24 mVpp. These differences could be accounted for due to RF losses in the printed circuit board traces, cable connections and different wire-bond lengths.

Conclusion and Future Work:

We have successfully characterized a P(VDF-TrFE) process for ultrasonic transducers, and used it to generate ultrasonic waves within the band of 400-600 MHz, using CMOS-compatible materials and processes. Future work will attempt to integrate this process flow with multimodal surgical silicon tweezers for tissue characterization, as well as CMOS for phased array circuit integration. Greater control of the ultrasonic beam is expected to result from the integration of P(VDF-TrFE) transducer arrays directly with CMOS. Alternate poling methods, such as magnetic field poling, will be addressed in the future to allow poling of multiple transducers at a time.

Acknowledgments:

This work was performed using the SonicMEMS laboratory, and the Cornell NanoScale Science and Technology Facility (CNF). I would like to thank Professor Amit Lal, and my mentors Jason Hoople and Po-Cheng Chen for their help and support, as well as the CNF staff. I also want to thank the National Science Foundation and the National Nanotechnology Infrastructure Network Research Experience for Undergraduates (NNIN REU) Program for the financial support and coordination of the program.

References:

[1] Li, C., et al., "Flexible Dome and Bump Shape Piezoelectric Tactile Sensors Using PVDF-TrFE Copolymer", *Journal of Microelectromechanical Systems*, Vol. 17, No. 2, April 2008.

Fabrication of Diamond Microwires for Quantum Information Processing Applications

Wu Joon Cha

Mechanical Engineering, Columbia University

NNIN REU Site: Howard Nanoscale Science & Engineering Facility, Howard University, Washington, DC

NNIN REU Principal Investigator: Dr. Gary L. Harris, Electrical Engineering, Howard University

NNIN REU Mentor: Michelle Chavis, Material Science and Engineering, Howard University

Contact: wc2444@columbia.edu, gharris1124@gmail.com, mac238@cornell.edu

Abstract:

The nitrogen-vacancy (NV) center in diamond has recently emerged as one of the potential candidates for quantum information processing applications due to its good coherence properties. However, interaction with the environment leads to decoherence — loss of quantum state. It has been reported that nanowire structures reduce interaction with the environment and increase coherence time. The purpose of this project was twofold: (1) grow and characterize diamond on silicon wafers, and (2) fabricate diamond microwires and nanowires using photolithography and electron-beam lithography. A hot filament chemical vapor deposition (HFCVD) system was used to grow nanocrystalline diamond on silicon wafers. Lift-off resists (LOR) 10B from MicroChem Corp. and Microposit S1818 from Shipley were used for a bilayer photoresist process followed by chrome (Cr) evaporation and liftoff process. An etch-back process was also studied to generate Cr patterns. Reactive-ion etching was used to etch diamond with an oxygen plasma with an etch rate of ~ 15 nm/min. We achieved ~ 3 μ m sized diamond cylinders, which were characterized using scanning electron microscopy (SEM) and atomic force microscopy (AFM).

Introduction:

Quantum information processing (QIP) is promised to solve certain computational problems by drastically improving acquisition, transmission, and processing of information. Although quantum computers have their advantages, they have limitations: they must be isolated from their environment at low temperatures and the slightest interaction leads to decoherence — loss of quantum state [1].

The nitrogen-vacancy (NV) center in diamond has been proposed as potential candidate for qubit, a basic information unit for quantum computers, for its good coherence properties. The NV-center is formed by two-point defect in the diamond crystal lattice by replacing two carbon atoms with a nitrogen atom and a neighboring vacancy. Because of the particular orientation of electrons, their total spin can be manipulated and easily measured at room temperature [2]. However, when an NV-center interacts with the environment, it loses its coherence easily. Hence, it is important to enhance the coherence duration of the NV-center by reducing its interaction with the environment.

It has been reported that the interaction with the environment is reduced dramatically in diamond nanowires compared to bulk structure [3]. This was shown by comparing their collection efficiency of emitted photon. Having more efficient collection of emitted photon, nanowire structures reduce the interaction with the environment and increase the coherence time. Therefore, it is important to develop fabrication processes for

diamond nanowires. In this work a method of diamond growth was studied and approaches to create micron-sized and nano-sized diamond wires were explored by using photolithography, electron-beam lithography process, and reactive-ion etching.

Methods:

We grew poly-crystalline diamond on silicon substrate via a HFCVD process, which flows current through filaments to increase their temperature in low pressure. The HFCVD system is from Blue Wave Semiconductors. At temperatures above $\sim 1800^\circ\text{C}$, the hydrogen dissociates and interacts with hydrocarbon gas and forms free radicals which are essential for diamond growth. All silicon substrates were cleaned with trichloroethylene, acetone, and methanol, and sonicated in a 1:1 (nanodiamond seed:methanol) solution. We grew at 2300°C . with a ratio of hydrogen to methane of 60:1 or 80:1. The growth rate was approximately 0.25 μ m per hour.

Photolithography was employed in this work. The fabrication processes are shown in Figure 1. A bilayer photoresist process was used for photolithography. Lift-off resists (LOR) 10B from MicroChem Corp and Microposit S1818 from Shipley were used to define etch patterns using a Karl Suss mask aligner. Next, a 150 nm Cr evaporation was performed followed by lift-off with acetone and Microposit Remover 1165 from Shipley that was heated at 90°C for 5 min.

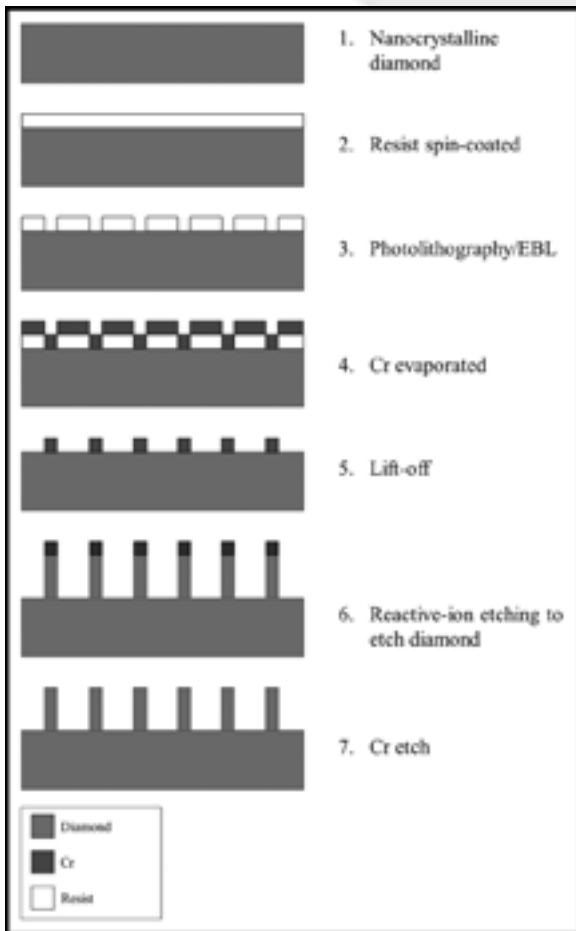


Figure 1: Fabrication process schematic.

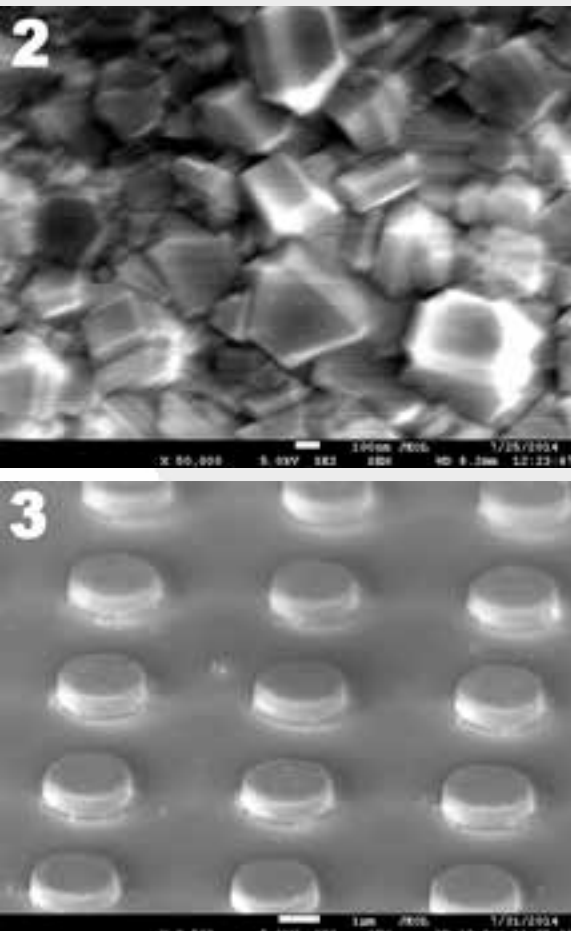


Figure 2, top: SEM image of grown nanocrystalline diamond.

Figure 3, bottom: SEM image of fabricated ~ 3 μ m sized diamond pillars.

Oxygen plasma cleaning was done to de-scum resist residue for effective lithography. Since oxygen plasma etches diamond, we also employed an etch-back process. In the etch-back process, the same lithography condition was used except Cr was deposited before resists.

A reactive-ion etching (RIE) system (Plasma-Therm 790) was used to etch the diamond and Cr. The etch recipe used for diamond etching consisted of an oxygen flow rate of 19.57 sccm, power of 100W and a chamber pressure of 10 mTorr. The etch recipe used for Cr etching consisted of an oxygen flow rate of 15 sccm and a flow rate of 35 sccm for chlorine, power of 50W, and a chamber pressure of 50 mTorr.

Results and Conclusions:

Nanocrystalline diamond was successfully grown as seen in the SEM image in Figure 2, which was characterized by SEM, AFM, and Raman spectroscopy. Micron-sized diamond pillars were successfully fabricated and were characterized by SEM and AFM. An SEM image of fabricated wires is shown in Figure 3. Reactive-ion etching was effective in etching diamond and Cr.

Future work includes fabricating nanowires with gold nanoparticles and electron-beam lithography using similar process. We hope to eventually dope nanocrystalline diamond with nitrogen to create NV-center embedded diamond pillars.

Acknowledgments:

I would like to thank my Principal Investigator, Dr. Gary Harris, my mentor, Michelle Chavis, site coordinator, Mr. James Griffin, collaborator, Ms. Anna-Kaye Barrett, and the staff of the Howard Nanoscale Science and Engineering Facility, the NNIN REU Program, and the NSF.

References:

- [1] C.H. Bennett, and D.P. DiVincenzo, Quantum information and computation. *Nature*. 404, 247-255 (March 2000).
- [2] M. W. Doherty, et al. The nitrogen-vacancy colour centre in diamond. *Physics Reports*. 528, 1-101 (2013).
- [3] B. J.M. Hausmann, et al. Fabrication of diamond nanowires for quantum information processing applications. *Diamond & Related Materials*. 19, 621-629 (January 2010).

Characterization of Ionic Liquid Gels used with Conformable Conducting Polymer and Textile Electrodes used for Electroencephalography

Dakota Crisp

Biomedical Engineering, University of Michigan

NNIN iREU Site: Centre Microélectronique de Provence, Ecole Nationale Supérieure des Mines de Saint Etienne, France

NNIN iREU Principal Investigator: George Malliaras, Department of Bioelectronics (BEL),

Centre Microélectronique de Provence, Ecole Nationale Supérieure des Mines de Saint-Étienne, France

NNIN iREU Mentors: Thomas Lonjaret and Dr. Esma Ismailova, Department of Bioelectronics (BEL),

Centre Microélectronique de Provence, Ecole Nationale Supérieure des Mines de Saint-Étienne, France

Contact: dncrisp@umich.edu, malliaras@emse.fr, thomas.lonjaret@emse.fr, ismailova@emse.fr

Abstract and Introduction:

Current electrodes for electroencephalography (EEG) and electrocardiography (ECG) recordings require the use of a liquid electrolyte to decrease the impedance at the electrode/skin interface. However, the liquid electrolyte can begin to dry within a few hours, limiting the time for usable data to be gathered. Recent efforts have been taken to combat this and other factors, leading to the creation of ionic liquid (IL) gels. IL is a substance that is conductive and liquid at room temperature, but can polymerize, creating a gel, upon UV curing. It has been shown that these IL gels have been mostly on par with its liquid electrolyte counterpart in terms of conductivity, and have also proven to maintain low impedance for much longer durations [1]. Additionally, a new gold (Au) electrode as well as the return of textile electrodes, are on their way to surpassing the performance of the standard medical electrode.

A more adhesive IL gel was produced to further improve the interface coupling. In this report, characterization of these new IL gels was performed, showing that improved adhesion does not compensate for conductivity lost due to deviation from the standard IL recipe. Information concerning trends in impedance with reference to IL gel volume, IL deposition, PEDOT:PSS deposition, and textile versus Au electrodes is also reported.

Device Fabrication:

A flexible Kapton® film sheet of 125 μm was used for the Au electrode substrate. CAD software was used to design the electrode schematics that were patterned on the Kapton sheet using a LPKF electronic laser cutter. Chromium (Cr) followed by Au were evaporated onto the substrate in thicknesses of ~ 30 nm and ~ 100 nm, respectively. Poly(3,4-ethylenedioxythiophene):poly(styrenesulfonate), or PEDOT:PSS, was deposited on the heads of the electrodes.

Our first deposition method used two drop casts. The first was baked at 90°C for 2-3 minutes. The second was baked at 110°C for one hour. Our second deposition method involved four spin

coatings, progressively getting thicker. The spin coater's RPM was as followed for each layer: 1500, 1300, 1000, 650. Finally, a single drop cast was performed.

Our third deposition method used a post-treatment of ethylene glycol. Replicas of these deposition methods were performed using a mixture of PEDOT:PSS and IPA in a 3:1 ratio. General cleaning and O₂ surface activation occurred between each major steps. Textile electrodes were patterned with polydimethylsiloxane (PDMS), saturated in PEDOT:PSS, and then baked at 110°C for one hour.

Ionic liquid gels, supplied by an outside company, came in two components, IL + monomer and photoinitiator. Components were mixed together using specified ratios provided by the company and drop-casted on the heads of previously fabricated Au electrodes. Separate molds were also used as a control to test conductivity versus adhesion. Ultraviolet (UV) curing was performed with curing times that were dependent upon the IL formula being used. Distance between the IL composite and the UV lamp remained a constant 3 cm. For textile electrodes, 20 μl of IL was deposited, followed by another 20 μl of IL composite before curing.

Experimental Procedure:

UV curing times were discovered by drop-casting small samples on a glass slide and using a UVGL-58 handheld UV Lamp, set to long wave-365 nm. Curing intervals of five seconds were performed while physically testing the degree of polymerization between each interval.

Total UV curing time was recorded when samples displayed desired polymerization characteristics. These polymerization characteristics were such that each sample was determined to be solid yet release IL upon physical stimulation. This insured that our samples were reasonably resilient and exhibited conductive capabilities. Samples that were too dry were very adhesive and had low conductivity.

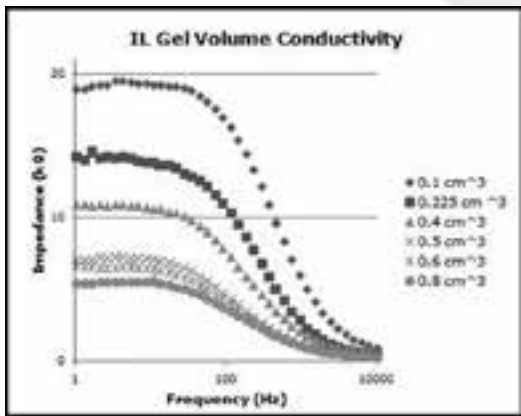


Figure 1: Impedance measurements of different IL gel volumes.

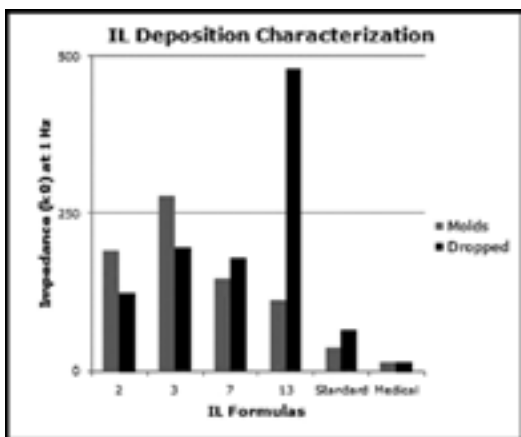


Figure 2: Impedance measurements of different IL formula differentiating drop casting versus external molds.

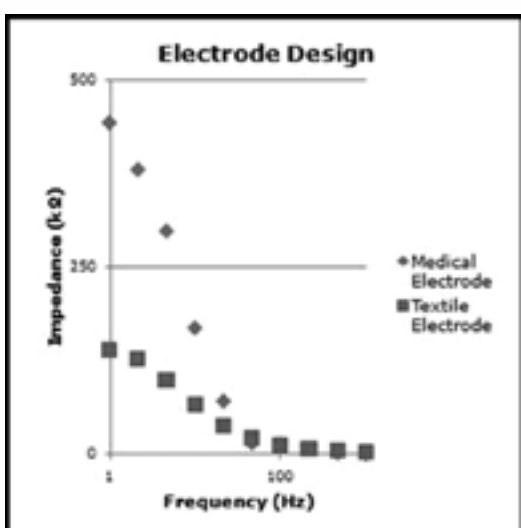


Figure 3: Impedance measurement of textile electrode versus standard medical electrode.

For impedance measurements, a cleaning solution of 75% H₂O and 25% ethanol was applied to the areas of the arm that would host the electrodes. The counter terminal was placed on the posterior side of the forearm, near the wrist. The working/source terminals were placed 3 cm superior to the counter electrode. The reference terminal was placed on the lateral side of the elbow, 20 cm superior of the working and source terminals. Standard medical electrodes were used as a control at the reference and counter terminals while the test electrodes were used at the working/source terminal. After each impedance test, the electrode in question was removed and the area on the skin was cleaned before the next test was performed.

Results and Conclusions:

It was shown that increasing IL gel volume decreased electrode impedance, instead of specifically thickness or surface area. However, this continuous decrease in electrode impedance was not linear and is assumed that a critical gel volume would then decrease conductivity. We also found that while some adhesive IL gels show a significant decrease in impedance when drop-casted directly on electrodes, as compared to an external IL gel mold, they exhibit overall less conductivity than the standard IL gel formula. Additionally, spin-coating four layers of PEDOT:PSS + ethylene glycol and then adding the extra drop-cast greatly improved the adhesion between the PEDOT:PSS and the Au, making it much more durable. However, conductive properties did not change. Finally, it was found that textile electrodes exhibited much less impedance than the Au or standard medical electrode.

Future Work:

Because there is still a potential for adhesive IL gels, more formulas will be synthesized and tested. Additionally, while the new PEDOT:PSS deposition method did exhibit more durable properties, the current process is very time consuming and wasteful of PEDOT:PSS. Thus, a more refined method, or possibly a better method, needs to be found.

Acknowledgments:

I would like to thank the National Nanotechnology Infrastructure Network International Research Experience for Undergraduates (NNIN iREU) Program for this fantastic opportunity. Credit also goes to the National Science Foundation (NSF) for funding. Finally, I would like to thank my PI, George Malliaras, my mentors, Thomas Longaret and Dr. Esma Ismailova, and everyone else at the Bioelectronics Lab (BEL) for all of their help and guidance.

References:

- [1] Leleux, P., C. Johnson, X. Strakosas, J. Rivnay, T. Hervé, R. Owens, and G. Malliaras. "Ionic Liquid Gel-Assisted Electrodes for Long-Term Cutaneous Recordings." *Advanced Healthcare Materials* (2014): Web.

The Effect of Low Temperature Growth and Annealing on the $\text{Al}_2\text{O}_3/\text{In}_{0.53}\text{Ga}_{0.47}\text{As}$ Interface

Megan Hill

Materials Science and Engineering, Cornell University

NNIN REU Site: UCSB Nanofabrication Facility, University of California, Santa Barbara, CA

NNIN REU Principal Investigator: Susanne Stemmer, Materials Department, University of California Santa Barbara

NNIN REU Mentor: Varistha Chobpattana, Materials Department, University of California Santa Barbara

Contact: moh9@cornell.edu, stemmer@mrl.ucsb.edu, varistha@mrl.ucsb.edu

Abstract:

This work summarizes the characterization of the $\text{Al}_2\text{O}_3/\text{In}_{0.53}\text{Ga}_{0.47}\text{As}$ interface grown and annealed at low temperature. Samples were pretreated using atomic layer deposition (ALD) cycles of N*/TMA, then $\sim 3\text{-}6$ nm of Al_2O_3 were grown using ALD and furnace annealed to passivate the interface. Varying the annealing process found that a 250°C forming gas anneal, nearly independent of time, gave the best interface. Additionally nine cycles of N*/TMA was found as the optimum pretreatment giving a maximum midgap D_{it} of $6.85 \pm 0.37 \times 10^{12} \text{ cm}^{-2}\text{eV}^{-1}$. Though a better quality Al_2O_3 film and aluminum oxide/indium gallium arsenide ($\text{Al}_2\text{O}_3/\text{InGaAs}$) interface are achieved at higher temperature, these results show acceptable D_{it} and C-V behavior for use when low temperature processing is necessary.

Introduction:

$\text{In}_{0.53}\text{Ga}_{0.47}\text{As}$ is the leading candidate for post-Si n-channel technology partially due to its low effective electron mass. Additionally, high- κ dielectrics, like Al_2O_3 , grown by atomic layer deposition (ALD) are being explored as gate oxides to prevent current leakage while maintaining high capacitances. However, high surface and interface defect concentrations lead to a high interface trap density (midgap D_{it}) at the $\text{Al}_2\text{O}_3/\text{InGaAs}$ interface. Previous work has shown that *in situ* surface pretreatments using alternating cycles of nitrogen plasma and trimethylaluminum (N*/TMA) can successfully passivate the interface for a 300°C growth and 400°C furnace anneal [1]. However, material limits make it desirable to modify this passivation technique for low temperature processing, working with growth temperatures near 115°C and a maximum annealing temperature of 250°C.

Experiment:

InGaAs/InP samples were initially cleaned using a three minute buffered HF dip in order to remove any surface contaminants. An ALD reactor (Oxford Instrument FlexAL) was used for an *in situ* surface pretreatment and Al_2O_3 growth. The surface was pretreated using N*/TMA cycles, five to nine times, at 115°C. This pretreatment allows for the removal of native oxides and the initial passivation of the InGaAs surface. Immediately following the pretreatment, $\sim 3\text{-}6$ nm of Al_2O_3 was grown using cycles of TMA and water vapor. $\text{Al}_2\text{O}_3/\text{InGaAs}$ samples were then post annealed in either a forming gas or N_2 environment for different times and temperatures below 250°C. Ni contacts (80 nm thick) were then deposited by thermal evaporation using a shadow mask. A Cr/Au contact (20/100 nm) was

deposited on the back of the InP substrate in order to form the metal-oxide-semiconductor capacitors (MOSCAPs) used for electrical measurements. The MOSCAPs were tested using a two-point probe measurement to determine capacitance density and conductance as a function of gate voltage between 1 kHz and 1 MHz.

Results and Discussion:

Conductance and capacitance data was used to analyze the quality of the $\text{Al}_2\text{O}_3/\text{InGaAs}$ interface. The optimum pretreatment and annealing conditions can be found by minimizing the frequency dispersion, but more importantly the midgap D_{it} response. The frequency dispersion is the difference in capacitance between 1 kHz and 1 MHz. This should be minimized both in the accumulation (high bias) and transition regions as seen in Figure 1. A high frequency dispersion can be a sign of a film with high trap densities, current leakage, and channel resistance, which limit device speed and cause break down at high bias [2]. In addition to this, we want to minimize the midgap D_{it} , which is the quantitative estimate of the interface trap density in the InGaAs midgap. The “conductance” method described in Reference 3 uses the measured capacitance and conductance to calculate the D_{it} at 1 kHz.

Figure 2 shows the frequency dispersion as a function of annealing conditions. The lowest frequency dispersion of $2.5 \times 10^{-8} \text{ F/cm}^2$ for the transition and $1 \times 10^{-7} \text{ F/cm}^2$ for accumulation is found for a 15 minute, 200°C furnace anneal in a forming gas environment. However, the D_{it} response (Figure 3) is high for the 200°C case at about $1.1 \cdot 10^{13} \text{ cm}^{-2}\text{eV}^{-1}$.

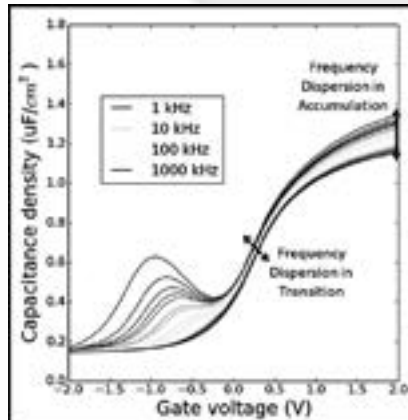


Figure 1: Example C-V curve for Al_2O_3 /InGaAs MOSCAP. Frequency dispersion should be minimized in transition and accumulation regions. (See full color version on page xxxvi.)

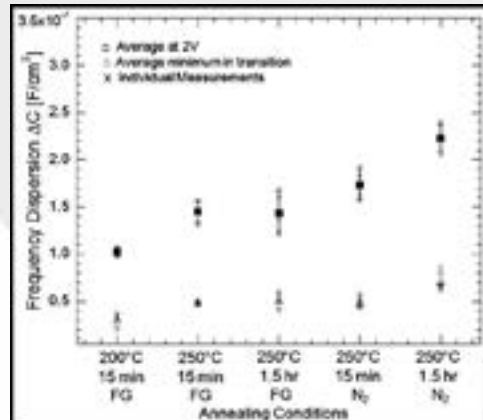


Figure 2: Frequency dispersion in accumulation and in transition versus annealing conditions. Samples were furnace annealed between 200°C and 250°C for 15 to 90 min in either a forming gas (5% H_2 /95% O_2) or N_2 environment.

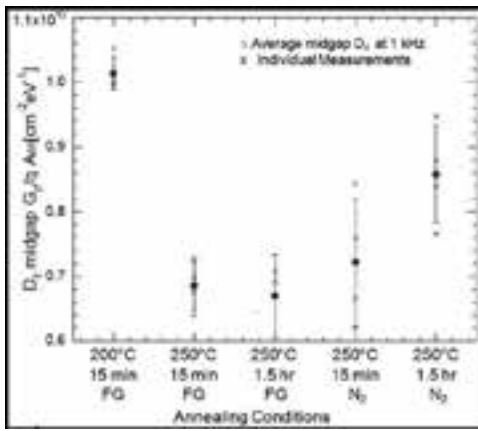


Figure 3: Midgap D_{it} response (estimate of interface trap density) versus annealing conditions.

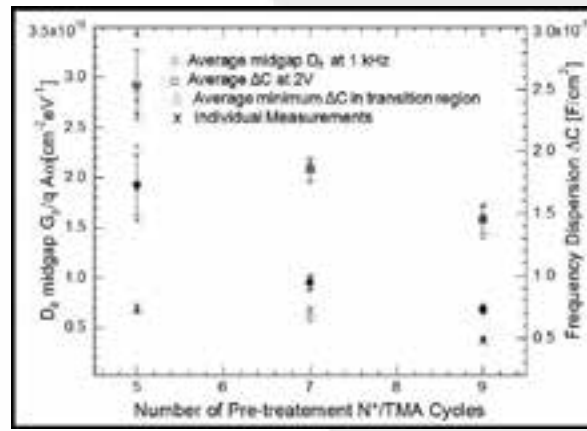


Figure 4: Midgap D_{it} response, frequency dispersion in accumulation, and frequency dispersion in transition versus number of N^*/TMA in situ pretreatment cycles.

A 250°C forming gas anneal gives the lowest D_{it} response with little time dependence.

The frequency dispersion and midgap D_{it} response were also compared to find the optimum number of pretreatment cycles. Figure 4 shows that nine cycles N^*/TMA is clearly the best condition for surface cleaning. It is possible that greater than nine cycles could give slightly better D_{it} results, but it is more likely that additional plasma exposure would damage the InGaAs surface.

Conclusions and Future Work:

It has been shown that it is possible to grow quality Al_2O_3 by ALD even at 115°C. C-V data show reasonable behavior with acceptable levels of current leakage. Additionally, a midgap D_{it} of $6.85 \pm 0.37 \times 10^{12} \text{ cm}^{-2}\text{eV}^{-1}$ has been achieved for a 250°C forming gas anneal with nine cycles of a N^*/TMA *in situ* pretreatment. High temperature processing has reported midgap D_{it} values around $2 \times 10^{12} \text{ cm}^{-2}\text{eV}^{-1}$ after optimization, but this result is still acceptable when low temperature processing is desired [1].

In the future, work may be done to further optimize this recipe by varying the plasma conditions during pretreatment. Additionally, further surface imaging has been started using AFM and SEM to better understand the film morphology and the affect of annealing time.

Acknowledgements:

I would like to thank my P.I. for her support on this project, and especially my mentor for her advice and guidance. Materials and project funding were provided by Northrop Grumman and the NSF. Student funding was provided by the SRC, NSF, and the National Nanotechnology Infrastructure Network Research Experience for Undergraduates (NNIN REU) Program.

References:

- [1] Chobpattana, Varistha, et al. APL 102.2 (2013): 022907.
- [2] Ali, A., et al. Electron Devices, IEEE Transactions 57.4 (2010): 742-8.
- [3] Engel-Herbert, et al. J. of Applied Physics 108.12 (2010): 124101.

Surface Micromachining of Microfluidic Devices

Staci Hill
Chemistry, Middlebury College

NNIN REU Site: Lurie Nanofabrication Facility, University of Michigan, Ann Arbor, MI

NNIN REU Principal Investigator: Professor Jianping Fu, Mechanical Engineering, University of Michigan, Ann Arbor

NNIN REU Mentor: Weiqiang Chen, Mechanical Engineering, University of Michigan, Ann Arbor

Contact: staci@middlebury.edu, jpfu@umich.edu, wqchen@umich.edu

Abstract:

Micro-through-holes were fabricated in thin-films of polydimethylsiloxane (PDMS). Standard photolithography was used to pattern photoresist coated on the PDMS substrate, while reactive ion etching (RIE) using both a capacitively coupled plasma (CCP) system and an inductively coupled plasma (ICP) system was used to transfer desired through-hole patterns from photoresist to underlying PDMS layers. By investigating the independent effects of RF power, total pressure, and gas composition ($SF_6:O_2$), an optimal etch recipe was identified for each RIE system. Optimal recipes were defined by the fastest PDMS etch rate with a respective etch selectivity over photoresist greater than one. Although the ICP system proved to be more time efficient, both systems were able to generate a desired $6\ \mu m$ diameter through-hole pattern with relatively vertical sidewall profiles.

Introduction:

Reactive ion etching (RIE) of thin-films of PDMS has been used to fabricate micro-through-holes for microfluidic devices [1-3]. Previous research has investigated PDMS etch rate trends under varying plasma conditions using hard masks such as aluminum [2-4]. Recently, a new surface micromachining technique reported by Chen, et al. introduced a method to pattern PDMS directly using conventional photolithography [1]. This method serves as an inexpensive patterning technique; however, research regarding the selectivity of the etch is limited. Additionally, the disparities between etching PDMS on a capacitively coupled plasma (CCP) system and inductively coupled plasma (ICP) system have not been characterized.

In this report, we present optimal recipes for etching thin-films of PDMS on both a CCP and ICP system. The plasmas studied were composed of varying ratios of SF_6 and O_2 . As proof of concept, optimal recipes were used to etch $6\ \mu m$ diameter through-holes in a $10\ \mu m$ thick PDMS layer. While both systems fabricated the desired feature, the PDMS etch rate was an entire order of magnitude greater on the ICP system. The etch was more selective using the CCP system; however, qualitative assessments found the ICP system generated less surface roughness and cracking of the PDMS in addition to more uniform features.

Experimental Procedures:

Etch rates of PDMS and photoresist were studied by varying total pressure, gas composition ($SF_6:O_2$), and RF power on both the CCP system (PlasmaTherm 790, Unaxis, Schwyz, Switzerland) and ICP system (LAM 9400, Lam Research,

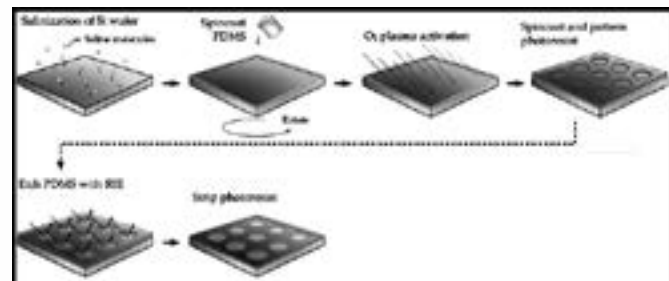


Figure 1: A schematic depicting the surface micromachining protocol used to fabricate micro-through-holes in thin-films of PDMS.

Fremont, CA). Thicknesses of thin-films of PDMS and photoresist were measured using a Dektak XT surface profilometer before and after each etch recipe, in which the difference divided by the total etch time was found to be the respective etch rate. Each recipe was done in triplicate.

Optimal etch recipes were determined based on PDMS etch rate, etch selectivity, and quality of transferred pattern. Optimal etch recipes were used to fabricate $6\ \mu m$ diameter holes in a $10\ \mu m$ thick PDMS film (Sylgard 10:1 base:curing agent), which was achieved by spin-coating PDMS pre-polymer at 7,200 rpm for 35 sec. This fabrication method is illustrated in Figure 1 and adopted from [1].

Results and Discussion:

The determined optimal etch recipes as well as their respective rates and selectivities are reported in Table 1. Optimal etch recipes were determined by selecting the recipe with the fastest

Plasma System	RF Power (Watts)	Total Pressure (mTorr)	Gas Composition	Etch Rate (nm/min)	Etch selectivity
CCP	100	30	100% SF ₆	188	2.6
ICP	500	10	94% SF ₆	1,180	1.8

Table 1: Optimal etch recipes for fabricating micro-through-holes using the surface micromachining method.

PDMS etch rate with a corresponding selectivity greater than 1.0 on both the CCP and ICP systems. A selectivity greater than 1.0 ensured that the 10 μm thick PDMS layer would be etched through prior to the patterned photoresist completely removed by RIE. Because the CCP system was not equipped with a cryogenic chuck, the photoresist would char as either RF power or total pressure increased. As a consequence, desired patterns would erode forming indistinguishable features. Therefore, the quality of the photoresist was also considered when defining an optimal recipe.

The etch rate of the optimal ICP recipe is an entire magnitude greater than the optimal CCP recipe. While the etch mechanism of PDMS is unknown [3] significant difference in etch rates can be attributed to the RF power and gas composition. A cryogenic chuck present on the ICP system allowed for a greater power supply while maintaining the quality of the photoresist. Additionally, the added oxygen was seen to increase the etch rate of PDMS, most likely by readily exposing the silicon in the PDMS to reactive fluorine species of the plasma [4]. Limitations on the CCP system prevented this idyllic ratio of SF₆ to O₂, and a plasma comprised of 100% SF₆ was seen to be optimal.

The features generated by the optimal etches can be seen in Figure 2 (a,b). Each system was able to fabricate features within 100 nm of expected diameter; however, the ICP system produced a clean, vertical sidewall. In contrast, the CCP system generated features with a rough perimeter.

Conclusions:

Both CCP and ICP systems can fabricate the desired micro-through holes. The ICP system proved more time efficient and generated less surface roughness. Due to the high cost of RIE, the possibility of a wet etch should be investigated.

Acknowledgements:

The National Science Foundation and the National Nanotechnology Infrastructure Network Research Experience for Undergraduates (NNIN REU) Program are acknowledged for funding this research. In addition, the support of Professor Jianping Fu and Weiqiang Chen is greatly appreciated.

References:

- [1] Chen, W., Lam, R.H.W., Fu, J.; *Lab Chip* 2011, 12, 391-395.
- [2] Ryu, K.S., Wang, X., Shaikh, K., Liu, C.; *J. Microelectromechanical Syst.*, 2004, 13, 568-575.
- [3] Hwang, S.J., Oh, D.J., Jung, P.G., Lee, S.M., Go, J.S., Kim, J.-H., Hwang, K.-Y., Ko, J.S.; *J. Micromechanics Microengineering*, 2009, 19, 095010.
- [4] Garra, J., Long, T., Currie, J., Schneider, T., White, R., Paranjape, M.; *J. Vac. Sci. Technol.*, A2002, 20, 975-982.

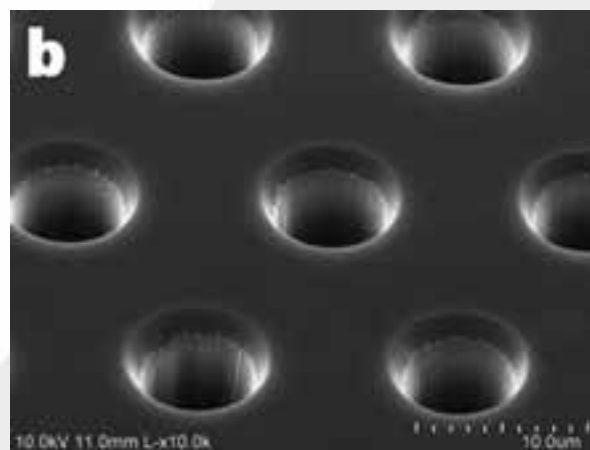
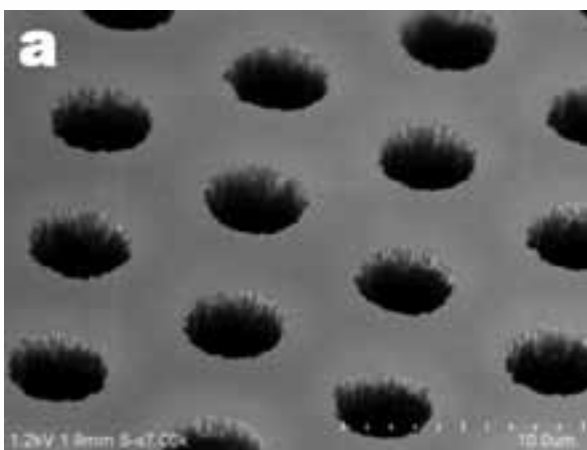


Figure 2: Fabricated 6 μm through-holes using the surface micromachining method etched by; a) CCP system, and b) ICP system.

Fabrication and Characterization of Diamond Field-Effect Transistors

Tiffany Huang
Electrical and Computer Engineering, Baylor University

NNIN iREU Site: National Institute for Materials Science (NIMS), Tsukuba, Ibaraki, Japan

NNIN iREU Principal Investigator: Yasuo Koide¹, Division Director, Research Network and Facility Services Division, (NIMS), Tsukuba, Ibaraki, Japan

NNIN iREU Mentors: Masataka Imura¹, Liu Jiangwei¹, Hirotaka Oosato², Eiichiro Watanabe², and Daiju Tsuya^{1,2}

**NNIN iREU Affiliations: 1. Wide Band-gap Materials Group, Optical and Electronic Materials Unit,
2. Nano-Integration Facility, Nanotechnology Innovation Station; Tsukuba, Ibaraki, Japan**

Contact: tiffanywhuang@yahoo.com, koide.yasuo@nims.go.jp

Abstract:

The next generation of communication technology requires materials that can handle higher frequency and higher power. Diamond's excellent physical properties, such as high band-gap, high breakdown field, and the highest thermal conductivity of all materials, make it ideal for communication applications. Improving diamond field-effect transistor (FET) performance will make diamond viable for such applications. We fabricated and characterized hydrogen-terminated diamond (H-diamond) FETs with an Al_2O_3 gate insulator using laser lithography, e-beam lithography, ozonolysis, e-gun sputtering, atomic layer deposition, microscopy, annealing, and FET device analysis. Challenges of this process included improving the process yield and the drain current. We found that the high stability of the H-diamond surface causing the metal electrodes to easily peel off the surface, causing a low process yield. Optimization of the fabrication process and annealing improved the process yield and the drain current, respectively.

Introduction:

As communication devices advance, they require materials that operate at higher frequency and higher power, and diamond's physical properties make it an ideal material for high frequency power applications. These properties include the highest breakdown field (10 MV cm^{-1}), a wide band-gap energy (5.47 eV), the highest thermal conductivity ($22 \text{ W cm}^{-1} \text{ K}^{-1}$), and the highest carrier mobility (2200 and 1800 $\text{cm}^2 \text{ V}^{-1} \text{ s}^{-1}$ for electrons and holes, respectively) [1, 2]. Improving the performance of diamond FETs would allow the next generation of communication devices to use these properties.

Diamond FETs consist of a gate, source, drain, gate insulator, and hydrogen-terminated diamond (H-diamond) surface [3], as shown in Figure 1a. This H-terminated surface provides hole carriers, and these holes allow current to flow from the drain to the source. Varying the gate voltage and the drain voltage to measure the induced drain current results in an I_d - V_d graph, as depicted in Figure 1b, and these graphs are used to characterize FET performance. FET performance is considered superior when the maximum drain current is higher. In this work, we seek to improve existing fabrication procedures to increase the maximum drain currents.

Fabrication Procedures:

Figure 2 depicts the fabrication procedures performed on H-diamond samples. We first patterned the surface to define FET areas using laser lithography. Defining FET areas involved exposing the sample to ozone in UV light. Oxygen passivated the exposed H-terminated surface, and liftoff left a surface patterned with H-terminated FET areas (Figure 2a). Next, we used e-beam lithography to obtain high resolution patterns for the source-drain electrodes. We deposited palladium (Pd), titanium (Ti), and gold (Au) by e-gun deposition (Pd and Ti acted as adhesion layers), before performing liftoff (Figure 2b). The third step consisted of depositing the gate insulator aluminum oxide (Al_2O_3) by atomic layer deposition (ALD) and defining the gate electrodes. We used laser lithography to pattern the surface, and we evaporated onto the surface Ti (as an adhesion layer) and Au (Figure 2c). Liftoff revealed fully fabricated diamond FETs (Figure 2d).

The previous and improved procedures were alike, except for the third and fourth steps. In the previous procedure, we deposited the photoresist before the Al_2O_3 and gate metal, and liftoff. However, many of the source-drain electrodes peeled off the surface, as shown in Figure 3a, nullifying 10/36 FETs.

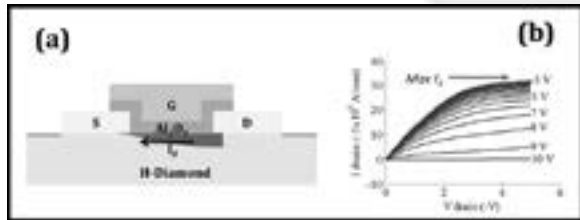


Figure 1: (a) Diamond FET. (b) I_dV_d characteristic of FETs.

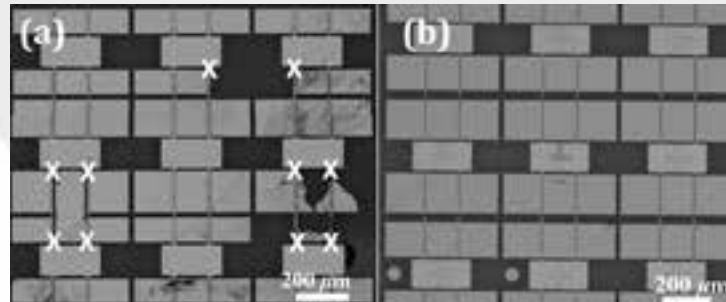


Figure 3: Sample following lift-off in (a) the previous, and (b) the improved processes.

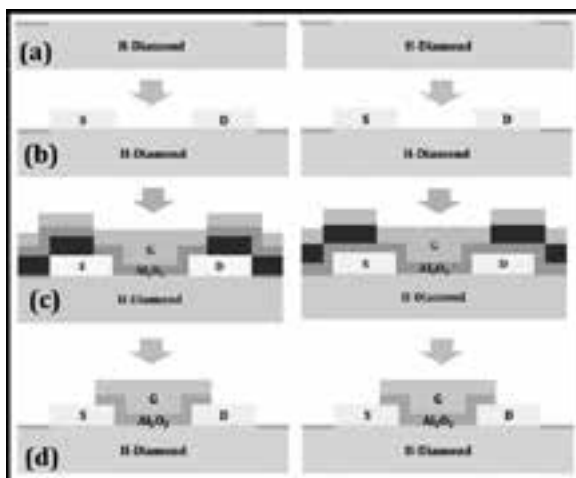


Figure 2: Previous (on left) and improved (on right) procedures for diamond FETs. (a) Defining FET areas. (b) Defining the source-drain electrodes. (c) Depositing gate insulator and defining the gate electrodes. (d) Lift-off to form diamond FET.

In the improved procedure, we deposited the Al_2O_3 before the photoresist and gate metal, and liftoff. This eliminated the peel-off behavior, as shown in Figure 3b. We then annealed the improved sample at 200°C for one hour in vacuum to improve device performance.

Characterization and Results:

Varying the last steps of the procedure eliminated the peel-off behavior due to the stability of H-diamond. The source-drain electrodes were weakly attached to the H-terminated surface. The photoresist to source-drain attachment may be stronger than the source-drain to H-diamond attachment. Thus, lifting off the photoresist may also peel off source-drain electrodes. Passivating the surface with Al_2O_3 removed this effect due to the unique properties of ALD Al_2O_3 . ALD Al_2O_3 is commonly used as a diamond gate insulator, because it both protects and strongly adheres to the H-terminated surface. Thus, passivating the entire surface with Al_2O_3 after defining the source-drain electrodes ensured the source-drain electrodes would not easily peel off.

Figure 4 shows the maximum drain current of the previous and improved process, and it shows the maximum drain current of the improved process post-annealing. Post-annealing significantly increased the average maximum drain currents

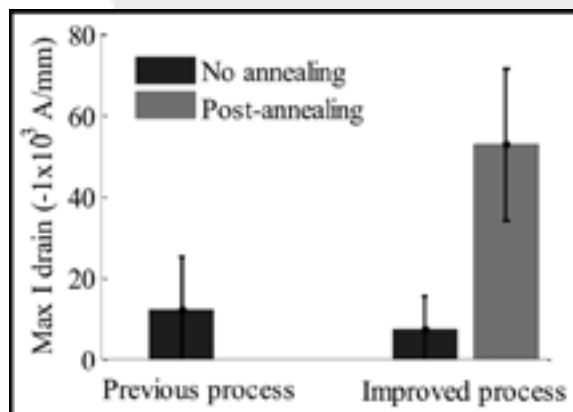


Figure 4: Maximum drain currents for the previous ($n = 7$) and improved ($n = 8$) fabrication processes.

of the procedures from 7.22 mA/mm to 52.6 mA/mm, and following annealing, one sample obtained a maximum drain current of 88.5 mA/mm. Annealing likely reduced the hole trap density in the Al_2O_3 and the interface between the Al_2O_3 and the H-diamond, although further work is needed to verify this hypothesis.

Conclusions and Future Work:

Improvements to the fabrication procedure of diamond FETs eliminated peel-off behavior, and post-annealing significantly increased the drain current of the FETs. Future research involves further investigation of the post-annealing phenomenon.

Acknowledgments:

Many thanks to the following people and groups for their support: M. Imura, L. Jiangwei, H. Oosato, E. Watanabe, D. Tsuya, Y. Koide, NIMS, NNIN iREU Program, and NSF.

References:

- [1] J. C. Angus and C. C. Hayman, *Science* 241 (1988) 913-921.
- [2] L. Reggiani, S. Bosi, C. Canali, F. Nava, and S. F. Kozlov, *Physical Review B* 23 (1981) 3050-3057.
- [3] H. Kawarada, M. Aoki, and M. Ito, *Applied Physics Letters* 65 (1994) 1563-1565.

Graphene Growth by Chemical Vapor Deposition

Laura Huddleston

Electrical Engineering, Georgia Institute of Technology

NNIN REU Site: Howard Nanoscale Science & Engineering Facility, Howard University, Washington, DC

NNIN REU Principal Investigator: Dr. Gary Harris, Electrical and Computer Engineering, Howard University

NNIN REU Mentor: Mr. Crawford Taylor, Electrical and Computer Engineering, Howard University

Contact: llhudd@gatech.edu, gharris1124@gmail.com, crawford@msrce.howard.edu

Abstract:

Graphene is a single layer of carbon atoms that is extremely strong, electrically conductive, transparent, and flexible. These properties lead it to have a variety of applications depending on how it is produced. Chemical vapor deposition (CVD) is the preferred method of production to implement in touch screens, smart windows and solar cells. The focus of this project was to determine the ideal conditions in which to grow graphene via CVD. Based on success in previous graphene experiments, the two materials chosen to use in this project were copper (Cu) and nickel (Ni). The samples were heated to 1000°C and both methane and hydrogen gasses were pumped through the system. Raman spectroscopy was used to characterize the samples, and it showed single-layer graphene on both Ni and Cu. Through this, a range of conditions has been deduced where it is most probable that graphene will grow.

Introduction:

CVD uses high process temperature to produce the high quality graphene needed in solar cells, however, CVD has a high production cost and only moderate sustainability. The goal of this project was to create a controlled environment where graphene could be efficiently reproduced. In order to achieve this goal, growth conditions had to be narrowed down to a specific range of conditions and ratio of gases. Once this was achieved, future work could shift to exploring graphene growth on other substances such as silicon and silicon dioxide.

Experimental Procedure:

The two main materials used were Cu foil and Ni evaporated onto silicon dioxide (SiO_2) wafers. These materials were pretreated by allowing them to soak in trichloroethylene, acetone, and methanol for three minutes each. The Cu was further treated by allowing it to sit in a warm acetic acid bath for five minutes. Ni was evaporated onto the SiO_2 wafers at varying thicknesses ranging from 150 to 3000 Å. The evaporated Ni was later switched out for annealed Ni foil.

Once the materials were placed inside the CVD system, they were annealed with hydrogen at 1000°C for 60 minutes. The methane gas was added to the hydrogen for the next 40 minutes during the growth phase. The furnace was then allowed to slowly cool to room temperature while still flowing the methane and hydrogen gases. Finally, the system was purged with argon for 15 minutes, so that the materials could be removed from the system.

Results and Conclusions:

The substrates were characterized by Raman spectroscopy, and this confirmed successful graphene growth on both Cu and

Ni. The results ranged from no growth to multi-layer graphene to graphite. This allowed the conditions to be narrowed down until a range was found where graphene would consistently grow. Graphene was determined to have optimal growth when hydrogen gas flow was 1-2% of the methane gas flow. A range for Ni was unable to be narrowed to a specific ratio.

The lack of consistent growth on Ni most likely was caused by the amount of Ni evaporated on the SiO_2 substrate. When there was a larger amount of evaporated Ni, it was found to form into beads during the growth process, which inhibited graphene formation. Future research would find the optimum thickness of evaporated Ni and would move on to attempt growth on other materials such as silicon.

Acknowledgements:

I would like to thank the following for their support: PI Dr. Gary Harris, Research Mentor Mr. Crawford Taylor, Site Coordinator Mr. James Griffin, the staff at the Howard Nanoscale Science and Engineering Facility, the National Nanotechnology Infrastructure Network Research Experience for Undergraduates (NNIN REU) Program, and the National Science Foundation.

References:

- [1] Pollard, B.. Growing Graphene via CVD. Thesis. Department of Physics, Pomona College, 2011. N.p.: n.p., n.d. Print.
- [2] "Review of CVD of Graphene and Related Applications." Accounts of Chemical Research 46.10 (2012): 2329-339. Web.

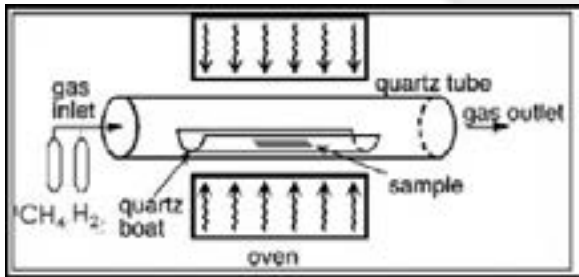


Figure 1: Diagram of simple CVD system.

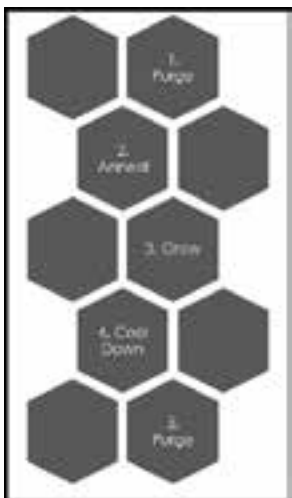


Figure 2: Diagram of CVD growth process.

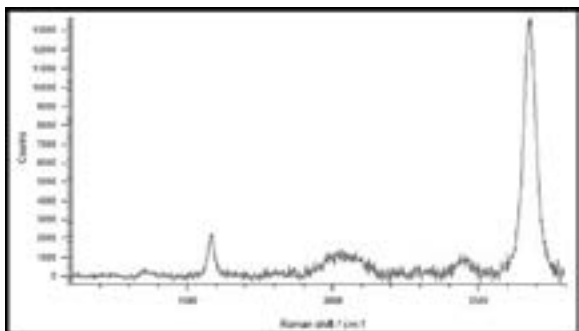


Figure 3: Raman spectroscopy results showing single-layer graphene growth on copper foil.

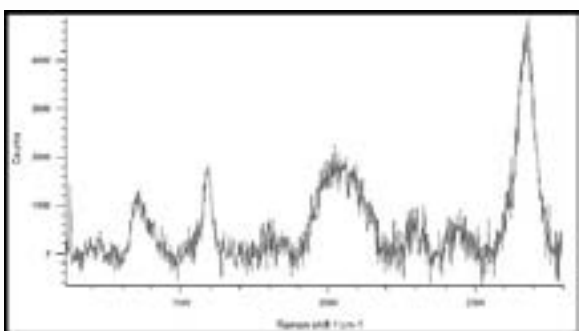


Figure 4: Raman spectroscopy results showing single-layer graphene growth on evaporated nickel.

Microtensiometers with Patterned Porous Silicon

Adriana Mulero

Chemical Engineering, University of Puerto Rico-Mayaguez

NNIN REU Site: Cornell NanoScale Science & Technology Facility, Cornell University, Ithaca, NY

NNIN REU Principal Investigator: Abraham Stroock, Chemical and Biomolecular Engineering, Cornell University

NNIN REU Mentor: Michael Santiago, Mechanical and Aerospace Engineering, Cornell University

Contact: adriana.mulero1@upr.edu, abe.stroock@cornell.edu, ms2343@cornell.edu

Abstract:

The mission of this project was to decrease significantly the porous membrane in our MEMS-fabricated tensiometer [1] to be used as a probe with high spatial-resolution. Following the protocol of Ohmukai [2], we used photolithography with image reversal to pattern the membrane. We modified the membrane's etching recipe since the area coverage was less than original devices. We reported on the characterization of the patterned membranes by optical and electron microscopy and the formation of test devices based on anodic bonding with glass. We concluded with our measurements of permeability of the patterned membranes and perspectives for future experiments and applications.

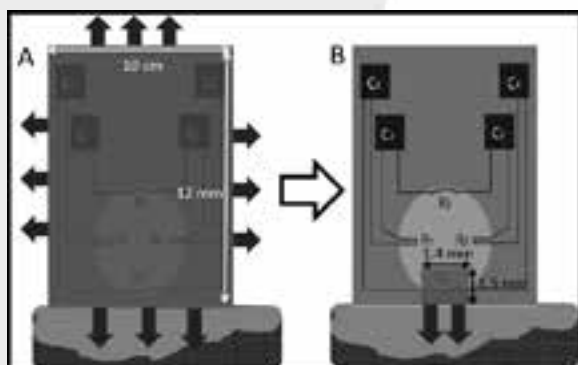


Figure 1: Mission. Two tensiometers measuring a soil sample with varying water potentials. Figure A represents a device with a full membrane receiving information from all its surroundings, while (B), with a smaller membrane, receives information from a specific area (higher resolution).

Introduction:

Our tensiometer quantifies the water potential in plants and soils directly as pressure. It measures the pressure in an internal water-filled cavity that equilibrates with the measured media through a porous silicon (PoSi) membrane, a layer of nanopores electrochemically etched on a silicon wafer. Previously the PoSi connected the cavity with the perimeter of the whole sensor, thus the sensor equilibrated with all its surroundings. Our goal (Figure 1) was to decrease the PoSi so the sensor will have a higher spatial resolution. We faced two main challenges. First, we had to use a technique to decrease the patterned area that did not compromise the bonding process or the ability to sustain large tensions. Second, there was a need to increase the permeability of the PoSi to compensate for the decrease in cross-sectional area relative to the original design.

In a broader view, by characterizing these devices we could improve water management in agriculture by providing *in situ* values of water availability in soils and plants.

Experimental Procedure:

Porous Membrane Patterning. We designed a mask using L-edit with the new porous membrane dimensions, 1.4 mm wide and 1.5 mm tall. The patterning process consisted of basic photolithography steps using S1827 photoresist. We did an image reversal and a hard bake. After the wafer was successfully patterned, we proceeded with creating the pores in the areas not covered by the photoresist.

PoSi Etching. Using the previously-used electrochemical etching setup [1], and a 1:1:2 HF:water:ethanol solution (mixed in a separate container) we were able to create the PoSi. We used the same current density as in the previous versions of the tensiometer's porous membrane of 20 mA/cm^2 , so given the change in the total area coverage from the whole wafer to 1.3%, the current had to change from 900 mA to 12 mA. However, the time the wafer was exposed to the current remained at five minutes. In order to increase permeability, we created bigger holes in some devices by lowering the HF concentration to 21%. After the wafer was successfully etched, it was anodically bonded to glass, diced using the dicing saw, and studied under an optical and electronic microscope.

Permeability Testing. We compared previous devices (full membrane) with new patterned devices with membrane containing small and big pores. The purpose of the tests was to determine how effective these new devices were. Test devices had a $16 \mu\text{m}$ -deep cavity ranging from 1.4 to 2 mm in diameter, and either a full or patterned membrane. First, each device was filled with water at high pressure ($\sim 950 \text{ psi}$) using a pressure

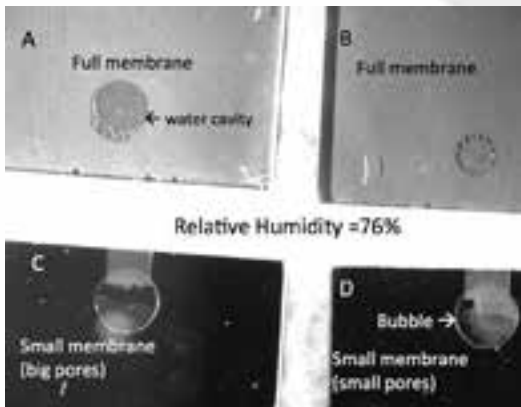


Figure 2: Permeability test. Devices (A) and (B) contain porous membrane covering them completely, while (C) and (D) have the new patterned porous membrane. All four of them (A, B, C and D) have bubbles in the water cavity, which means they have started to empty.



Figure 3: Top view of tensiometer with the new patterned membrane.

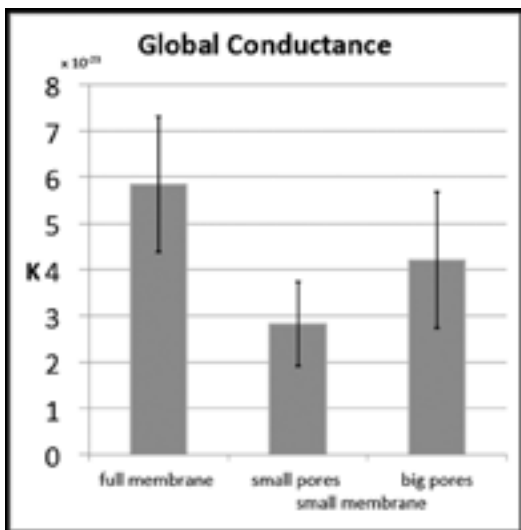


Figure 4: Global water conductance graph.

bomb [1]. Second, three to four water-filled tensiometers were placed in a sealed Petri® dish that contained a saturated NaCl salt solution setting a relative humidity of 76%. Finally, the devices were placed under a stereoscope to record the time each of them took to empty. The experimental setup can be found in Figure 2.

Results and Conclusions:

We successfully decreased the patterned area with photolithography patterning (Figure 3). Regarding its thickness, the membrane was expected to be $\sim 5 \mu\text{m}$ thick, however it measured $\sim 2 \mu\text{m}$. We tried to correct this issue—altering the etching by increasing the current density and the exposure time—but the wafer deformed quickly. One reason for the decrease in thickness was that the larger ratio of edge to bulk etch areas led to a larger portion of the current passing through the edges, decreasing etching of the central area. Also, the devices were bondable.

With the emptying times, the membrane total area coverage, and the Darcy's law, we were able to compare each type's global conductance and permeability. Darcy's law states that the global conductance is directly proportionate to the area of PoSi, so it was expected that the full membrane devices had a higher conductance (Figure 4). The small membrane/small pores devices were two times less conductive than full membrane devices. Bigger pores were created in the patterned devices to compensate for the membrane area loss, however these were not as conductive as wanted. The permeability stayed approximately the same; values ranged from 1.25 to 2.25. We concluded that there is a need to increase conductivity for faster response time.

Acknowledgements:

I want to thank the Cornell NanoScale Facility, the NNIN REU Program, the NSF, the Air Force Office of Scientific Research, and the USDA. A special thanks goes to my mentor Michael and my PI Abe for their constant support throughout the program, along with Melanie-Claire Mallison and Rob Ilic, the CNF program coordinators.

References:

- [1] Pagay, V., et al. *Lab Chip* 14, 2806-17 (2014).
- [2] Ohmukai, M., et al. *J. Mater. Sci.* 16, 119-121 (2005).

Index of 2014 Reports, by Site

NNIN REU & iREG Sites

ASU NanoFab, Arizona State University 14, 52, 66, 98

Cornell NanoScale Facility, Cornell University 2, 32, 42, 60, 94, 126, 134, 148

Institute for Electronics and Nanotechnology, Georgia Institute of Technology 16, 48, 58, 64, 72, 90, 92, 110

Center for Nanoscale Systems, Harvard University 4, 8, 22, 118, 132

Howard Nanoscale Science and Engineering Facility, Howard University 36, 76, 78, 136, 146

Penn State Nanofabrication Laboratory, The Pennsylvania State University 56, 62, 70, 74, 106

Stanford Nanofabrication Facility, Stanford University 26, 46, 54, 84, 88

UCSB Nanofabrication Facility, University of California, Santa Barbara 68, 80, 82, 86, 96, 114, 120, 140

Lurie Nanofabrication Facility, University of Michigan, Ann Arbor 34, 50, 108, 112, 142

Minnesota Nano Center, University of Minnesota-Twin Cities 12, 24, 38, 116, 128

Washington Nanofabrication Facility & Molecular Analysis Facility, University of Washington 6, 30, 44, 124, 130

NNIN iREU Sites

Centre Microélectronique de Provence, Ecole Nationale Supérieure des Mines de Saint Etienne, France 40, 138

National Institute for Materials Science (NIMS), Tsukuba, Ibaraki, Japan 10, 18, 20, 28, 100, 102, 104, 122, 144

Index of 2014 NNIN Interns (in Bold), Mentors, and Principal Investigators

A

Aggarwal, Sunny 56
Ahlfeld, John 48
Aldosari, Haila Mohammed 56
Alford, Patrick W. 38
Alford, T. L. 66
Anderson, William 46
Andrade, Nicolás 132
Antoniou, Antonia 92
Aoyagi, Takao 20
Arias, Mariella 134
Arthur, Samuel 112
Austin, Caitlin 16
Ayazi, Farrokh 110

B

Bao, Zhenan 84
Basu, Anindita 4
Bernardini, Simone 52
Bersch, Brian 74
Bertoni, Mariana 52
Bhatti, Pamela T. 110
Bigelow, Nichloas W. 124
Boehm, Sarah J. 62
Bosworth, Allison 2
Bowman, III, Arthur 122
Brambila, Carlos J. 4
Brower-Thomas, Tina 36
Bruner, Christopher 88
Busche, Jacob 124
Byington, Eve 6

C

Campbell, Stephen A. 12
Cao, Ji 54
Capasso, Federico 118
Ceron, Steven 8
Cha, Wu Joon 136
Chan, Lesley 114
Chavis, Michelle 136
Cheng, Po-Chen 134
Chen, Guoping 28
Chen, Weiqiang 142
Chen, Xiaoshu 128
Chobpattana, Varistha 140
Choi, Jongsoo 108
Choudhary, Prateek 82
Christen, Jennifer Blain 14
Clark, Genevieve 130
Clemens, Bruce 46
Cofell, Emiliana 116
Cola, Baratunde A. 72
Corber, Samantha Renee 10
Crisp, Dakota 138



D

Dauskardt, Reinhold 88
Davidson, Christopher .. 12
Davidson, Patricia 2
Dieke, Nnenna E. 58
Dominguez, Fatima-Joyce 14
Dorfman, Kevin 24
Dulal, Prabesh 116

E

Elborg, Martin 122
Elliott, Alicia M. 60
Emery, Robyn 62
Engstrom, James R. 60
Esch, Mandy B. 32

F

Filler, Michael 90
Foley, Brandon 118
Forest, Craig R. 16
Freas, Dylan J. 64
Frost, Bradley 50
Fu, Jianping 142
Fujita, Daisuke 100

G

Gonzalez, Federico Lora 114
Gordon, Michael J. 114
Griffin, James 78
Gunawansa, Taliya 66
Gupta, Damini 24

I

Imura, Masataka 144
Innocent-Dolor, Jon-L 70
Ismailova, Esma 138

J

Jiang, Jing 94
Jiangwei, Liu 144

H

Hainey, Jr., Mel 70
Hama, Adel 40
Hanagata, Nobutaka 10
Harris, Gary L. 76, 78, 136, 146
Hartensveld, Matthew ... 68
Haslam, Gareth 8
Herrera-Fierro, Pilar 34
Hill, Megan 140
Hill, Staci 142
Hirata, Shinsuke 42
Homsy, Michael 106
Hoople, Jason 134
Hu, Lucy 16
Huang, Tiffany 144
Huddleston, Laura 146
Hui, Ho Yee 90

K

Kang, Samantha 108
Kazanski, Meghan 18
Keating, Christine D. 62
Khumwan, Pakapreud 30
Kim, Deok-Ho 6
Kimura, Yasuhiro 72
Kitamura, Yu 110
Koehler, Matthew 74
Kohl, Paul 48
Koide, Yasuo 144
Kpulun, Tewa 76
Kurtis, Kimberly E. 64



L

Lal, Amit 134
Lammerding, Jan 2
Lanz, A. 66
Lee, Jason 44
Liang, Xiaogan 112
Li, Jasmine 28
Lim, Rachel **78**
Little, Austin **126**
Liu, Guigao 102
Liu, Lulu 118
Lončar, Marko 132
Lonjaret, Thomas 138
López Marcial, Gabriel R. **20**
Lucas, Rachel **80**
Luo, Tao 14
Luscombe, Christine K. 44

M

Madsen, Steven 26
Malliaras, George 40, 138
Mares-Davila, Fausto **48**
Markman, Brian **82**
Martin-Noble, Geoffrey C. **84**
Maruyama, Satofumi 104
Masiello, David J. 124
Maurer, Robert 68
Mazutis, Linas 4
McSkimming, Brian 80, 96
Mellnik, Alex 126
Miller, Julie **50**
Mohney, Suzanne 56
Mori, Takao 104
Morita, Hiromi 10
Morse, David **22**
Motes, Marlee **86**
Mulero, Adriana **148**

N

Nadelman, Elizabeth I. 64
Nakanishi, Jun 18
Namekawa, Koki 20
Ness, Luke **128**
Nietzold, Tara **52**
Nitzberg, G. Emily **88**
Noda, Takeshi 122

O

Ober, Christopher K. 94
Oh, Sang-Hyun 128
Oldham, Kenn 108
Oosato, Hirotaka 144
Owens, Róisín 40



P

Pagkaliwangan, Mark 24

Palmstrøm, Christopher 86, 120

Pendharkar, Mihir 120

Peterson, Rebecca L. 50

Q

Qin, Dong 58

Quillin, Steven C. 124

R

Ralph, Daniel 126

Ratner, Daniel M. 30

Redwing, Joan 70

Ren, John 44

Robinson, Joshua 74

Rodwell, Mark 68, 82

Rose, William 76

Rubenstein, Shmuel 8

S

Sagisaka, Keisuke 100

Sai, Hiroaki 42

Sakaki, Hiroyuki 122

Salmon, Matthew 90

Santiago, Michael 148

Sato, Aki 92

Schmidt, Shon 30

Shah, Ashka 26**Shapturenka, Pavel 94**

Shaw, Leo 84

Shin, Woo Jung 98

Shojaei, Borzoyeh 86

Shuler, Michael L. 32

Sinclair, Robert 26

Singh, Virendra 72

Smith, Bethany 96

Speck, James 80, 96

Stadler, Bethanie 116

Stemmer, Susanne 140

Stone-Weiss, Nicholas . 130

Stroock, Abraham 148

Su, Peter 28

T

Tao, Meng 98

Tatum, Wesley 98

Taylor, Crawford 146

Thompson, Emily 30

Tsui, Jonathan 6

Tsuya, Daiju 144

U

Ueno, Hidetaka 32

V

Vizy, Benjamin 34

W

Wainwright, Kaleel 36

Wang, Cheng 132

Watanabe, Eiichiro 144

Weitz, David A. 4, 22

Wenderott, Jill 100

Wiesner, Ulrich 42

Win, Zaw 38

Wi, Sungjin 112

Wondra, II, James Paul .. 38

Wong, H.-S. Philip 54

Wongpiya, Ranida 46

Woolf, Alexander 118

Wu, Connie 102

Wu, Shanel 54

Wustrow, Allison 104

X

Xia, Yiqiu 106

Xu, Xiaodong 130

Z

Zhang, Wenyu 60

Zhao, Zhao 66

Zheng, Siyang 106

Ziblat, Roy 22

Y

Yang, Yin 58

Yasanayake, Chanud ... 120

Ye, Jinhua 102

Yoo, Daehan 128

Young, Ashlyn 40

Yuasa, Takeshi 42

Yu, Shih-Ying 56





Vac-High

10 kV \times 700